ADVANCES IN DNA-PAINT SUPER-RESOLUTION MICROSCOPY

MAXIMILIAN THOMAS STRAUSS

München 2018

ADVANCES IN DNA-PAINT SUPER-RESOLUTION MICROSCOPY

MAXIMILIAN THOMAS STRAUSS

Dissertation
durchgeführt an der Fakultät für Physik
der Ludwig-Maximilians-Universität
München

vorgelegt von
Maximilian Thomas Strauß
aus Ebersberg

München, 2018

Erstgutachter: Prof. Dr. Ralf Jungmann
Zweitgutachter: Prof. Dr. Petra Schwille

Tag der Abgabe: 30.08.2018

Tag der mündlichen Prüfung: 16.11.2018

ZUSAMMENFASSUNG

Die Fluoreszenzmikroskopie ist seit Langem ein Standardverfahren, welches verwendet wird, um biologische Systeme zu untersuchen. Mit Hilfe der wegweisenden Entwicklung der Superauflösungsmikroskopie ist es möglich, in den Nanometerbereich vorzudringen.

Die Erfolge der DNA-Nanotechnologie in den letzten Jahren haben gezeigt, dass es gelingt, DNS als strukturelles Baumaterial zu verwenden. Ein bekanntes Beispiel ist *DNA-Origami*, mit dessen Hilfe man Strukturen mit beliebigen Formen und Mustern mit Nanometerpräzision erzeugen kann.

Das Zusammenspiel von Fluoreszenzmikroskopie und DNA-Nanotechnologie erzeugt eine effiziente Symbiose: Wissenschaftler sind heute in der Lage, Modellsysteme aus DNS zu bauen, mit denen Fluoreszenzmethoden mit bis jetzt noch nie dagewesener Genauigkeit analysiert werden können. Damit ist es nicht nur möglich, die Fluoreszenzmethoden zu optimieren, sondern auch die Modellsysteme selbst zu charakterisieren. Letztendlich können die optimierten Fluoreszenzmethoden dazu verwendet werden, biologische Systeme mit bisher unerreichter Auflösung zu studieren.

In der vorliegenden Arbeit präsentiere ich Projekte, die an der Schnittstelle von DNA-Nanotechnologie und Fluoreszenzmikroskopie mit Schwerpunkt auf Superauflösungsmikroskopie angesiedelt sind.

Der erste Abschnitt befasst sich damit, wie DNA-Origami als Werkzeug in der Fluoreszenzmikroskopie verwendet werden können. Hierfür werden rechteckige, flache DNA-Origami-Strukturen mit Farbstoffen versehen, um somit eine große Anzahl an unterschiedlichen Konstrukten zu erzeugen, die anhand ihrer Fluoreszenzsignatur eindeutig zugeordnet werden können. Ferner verwende ich die Superauflösungstechnik DNA-PAINT dazu, DNA-Nanostrukturen zu analysieren. Dabei wird die Einbauwahrscheinlichkeit und Verfügbarkeit der DNS-Stränge, aus der eine DNA-Nanostruktur besteht, auf Einzelmolekülebene untersucht.

Im zweiten Teil stelle ich ein Protokoll vor, anhand dessen die Superauflösungstechnik DNA-PAINT durchgeführt werden kann. Dieses beinhaltet alle notwendigen Schritte, von der Probenpräparation, der Aufnahme von Superauflösungsbildern bis zur Datenauswertung und basiert auf dem Computerprogramm Picasso, das eigens für diese Anwendung geschrieben wurde. Als Nächstes diskutiere ich weiterführende

Computertechniken wie die Simulation von Fluoreszenzexperimenten.

Zum Schluss präsentiere ich diverse Weiterentwicklungen von DNA-PAINT, an denen ich gearbeitet habe. Diese zielen darauf ab, die Anwendbarkeit von DNA-PAINT zum Studium von biologischen Systemen zu erweitern. Als Erstes wird eine Methode vorgestellt, mit deren Hilfe die Auflösung durch sequenzielle Bildaufnahme erhöht werden kann. Als Zweites zeige ich einen Ansatz, mit dem absolute Molekülzahlen bestimmt werden können. Als Drittes demonstriere ich die Verwendung von SNAP-tag als Marker zur Bildgebung des NUP107-Proteins der Kernpore mit Hilfe von DNA-PAINT.

ABSTRACT

Fluorescence microscopy is a long established tool to investigate biological systems, with recent groundbreaking technological advancements of super-resolution microscopy it advances in nanometer length scales.

In recent years the advent of DNA nanotechnology has proven the applicability of DNA as a structural building material. A prominent example is *DNA origami*, which allows the creation of structures with arbitrary shapes and patterns with nanometer precision.

The interplay of the achievements in DNA nanotechnology and fluorescence microscopy creates a powerful symbiosis: Researches now can build defined model systems made out of DNA that can be used to benchmark fluorescence methods with unprecedented precision. Not only can these be used to improve and systematically optimize the techniques but also to characterize the model systems. Ultimately, improved fluorescence methods can be used to study biological systems with unprecedented detail.

This thesis contains projects at the intersection of DNA nanotechnology and fluorescence microscopy with a focus on super-resolution.

In the first part, I show how DNA origami can be used as a tool for fluorescence microscopy. For this, a rectangular flat DNA origami structure is decorated with fluorophores to create a large variety of molecular barcodes that can be distinguished by their unique fluorescence signature. Additionally, I present how DNA-PAINT super-resolution microscopy can be used to study DNA nanostructures. Here, the incorporation and accessibility of DNA strands that compose a DNA nanostructure are investigated on a single-molecule level.

In the second part, I present a protocol on how to perform the super-resolution microscopy method DNA-PAINT. The protocol covers all essential steps from sample preparation to image acquisition and data processing, and introduces the software package Picasso that was specifically written for this task. Moreover, I discuss advanced computational techniques such as the simulation of fluorescence experiments.

Lastly, I demonstrate technological advancements for DNA-PAINT that I have been working on to improve its capability to study biological systems. First, I present a method to enhance resolution by sequential imaging. Second, I introduce an approach to perform

absolute counting of molecules. Third, I demonstrate the usage of a SNAP-tag label for DNA-PAINT experiments with super-resolution imaging of the nuclear pore complex protein NUP107.

ACKNOWLEDGEMENTS

I would like to thank my parents, my siblings, and Victoria for their unconditional support. For all the late nights in the lab and having the mind somewhere else.

Thank you, Ralf, for being a great supervisor and friend for the last couple of years. Being part of the Boston-crowd, moving to the MPI and setting up a whole lab and getting everything to run successfully was a fantastic and truly educational experience.

Special thanks to my TAC members Petra Schwille and to Joachim Rädler for helpful feedback and guiding my thesis. Your encouraging words were very much appreciated.

A big thanks to Florian for being a great friend, discussion partner, scientist, and fellow through this journey.

Thanks to Jörg who introduced me to Python programming and educated me on how to write proper code.

Thanks to Philipp for sharing his extensive knowledge of DNA nanotechnology and sharing his ideas on how the sciences should be.

Thanks to Thomas for helping me to get acquainted with the biological sciences.

Thanks to Alex for sharing his knowledge as a physicist.

Thanks to Kimberly for proofreading this thesis.

Last but not least, I want to thank all my collaborators, the current and former members of the group, and all the other people that supported me.

Thank you!

CONTENTS

LIST OF FIGURES

ACRONYMS

bp base pair

BG benzylguanine

DNA deoxyribonucleic acid

EPI epifluorescence

FRET Förster resonance energy transfer

FOV field of view

FWHM full width at half maximum

HILO highly inclined and laminated optical sheet

NA numerical aperture

NeNA nearest neighbor based analysis

NPC nuclear pore complex

PAINT point accumulation for imaging in nanoscale topography

PALM photo-activated localization microscopy

PSF point spread function

SIM structured illumination microscopy

SMLM single-molecule localization microscopy

SNR signal-to-noise ratio

SOFI super-resolution optical fluctuation imaging

STED stimulated emission depletion

STORM stochastic optical reconstruction microscopy

TIR total internal reflection

TIRF total internal reflection fluorescence

TIRFM total internal reflection fluorescence microscopy

1 INTRODUCTION

To study biological systems, it is imperative to gain knowledge of the interplay of the tiniest objects that compose an organism. Even the larger building blocks such as cells, which reach sizes of a few microns, require the magnification of a microscope to be successfully visualized. Here, the resolving power is dictated by the wave nature of light: Higher resolution comes at a price of higher energy. This is disadvantageous when ideally wanting to study the systems in physiological conditions, and exploring of the domain of nanometers was long restricted to electron microscopes. Another challenge arises in the staining of samples: Ideally one only wants to visualize the molecules of interest and not all parts of a cell. For this, fluorescence microscopy is a widely used tool. With the recent advancement of super-resolution microscopy, researchers are now able to investigate structures with nanometer resolution.
Another research area which experienced significant progress in recent years is the field of DNA nanotechnology. The scientist of today is able to create nanometer-sized objects with desired shapes and patterns. For the symbiosis of fluorescence microscopy and DNA nanotechnology this is is a stroke of luck: In order to optimize fluorescence methods, one no longer needs to rely on known biological reference structures which are subject to the intrinsic heterogeneity but now can create defined synthetic reference structure. Complementary to that, fluorescence methods can be used to study DNA nanostructures with unprecedented precision.
In this chapter, I will present a brief introduction to the fundamentals of fluorescence microscopy, super-resolution microscopy, and DNA nanotechnology.

1.1 AN INTRODUCTION TO FLUORESCENCE MICROSCOPY

Fluorescence microscopy has become a standard tool in biology. It allows scientists to directly visualize target molecules by simply attaching fluorescent entities to them and detecting the fluorescent emission. This chapter will give a brief introduction on fluorescence microscopy; its theoretical foundations, Förster resonance energy transfer (FRET), the idea of total internal reflection fluorescence microscopy (TIRFM) and present the components of a typical fluorescence microscope setup.

1.1.1 *Fluorescence*

The foundation of fluorescence microscopy is the phenomenon of fluorescence. In general, the emission of light from any substance that occurs from an electronically excited state is called luminescence. Depending on the underlying mechanism it can be divided into either to fluorescence or phosphorescence. Fluorescence describes the rapid emission of a photon by depletion of an excited state to the ground state with typical lifetimes of nanoseconds. Phosphorescence is the emission from triplet excited states with lifetimes in the range of milliseconds to seconds or longer [1].
An illustrative way of displaying the electronic states or energy levels and their transitions is the Jablonski diagram, named after Aleksander Jabłoński, a polish physicist. A sample Jablonski diagram is depicted in Figure 1.
In essence, a fluorophore can exist in a singlet ground (S_0), first (S_1) and second (S_2) electronic state which each has a number of vibrational energy levels (0,1,2). After light absorption, the fluorophore is excited to a higher level S_1 or S_2. Usually, molecules relax to the lowest level of S_1 in a process called internal conversion. As this process occurs within 10^{-12} s and fluorescence lifetimes are 10^{-8} s the internal conversion is usually complete before emission. An alternative pathway that is

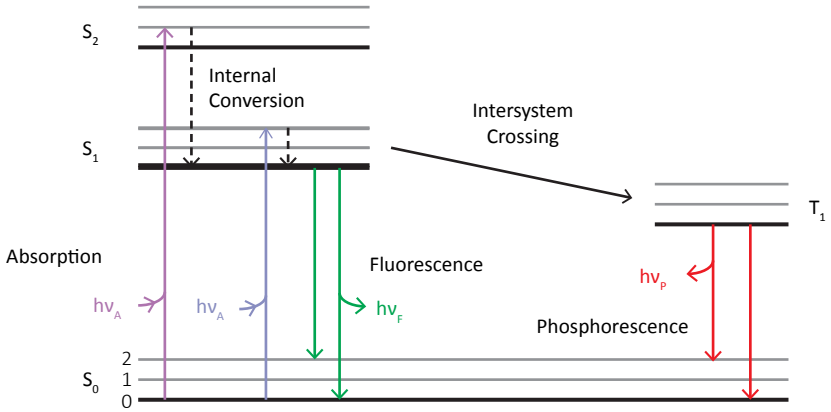

Figure 1: Jablonski diagram. A fluorophore can exist in a singlet ground (S_0), first (S_1) and second (S_2) electronic state that each have a number of vibrational energy levels (0,1,2). After light absorption, the fluorophore is excited to a higher level S_1 or S_2. Usually, molecules relax to the lowest level of S_1 in a process called internal conversion. As this process occurs within 10^{-12} s and fluorescence lifetimes are 10^{-8} s the internal conversion is usually complete before emission. Also displayed is intersystem crossing, which is an alternate pathway, that describes a spin conversion to the first triplet state T_1. Emission from T1 is called phosphorescence. Image adapted from [1].

depicted in the Jablonski diagram is the intersystem crossing, which describes a spin conversion to the first triplet state T_1. Emission from T_1 is called phosphorescence [1].
A key aspect of fluorescence, which is directly visible in the Jablonski diagram, is that the energy of the emitted light is less than the energy of the excitation light. In 1884 Sir George Gabriel Stokes reproduced prior experiments of Sir John Herschel regarding this phenomenon and noted:

> *After passing through this stratum, the incident light, though not sensibly enfeebled nor coloured, has lost the power of producing the same effect, and therefore may be considered as in some way or other qualitatively different from the original light* [2].

What is being observed, the loss of power is termed Stokes Shift; the emission wavelength is longer than the excitation wavelength, it is redshifted. Ultimately, this is the foundation for a fluorescence microscope as excitation light can be separated from emission light. The magnitude of the Stokes shift can be influenced by solvent effects, excited-state reactions, complex formation, and/or energy transfer.

1.1.2 *Förster resonance energy transfer*

FRET describes the phenomenon that energy absorbed by a fluorescence molecule, termed donor dye, is transferred to another nearby molecule, termed acceptor dye, by resonance energy transfer. This energy transfer happens through nonradiative dipole-dipole coupling and is distance-dependent. By coupling a FRET donor-acceptor pair to two molecules of interest and recording their fluorescence intensity, it can be used to measure distances or observe changes in distance. A FRET donor-acceptor pair can be characterized by their FRET-radius R_0, the distance at which the FRET efficiency E is 0.5. Typical FRET-radii are in the range of 5 nm to 8 nm. The FRET efficiency varies as the inverse 6th power of the distance [1, 3]:

$$E = \frac{1}{1 + (\frac{r}{R_0})^6}.$$

FRET can happen when the emission spectrum of a donor dye is overlapping with the excitation spectrum of an acceptor dye, as it is illustrated in Figure 2. In Chapter 2, FRET will be discussed as an effect that occurs when placing spectrally different fluorophores on a DNA origami nanostructure with neighboring distances as close as 5 nm, being in the range of typical FRET-radii. Here, FRET distorts the excepted fluorescence signature and is successfully prevented by organizing fluorophores in columns and separating spectrally different fluorophores.

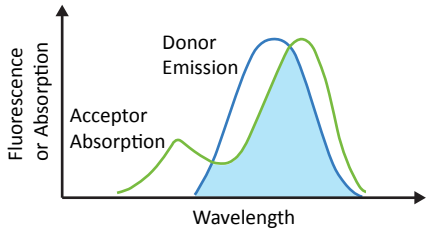

Figure 2: Requirement for FRET. FRET can happen, if the excitation spectrum (Acceptor Absorption, green) of an acceptor dye is overlapping with the emission spectrum of a donor dye (Donor Emission, blue). Energy transfer happens through nonradiative dipole-dipole coupling when the dye pair is in close proximity. Image adapted from [1].

1.1.3 *The fluorescence microscope*

As previously highlighted, the underlying principle of a fluorescence microscope is the Stokes shift. It allows to separate the excitation light from the emission light of the sample and thus allows efficient detection of fluorescence.
The working principle of a fluorescence microscope can be readily comprehended when following the light path through the microscope as it is displayed in Figure 3.
First, light is emitted from a light source, which can range from lamps (e.g., mercury-arc or tungsten-halogen) that emit broad spectra to light-emitting diodes with narrow spectra and lasers with defined wavelengths. The light travels through an excitation filter that only passes the wavelengths desired for excitation and blocks all unwanted wavelengths. In order to achieve fluorescence, the excitation light must overlap with the excitation spectrum of the fluorophore. The filtered excitation light passes a dichroic mirror that is reflective for the excitation light and transparent for the emission light. The mirror is placed at a 45-degree angle so that the emission light is reflected at a 90-degree angle. The beam is then guided to an objective and ultimately to the sample. Upon illuminating the sample, it exhibits fluorescence which is captured by the objective. The resulting wavelength is red-shifted for which the dichroic mirror is transparent. The emission light travels through and additionally gets filtered by an emission filter. Typically, excitation filter, dichroic mirror, and emission filter are assembled in a so-called filter cube. Having several filter cubes allows fast switching of the filter sets for different excitation and emission wavelengths. Ultimately, the emission light then is detected, e.g., by the eye or a camera.

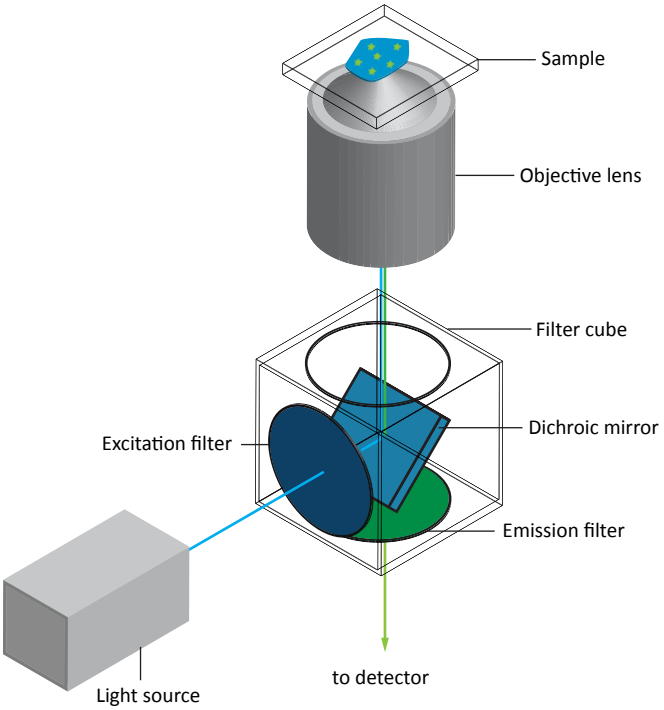

Figure 3: Lightpath of a fluorescence microscope. Light travels from the light source through the filter cube. It is filtered by an excitation filter, reflected by the dichroic mirror and directed to the sample plane by an objective. The illumination of the sample with excitation light causes fluorescence, that is guided through the objective, the dichroic and emission filter and projected onto a detector.

1.1.4 *Total internal reflection*

Depending on how the excitation beam passes through the sample, different modes of illumination can be distinguished. This is illustrated in Figure 4. Before entering the sample, the light path is parallel to the optical axis of the objective. If the beam is coupled to the center of the objective, it will illuminate a vertical column through the sample. This illumination mode is termed EPI. Here, the deep penetration of the sample will create a significant background signal. The light path can be shifted parallel to the optical axis (Δx), causing the illumination column to tilt. This allows to increase the signal-to-noise ratio (SNR), the imaging at a steep angle is known as HILO [4]. Once a critical angle is reached, the beam is reflected, which is known as TIR. The first case to use TIR as a mode of illumination for fluorescence was demonstrated in 1956 by E.J. Ambrose:

> *In order to study the contacts formed between cells and solid surfaces, it is possible to make use of the slight penetration of light waves into the less dense medium when totally internally reflected at a glass/water interface* [5].

The nature of this slight penetration was described in more detail by Daniel Axelrod in 1981, who extended this concept to the idea of TIRFM. Specifically, this light is an electromagnetic field, named *evanescent*

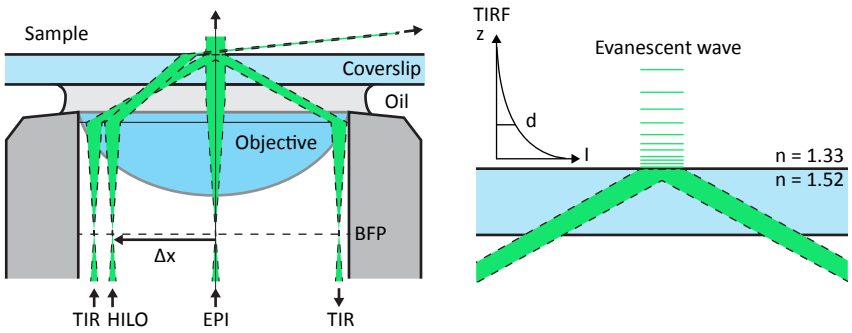

Figure 4: Modes of illumination and TIRF. Left: Depending on the orientation of the light path, different modes of illumination can be distinguished. If the beam is centered within the objective, it will illuminate a vertical column through the sample. This illumination mode is termed EPI. When shifting the beam path parallel to the optical axis (Δx) the sample is illuminated at a steep angle. This mode is known as HILO. Once a critical angle is reached, the beam is reflected, and TIR is reached. Right: Illustration of total internal reflection fluorescence TIRF. When achieving total internal reflection, the sample is illuminated by an evanescent wave that is exponentially decaying. The evanescent wave can be described with a characteristic penetration depth d which is in the order of hundreds of nanometers. This allows to illuminate a small area close to the surface and successfully reducing background fluorescence. Image adapted from [4].

wave that propagates parallel to the surface and experiences an exponential decay and hence significantly decreases background fluorescence [6]. The evanescent wave is depicted in Figure 4 and can be described with the following equation:

$$I(z) = I_0 \cdot exp(\frac{-z}{d}).$$

With I_0 being the Intensity at the surface, $I(z)$ the intensity at the position that is z away from the surface and d the characteristic penetration depth.
Knowing the refraction indices n_1 of the incident medium and n_2 of the sample as well as the incident angle, the penetration depth can be calculated as follows [7]:

$$d = \frac{\lambda}{4\pi} \frac{1}{\sqrt{{n_1}^2 sin^2(\Theta) - {n_2}^2}}.$$

The incident angle can be readily calculated when considering Snells' law:

$$\frac{sin\Theta_1}{sin\Theta_2} = \frac{n_2}{n_1}.$$

For total internal reflection $\Theta_2 = 90°$. Estimating for the glass ($n_1 = 1.52$) and water ($n_2 = 1.33$) intersection gives an incidence angle of:

$$\Theta_1 = arcsin(\frac{n_1}{n_2}) = arcsin(\frac{1.33}{1.52}) = 61.04°.$$

The range of angles at which an objective can accept or emit light is typically characterized by its numerical aperture (NA) $= n \cdot sin(\Theta)$. This implies that total internal reflection can only be achieved for high NA objectives that have NA $> n_2$.
For a wavelength of $\lambda = 561\,\text{nm}$ the penetration depth can be readily estimated to be:

$$d(65°, 561\,\text{nm}) = \frac{\lambda}{4\pi} \frac{1}{\sqrt{{n_1}^2 sin^2(\Theta) - {n_2}^2}} = 68.04\,\text{nm}.$$

Therefore, the intensity at a distance of $z = 100\,\text{nm}$ is only approximately 23% of the intensity at the surface:

$$\frac{I(z)}{I_0} = exp(\frac{-z}{d}) = exp(\frac{-100\,\text{nm}}{68.04\,\text{nm}}) \approx 0.23.$$

This highlights the potential of this technique to perform studies close at the glass surface with little background fluorescence.

1.2 SUPER-RESOLUTION MICROSCOPY

In 1873, Ernst Abbe proposed that a microscope has, regardless of its magnification, a fundamental limitation in its capability to resolve structures.

> *.. so folgt, dass, wie auch das Mikroskop in Bezug auf die förderliche Vergrösserung noch weiter vervollkommnet werden möchte, die Unterscheidungsgrenze für centrale Beleuchtung doch niemals über den Betrag der ganzen, und für äusserste schiefe Beleuchtung niemals über den der halben Wellenlänge des blauen Lichts um ein Nennswerthes hinausgehen wird.*

More specifically, he noted that:

> *.. die physikalische Unterscheidugnsgrenze dagegen hängt allein vom Oeffnungswinkel ab und ist dem Sinus seines halben Betrages proportional* [8].

By extending this rule with the diffraction index of the sample n, Hermann von Helmholtz was able to condense this into the well-known equation one year later [9]:

$$d = \frac{\lambda}{2n\sin\alpha} = \frac{\lambda}{2NA}.$$

With d being the smallest distance between two lines that can be resolved and α the maximal half-angle of the cone of light that can enter or exit the lens. When illuminating a sample with a green laser (i.e., 561 nm) and using an objective with a NA of 1.45 this would be $d = \frac{561\,\text{nm}}{1.45} \approx 387\,\text{nm}$. Note that this a sample calculation for conventional microscopy which assumes that no excitation and emission occurs and thus only considers one wavelength.
For fluorescence microscopy, where emission and excitation wavelength are shifted, and the emission light originates from the dye, an intuitive way to understand resolution is presented by the Rayleigh criterion, which originates from astronomy. When an optical system images a point-like emitter (in the case of fluorescence microscopy a fluorophore),

it is not imaged as a point but as the diffraction pattern of the system's effective aperture. This pattern, also known as *Airy-disc*, is referred to as the point spread function (PSF). When thinking about resolving of two points in close vicinity, the Rayleigh criterion states that the two points are resolved if the central maximum of the diffraction pattern from the first point coincides with the first zero of the second point's diffraction pattern [10]. Mathematically it can be described as:

$$d_R = 1.22\frac{\lambda}{2NA}.$$

Other ways to asses resolution include Sparrow's resolution limit and full width at half maximum (FWHM) $\approx 2.3548\sigma$.
With the advent of super-resolution microscopy techniques, researchers are able to overcome these fundamental limitations. Breaking the diffraction limit of light allows fluorescence microscopy to explore cells with unprecedented resolution. The significance of this advancement was highlighted when in 2014 the Nobel Prize in Chemistry was awarded to Eric Betzig, Stefan W. Hell and William E. Moerner *for the development of super-resolved fluorescence microscopy.*
In general, super-resolution methods can be divided into two groups, depending on their underlying working principle: Methods that engineer the illumination pattern (structured illumination microscopy (SIM) and stimulated emission depletion (STED)) and those that are single-molecule-localization-based (photo-activated localization microscopy (PALM) and stochastic optical reconstruction microscopy (STORM)). In the following sections, the techniques are briefly discussed.

1.2.1 *Stimulated emission depletion*

The idea behind STED is to increase resolution by inhibiting fluorescence in the outer regions of the PSF. For this, a scanning beam, as in confocal microscopy, is used. The beam is overlayed by an additional STED beam. It is meant to deplete the excited state of the fluorophore by stimulated emission before fluorescence takes place [11].
The most common approach for depletion is making the STED beam doughnut-shaped [12] by using a helical phase ramp. The achievable resolution of STED is ultimately limited by the doughnut's capability of reducing the PSF and hence shows an inverse square-root proportionality to its saturation intensity I_S [13]. It can be approximated as an extension of Abbe's equation [9]:

$$d(I) = \frac{\lambda}{2NA} \cdot \frac{1}{\sqrt{1 + \frac{I}{I_S}}}.$$

1.2.2 *Single molecule localization microscopy*

Another way to achieve super-resolution microscopy is by single-molecule localization-based approaches, also known as single-molecule localization microscopy (SMLM). Here, target molecules are stochastically changing between an ON- and OFF-state during continuous illumination, which becomes apparent as blinking. This allows the observation of individual molecules one at a time. The PSF that arises from a single molecule can be fitted to determine the center position of the molecule with subdiffraction precision. The localization precision of such a fit will strongly depend on the SNR of the image. Thompson et al. laid the theoretical framework to estimate the localization precision of such a fit [14]. Hence, the error in localization Δx can be calculated as follows:

$$\langle (\Delta x)^2 \rangle = \frac{s^2 + a^2/12}{N} + \frac{4\sqrt{\pi s^3 b^2}}{aN^2}.$$

Here, the first expression is referring to the photon-counting and pixelation noise (with s being the standard deviation of the PSF and a the size of the pixel), and the second expression to the background noise b. As for large photon numbers N, the first part dominates the equation. Therefore the localization precision scales with the inverse square root of the number of photons that are fitted: $\Delta x \approx \frac{1}{\sqrt{N}}$.
In PALM, the blinking behavior is created by attaching photoactivatable fluorescent protein (PA-FP) molecules to the structure of interest and stochastically activating them until depletion [15]. In the same year, Hess et al. published the idea of fluorescence photoactivation localization microscopy, FPALM, where PA-GFP molecules were used [16].
In contrast to PALM, STORM uses photoswitchable organic fluorophores instead of fluorescence proteins [17].
A recent development that combines the doughnut-shaped STED beam and single-molecule localization is called MINFLUX, *minimal emission fluxes*, that achieved a localization precision of $\approx 1\,\text{nm}$ [18].
Another way to achieve blinking behavior is point accumulation for imaging in nanoscale topography (PAINT) [19]. Here, instead of having fixed fluorophores at the target molecule, freely diffusing dyes or dye-labeled ligands [20] are used. Each probe that hits the structure of interest and becomes immobilized can be localized.

1.2.3 *DNA-PAINT*

A variation of the PAINT approach is called DNA-PAINT. Here, transient DNA hybridization is used to create programmable blinking behavior. A DNA-PAINT system consists of a docking strand and an imager strand, both being short complementary single-stranded DNA oligomers. The

docking strand is attached to the target structure, while the imager strand has a fluorophore coupled to it and diffuses freely through the imaging solution, as it is depicted in Figure 5. In this state, the diffusing imager strands are detected as background signal as they diffuse over several pixels during the integration time of one frame, resulting in an OFF-signal. Upon binding of an imager strand to a target strand, the signal locally increases, and the binding event can be detected as an ON-signal. This binding and unbinding of a DNA-PAINT system on the surface can be roughly described as a pseudo-first-order reaction which is characterized by an association (k_{ON}) and dissociation rate (k_{OFF}) [21]:

$$A + B \underset{k_{OFF}}{\overset{k_{ON}}{\rightleftharpoons}} C.$$

Here, A is the imager strand, B the target strand and C the duplex. Then, the average time spent in the ON-state τ_B (*bright* or *bound* time) is defined as:

$$\tau_B = \frac{1}{k_{OFF}}.$$

The ON state is designed to be transient by using oligomers that are 8-10 nucleotide long, resulting in τ_B values in the range of hundreds of milliseconds to seconds in imaging buffer. The dissociation rate is exponentially dependent on the duplex length, hence as a rule of thumb, τ_B increases one order of magnitude for each base pair (bp) added. Reported values for a 9 bp interaction are 0.625 s and 5 s for a 10 bp interaction [21]. Consequently, the binding and unbinding creates a blinking

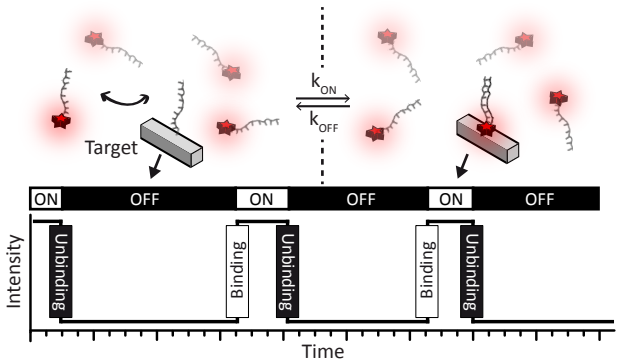

Figure 5: DNA-PAINT. A target structure is decorated with a docking strand that is the reverse complement to imager strands with fluorophores in solution. Upon binding of the imager strand to docking strand, the signal intensity locally increases. Repeated binding and unbinding becomes apparent as blinking and can be used for super-resolution microscopy.

fluorescence signature and can be used for super-resolution microscopy. The binding duration can be precisely tuned by changing the strand length, GC content, temperature or buffer salinity. Additionally, the frequency of binding can be tuned by either changing the concentration of imager strands c or the association constant k_{ON}. Here, the average time in the OFF-state τ_D (*dark* or *dissociated* time) is defined as:

$$\tau_D = \frac{1}{k_{ON} \cdot c}.$$

DNA-PAINT kinetics are described in more detail in Chapter 3 when the *in silico* simulation of DNA-PAINT data is discussed.
The tunability of τ_D and τ_B when using DNA-PAINT allows one to collect large photon numbers and achieve very high localization precision in the subnanometer-range. A key advantage of DNA-PAINT is that multiplexing through orthogonal DNA sequences is possible. In this approach, termed Exchange-PAINT [22], targets are labeled with orthogonal sequences. By sequential imaging of one target at a time and subsequent buffer exchange, multiple targets can be recorded using the same dye. This circumvents the limitation of being restricted to spectrally distinct dyes and bypasses chromatic aberration corrections. I will introduce a technique that uses Exchange-PAINT to increase resolution in Chapter 4. As the blinking of DNA-PAINT originates from DNA hybridization it is highly predictable and can, therefore, be used to gain quantitative information. Even if a spot cannot be resolved, its kinetic signature can be used to estimate the number of DNA-PAINT docking sites within. This technique is called qPAINT [23] and will be discussed in more detail in Chapter 4.

1.3 DNA NANOTECHNOLOGY AND DNA ORIGAMI

This section will give an introduction to DNA nanotechnology starting with the properties of deoxyribonucleic acid (DNA), which is followed by a brief historical overview of the key developments of DNA nanotechnology and DNA origami.

1.3.1 *Properties of DNA*

While DNA is widely known as the carrier of genetic information, it is also a biopolymer with remarkable properties that make it ideal to use as a programmable building block for the creation of DNA nanostructures. DNA consists of two long polynucleotide chains that are composed of four different nucleobases, *adenine* (A), *cytosine* (C), *guanine* (G) and *thymine* (T). Each nucleobase is covalently linked to a phosphate and sugar, and this subunit is called nucleotide. The sugars and phosphates form an alternating chain also known as the *backbone*. Per convention, the 5'end of the DNA polymer carries a phosphate group, while the 3'-end has a hydroxyl group. [24]. The shapes and chemical structures of the bases allow hydrogen bonds to form between A and T and G and C. For A and T, two bonds form, while for G and C three bonds form. This *complementary base pairing*, which is commonly known as the Watson-Crick base pairing, enables the base pairs to form a three-dimensional structure, the double-helix that is the energetically most favorable arrangement. Here, the coiling of two strands creates two grooves, a wider major groove, and a smaller minor groove. Ultimately, Watson-Crick base pairing enables to design programmable binding interactions for supramolecular assembly. This is the foundation of DNA nanotechnology.

As the base pairs are horizontal in the double helix, their π bonds can interact with each other. This phenomenon, called π stacking or base stacking, is reported to be the main stabilizing factor in the DNA double helix [25].

Reported values for B-DNA which is the typical form for base pairing in standard conditions are 10.5 nucleotide pairs per turn with a center-to-center distance between adjacent nucleotides of 0.34 nm and a diameter of 2 nm with a right-handed helix.

For a schematic overview of the DNA double helix and the chemical structure refer to Figure 6. In the context of this thesis *ssDNA* will refer to single-stranded-DNA while *dsDNA* refers to the duplex.

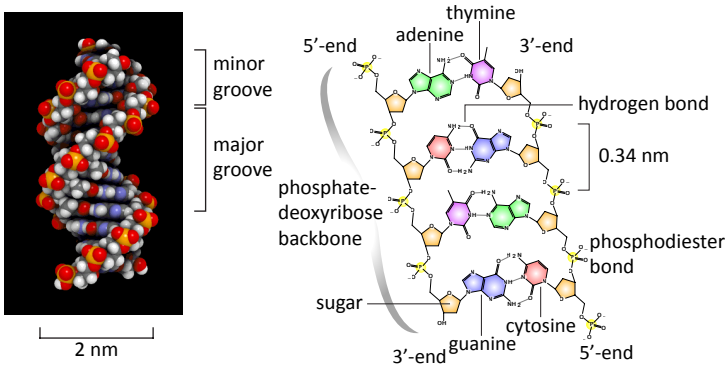

Figure 6: The DNA double helix. The left image shows a space-filling model of the DNA double helix that shows the major and minor groove. The right side shows the chemical structure of DNA. For B-DNA, each turn is made up of 10.5 nucleotide pairs with a center-to-center distance between adjacent nucleotide pairs being 0.34 nm. The nucleobases are held in place by a chain of phosphates and sugars. Per convention, the 5'-end of the DNA polymer is carrying a phosphate group, while the 3'-end has a hydroxyl group. Bases form either two (A - T) or three (G - T) hydrogen bonds. The complementary Watson-Crick base pairing makes DNA a programmable building material. Image adapted from [26, 27].

.

1.3.2 *Historical overview*

Not only does DNA store and transmit genetic information, in the field of DNA nanotechnology it is successfully used as a structural building material. Its origins go back to Nadrian C. Seeman, who in 1982 proposed using base pairing of single-stranded overhangs of short DNA strands to form junctions. The use of the predictable Watson-Crick base pairing interaction was intended to create 3D crystals to create a scaffold for the 3D organization of molecules [28]. In the following decades, it was possible to build extended DNA structures using double-crossover (DX) molecules compromising two DNA double helices linked together by two strand exchanges [29].
A major breakthrough in DNA nanotechnology was achieved by the idea of DNA origami by Paul Rothemund in 2006. Here, a long viral DNA strand is folded into desired shapes and patterns. This is achieved by adding short complementary single-stranded DNA strands, that bind together selected parts of the DNA and held the structures in places. This allowed making structures of arbitrary complexity with nanometer precision, such as the map of the Americas, smiley faces, stars, and rectangles [30].
The design process was significantly facilitated with the introduction of caDNAno by Shawn M. Douglas in 2009. This is an open-source software package with a graphical user interface that allows the design and definition of staple strands for DNA origami structures [31]. Additional software tools that facilitate the design are vHelix [32] and CanDo that allows the simulation and prediction of 3D solution shape and flexibility of DNA nanostructures [33].
Recent advances in the design principles of DNA nanostructures include the idea of single-stranded tiles. Here, a structure is composed out of small LEGO-like molecular bricks without the need for a scaffold strand [34, 35]. This design principle was successfully used to create 3D structures with gigadalton size with 10,000 unique components [36].

1.3.3 *The rectangular origami*

In Paul W. K. Rothemund's initial publication of 2006, a rectangular DNA origami structure was demonstrated. Jungmann et al. corrected for the presence of a superhelical twist that occurs as inter-strand crossovers arise every 32 bp, resulting in 10.67 bp per helix turn. Compared to the 10.5 bp per helix turn, the helical periodicity of double-stranded DNA in its B-Form results in the helices in the structure to be slightly underwound [37].
In the context of this thesis, the twist-corrected rectangular DNA origami – tcRRO, which will here be referred to as RRO, was used as a molecular pegboard. It has dimensions of approx. 60 nm x 90 nm and consists of 192 staples and was folded with a 7249 bases long (M13mp18)

scaffold strand. Consisting out of one layer of 25 parallel DNA helices, it is a flat structure with a height of 2 nm. For surface attachment, eight biotinylated extensions were included - leaving 176 positions for staple extensions. The staples are designed so that within one helix a 3'-extension, as well as a double crossover, is found every 32 bases. As the pattern is shifted on the adjacent helix, a hexagonal grid pattern is achieved with 5 nm distance between each hexagon in x- and y-direction. Extensions at the 3'-end of the staples above the biotin anchors will point downwards. Refer to Figure 7 for an overview of the staple routing and the pegboard scheme.

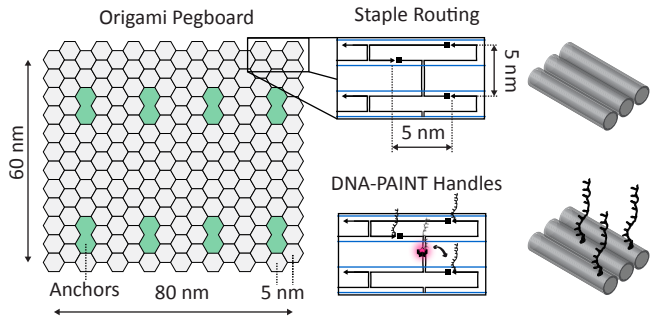

Figure 7: Rectangular origami pegboard. The origami pegboard is a flat DNA origami nanostructure that has 176 positions arranged in a hexagonal grid pattern that can be extended to have DNA-PAINT handles at specific positions. The center-to-center distance of each hexagon is 5 nm. For surface attachment, eight positions have been modified (green hexagons) to have biotinylated strands pointing downwards out of the structure for surface attachment.

2

DNA ORIGAMI AND FLUORESCENCE MICROSCOPY

As noted in the introductory chapter, DNA nanostructures allow nanometer-precise placement of guest molecules and can function as a molecular breadboard. In the past, they have been extensively used to serve as tools in fluorescence microscopy. Previous demonstrations in this domain included FRET rulers [38], brightness standards [39], nanobarcodes [40] and nanoscopic rulers [41].
In this chapter, I will discuss the use of DNA origami as tools for fluorescence microscopy with two examples. First, I will introduce the concept of *Metafluorophores*, referring to DNA origami nanostructures with digitally tunable optical properties. Second, I will show how superresolution microscopy can be used to study accessibility and incorporation of DNA nanostructures.

2.1 METAFLUOROPHORES

One major advantage of fluorescence microscopy is that multiple molecular species in one sample can be detected simultaneously by using spectrally distinct fluorescent tags. However, the number of targets that can be identified at the same time is limited by the number of unambiguously detectable dyes. Ideally, one wants to study the interaction of hundreds of molecular species at the same time, which creates the need for a novel type of programmable tag that allows multiplexing and can be reliably distinguished.
To address this challenge, we explored the capability of transforming DNA origami into such a label by decorating it with various amounts of fluorophores in specific patterns. As we chose a rectangular structure with dimensions of 90 nm x 60 nm, well below the diffraction limit, it cannot be distinguished from a conventional fluorophore when using conventional fluorescence microscopy. We, therefore, named this type of structure *Metafluorophore*.

2.1.1 *Decorating origami with fluorophores*

To explore the capabilities of DNA origami to serve as a new kind of fluorophore, we constructed structures with a prescribed number of dyes, ranging from 6 to 132. We found that there is a linear dependence of fluorescence intensity on the number of dyes. This was confirmed for Atto647N, Cy3, and Atto 488 dyes, showing we could precisely engineer the brightness of our metafluorophores. We then cre-

ated multicolor metafluorophores by combining the different dyes on the origami. We noticed a significant decrease in fluorescence intensity due to FRET. To circumvent this, we arranged fluorophores of the same species in columns and introduced spacing between fluorophores of different species. The resulting design resembled a barcode and was found to prevent FRET successfully.

2.1.2 *Creating distinguishable tags*

As one ideally wants to create a tag that can be unambiguously distinguished from another, we performed experiments to identify separable intensity levels. We found that the four intensity levels, containing 6, 14, 27 and 44 fluorophores, showed only little overlap, allowing the unique identification of labels. By combinatorially labeling the different intensity levels we created a total of 124 distinguishable structures. The performance was tested by randomly selecting 25 structures and measuring them together in a sample. Here, only 12.6% of the detected structures were unexpected (that were detected albeit not being in the sample). We could increase this performance by creating more robust subsets (e.g., using intensity levels with less overlap) at the cost of reducing the total number, and had 4.6% unexpected structures for a subset with 64 structures and 0.4% unexpected structures for a subset with 20 structures.

2.1.3 *Further developments*

As a potential application for our newly created metafluorophores, we successfully performed quantitative nucleic acid detection. Here, we extended our metafluorophores with a handle region that would bind to the target DNA strand. By additionally adding biotinylated capture strands we could capture the probes on the surface and perform a readout.
As a way to further increase the number of distinguishable metafluorophores, we chose to characterize dyes that spectrally overlap according to their photostability. The acquisition of several images and subsequent determination of the decay constant revealed distinguishable species.
To address potential limitations of metafluorophores coming from their size and subsequent limitation in diffusability, we additionally explored how metafluorophores could be directly assembled at the target site.

2.1.4 *Associated publication P1*

Sub–100-nm metafluorophores with digitally tunable optical properties self-assembled from DNA

By

Johannes B. Woehrstein*, **Maximilian T. Strauss***, Luvena L. Ong, Bryan Wei, David Y. Zhang, Ralf Jungmann°, Peng Yin°

* *These authors contributed equally to this work*

° *Co-corresponding authors*

published in

Science Advances (2017)

SCIENCE ADVANCES | RESEARCH ARTICLE

BIOCHEMISTRY

Sub–100-nm metafluorophores with digitally tunable optical properties self-assembled from DNA

Johannes B. Woehrstein,[1,2,3]* Maximilian T. Strauss,[1,2,3]* Luvena L. Ong,[1,4] Bryan Wei,[1,5†] David Y. Zhang,[1,5‡] Ralf Jungmann,[1,2,3,5§] Peng Yin[1,5§]

Fluorescence microscopy allows specific target detection down to the level of single molecules and has become an enabling tool in biological research. To transduce the biological information to an imageable signal, we have developed a variety of fluorescent probes, such as organic dyes or fluorescent proteins with different colors. Despite their success, a limitation on constructing small fluorescent probes is the lack of a general framework to achieve precise and programmable control of critical optical properties, such as color and brightness. To address this challenge, we introduce metafluorophores, which are constructed as DNA nanostructure–based fluorescent probes with digitally tunable optical properties. Each metafluorophore is composed of multiple organic fluorophores, organized in a spatially controlled fashion in a compact sub–100-nm architecture using a DNA nanostructure scaffold. Using DNA origami with a size of 90 × 60 nm^2, substantially smaller than the optical diffraction limit, we constructed small fluorescent probes with digitally tunable brightness, color, and photostability and demonstrated a palette of 124 virtual colors. Using these probes as fluorescent barcodes, we implemented an assay for multiplexed quantification of nucleic acids. Additionally, we demonstrated the triggered in situ self-assembly of fluorescent DNA nanostructures with prescribed brightness upon initial hybridization to a nucleic acid target.

INTRODUCTION

Fluorescence microscopy is a powerful tool for biological research (*1*). Beyond imaging molecules in bulk, its high specificity and sensitivity allow the detection of single biomolecules (*2*, *3*). This is usually achieved with fluorescent tags, such as genetically encodable fluorescent proteins (*4*, *5*), organic dyes, or inorganic fluorescent nanoparticles (*6*). While fluorescent proteins can be coexpressed with the target protein of interest, organic and inorganic dyes need to be coupled, for example, to antibodies, small molecules, or DNA to specifically label targets such as proteins or nucleic acids (*7*).

A major advantage of fluorescence microscopy is the possibility of simultaneously detecting and identifying multiple molecular species in one sample by using spectrally distinct fluorescent tags (colors). However, this so-called multiplexed detection is typically restricted by the number of unambiguously detectable spectral colors in the visible range; the broad emission spectra of organic fluorophores limit spectral multiplexing to about four to five dyes.

Thus, fluorescence microscopy is in need of novel types of programmable tags, which allow the unambiguous detection of ideally hundreds of distinct target species while maintaining the desired properties of "classical" dyes, such as their nanoscale size and target labeling capabilities. However, only limited success toward programmable molecular tags has been achieved so far (*8*–*10*), mainly because of the lack of independent and precise control of properties, such as intensity, color, size, and molecular recognition.

Here, we introduce a general framework for engineering sub–100-nm–sized tags with digitally tunable optical properties, such as brightness and color, using tools from DNA nanotechnology (*11*–*16*). Each tag is composed of multiple organic fluorophores, organized in a spatially controlled fashion in a compact subdiffraction volume. This makes the composite fluorophore tag appear similar to a traditional organic fluorophore when visualized under a diffraction-limited microscope. Inspired by the definition of metamaterials, we therefore call this tag a metafluorophore.

However, unlike a traditional organic fluorophore, this metafluorophore has digitally and independently tunable optical properties, such as intensity levels and color mixing ratios. To construct these particles, we use DNA nanostructures as a platform to organize organic fluorophores in a subdiffraction volume. A great variety of fluorescent nanoparticles have been constructed by doping or filling a suitable carrier [for example, silica nanoparticles (SiNP), polystyrene particles, hydrogels, and dendrimers] with fluorophores (*17*) and have been used in diverse bioimaging applications. In contrast to these previous fluorophore-decorated nanoparticles, the DNA nanostructure–based metafluorophore has the unique advantage of enabling digitally tunable control of the exact copy number of the fluorophores over a large dynamic range (one to hundreds) and digitally precise control of the color ratio as well as the spatial arrangement of these fluorophores.

This independent tunability of both intensity and color enables the construction of more than 100 well-defined metafluorophores. An intensity-based multiplexing approach expanded with combinations of multiple colors can thus overcome the limitations of spectral multiplexing, and the metafluorophores can serve as nanoscale intensity codes (analogous to "barcodes" and hereafter referred to as such) for high-content imaging.

Traditionally, there have been several ways to create unique barcode signatures based on properties such as geometry (*10*, *18*–*26*) and intensity (*8*–*10*, *25*, *27*–*31*). Geometrical barcoding is achieved by spacing distinct fluorescent sites beyond the spatial resolution of the used imaging system (that is, >250 nm for diffraction-limited systems and >20 to

[1]Wyss Institute for Biologically Inspired Engineering, Harvard University, Boston, MA 02115, USA. [2]Department of Physics and Center for NanoScience, Ludwig Maximilian University, 80539 Munich, Germany. [3]Max Planck Institute of Biochemistry, 82152 Martinsried near Munich, Germany. [4]Harvard-MIT Division of Health Sciences and Technology, Massachusetts Institute of Technology, Cambridge, MA 02139, USA. [5]Department of Systems Biology, Harvard Medical School, Boston, MA 02115, USA.
*These authors contributed equally to this work.
†Present address: School of Life Sciences, Tsinghua University, Beijing, China.
‡Present address: Department of Bioengineering, Rice University, Houston, TX 77030, USA.
§Corresponding author. Email: py@hms.harvard.edu (P.Y.); jungmann@biochem.mpg.de (R.J.)

40 nm for super-resolution systems). In combination with spectrally distinct fluorophores, combinatorial labeling exponentially increases the number of distinguishable barcodes. However, geometrical barcoding leads to an increased label size due to the necessity of spacing fluorophores sufficiently apart for accurate detection of the spatial pattern of the barcode. So far, only a few submicrometer barcode systems based on geometry or fluorescence intensity have been reported (*9*, *10*, *24*–*26*, *28*), whereas none demonstrated hundreds of barcodes with sizes below 100 nm.

In intensity barcoding implementations, distinguishable barcodes are usually realized by controlling the number of fluorophores per species, thus allowing the unambiguous detection of different intensity levels. Compared to geometrical barcodes, the key advantage of intensity barcodes is that they require neither the construction nor the detection of spatially resolvable fluorescent features. Thus, intensity barcodes could be much smaller.

Although intensity barcodes with thousands of colors have been proposed, in practice, only bulky and micrometer-sized barcodes have been constructed for hundreds of species (*8*, *32*). This extended spatial size is necessary to ensure robust separation between intensity levels because these approaches lack the molecular tunability of fluorophore number, spacing, and positioning, leading to unwanted photophysical effects, such as self-quenching and Förster resonance energy transfer (FRET) (*33*) between dye molecules. Because our proposed metafluorophores feature precise molecular control over number, spacing, and arrangement of fluorophores in a nanoscale volume, they can serve as a platform for intensity barcodes without the discussed drawbacks.

Beyond the prescribed tunability of size, color, and brightness, the DNA origami approach also permits the use of other tunable optical properties to further increase the multiplexing level of metafluorophores. As an example of this approach, we report here metafluorophores with tunable photostability.

We also apply these metafluorophores as molecular barcodes in a multiplexed nucleic acid detection assay. By functionalizing distinctly colored metafluorophores with specific, single-stranded DNA handles, we are able to capture and subsequently identify and quantify a multitude of synthetic DNA targets.

Finally, we can also use DNA nanotechnology (*34*–*38*) to achieve control over both the position and the order of assembly of the structure's components. Specifically, using reconfigurable DNA monomers, we can explicitly control the location and kinetic pathway of the metafluorophore assembly. To demonstrate this, we implemented a triggered version of our metafluorophore that dynamically self-assembles from metastable monomers only in the presence of a biomolecular trigger in situ.

RESULTS

Designing a metafluorophore

Nanoscale metafluorophores can be designed and fabricated with tunable properties. Structural DNA nanotechnology enables researchers to build nanoscale shapes and patterns with almost arbitrary complexity in a self-assembled fashion. Here, we use the DNA origami technique (*12*, *14*) as a building platform for our metafluorophore.

In DNA origami, a long, single-stranded DNA molecule (called the "scaffold") is folded into programmable shapes by ~200 short, single-stranded DNA strands (called "staples") (*12*). Every staple has a defined sequence and specifically binds certain parts of the scaffold together. Structures are usually assembled in a one-pot reaction using thermal annealing. After the self-assembly is completed, the scaffold is "folded" into the desired shape, with the staple strands at prescribed positions in the final origami.

Here, we use a two-dimensional (2D), rectangular DNA origami consisting of 24 parallel DNA double helices with dimensions of 90 × 60 nm^2 (Fig. 1A, fig. S1, and tables S1 and S2). This specific structure contains 184 uniquely addressable staple strands, which can be functionalized to display a large variety of molecules, such as fluorophores, nanoparticles, etc. (*14*).

One modular and economic way to attach molecules of interest to this molecular pegboard is the use of so-called "handle" and "antihandle" strands (*12*). Here, the staple strand at the position where one wants to attach a molecule is extended with a 21-nt-long single-stranded handle sequence (table S3). The complementary antihandle is functionalized with the entity that should be arranged on the DNA origami structure (Fig. 1A). Staples carrying the handle sequences and the functionalized antihandle strands are usually part of the one-pot assembly mix. Distinct target species can be attached to the origami pegboard by using orthogonal handle strand sequences (*26*).

To "label" targets with our DNA origami–based metafluorophore, we could use specific target-binding staple strands. Labeling can either be achieved by direct hybridization to a DNA or RNA strand on the target molecule (handle-/antihandle-binding) or be mediated by using antibodies or small-molecule binders for protein labeling (*39*, *40*).

Tunable brightness

DNA origami has already proven useful as a versatile platform in many fluorescence applications, such as single-molecule studies (*41*, *42*) and super-resolution microscopy (*41*, *43*–*47*). Recently, DNA origami has been used to create brightness standards for fluorescence microscopy (*48*, *49*).

Here, we engineered metafluorophores with tunable brightness. We designed DNA origami structures with a prescribed number of dyes, ranging from 6 to 132 (Fig. 1A and fig. S2). We assembled each origami species using a staple strand mix that contained dye-labeled antihandle versus handle strands in a 2.25:1 molar ratio (protocol S1). After self-assembly and purification, the metafluorophores (carrying eight biotinylated capture strands) were immobilized on streptavidin-coated glass slides in custom-made flow chambers (protocol S2) (*26*, *46*, *47*).

Imaging was performed on a ~100 × 100–μm^2 area containing ~1000 DNA origami structures, and single images were acquired for 10 s using light-emitting diode (LED) illumination on an inverted epifluorescence microscope (see the Supplementary Materials). Surface density was adjusted so that individual origami structures appeared as distinct bright spots in the fluorescent image. After image acquisition, a spot detection algorithm was used to identify individual DNA origami structures. In a subsequent step, a 2D Gaussian fit was performed within a 10 × 10–$pixel^2$ area containing a spot. The volume under the Gaussian function was used as the measure of intensity. Narrow intensity distributions for experiments with only one metafluorophore population revealed that most of the spots are well-formed single DNA origami, which is in good agreement with earlier super-resolution studies (*50*).

Our structures showed a linear dependence of fluorescence intensity on the number of dyes. We confirmed this linear dependence for Atto 647N, Cy3, and Atto 488 dyes using DNA structures carrying up to 132 dyes per DNA origami (Fig. 1, B to D, and figs. S3 and S4). Dyes were spaced approximately equidistantly (see pictograms) on the DNA origami. After evaluating optimal acquisition settings (figs. S5

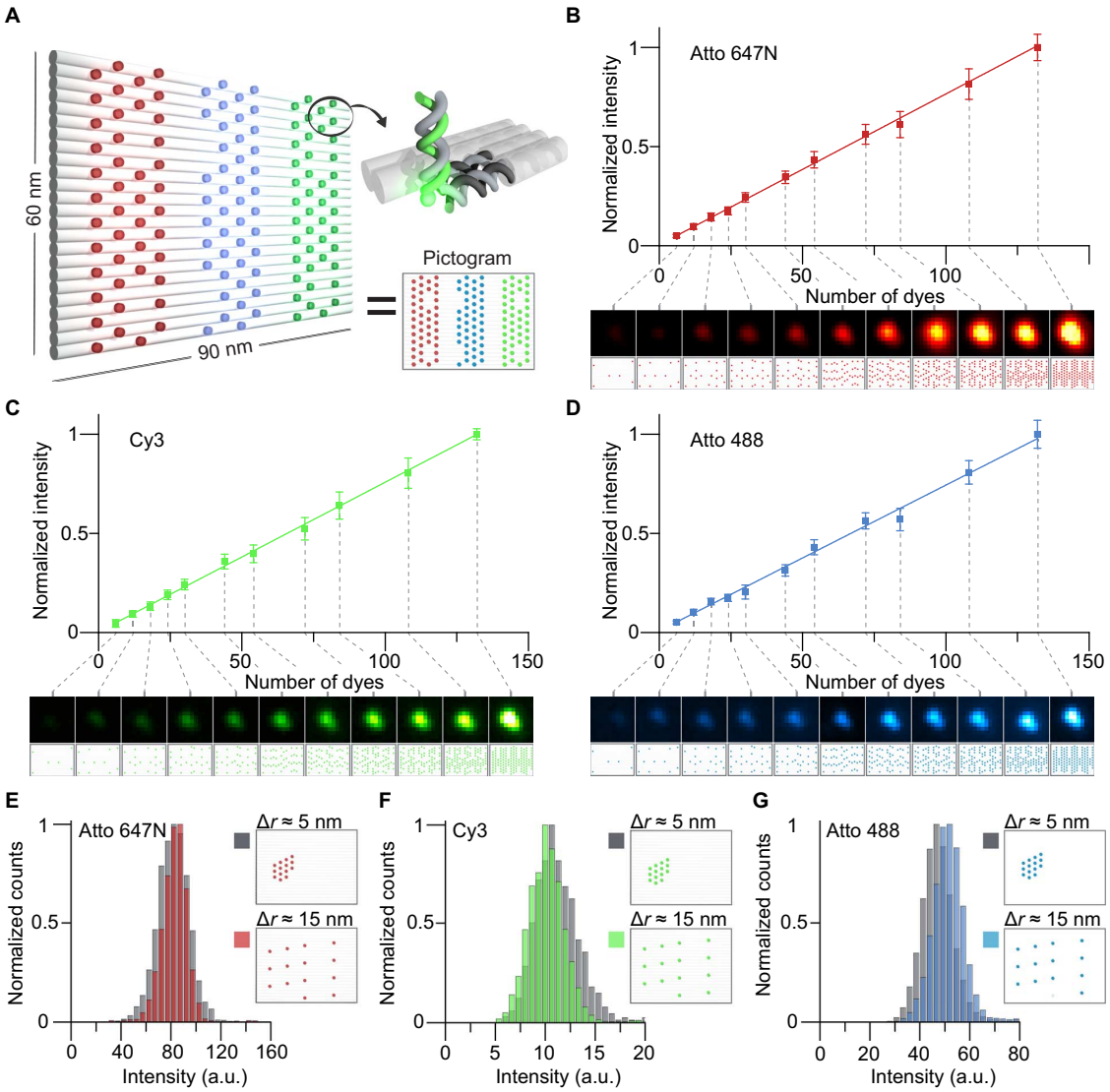

Fig. 1. DNA-based metafluorophores. (**A**) Labeling pattern for DNA origami–based metafluorophores. Cylinders represent DNA double helices. Selected strands are extended with 21–nucleotide (nt) handles on the 3′ end, which bind complementary fluorescently labeled antihandles. Labeling patterns are represented as pictograms, where each colored dot represents a dye-labeled handle. (**B** to **D**) Fluorescence intensities increase linearly with the number of dyes attached to a metafluorophore (here, up to 132 dyes per structure). Insets show diffraction-limited fluorescence images of metafluorophores and the corresponding labeling pattern. Image sizes, 1.2 × 1.2 μm^2. (**E** to **G**) Metafluorophores allow dense labeling (~5-nm dye-to-dye distance) without self-quenching. Pictograms illustrate dense and sparse labeling patterns for 14 dyes. Corresponding intensity distributions of the two patterns overlap for each color, showing no significant change in intensity. a.u., arbitrary units.

and S6), measurements for all species were performed independently by analyzing ~10,000 molecules.

Intrinsic variations in measured fluorescence intensity are likely due to structure-to-structure variations on the number of dyes as well as stochastic properties of fluorescence emission of the dyes themselves (*51*). Extrinsic variations from sample to sample mainly originate from differences in image acquisition, such as slightly different focal planes or photobleaching. If the fluorescence emission from a dye molecule is not acquired in perfect focus, fewer photons will be collected, and thus, the measured intensity will be decreased. To minimize this effect, we used a focus-maintaining system. Repeated image acquisition of the same sample with intermittent refocusing yields mean-to-mean variations of ~5% (fig. S7). Additionally, each image acquisition "bleaches" the samples by ~0.8 to 2.8%, depending on the dye (fig. S8).

An important feature of a metafluorophore is its nanoscale size. To engineer and construct compact metafluorophores, dye molecules need to be spaced close together while preventing unwanted dye-dye interactions, such as self-quenching (*52*). To demonstrate that dye-dye interactions are effectively prevented in our metafluorophore design, we performed experiments with origami structures carrying 14 dyes with

low labeling density (~16-nm dye-to-dye distance) or 14 dyes with high labeling density (~5-nm dye-to-dye distance) and compared their fluorescence intensity distributions (Fig. 1, E to G, and fig. S9). Atto 647N–, Cy3-, and Atto 488–labeled structures with low and high labeling densities showed the same fluorescence intensities within our measurement accuracy.

Tunable color

A key requirement for multicolored nanoscale metafluorophores is the ability to tune brightness and color independently. As briefly mentioned above, our DNA-based metafluorophores can be "functionalized" with multiple orthogonal handle strands that can, in turn, bind spectrally distinct dye-labeled antihandle strands. Thus, we can design structures labeled with either Atto 647N, Cy3, Atto 488, or any combination thereof.

If spectrally distinct fluorophores are brought into close proximity (that is, closer than ~10 nm), they may exhibit FRET (*33*). In FRET, the fluorophore with the shorter excitation wavelength (donor) transfers energy to the fluorophore with the longer excitation wavelength (acceptor) through nonradiative dipole-dipole coupling. If FRET occurs, the donor dye's emission fluorescence intensity will be decreased, depending, inter alia, on the proximity and number of adjacent acceptor dyes.

To maintain prescribed fluorescence intensities when using multiple fluorescent colors in our metafluorophores, we must prevent potential FRET between spectrally distinct dye molecules. Thus, we investigated whether FRET occurs in our metafluorophore designs and thereby limits our capability to precisely design their fluorescence intensity and color. We first investigated a design with 44 randomly arranged Atto 647N, Cy3, and Atto 488 dyes (Fig. 2, A to C, respectively, and fig. S10). This random arrangement was tested by comparing two different sample species: One contained all three dyes, and one contained only a single species. The resulting intensity distributions suggest that Atto 488 and Cy3 act as FRET donors because they exhibited a significant decrease in fluorescence intensity for the origami species containing possible acceptor fluorophores. The mean intensities for Atto 488 and Cy3 dyes were reduced by approximately 50 and 40%, respectively, compared to the control species with only one single fluorescent color. However, the mean fluorescence intensity for Atto 647N was unchanged because this dye lacked a potential FRET acceptor fluorophore.

The finding that FRET can alter fluorescence emission intensity of the metafluorophore by as much as 50% in randomly labeled structures limits our ability to control fluorescence color and intensity independently. However, the precise programmability of DNA origami allows us to increase the spacing of spectrally distinct dyes, thus preventing FRET while maintaining high labeling densities and nanoscale structure dimensions.

To prevent the undesired FRET, we changed the random dye layout to a "column-like" arrangement, where the three dye species are positioned in spatially distant zones (Fig. 2, D to F, and figs. S10 and S11). Repeating the same experiments as in Fig. 2 (A to C), fluorescence intensities between multi- and single-color species were unchanged; thus, our modified column-like layout prevents FRET (Fig. 2, D to F). This finding now allows us to tune the brightness and color of our metafluorophores independently. Having established the ability to engineer photophysical properties, such as intensity and color, we will next investigate potential applications of DNA-based metafluorophores.

Multiplexed tagging

One of the most important features of metafluorophores is their usefulness as labeling probes for multiplexed target detection. We now have to consider the question of how to construct metafluorophores as multiplexed labels on the basis of intensity and color combinations. This poses the challenge that we need to be able to unambiguously identify prescribed intensity levels.

Because of stochastic photon emission, imperfect labeling, and incomplete staple incorporation, the DNA origami–based metafluorophores show a finite intensity distribution for a structure with a designed number of dyes (Fig. 3A). If the intensity distributions of two distinct barcode levels (or numbers of dyes per structure) are engineered to have no overlap, each measured intensity value can be unambiguously assigned to a specific barcode. The number of distinct barcode species N scales as $N = a^b$, with b being the number of spectrally distinct colors and a the number of distinguishable intensity levels per color.

With a maximum number of 132 staple strands available for modification and 3 distinct dyes, the largest number of dyes per color per structure is 132/3 = 44. The smallest number of dye molecules that can be robustly detected using our standard inverted fluorescence microscope is 6.

By measuring the width of the intensity distribution for different numbers of dyes on a DNA origami, we identified a total of four nonoverlapping levels that can be used in a barcoding application, corresponding to 6, 14, 27, and 44 dyes (fig. S12). Combinatorial labeling with three spectrally distinct dyes and five intensity levels (including 0), allows for a maximum of $5^3 - 1 = 124$ barcodes with our current design.

We tested our ability to design, fabricate, and robustly identify all 124 possible barcodes. After self-assembly and purification of the barcodes, we pooled and immobilized them in a streptavidin-modified flow chamber (Fig. 3, B and C). Here, image acquisition was performed sequentially, starting with the longest wavelength and subsequently imaging the shorter wavelengths to minimize photobleaching. Data analysis (spot detection and intensity measurement) was performed as described above and carried out in each color channel separately. During image analysis, each detected spot (and thus barcode) was assigned a coordinate and corresponding intensity value for each color. Spots that appeared at the same position in two or more color channels (colocalization) were combined and assigned to the same metafluorophore (for details, see the Supplementary Materials).

To identify our metafluorophore with a specific barcode ID, the measured intensity values were compared to a lookup table to assign the correct intensity level (for details, see the Supplementary Materials). One can further obtain a lookup table for each sample acquisition by creating a histogram of all measured intensity values (fig. S12). This has the benefit of a "real-time" test for sample performance (for details, see the Supplementary Materials). The overlap of adjacent distributions is an important measure for barcoding performance because it represents intensity levels that cannot be unambiguously assigned to a specific barcode level. To quantify this overlap and discard corresponding barcodes, we fitted a Gaussian function to the intensity distribution of each level. The intersection points of adjacent Gaussians were calculated and subsequently used to determine regions without overlap (for details, see the Supplementary Materials).

Our ability to fabricate and identify all possible 124 barcodes in one sample is demonstrated in Fig. 3D. Variations in molecule counts are due to different DNA origami concentrations, likely introduced in their folding and purification process.

To benchmark the barcoding performance of our metafluorophores, we studied subsets of barcodes (that is, only 25 of the possible 124 barcodes in one sample) and introduced the following measures: From all detected metafluorophores, those with valid intensity values (for example,

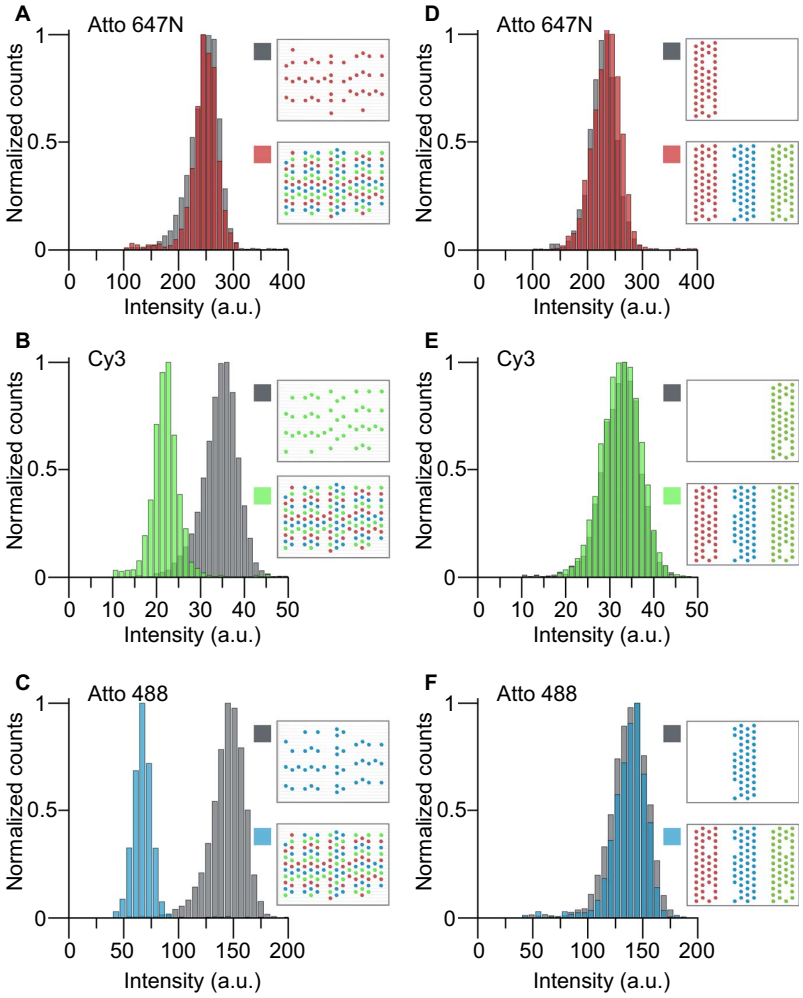

Fig. 2. Multicolor metafluorophores. (**A** to **C**) "Randomly" labeled metafluorophores may result in significant decrease in fluorescence intensity (B and C) due to FRET, when labeled with spectrally distinct dyes. Metafluorophores with only 44 dyes of the same color serve as references (gray distributions). If Atto 647N, Cy3, and Atto 488 are all present on the same structure (44 dyes each), the intensity distributions (colored) for Cy3 (B) and Atto 488 (C) are significantly shifted to lower values. However, this fluorophore arrangement does not provide an acceptor for Atto 647N fluorescence; thus, its intensity distribution is not altered (A). Pictograms illustrate labeling patterns. (**D** to **F**) Column-like metafluorophore labeling pattern prevents energy transfer (FRET). Metafluorophores labeled with 44 dyes of one species (gray) show identical intensity distributions as structures labeled with all three species (colored). Pictograms illustrate labeling patterns.

outside levels of overlapping intensity distributions) are qualified barcodes. As barcode subsets are measured, these qualified barcodes may consist of two subpopulations: expected barcodes (that is, the 25 barcodes in the sample) and unexpected (or false-positive) barcodes (the 99 barcodes not present in the sample). Consequently, we defined a signal-to-noise ratio (SNR) as ⟨expected⟩/⟨unexpected⟩. Together, these measures determine the overall performance of our barcoding system.

The first subset contained 25 randomly selected barcodes of the 124 barcodes in Fig. 3D (Fig. 3E and table S4). We measured 2155 spots, of which 13.5% were discarded as unqualified barcodes with intensity values within overlapping regions. The discarded spots included misfolded structures as well as spots comprising multiple barcodes (that is, spaced closer than the spatial resolution of our imaging system). For this 25-barcode subset, 87.4% of the qualified barcodes were the expected ones. We determined an SNR of 27. A substantial population of false positives were single-colored barcodes with low fluorescence intensities (that is, identified as "6-0-0," "0-6-0," or "0-0-6"). We hypothesize that this is an artifact arising from fluorescent surface impurities.

In case the maximum multiplexing capacity is not required, more robust barcode sets with higher performance can be designed. One strategy is to use three-color barcodes (that is, all three colors must be present for each barcode species), making detection and identification more robust (that is, allowing the rejection of single- and double-colored spots). A total of $4^3 = 64$ three-color barcodes can be constructed using our current metafluorophore design. We benchmarked these barcodes by acquiring a subset of 12 structures (Fig. 3F and table S5). Here, 512 spots were detected, and 92.5% were qualified barcodes, of which 95.4% were the expected ones. The SNR was determined to be 90.

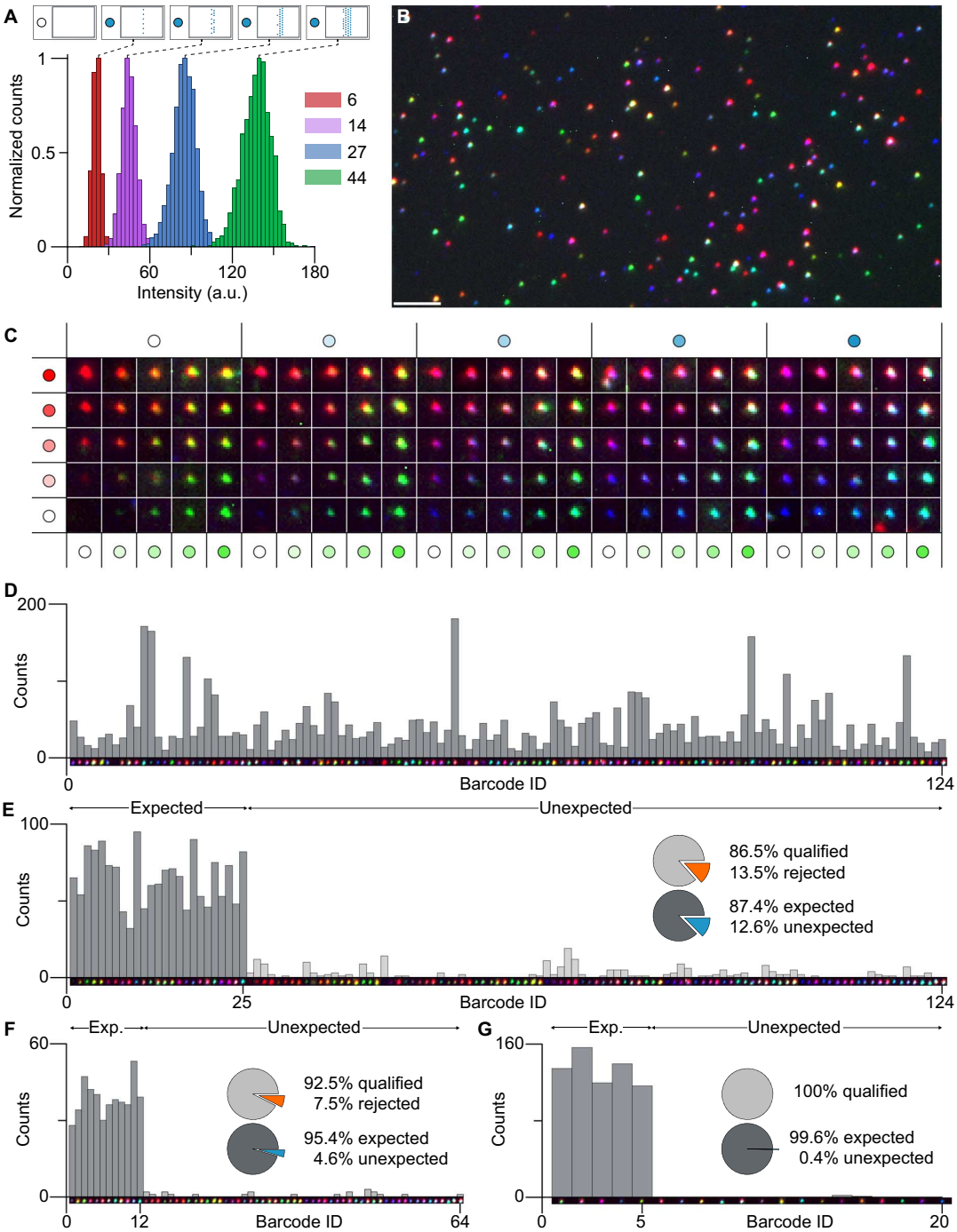

Fig. 3. Metafluorophores for intensity barcoding. (**A**) Intensity distributions for Atto 488 (red, 6 dyes per structure; purple, 14 dyes; blue, 27 dyes; green, 44 dyes). Non-overlapping intensity distributions can be achieved by the precise control over the number of dyes per metafluorophore. (**B**) Fluorescence image of 124 distinct metafluorophores deposited on a glass surface. Scale bar, 5 μm. (**C**) Matrix of representative fluorescence images of 124 distinct metafluorophores. (**D**) Metafluorophore-based intensity barcodes (124) in one sample. A total of 5139 barcodes were recorded, and all 124 barcode types were detected. (**E**) Subset of 25 of 124 barcodes. A total of 2155 barcodes were recorded, where 86.5% were qualified barcodes and 87.4% thereof were expected barcodes. (**F**) Subset of 12 of 64 barcodes. All barcodes have all three fluorophore species, making their detection more robust. A total of 521 barcodes were recorded, where 92.5% were qualified and 95.4% thereof were expected barcodes. (**G**) Subset of 5 of 20 barcodes. A total of 664 barcodes were recorded, where 100% were qualified and 99.6% thereof were expected barcodes.

Another strategy is to reduce the number of intensity levels, thereby reducing overlapping intensity distributions. As a demonstration, we constructed barcodes with three intensity levels (0, 14, and 44 dyes). Additionally, barcodes were required to consist of at least two colors, allowing a maximum of $3^3 - 6 - 1 = 20$ distinguishable barcodes. We measured a subset of 5 barcodes ($N = 664$) with a qualification ratio of 100%; that is, all detected spots were positively identified as valid barcodes (Fig. 3G and table S6). Here, only three false positives were counted, yielding 99.6% expected barcodes.

We note that the number of barcodes in a subset is a crucial factor when evaluating the barcoding performance of a system. When using large subsets, one may make a false identification of a spot without noticing because the identified barcode may also be part of the used subset. On the opposite side, when using a small subset, identification accuracy may be biased because only a small fraction of the barcodes is tested.

Ultrasensitive, quantitative, and multiplexed nucleic acid detection

Multiplexed detection applications are readily realized by combining the metafluorophore's reliable identification capabilities with barcode-specific target recognition. Inspired by the NanoString nCounter digital nucleic acid quantification system, where structurally flexible, surface-immobilized, and geometrically encoded fluorescent barcodes are used in highly multiplexed digital counting of molecular targets (*22*), we implemented a multiplexed in vitro nucleic acid detection assay using metafluorophores. Similarly, our method allows for highly multiplexed molecular quantification with in-principle similar multiplexing capability. Compared to the nCounter system, our metafluorophore-based assay has four unique advantages. First, our method has a much simpler operational workflow: Our system does not require electrophoretic stretching of the structurally flexible barcodes or sophisticated software to decode these geometrical patterns; additionally, no target-barcode purification is required. Second, because the metafluorophore can pack many more dyes per area [132 dyes on one origami (90 nm × 60 nm) in contrast to 1 dye per 50 base pairs (17 nm) for nCounter], it enables faster image acquisition speed and thus higher throughput (because we have brighter spots). Third, the higher dye density also allows the use of potentially simpler, lower-cost, and standard imaging platforms (we used commercially available confocal and widefield microscopes). Finally, the metafluorophore is manufactured using a simple one-pot self-assembly reaction that, in principle, can be fully automated rather than labor-intensive manual in vitro transcription methods.

In our detection assay, each nucleic acid target (here, eight synthetic DNA strands) was associated with a metafluorophore. The chosen metafluorophores were programmed to specifically bind the target by replacing the eight biotinylated staples (previously used to attach the metafluorophore to the surface) with staples that are extended with a target-complementary 21-nt-long sequence at the 5′ end. To increase the chance of hybridization (and thus the speed of the detection), we used eight target-specific strands per metafluorophore. Because of their high excess over targets, we expect each metafluorophore to bind either one or no target. To detect the target-metafluorophore duplexes on a microscopy slide (comparable to the experiments in Fig. 3), we introduced a biotinylated DNA strand ("capture strand") complementary to a second 21-nt region on the target (see Fig. 4, A and B).

The three components were combined in a hybridization buffer and incubated for 24 hours (see Materials and Methods). We chose concentrations of 1 nM biotinylated capture strands and approximately 250 pM metafluorophores per target. With this high excess of metafluorophores over targets, we assumed that every target molecule was labeled with one barcode. Targets were added in different amounts to assay quantification and sensitivity (see Fig. 4C and table S7). After incubation, the mixture was added into streptavidin-coated flow chambers as before and incubated for 10 min. The chamber was subsequently washed and sealed.

Data acquisition can be performed on a large variety of fluorescence microscopes. Widefield microscopes, as used in the characterization of the fluorescently labeled DNA origami described above, can efficiently record large areas and are readily available in many laboratories and so are laser scanning confocal microscopes. To demonstrate that the metafluorophores can be platform-independently identified in a robust fashion and thus easily used in most laboratories, we used confocal microscopes for data acquisition in the nucleic acid detection experiments.

To assess the precision of this nucleic acid detection platform, we designed eight capture-target-metafluorophore triplets and added

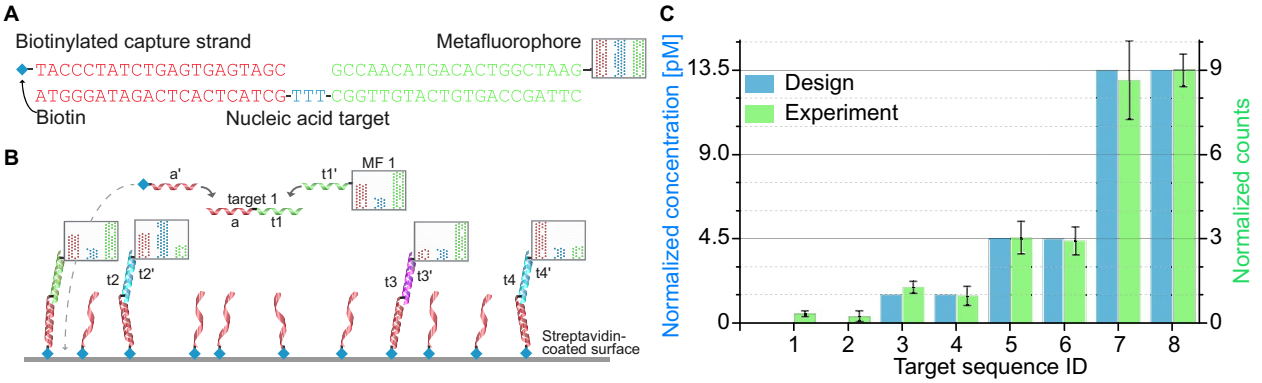

Fig. 4. Quantitative nucleic acid detection. (**A** and **B**) Schematic of the hybridization reaction. A metafluorophore is programmed to hybridize to part (green) of a specific nucleic acid target. A biotinylated capture strand binds to a second region (red) and thus immobilizes the complex on a streptavidin-coated surface, yielding fluorescence images comparable to Fig. 3B. Each positively identified metafluorophore indicates a single copy of a nucleic acid target. (**C**) The number of detected targets is directly proportional to their concentration in the sample of interest. Targets were added with defined concentrations (blue bars) and subsequently identified in the expected ratios (green bars). Five different field of views have been recorded, enabling the calculation of error bars. The lowest target concentration [target 3 (t3) and target 4 (t4)] was 1.5 pM. Target 1 (t1) and target 2 (t2) were not added, and corresponding identifications are due to nonspecific binding of metafluorophores to the surface and potential false-positive identifications.

different amounts of six targets to the reaction. The remaining two targets were not added and, thus, indicated barcodes nonspecifically bound to the surface (that is, without cognate target) and false positives as before (see fig. S13 for exemplary fluorescent image). The number of detected triplets is directly proportional to the initial target concentration, and the targets can thus be quantified relative to each other. Figure 4C shows the successful detection and precise quantification of targets with initial concentrations of 13.5, 4.5, and 1.5 pM, the latter corresponding to a target amount of only ~100 fg. The number of counted metafluorophores has been adjusted by using a calibration sample with equally concentrated targets, to minimize effects of unequal initial concentrations (fig. S14).

Additional metafluorophore properties

Beyond brightness and color, we can use additional dye properties to expand the tunability of our metafluorophores. This is done by the controlled modification of the structures with groups of fluorescent molecules displaying the desired property. Suitable dye properties include fluorescence lifetime, the ability to photoactivate and switch, and photostability. These parameters can be tuned independently, similar to brightness and color, thus presenting additional orthogonal axes of adjustability. This is especially valuable for multiplexed tagging because the number of unambiguous labels scales with the power of independent parameters.

Here, we demonstrate the differentiation and identification based on the photostability of dyes. As a proof of concept, we designed metafluorophores that contained two dyes with similar emission spectra but different photostability under our imaging conditions. We chose Atto 647N as a dye with slower bleaching constant (that is, more photostable) and Alexa 647 as a dye with faster bleaching constant (that is, less photostable). In a time-lapsed image acquisition experiment, the structures containing Alexa 647 dyes bleach faster than the ones with Atto 647N dyes. As the fluorescence intensity decreases exponentially, we can measure the decay constant, which is then used as a parameter for photostability.

Figure 5A shows a time-lapsed series of images of the two types of structures in one sample, where one species bleaches faster than the other. Metafluorophores that contain multiple orthogonal properties can be identified in a multidimensional graph (Fig. 5B). For example, we can plot the bleaching (or decay) constant versus the fluorescence intensity. Distinct populations corresponding to different metafluorophore configurations can be easily separated and identified (Fig. 5B). A 1D histogram of the decay constants (Fig. 5C) demonstrates that the photostability can be used as an orthogonal tunable metafluorophore property, similar to intensity discussed above.

Triggered assembly of metafluorophores

DNA nanotechnology allows us to program the formation of metafluorophores in an environmentally responsive fashion: Structures can be programmed to form only upon detection of a user-specified trigger. By building on previous triggered assembly schemes (*34*, *36*), we use here short fluorescently labeled, metastable hairpins that assemble into a finite triangular structure if, and only if, a target molecule acting as trigger is present (Fig. 6A and table S8). As a proof-of-concept study, we showed the in vitro triggered assembly of a prescribed-size (10 dyes) triangular metafluorophore using a trigger strand, immobilized by a dye-labeled capture strand on a glass surface.

First, an Alexa 647–labeled and biotinylated capture strand and a trigger strand were annealed and immobilized on a glass surface coated

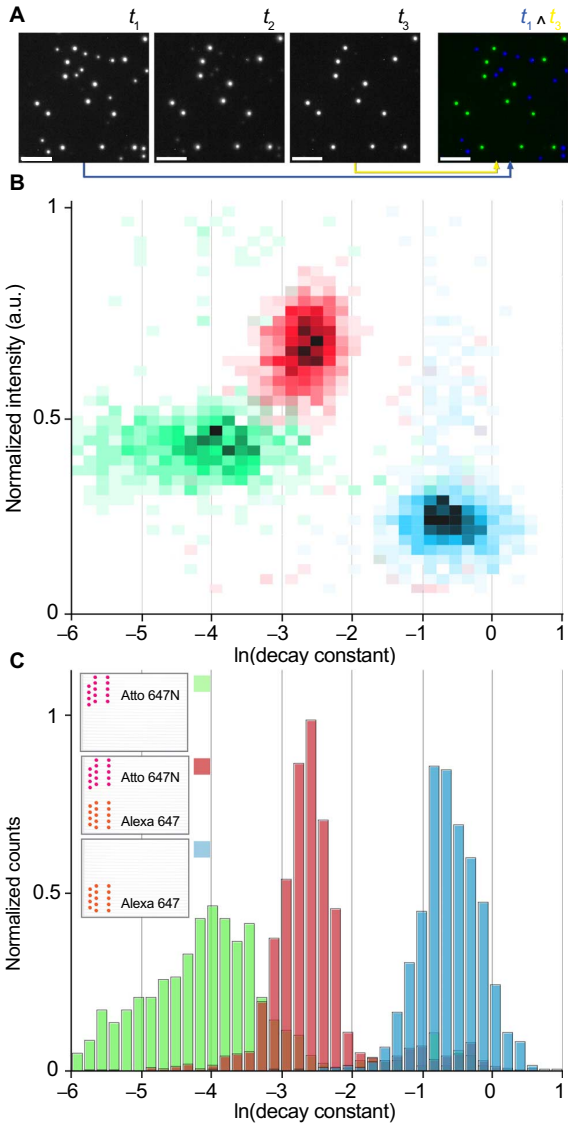

Fig. 5. Metafluorophores with different photostability. (**A**) Time-lapsed fluorescence micrographs of a sample composed of two spectrally indistinct metafluorophore species: one containing 44 Atto 647N dyes (more photostable) and one containing 44 Alexa 647 dyes (less photostable). Images were acquired at $t_1 = 0$ s, $t_2 = 20$ s, and $t_3 = 40$ s, with an integration time of 10 s, whereas the sample was constantly illuminated during acquisition. The time-lapsed micrographs show two species where one bleaches faster than the other. The two species can be visually identified by superimposing the images taken at t_1 (false color blue) and t_3 (false color yellow). The metafluorophore containing more photostable dyes (that is, Atto 647N) appears green (blue + yellow), whereas the one with the less photostable dyes (that is, Alexa 647) appears blue. The fluorescence decay constant can be used as a parameter to quantitatively describe the photostability. The decay constant is obtained by fitting a single exponential decay to the intensity versus time trace. Scale bars, 5 μm. (**B**) Intensity versus decay constant histograms for three different metafluorophore samples containing Atto 647N dyes (green), Alexa 647 dyes (blue), and both dyes (red), respectively (note that only one species was present in each sample). (**C**) 1D histogram of the decay constants shows three distinguishable decay constant distributions (schematics in the legend show the dye arrangement on the metafluorophores).

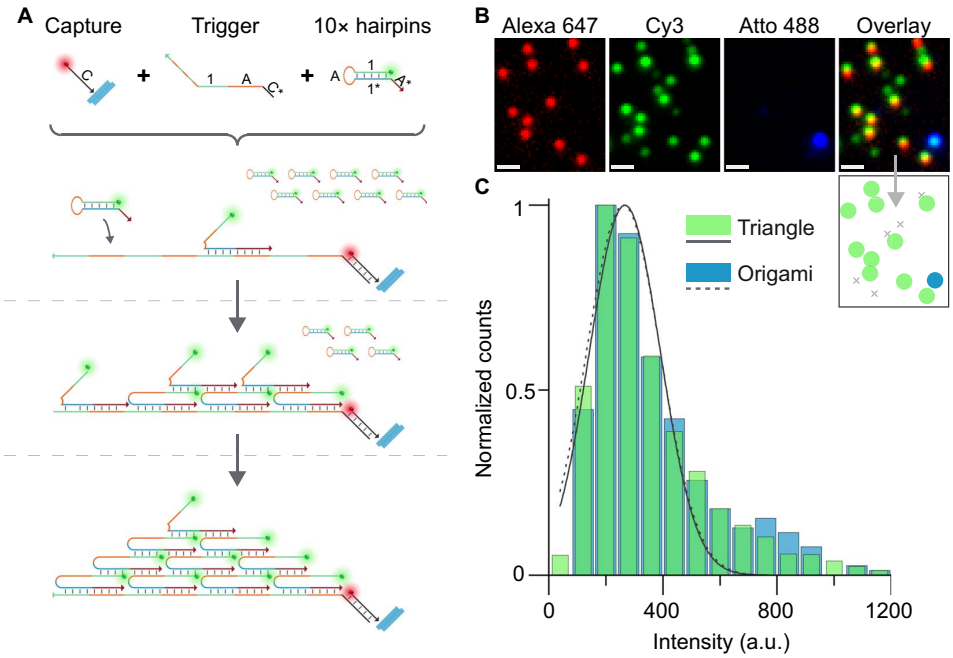

Fig. 6. Triggered assembly of metafluorophores. (**A**) Schematic of triggered assembly of triangular metafluorophores constructed from 10 metastable Cy3-labeled DNA hairpin strands. A so-called capture strand (labeled with Alexa 647) is attached to a glass surface via biotin-streptavidin coupling. A long "trigger strand" can hybridize to the capture strand. The trigger strand consists of four concatenated domains, "1-A," where the subdomain "1" is 20 nt long and the subdomain "A" is 12 nt long. Hairpin strands coexist metastably in the absence of the trigger and only assemble into the desired structure upon exposure to the trigger. More specifically, the introduction of a repetitive single-stranded trigger initiates the assembly of kinetically trapped fluorescent hairpin monomers, which produce a second row of binding sites. These binding sites further enable the assembly of successive rows of monomers, with each row containing one fewer monomer than the previous. After assembly of 10 hairpins (labeled with Cy3) to a single trigger strand, no further trigger sequences are displayed, and assembly is terminated, yielding a triangular-shaped metafluorophore of fixed dimensions. (**B**) Fluorescence images of triangles assembled in situ on a glass surface. The capture strands are labeled with Alexa 647 (red), whereas the hairpins are labeled with Cy3 (green). DNA origami with 10 Cy3 and 44 Atto 488 (blue) dyes were added to the sample as intensity references. DNA origami can be identified at the positions where Atto 488 and Cy3 signals colocalize. In the schematic below the overlay fluorescence image, the blue spot indicates the Atto 488–labeled origami marker; green spots indicate the expected overlay of Alexa 647–labeled capture strand and the triangle composed of Cy3-labeled hairpin monomers. Gray crosses indicate nonspecific binding of hairpins to the surface. Scale bars, 1 μm. (**C**) Triangular metafluorophores (green) and reference DNA origami (blue) intensity distributions are overlapping, thus indicating the formation of the triangles as expected.

with bovine serum albumin (BSA)–biotin–streptavidin. Second, Cy3-labeled metastable hairpins were flown in and incubated for 60 min (protocol S3). Last, DNA origami–based metafluorophores carrying 44 Atto 488–labeled and 10 Cy3-labeled strands were bound to the surface, as intensity reference.

Image acquisition was carried out by sequentially recording the Alexa 647, Cy3, and Atto 488 channels (Fig. 6B). Colocalization in the Alexa 647 and Cy3 channels represents the triangles, whereas Atto 488 and Cy3 colocalization identifies the origami references.

To benchmark the formation performance of the triangles, we compared the intensities of the origami reference structures with the intensities of the triangles in the Cy3 channel (Fig. 6C). Gaussian fits to both intensity distributions reveal an almost perfect overlap with a mean-to-mean variation of less than 2%, suggesting successful triangle formation. Both the formation of the triangle in the presence of the trigger and the metastability of the hairpins in the absence of the trigger were further confirmed by a formation gel assay (fig. S15 and protocol S4).

We note that the triggered assembly scheme used here demonstrates a number of novel features compared to previous triggered assembly schemes. Unlike hybridization chain reaction (HCR) (*34*), which produces a linear polymer structure of unspecified length, a structure of precisely defined size and shape is formed here. Additionally, unlike previous triggered assembly of defined-size structures [for example, dendrimers (*36*) and tetrahedron (*35*)] that uses a large number of unique monomer species, the scheme here uses only one monomer species, and its final size and shape are controlled by the length of the trigger strand.

We expect the triggered formation of the metafluorophore to be particularly useful for future in situ imaging applications: The fluorescent hairpin monomers, upon detecting a trigger attached to the target (for example, an mRNA or a protein), will form the metafluorophore in situ. Compared to structures preformed ex situ, the in situ ones have two critical conceptual advantages. First, the monomer has a smaller size than the metafluorophore and thus can more easily penetrate deep tissues with faster diffusion kinetics. Second, because the bright metafluorophore only forms at the target site, possible false positives caused by nonspecific interactions of preassembled barcodes with cellular components can be avoided, and the signal amplification at the target site that resulted from the triggered aggregation of fluorescent monomers will help to increase signal-to-background ratios.

Related in situ fluorescence imaging approaches have been demonstrated with great success, such as single-molecule fluorescence in situ

hybridization (smFISH) (*9*, *53*, *54*) and HCR (*34*, *55*). Compared to previous approaches, metafluorophores have several conceptual advantages. Compared to smFISH, the tunability of our metafluorophores allows us to assemble more complex structures at the target site by, for example, using a transducer (initiator) molecule that is used to program complex structure assembly on-site. Compared to HCR, where the length of the polymerization and, thus, the number of fluorophores per target are not well defined, the metafluorophore has a precisely defined size and, thus, controlled intensity, which may eventually lead to higher multiplexing capability.

DISCUSSION

Here, we introduced the concept of a metafluorophore, which can be viewed as a new kind of dye with digitally tunable optical properties, can be hundreds of times brighter with arbitrarily prescribed intensity levels, and has digitally tunable "color." We implemented this concept using DNA origami–based self-assembled nanostructures and were thus able to design metafluorophores with high labeling density (~5-nm dye-to-dye distance) while preventing self-quenching. Furthermore, the precise spatial control over dye positions on the nanostructures allowed us to successfully construct nanoscale multicolor metafluorophores, where FRET between spectrally distinct dyes is prevented.

Combining these features, we were able to construct 124 unique intensity barcodes for high-content imaging. We demonstrated the feasibility of this approach, benchmarked the in vitro performance, and showed the high specificity, identification accuracy, and low false-positive rate.

We also demonstrated the ultrasensitive detection and precise quantification of nucleic acids in an easy, multiplexed, and fast assay. Beyond surface-based microscopy applications, the combination of high brightness, small size, and high multiplexing capacity of metafluorophores suggests potential future applications, such as flow cytometry and fluorescence-activated cell sorting (a subtype of flow cytometry) for high-throughput identification. We also envision our DNA nanostructure–based metafluorophores to be extended to even smaller sizes by using the recently developed single-stranded tile assembly approach (*15*, *16*, *56*). Finally, we envision our metafluorophores based on triggered assembly to be a particularly useful tool for improving SNR and labeling efficiency in quantitative smFISH applications.

MATERIALS AND METHODS

DNA origami self-assembly

Self-assembly was performed in a one-pot reaction with a total volume of 20 µl containing 10 nM scaffold strands (M13mp18), 100 nM folding staples, 150 nM biotinylated strands, 100 nM strands with dye-handle extension, and 225 nM fluorescently labeled antihandles in folding buffer (1× TAE buffer with 12.5 mM $MgCl_2$). The solution was heated up to 65°C for 5 min and subsequently cooled down to 4°C over the course of 1 hour. DNA origamis were purified by agarose gel electrophoresis (1.5% agarose and 1× TAE buffer with 12.5 mM $MgCl_2$) at 4.5 V/cm for 1.5 hours on ice. Gel bands were cut, crushed and filled into a Freeze 'N Squeeze column, and spun for 5 min at 1000*g* at 4°C.

Microscopy sample preparation

Coverslips (No. 1.5, 18 × 18 mm^2, ~0.17 mm thick) and microscopy slides (3 × 1 $inch^2$, 1 mm thick) were cleaned with isopropanol. Flow chambers were built by sandwiching two strips of double-sided sticky tape between the coverslip and the glass slide, resulting in a channel with a volume of ~20 µl. The channel was incubated with 20 µl of BSA-biotin solution (1 mg/ml) in buffer A [10 mM tris-HCl, 100 mM NaCl, and 0.05% Tween 20 (pH 8)] for 2 min. The chamber was subsequently washed with 40 µl of buffer A, then incubated with 20 µl of streptavidin solution (0.5 mg/ml) in buffer A for 2 min. Next, a buffer exchange was performed by washing the chamber with 40 µl of buffer A, followed by addition of 40 µl of buffer B [5 mM tris-HCl, 10 mM $MgCl_2$, 1 mM EDTA, and 0.05% Tween 20 (pH 8)]. Then, 20 µl of buffer B with ~300 pM DNA origami metafluorophores was added and incubated for 2 min and subsequently washed with 40 µl of buffer B. Finally, the chamber was sealed with epoxy before imaging.

Image acquisition parameters

Image acquisition parameters for Figs. 1, 2, 3, and 5A were integration time of 10 s and LED power of 60%, whereas parameters for Figure 5B were integration time of 5 s and LED power of 60%. The decay constant was determined by acquiring a series of 10 consecutive frames and fitting the intensity versus time trace with a single exponential decay function. Data acquisition was performed on a Zeiss Axio Observer microscope with Colibri LED light source.

Multiplexed nucleic acid detection

Incubation was performed at room temperature in saline-sodium citrate (SSC)–based hybridization buffer [4× SSC, 5× Denhardt's solution, 5% dextran sulfate, 0.1% Tween 20, and salmon sperm DNA (0.1 mg/ml)]. Flow chamber volume was designed to be ~5 µl. Data acquisition was performed on a Zeiss LSM 780 confocal microscope.

Triggered assembly on a surface

Capture and trigger strands were annealed in a thermocycler directly before adding to the sample at 1 µM in 1× TAE with 12.5 mM $MgCl_2$ and 0.05% Tween 20 (85°C for 5 min, gradient from 85° to 10°C in 15 min). Hairpin strands were annealed in a thermocycler directly before adding to the sample at 1 µM in 1× TAE with 12.5 mM $MgCl_2$ (85°C for 5 min, gradient from 85° to 10°C in 15 min). A flow chamber (see above) was prepared with three layers of sticky tape, resulting in a volume of ~60 µl. The chamber was then incubated with 60 µl of BSA-biotin solution (1 mg/ml) in buffer A for 2 min and then washed with 120 µl of buffer A. Next, the chamber was incubated with 60 µl of streptavidin solution (0.5 mg/ml) in buffer A for 2 min, followed by a washing step with 120 µl of buffer A. Subsequently, a buffer exchange was performed by adding 120 µl of buffer C (1× TAE with 12.5 mM $MgCl_2$ and 0.05% Tween 20). Then, 60 µl of buffer C with 25 pM annealed capture-trigger duplexes were added and incubated for 1 min. The chamber was washed with 120 µl of buffer C and incubated with 60 µl of 100 pM DNA origami standards for 2 min. After washing with 120 µl of buffer C, 60 µl of buffer C with 30 nM annealed hairpin was added. After 20-min incubation, the chamber was washed with 120 µl of buffer C. Hairpin incubation was repeated three times. Finally, the chamber was washed with 120 µl of buffer C and sealed with epoxy before imaging.

SUPPLEMENTARY MATERIALS

Supplementary material for this article is available at http://advances.sciencemag.org/cgi/content/full/3/6/e1602128/DC1

fig. S1. caDNAno DNA origami design.

fig. S2. Schematic DNA origami staple layouts of single-color metafluorophores (6 to 132).

fig. S3. Linear dependence of intensity on the number of dyes per DNA origami (calibrated).

fig. S4. Intensity distributions for 6 to 132 dyes.

REFERENCES AND NOTES

1. J. W. Lichtman, J.-A. Conchello, Fluorescence microscopy. *Nat. Methods* **2**, 910–919 (2005).
2. S. Weiss, Fluorescence spectroscopy of single biomolecules. *Science* **283**, 1676–1683 (1999).
3. C. Joo, H. Balci, Y. Ishitsuka, C. Buranachai, T. Ha, Advances in single-molecule fluorescence methods for molecular biology. *Annu. Rev. Biochem.* **77**, 51–76 (2008).
4. R. Y. Tsien, The green fluorescent protein. *Annu. Rev. Biochem.* **67**, 509–544 (1998).
5. B. N. G. Giepmans, S. R. Adams, M. H. Ellisman, R. Y. Tsien, The fluorescent toolbox for assessing protein location and function. *Science* **312**, 217–224 (2006).
6. U. Resch-Genger, M. Grabolle, S. Cavaliere-Jaricot, R. Nitschke, T. Nann, Quantum dots versus organic dyes as fluorescent labels. *Nat. Methods* **5**, 763–775 (2008).
7. M. S. Gonçalves, Fluorescent labeling of biomolecules with organic probes. *Chem. Rev.* **109**, 190–212 (2009).
8. M. Han, X. Gao, J. Z. Su, S. Nie, Quantum-dot-tagged microbeads for multiplexed optical coding of biomolecules. *Nat. Biotechnol.* **19**, 631–635 (2001).
9. J. M. Levsky, S. M. Shenoy, R. C. Pezo, R. H. Singer, Single-cell gene expression profiling. *Science* **297**, 836–840 (2002).
10. Y. Li, Y. T. H. Cu, D. Luo, Multiplexed detection of pathogen DNA with DNA-based fluorescence nanobarcodes. *Nat. Biotechnol.* **23**, 885–889 (2005).
11. N. C. Seeman, Nucleic-acid junctions and lattices. *J. Theor. Biol.* **99**, 237–247 (1982).
12. P. W. K. Rothemund, Folding DNA to create nanoscale shapes and patterns. *Nature* **440**, 297–302 (2006).
13. S. M. Douglas, H. Dietz, T. Liedl, B. Högberg, F. Graf, W. M. Shih, Self-assembly of DNA into nanoscale three-dimensional shapes. *Nature* **459**, 414–418 (2009).
14. T. Tørring, N. V. Voigt, J. Nangreave, H. Yan, K. V. Gothelf, DNA origami: A quantum leap for self-assembly of complex structures. *Chem. Soc. Rev.* **40**, 5636–5646 (2011).
15. B. Wei, M. Dai, P. Yin, Complex shapes self-assembled from single-stranded DNA tiles. *Nature* **485**, 623–626 (2012).
16. Y. Ke, L. L. Ong, W. M. Shih, P. Yin, Three-dimensional structures self-assembled from DNA bricks. *Science* **338**, 1177–1183 (2012).
17. O. S. Wolfbeis, An overview of nanoparticles commonly used in fluorescent bioimaging. *Chem. Soc. Rev.* **44**, 4743–4768 (2015).
18. S. R. Nicewarner-Peña, R. G. Freeman, B. D. Reiss, L. He, D. J. Peña, I. D. Walton, R. Cromer, C. D. Keating, M. J. Natan, Submicrometer metallic barcodes. *Science* **294**, 137–141 (2001).
19. M. S. Gudiksen, L. J. Lauhon, J. Wang, D. C. Smith, C. M. Lieber, Growth of nanowire superlattice structures for nanoscale photonics and electronics. *Nature* **415**, 617–620 (2002).
20. K. Braeckmans, S. C. De Smedt, C. Roelant, M. Leblans, R. Pauwels, J. Demeester, Encoding microcarriers by spatial selective photobleaching. *Nat. Mater.* **2**, 169–173 (2003).
21. M. J. Dejneka, A. Streltsov, S. Pal, A. G. Frutos, C. L. Powell, K. Yost, P. K. Yuen, U. Müller, J. Lahiri, Rare earth-doped glass microbarcodes. *Proc. Natl. Acad. Sci. U.S.A.* **100**, 389–393 (2003).
22. G. K. Geiss, R. E. Bumgarner, B. Birditt, T. Dahl, N. Dowidar, D. L. Dunaway, H. P. Fell, S. Ferree, R. D. George, T. Grogan, J. J. James, M. Maysuria, J. D. Mitton, P. Oliveri, J. L. Osborn, T. Peng, A. L. Ratcliffe, P. J. Webster, E. H. Davidson, L. Hood, K. Dimitrov, Direct multiplexed measurement of gene expression with color-coded probe pairs. *Nat. Biotechnol.* **26**, 317–325 (2008).
23. M. Xiao, E. Wan, C. Chu, W.-C. Hsueh, Y. Cao, P.-Y. Kwok, Direct determination of haplotypes from single DNA molecules. *Nat. Methods* **6**, 199–201 (2009).
24. X. Li, T. Wang, J. Zhang, D. Zhu, X. Zhang, Y. Ning, H. Zhang, B. Yang, Controlled fabrication of fluorescent barcode nanorods. *ACS Nano* **4**, 4350–4360 (2010).
25. E. Lubeck, L. Cai, Single-cell systems biology by super-resolution imaging and combinatorial labeling. *Nat. Methods* **9**, 743–748 (2012).
26. C. Lin, R. Jungmann, A. M. Leifer, C. Li, D. Levner, G. M. Church, W. M. Shih, P. Yin, Submicrometre geometrically encoded fluorescent barcodes self-assembled from DNA. *Nat. Chem.* **4**, 832–839 (2012).
27. H. Xu, M. Y. Sha, E. Y. Wong, J. Uphoff, Y. Xu, J. A. Treadway, A. Truong, E. O'Brien, S. Asquith, M. Stubbins, N. K. Spurr, E. H. Lai, W. Mahoney, Multiplexed SNP genotyping using the Qbead system: A quantum dot-encoded microsphere-based assay. *Nucleic Acids Res.* **31**, e43 (2003).
28. C. Lin, Y. Liu, H. Yan, Self-assembled combinatorial encoding nanoarrays for multiplexed biosensing. *Nano Lett.* **7**, 507–512 (2007).
29. J. Livet, T. A. Weissman, H. Kang, R. W. Draft, J. Lu, R. A. Bennis, J. R. Sanes, J. W. Lichtman, Transgenic strategies for combinatorial expression of fluorescent proteins in the nervous system. *Nature* **450**, 56–62 (2007).
30. S. Fournier-Bidoz, T. L. Jennings, J. M. Klostranec, W. Fung, A. Rhee, D. Li, W. C. W. Chan, Facile and rapid one-step mass preparation of quantum-dot barcodes. *Angew. Chem. Int. Ed.* **47**, 5577–5581 (2008).
31. L. Marcon, B. J. Battersby, A. Rühmann, K. Ford, M. Daley, G. A. Lawrie, M. Trau, 'On-the-fly' optical encoding of combinatorial peptide libraries for profiling of protease specificity. *Mol. Biosyst.* **6**, 225–233 (2010).
32. M. F. Elshal, J. P. McCoy, Multiplex bead array assays: Performance evaluation and comparison of sensitivity to ELISA. *Methods* **38**, 317–323 (2006).
33. T. Förster, Zwischenmolekulare energiewanderung und fluoreszenz. *Ann. Phys.* **437**, 55–75 (1948).
34. R. M. Dirks, N. A. Pierce, Triggered amplification by hybridization chain reaction. *Proc. Natl. Acad. Sci. U.S.A.* **101**, 15275–15278 (2004).
35. J. P. Sadowski, C. R. Calvert, D. Y. Zhang, N. A. Pierce, P. Yin, Developmental self-assembly of a DNA tetrahedron. *ACS Nano* **8**, 3251–3259 (2014).
36. P. Yin, H. M. Choi, C. R. Calvert, N. A. Pierce, Programming biomolecular self-assembly pathways. *Nature* **451**, 318–322 (2008).
37. B. Yurke, A. J. Turberfield, A. P. Mills Jr., F. C. Simmel, J. L. Neumann, A DNA-fuelled molecular machine made of DNA. *Nature* **406**, 605–608 (2000).
38. D. Y. Zhang, G. Seelig, Dynamic DNA nanotechnology using strand-displacement reactions. *Nat. Chem.* **3**, 103–113 (2011).
39. Y. Liu, C. Lin, H. Li, H. Yan, Aptamer-directed self-assembly of protein arrays on a DNA nanostructure. *Angew. Chem. Int. Ed.* **44**, 4333–4338 (2005).
40. S. Rinker, Y. Ke, Y. Liu, R. Chhabra, H. Yan, Self-assembled DNA nanostructures for distance-dependent multivalent ligand-protein binding. *Nat. Nanotechnol.* **3**, 418–422 (2008).
41. R. Jungmann, M. Scheible, F. C. Simmel, Nanoscale imaging in DNA nanotechnology. *Wiley Interdiscip. Rev. Nanomed. Nanobiotechnol.* **4**, 66–81 (2012).
42. A. Gietl, P. Holzmeister, D. Grohmann, P. Tinnefeld, DNA origami as biocompatible surface to match single-molecule and ensemble experiments. *Nucleic Acids Res.* **40**, e110 (2012).
43. C. Steinhauer, R. Jungmann, T. L. Sobey, F. C. Simmel, P. Tinnefeld, DNA origami as a nanoscopic ruler for super-resolution microscopy. *Angew. Chem. Int. Ed.* **48**, 8870–8873 (2009).
44. R. Jungmann, C. Steinhauer, M. Scheible, A. Kuzyk, P. Tinnefeld, F. C. Simmel, Single-molecule kinetics and super-resolution microscopy by fluorescence imaging of transient binding on DNA origami. *Nano Lett.* **10**, 4756–4761 (2010).
45. A. Johnson-Buck, J. Nangreave, D.-N. Kim, M. Bathe, H. Yan, N. G. Walter, Super-resolution fingerprinting detects chemical reactions and idiosyncrasies of single DNA pegboards. *Nano Lett.* **13**, 728–733 (2013).
46. R. Iinuma, Y. Ke, R. Jungmann, T. Schlichthaerle, J. B. Woehrstein, P. Yin, Polyhedra self-assembled from DNA tripods and characterized with 3D DNA-PAINT. *Science* **344**, 65–69 (2014).
47. R. Jungmann, M. S. Avendaño, J. B. Woehrstein, M. Dai, W. M. Shih, P. Yin, Multiplexed 3D cellular super-resolution imaging with DNA-PAINT and Exchange-PAINT. *Nat. Methods* **11**, 313–318 (2014).
48. J. J. Schmied, A. Gietl, P. Holzmeister, C. Forthmann, C. Steinhauer, T. Dammeyer, P. Tinnefeld, Fluorescence and super-resolution standards based on DNA origami. *Nat. Methods* **9**, 1133–1134 (2012).

49. J. J. Schmied, M. Raab, C. Forthmann, E. Pibiri, B. Wünsch, T. Dammeyer, P. Tinnefeld, DNA origami–based standards for quantitative fluorescence microscopy. *Nat. Protoc.* **9**, 1367–1391 (2014).
50. T. Schlichthaerle, M. T. Strauss, F. Schueder, J. B. Woehrstein, R. Jungmann, DNA nanotechnology and fluorescence applications. *Curr. Opin. Biotechnol.* **39**, 41–47 (2016).
51. T. Ha, P. Tinnefeld, Photophysics of fluorescent probes for single-molecule biophysics and super-resolution imaging. *Annu. Rev. Phys. Chem.* **63**, 595–617 (2012).
52. G. P. Anderson, N. L. Nerurkar, Improved fluoroimmunoassays using the dye Alexa Fluor 647 with the RAPTOR, a fiber optic biosensor. *J. Immunol. Methods* **271**, 17–24 (2002).
53. J. M. Levsky, R. H. Singer, Fluorescence in situ hybridization: Past, present and future. *J. Cell Sci.* **116**, 2833–2838 (2003).
54. A. Raj, P. van den Bogaard, S. A. Rifkin, A. van Oudenaarden, S. Tyagi, Imaging individual mRNA molecules using multiple singly labeled probes. *Nat. Chem. Biol.* **5**, 877–879 (2008).
55. H. M. T. Choi, V. A. Beck, N. A. Pierce, Next-generation in situ hybridization chain reaction: Higher gain, lower cost, greater durability. *ACS Nano* **8**, 4284–4294 (2014).
56. C. Myhrvold, M. Dai, P. A. Silver, P. Yin, Isothermal self-assembly of complex DNA structures under diverse and biocompatible conditions. *Nano Lett.* **13**, 4242–4248 (2013).

Acknowledgments: We thank T. C. Ferrante from the Wyss Institute for Biologically Inspired Engineering Imaging Core for support with microscopy. We also thank Y. Niyaz from Carl Zeiss AG and M. Spitaler from the Max Planck Institute of Biochemistry for data acquisition support. We also acknowledge W. Sun and S. M. Douglas for initial designs and experiments. **Funding:** This work is supported by an NIH Director's New Innovator Award (1DP2OD007292), an NIH Transformative Research Award (1R01EB018659), an NIH grant (5R21HD072481), an Office of Naval Research (ONR) Young Investigator Program Award (N000141110914), ONR grants (N000141010827 and N000141310593), an NSF Faculty Early Career Development Award (CCF1054898), an NSF grant (CCF1162459), and a Wyss Institute for Biologically Engineering Faculty Startup Fund to P.Y. J.B.W., M.T.S., and R.J. acknowledge support from the Deutsche Forschungsgemeinschaft through the Emmy Noether Programme (DFG JU 2957/1-1) and the SFB 1032 (Nanoagents for the spatiotemporal control of molecular and cellular reactions), the European Research Council (ERC) through an ERC Starting Grant (MolMap; grant agreement number 680241), the Max Planck Society, the Max Planck Foundation, and the Center for NanoScience. M.T.S. acknowledges support from the International Max Planck Research School for Molecular and Cellular Life Sciences. D.Y.Z. acknowledges support from an NIH Pathway to Independence Award (K99EB015331). **Author contributions:** J.B.W. and M.T.S. contributed equally to this work. J.B.W., M.T.S., and R.J. designed and performed the experiments, analyzed the data, developed the software, and wrote the manuscript. L.L.O., B.W., and D.Y.Z. designed the triggered assembly of metafluorophores and performed preliminary experiments. P.Y. and R.J. conceived and supervised the study, interpreted the data, and wrote the manuscript. All authors reviewed and approved the manuscript. **Competing interests:** P.Y. and R.J. are cofounders of Ultivue Inc. R.J., M.T.S., J.B.W., and P.Y. are inventors on a pending patent related to this work, filed on 16 December 2015 (PCT/US2015/065962). R.J., L.L.O., D.Y.Z., B.W., and P.Y. are inventors on a pending patent related to this work, filed on 16 December 2015 (PCT/US2015/065948). All other authors declare that they have no other competing interests. **Data and materials availability:** All data needed to evaluate the conclusion in the paper are present in the paper and/or the Supplementary Materials. Additional data related to this paper may be requested from the authors.

Submitted 6 September 2016
Accepted 28 April 2017
Published 21 June 2017
10.1126/sciadv.1602128

Citation: J. B. Woehrstein, M. T. Strauss, L. L. Ong, B. Wei, D. Y. Zhang, R. Jungmann, P. Yin, Sub–100-nm metafluorophores with digitally tunable optical properties self-assembled from DNA. *Sci. Adv.* **3**, e1602128 (2017).

2.2 INCORPORATION STUDY

In the prevision section, the applicability of DNA origami as a tool for fluorescence microscopy was demonstrated with the metafluorophores and highlights how fluorescence microscopy can benefit from the field of DNA nanotechnology. However, this positive interaction is not one-sided. On the other hand, fluorescence microscopy and super-resolution microscopy, in particular, can be used to study DNA origami nanostructures. In the following section, I will introduce the idea of the incorporation study, where I used DNA-PAINT super-resolution microscopy to systematically study the incorporation and accessibility of staples in DNA origami.
The self-assembly of DNA nanostructures is a remarkable process, which can be stressed by recapitulating a typical folding mix with nanomolar (10^{-9}) concentrations and microliter (10^{-6}) volumes. Given Avogadro's constant (10^{23}) this leaves one with 10^8 structures that each self-assembled into a previously designed structure. Here, a central point is to assess how successful the folding is on a single-molecule level. This can be further stressed when thinking about achieving the goal of turning static DNA nanostructures into dynamic nanomachines. It is evident that even one missing staple is of great importance for the functionality of the final machine. An immediate example of how this affects the efficiency of a technique is given with the metafluorophores from the previous section. Here, one reason for the fluorophore level broadness arises from incorporation and is therefore directly affecting the sensitivity of this technique.

2.2.1 *DNA-PAINT to study incorporation*

Typically, the effectiveness of folding is analyzed by bulk gel assays. In 2014 Wagenbauer et al. proposed the usage of a de-Bruijn probe to quantify the number of unpaired base pairs as a measure of folding efficiency via gel readout [43]. Three years later, Myhrvold et al. published a technique that uses sequencing to quantify the amount of staple abundance [44]. When imaging a DNA nanostructure with DNA-PAINT, there are, in contrast to the design, spots missing. A typical example is a 20 nm grid structure, that is designed to have 12 binding sites. On average, only 10 binding sites will be imaged with DNA-PAINT. As the imaging of DNA-PAINT sites is a direct visualization of not only the successful folding of a strand into a structure but also its accessibility for the imaging strand, DNA-PAINT is an ideal technique to systematically study DNA origami nanostructures on a single molecule and staple level.
First, we developed a software tool that assesses incorporation of DNA origami datasets that were acquired with DNA-PAINT. The software tool was thoroughly benchmarked with simulated data containing a known

ground truth and was able to accurately determine incorporation. We then systematically analyzed different folding parameters, such as different foldings ramps, $MgCl_2$-concentrations, and variations in staple excess, and found that they have little influence on the incorporation of staples. A parameter that had considerable influence on the incorporation was the excess of staple strands with respect to the scaffold. Here, we concluded that an excess of at least 50x is recommended.
After finding that incorporation values could be differentiated on a single staple level, we systematically evaluated all accessible staples of the flat rectangular DNA origami structure. We found an average incorporation efficiency of 84% with higher incorporation values towards the center and lower towards the edges.

2.2.2 *Incorporation and accessibility*

Additional experiments were conducted to untangle incorporation from accessibility which resulted in a 7% offset when translating the measured accessibility values to determine incorporation. By using a force-clamp structure to probe staples away from the surface, and probing the accessibility of scaffold loops we tested for effects that were induced by surface interaction. We concluded that surface-interaction is not significantly affecting the experimental results.

2.2.3 *Associated publication P2*

Quantifying absolute addressability in DNA origami with molecular resolution

By

Maximilian T. Strauss*, **Florian Schüeder***, **Daniel Haas***, P. Nickels, Ralf Jungmann

** These authors contributed equally to this work*

published in

Nature Communications (2018)

nature COMMUNICATIONS

ARTICLE

DOI: 10.1038/s41467-018-04031-z OPEN

Quantifying absolute addressability in DNA origami with molecular resolution

Maximilian T. Strauss[1,2], Florian Schueder[1,2], Daniel Haas[1,2], Philipp C. Nickels[1,2] & Ralf Jungmann[1,2]

Self-assembled DNA nanostructures feature an unprecedented addressability with sub-nanometer precision and accuracy. This addressability relies on the ability to attach functional entities to single DNA strands in these structures. The efficiency of this attachment depends on two factors: incorporation of the strand of interest and accessibility of this strand for downstream modification. Here we use DNA-PAINT super-resolution microscopy to quantify both incorporation and accessibility of all individual strands in DNA origami with molecular resolution. We find that strand incorporation strongly correlates with the position in the structure, ranging from a minimum of 48% on the edges to a maximum of 95% in the center. Our method offers a direct feedback for the rational refinement of the design and assembly process of DNA nanostructures and provides a long sought-after quantitative explanation for efficiencies of DNA-based nanomachines.

[1] Department of Physics and Center for Nanoscience, Ludwig Maximilian University, 80539 Munich, Germany. [2] Max Planck Institute of Biochemistry, 82152 Martinsried near Munich, Germany. These authors contributed equally: Maximilian T. Strauss, Florian Schueder, Daniel Haas. Correspondence and requests for materials should be addressed to R.J. (email: jungmann@biochem.mpg.de)

Structural DNA nanotechnology[1,2] has revolutionized the field of molecular self-assembly by harnessing the programmability and specificity of DNA hybridization for sequence-guided self-assembly. DNA origami[3], in particular, marked a breakthrough, allowing researchers to readily design and build structures of almost arbitrary shape and complexity[4–11]. In DNA origami, a long single strand (the "scaffold") is folded into a pre-designed shape by ~200 short, complementary strands (the "staples"). Each staple has a unique sequence and specifically binds parts of the scaffold together during thermal annealing, thus folding the scaffold into the pre-designed shape. While the large variety of shapes constructed to-date is impressive, the true power of DNA origami lies in the addressability of specific sites on the structure with sub-nanometer precision and accuracy[12–16] via the modification of single staples. Successful addressability of a staple is directly linked to its incorporation and accessibility: the staple has to be incorporated efficiently and it needs to be accessible for downstream attachment of guest molecules, e.g., via complementary strand hybridization or direct chemical modification. Hence, it is necessary to characterize both factors on the single-staple level with absolute quantification. Although, recent studies assessed the overall structural integrity using bulk gel assays[17] and the relative abundance of single staples using next-generation sequencing[18], we still lack the ability to quantify incorporation and accessibility in an absolute manner on the level of single staples. Recent advancements in optical super-resolution microscopy[19] allow for precise, noninvasive characterization of objects below the diffraction limit of light. Specifically, DNA Points Accumulation in Nanoscale Topography (DNA-PAINT)[20,21] super-resolution microscopy is well-suited to characterize DNA nanostructures because it can achieve the thus far unprecedented spatial resolution of ~5 nm, enabling the quantification of the accessibility and absolute incorporation efficiency of every single staple in a DNA origami structure[22].

Results

In silico validation of the method. Transient, repetitive binding of dye-labeled oligonucleotides ("imager" strands) to their complementary targets ("docking" sites) can be observed as apparent blinking (Fig. 1a). The apparent blinking is used to reconstruct super-resolution images that visualize the designed pattern of docking sites, e.g., a 20-nm-grid structure (based on the two-dimensional (2D) rectangular DNA origami, details about the design are shown in Supplementary Figs. 1 and 2). These 20-nm-grids, however, stochastically miss reconstructed points at designed sites[21,23] because the docking sites at these missing points are not transiently visited by an imager strand. This could be explained by two mechanisms: (1) staples are not incorporated into the structure; or (2) staples are incorporated, but docking sites are not available for binding of imager strands (i.e., sequestered). As a result, these positions are not accessible for downstream modification (Fig. 1b). To assess this accessibility, we developed a software tool that detected DNA origami structures in a reconstructed DNA-PAINT image and subsequently aligned them to a template structure to create a sum image (Fig. 1c and Supplementary Figs. 3 and 4). Then, we quantified the number of localizations at each docking site in the sum image. As the binding of imager strands to their docking sites is repetitive, we defined a minimum number of localizations as a threshold value: sites with values below this threshold were classified as not detected (Fig. 1c). To validate our analysis workflow, we performed in silico DNA-PAINT experiments of 20-nm-grids with an occurrence probability of individual docking sites ranging from 30 to 100% using the software program Picasso[21]. The number of detected docking sites was in good agreement with the number of simulated docking sites (Fig. 1d), which confirmed the applicability of our analysis approach to measure the detectability of single docking sites.

Investigating incorporation and accessibility. Next, we decoupled the two possible underlying mechanisms for non-detectable docking sites: (1) incorporation and (2) accessibility. In order to assay each mechanism, we designed a 20-nm-grid carrying staples that are simultaneously extended with orthogonal docking sites on the 3′- and 5′-end (Fig. 2a). We then performed sequential two-color DNA-PAINT imaging and interactively evaluated 100 origami structures with a total of 1200 designed docking sites (the imaging results are shown in Fig. 2b and Supplementary Fig. 5). In 78.5% of the cases, we detected a signal from both docking sites (3′- and 5′-end). In 5%, we only detected the 3′-end site, and in 7.2%, only the 5′-end site. No site at all was detected in 9.3% of all cases. Since the detection of 3′- and 5′-ends should be independent of each other, we estimated that there was a ~2.4% probability that neither the 3′-end nor the 5′-end of an actually incorporated staple was detected. Therefore, we concluded that in the 9.3% of the cases (in which no site was detected) the staple was indeed not incorporated. Ultimately, this allowed us to assess the accessibility of docking sites for downstream studies, as well as to quantify the actual incorporation efficiency of single staples. To translate accessibility to absolute staple incorporation efficiency, we added an offset of +7% when imaging the accessibility of a 3′-end site (since we typically use 3′-end extensions as docking sites in DNA-PAINT, we concentrated on 3′-ends for the following experiments). Nevertheless, as the vision of structural DNA nanotechnology[24] is to arrange matter in a prescribed manner by site-specific attachment of molecular entities, we believe the ultimate measure of quality for DNA origami should be the accessibility of docking sites. Therefore, we focus on detection efficiencies (i.e., accessibility) for the rest of this study.

Assembly conditions and staple detection. We investigated the influence of different assembly conditions on the detection efficiency of individual staples. First, we evaluated the number of detected sites as a function of the annealing time: for the 20-nm-grid, we tested annealing times ranging from 5 min to 3 days (Fig. 3b) and determined detection efficiencies for all 12 staple positions separately. Since the 20-nm-grid has rotational and mirror symmetry, we then averaged over all 12 sites of a single grid to obtain an average detection efficiency per origami. We measured an average detection efficiency of ~82% for all annealing times (standard deviation $\sigma = 1.3\%$), underlining the remarkable robustness of the 2D rectangular DNA origami[25]. Additionally, magnesium concentrations between 8 and 16 mM during folding, as well as the long-term storage at room temperature of purified 20-nm-grids did not result in any significant change in detection efficiency (Supplementary Figs. 6 and 7). Second, we investigated the detection efficiency of staples with respect to their molar excess over the scaffold ranging from ten times to ~500 times molar excess (Fig. 3c and Supplementary Fig. 8). The efficiency improved by more than 10% when increasing the excess from ten times to ~500 times (from 72 to 84% on average) and followed a Michaelis–Menten kinetic (for fit parameters see Supplementary Table 1).

Quantifying the accessibility of individual docking sites. Next, we moved away from an average measure of detection efficiency and tested our capability to accurately quantify the accessibility of single docking sites. Accordingly, we designed two distinct structures that break the rotational and mirror symmetry of the regular 20-nm-grid. Each structure carried an alignment pattern

NATURE COMMUNICATIONS | DOI: 10.1038/s41467-018-04031-z ARTICLE

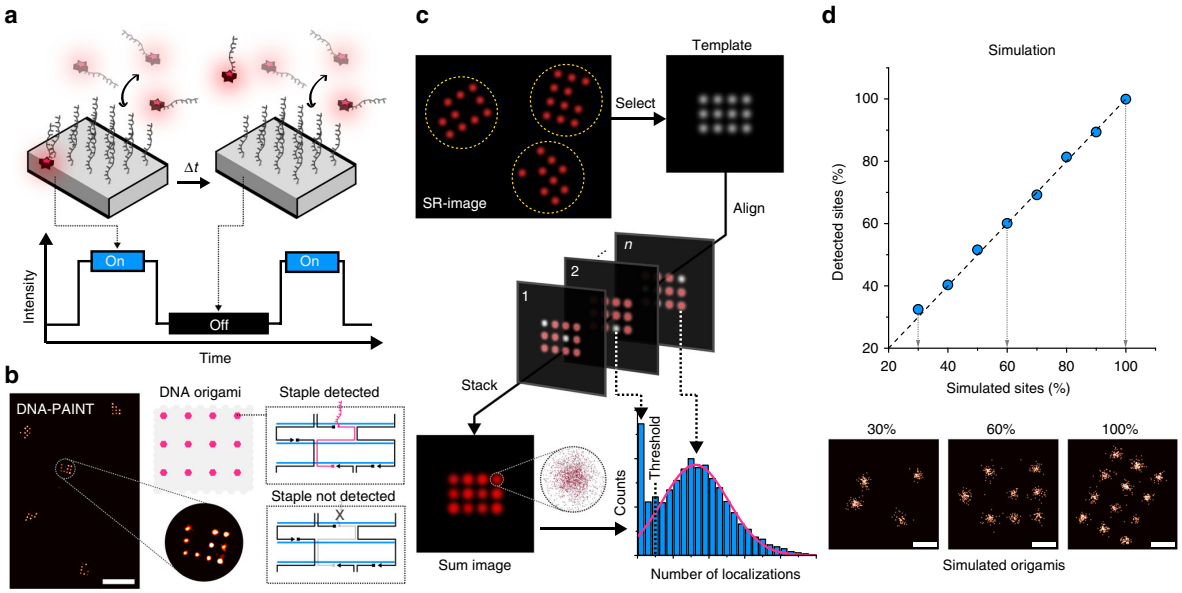

Fig. 1 Quantification of detected staples in DNA origami using super-resolution. **a** DNA-PAINT concept: transient hybridization of dye-labeled imager strands to docking sites on DNA origami enables super-resolution imaging. **b** Typical DNA-PAINT image of 20-nm-grids allows distinction of individual binding sites. Zoom-in of a 20-nm-grid shows that some of the 12 grid sites were not detected. **c** Quantification workflow for assessing abundance of docking sites. Single structures were selected and aligned to a template of the designed grid structure by image cross-correlation. Subsequently, a histogram of localizations per grid site was used to determine a cut-off threshold below, which a site is defined as not detected. This threshold is defined as the number of localizations at half-maximum as determined by the Gaussian fit (magenta curve). **d** Benchmarking of the detection workflow was performed using simulated ground-truth DNA-PAINT data. Blue dots represent simulated 20-nm-grids with varying percentage of simulated docking sites and their evaluation result. The dashed line is the identity line. Scale bars: 100 nm in **b**, 20 nm in **d**

in the form of an arrowhead and a line, as well as three (3 binding sites (BS)) or six (6 BS) docking sites (Fig. 3d). These two structures enabled us to probe the following: first, false positives (i.e., detected sites in 3 BS that are only present in 6 BS); second, the ability to site-specifically probe the detection efficiency. We first tested for false positives and detection efficiencies of single sites using in silico DNA-PAINT data and detected 0% false positives and 100% of the simulated true positive staples (number of simulated structures $n = 50$). Then, we performed in vitro DNA-PAINT experiments (Supplementary Figs. 9 and 10) and detected an average of 2% false positives (number of analyzed structures $n = 250$). Furthermore, the standard deviation between detection efficiencies of the same sites on the two different structures was ~2.6%. These findings suggested that there are no systematic errors induced by our approach, emphasizing our ability to quantify absolute numbers of detected sites in DNA origami structures. At the same time, we measured a large difference (>10%) in the percentage of detected sites for positions 4–6 on both 3 BS and 6 BS structures (in the range of 72–83%), which indicated that there is a positional dependency of detection and therefore staple incorporation.

Quantifying every staple in a DNA origami structure. Finally, this led us to quantify the accessibility of every single staple in the 2D rectangular DNA origami structure. We designed a total of 18 different rectangles, each comprising of an alignment pattern (arrowhead + line) and a unique arrangement of 12 detection sites per rectangle (Fig. 4a and Supplementary Fig. 11) to allow template identification for each structure (Fig. 4b). These 18 unique designs enabled us to individually probe a total of 168 staples in a single DNA-PAINT acquisition experiment (Supplementary Figs. 12 and 13). We deliberately left out staple strands surrounding the biotinylated strands for surface attachment (white hexagons in Fig. 4c), as staple orientation and routing at these locations are inconsistent with the standard design of the rectangle. We then quantified the accessibility for all 168 staples and constructed a heatmap of the rectangle displaying the accessibility as a function of docking-site position (Fig. 4c). The results indicate a consistently lower efficiency of detection on the outside of the structure (with a minimum of 41%) compared to inner areas where detection efficiencies reached 88% (the average detection efficiency for all strands was 77%). Taking the detection efficiency offset of 7% determined by the results from Fig. 2, this translates to absolute incorporation efficiencies of 48–95% with an average of 84%, in good agreement with qualitative results of relative staple abundance from next-generation sequencing[26]. A heatmap displaying the translated values of absolute incorporation efficiencies is shown in Supplementary Fig. 14.

To further evaluate our assumption that we can directly translate the detection efficiency offset from Fig. 2 to strand incorporation and eliminate possible accessibility effects, we targeted a single-stranded section of the scaffold strand (Supplementary Fig. 16a) on the edge of the 2D rectangular origami (scaffold loop). The assumption was that this scaffold loop must be present in every structure. We detected the scaffold loop in 90% of all cases. To further investigate the effect of potential surface interaction, we used a three-dimensional DNA origami structure, the force clamp[27]. This structure spans a section of the scaffold strand between two pillars more than 20 nm above the surface. Here, we mimicked the single-stranded scaffold loop we targeted in the 2D rectangular origami (Supplementary Fig. 16b) and found a 91% detection efficiency, indicating that there is no significant effect arising from surface interactions. We additionally used the force-clamp structure to

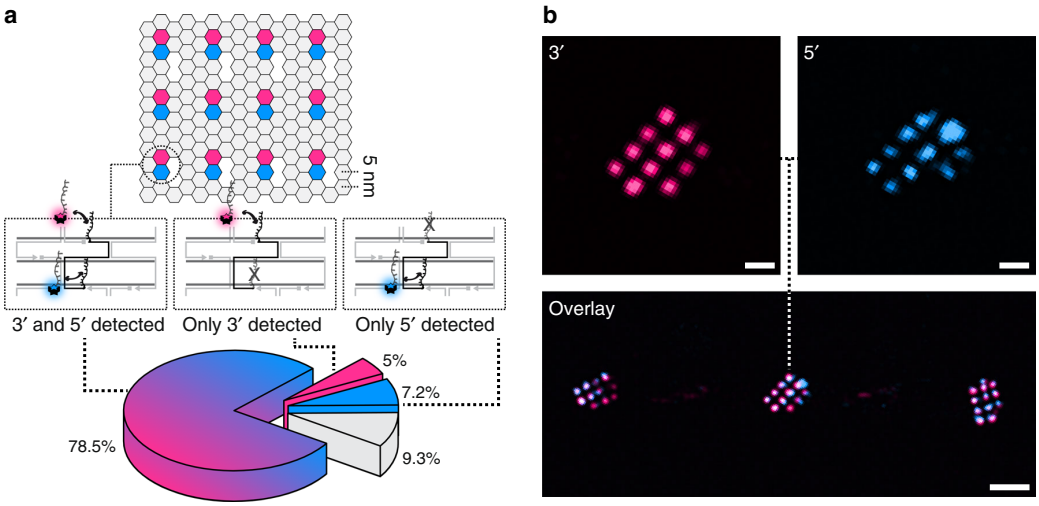

Fig. 2 Experimental validation of accessibility and incorporation efficiency. **a** The 20-nm-grid staples were extended with orthogonal DNA-PAINT docking sites on the 3′-end (magenta) and 5′-end (blue) and subsequently imaged using Cy3B-(magenta) and Atto647N-labeled (blue) imager strands. The pie chart shows the percentage of docking sites where both ends were detected (blue to magenta slice), only the 3′-end (magenta slice), only the 5′-end (blue slice), and no end was detected at all (gray slice). **b** Overlay and color-separated zoom-ins of the two-color DNA-PAINT measurement. Scale bars: 20 nm in **b** (top), 100 nm in **b** (bottom)

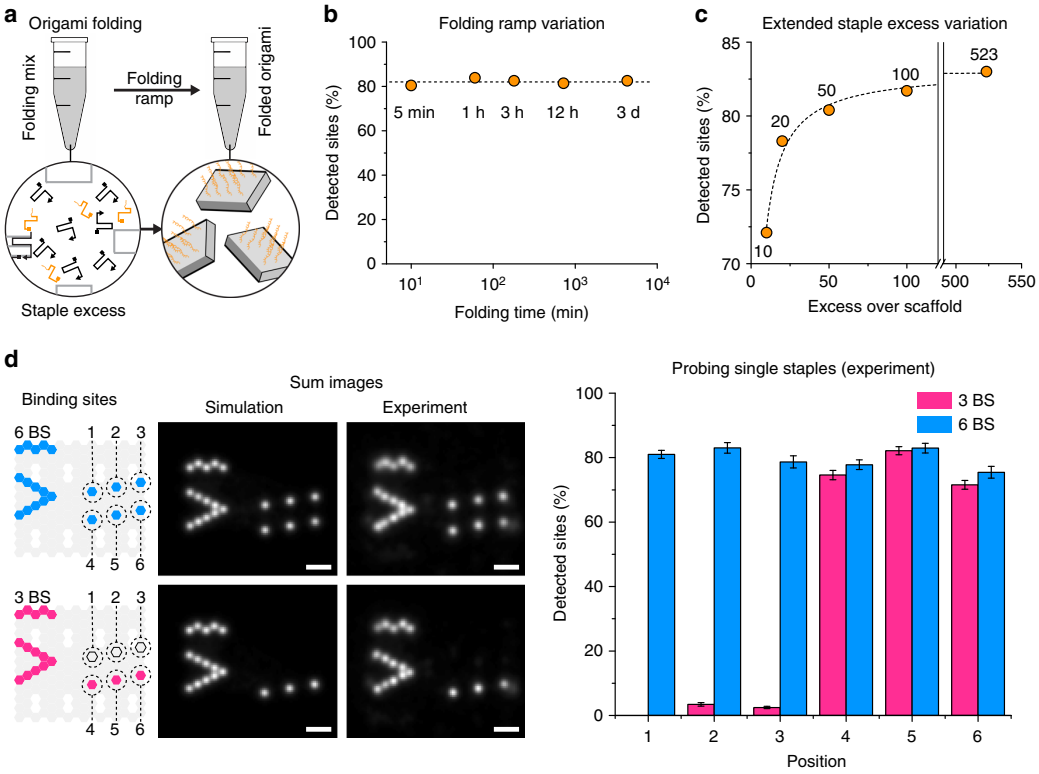

Fig. 3 Influence of folding conditions and experimental validation of accessibility of single sites. **a** Schematic folding of 20-nm-grids with the staples that carry detection sites in orange. **b** Percentage of detected sites as a function of folding time. The dashed line represents the mean of all 5 measurements (mean: ~82%). **c** Percentage of detected sites as a function of molar staple excess over scaffold. The dashed line represents the fit of a Michaelis–Menten curve (saturation: 83%). **d** Schematics of the 6 BS (blue) and 3 BS (magenta) structures with the arrowhead + line alignment pattern, their DNA-PAINT sum images, and the percentage of detected sites depending on the position. Error bars represent the standard deviation and were generated by repeated ($n = 10$) random selection of a subset of 250 structures from all selected structures of the whole field of view. Scale bars, 20 nm in **d**

NATURE COMMUNICATIONS | DOI: 10.1038/s41467-018-04031-z ARTICLE

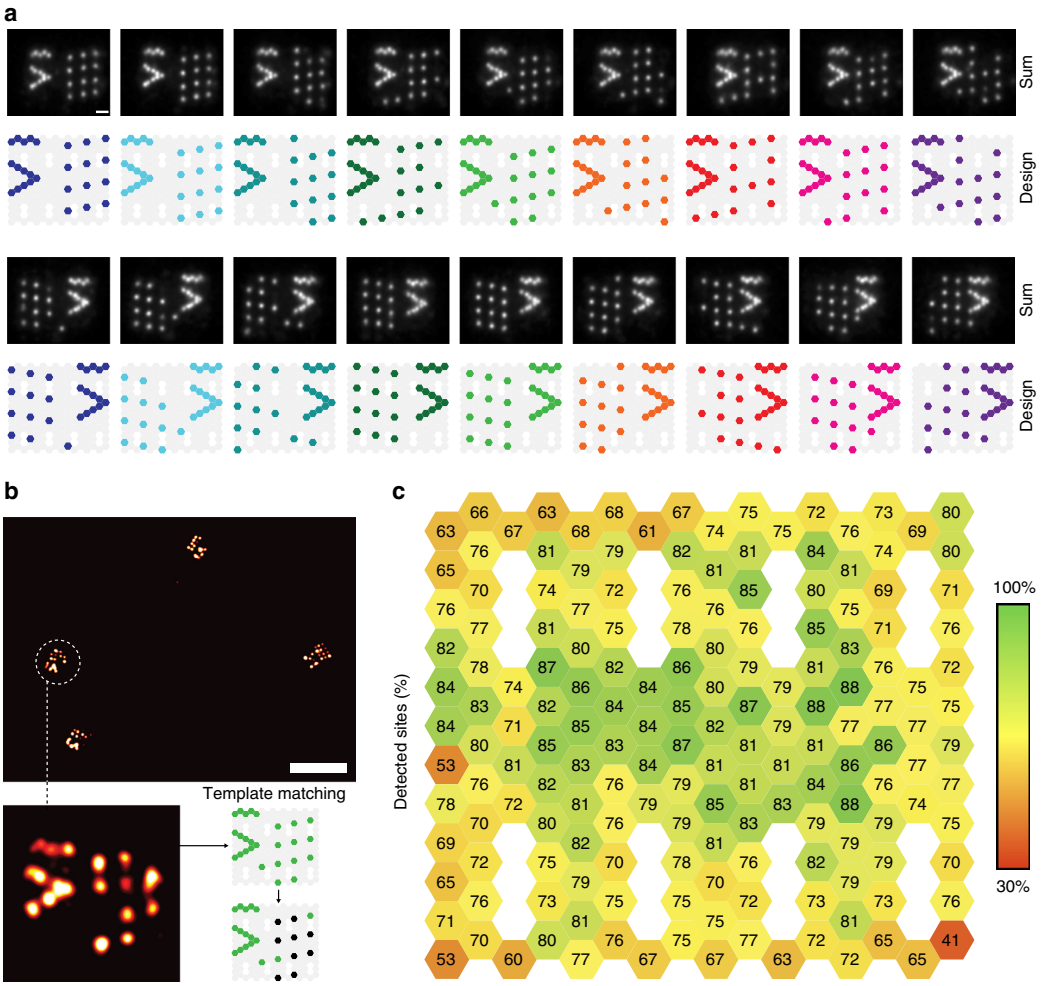

Fig. 4 Accessibility of all staples in a 2D rectangle. **a** A total of 18 design variants were used to probe all addressable staples in a 2D rectangular DNA origami structure in a single experiment. Designed patterns and sum images of experimentally obtained DNA-PAINT images are shown. **b** Arrowhead + line alignment patterns allowed the unique assignment of a detected structure to the design template. Shown in the zoom-in is a single structure matched to a template with black sites identified as detected. **c** Heatmap of 168 individually probed staples of the 2D rectangle, generally showing higher detection efficiencies in the center of the structure and lower detection efficiencies towards the edges. Average detection efficiency: 77% (corresponding to an average incorporation efficiency of 84%). Scale bars, 20 nm in **a**, 100 nm in **b**

directly investigate the effect of accessibility on the detection efficiency. For this we modified the force clamp structure to exhibit a slightly stretched and thus ideally accessible scaffold section (Supplementary Fig. 16c). The measured detection efficiency of 97% suggests that the maximum error arising from accessibility is 3%. To translate our results back to incorporation, we hybridized a staple to the scaffold between the two pillars of the force clamp (Supplementary Fig. 16d). The 32 nt staple (same length as the staples in the 2D rectangular origami) was extended with the 3′-end docking site used throughout this study. Here, we measured a detection efficiency of the docking site of 94%, suggesting an error of 3% caused by incomplete incorporation. Ultimately, we conclude that the offset determined in Fig. 2 can be used to directly estimate incorporation from measured detection efficiency.

The transient binding of imager strands to their docking sites should not be affected by the position of the docking site on the DNA origami bound to flat surface[20,26]. Therefore, we argue that the change in detection efficiency as a function of docking site position is indeed an effect of an underlying change in incorporation efficiency. This could be explained by the fact that staples at the edges and corners are missing neighboring helices and/or lack stacking interactions to neighboring strands. This hypothesis is further supported by qualitatively comparing our heatmap to finite-element-based modeling (Supplementary Fig. 15) of thermal fluctuation of the same rectangular origami using the software tool Cando[28]. Further quantitative assessment of these effects could be achieved by sequence-level coarse-grained[29] or fully atomistic[30] molecular dynamics simulations.

Discussion

In recent years, many DNA origami-related studies reported on the attachment yield of various functional entities, such as streptavidin[16,20], DNA walkers[31,32], gold nanoparticles[33], motor proteins[34], and DNA strands[23,35]. We collected eight values for reported yields and translated these values into incorporation efficiencies of single staples (Supplementary Table 2). The translated incorporation values are either in good agreement with

our average incorporation efficiency of 84% or match our measured maximum incorporation of 95%. Thus, our study now provides a quantitative explanation of these reported attachment yields. From our results, we derive two recommendations for researchers planning to use DNA origami structures for the arrangement of functional entities. First, staples that are used as sites for downstream modification should be included in at least a 50 times molar excess over the scaffold to maximize the incorporation and thus efficiency of downstream modifications. Second, attachment points of downstream modifications, as well as tracks for hybridization cascades (e.g., for DNA walkers of localized chemical reaction networks) based on the rectangular origami design should be placed at points of high incorporation efficiency (Fig. 4c) and should—if possible—be designed redundantly (as already established for the attachment of metallic nanoparticles[36]).

In conclusion, we presented a method for the absolute quantification of single strand incorporation and downstream modification accessibility by using the unique capabilities of DNA-PAINT super-resolution microscopy to achieve single-staple-level resolution (we achieved a maximum localization precision of 1.37 nm as calculated by a nearest neighbor based analysis[37], see Supplementary Table 3). We believe that our method will allow for rational engineering of the design and assembly process of DNA nanostructures in order to maximize downstream attachment. This method is not limited to the 2D rectangular DNA origami structure shown here, but can be applied to virtually any DNA-nanostructure geometry. Additionally, this approach can be directly used to characterize the labeling efficiency of antibodies or cellular proteins and nucleic acids, potentially making it of great interest for super-resolution microscopy in general and quantitative structural biology in particular.

Methods

Materials and buffers. Unmodified, dye-labeled, and biotinylated DNA oligonucleotides were purchased from MWG Eurofins or Integrated DNA Technologies. DNA scaffold strands were purchased from Tilibit (p7249, identical to M13mp18). Streptavidin was purchased from Thermo Fisher (catalog number: S-888). Bovine serum albumin (BSA) and BSA-biotin obtained from Sigma-Aldrich (catalog number: A8549). Glass slides and coverslips were purchased from Marienfeld (cat. no. 0107032) and Thermo Fisher (cat. No. 10756991). Freeze 'N Squeeze columns were ordered from Bio-Rad (cat. no. 732-6165). Polyethylene glycol (PEG)-8000 was purchased from Merck (cat. No. 6510-1KG). Four buffers were used for sample preparation and imaging: buffer A (10 mM Tris-HCl pH 7.5, 100 mM NaCl, 0.05% Tween 20, pH 7.5); buffer B (5 mM Tris-HCl pH 8, 10 mM $MgCl_2$, 1 mM EDTA, 0.05% Tween 20, pH 8); buffer O (5 mM Tris-HCl pH 8, 12.5 mM $MgCl_2$, 1 mM EDTA, 0.05% Tween 20, pH 8) and buffer O^+ (same as O, but supplemented with 1× PCA, 1× PCD, and 1× Trolox). A concentration of 100× Trolox: 100 mg Trolox, 430 µl 100% Methanol, 345 µl 1 M NaOH in 3.2 ml H_2O. A concentration of 40× PCA: 154 mg PCA, 10 ml water, and NaOH were mixed and adjusted to pH 9.0. 100× PCD: 9.3 mg PCD, 13.3 ml of buffer (100 mM Tris-HCl pH 8, 50 mM KCl, 1 mM EDTA, 50% Glycerol). PEG-buffer was used for PEG precipitation[37] (15% PEG-8000, 500 mM NaCl, 12.5 mM $MgCl_2$ in TAE pH 8.0).

Super-resolution microscopy setup. Fluorescence imaging was carried out on an inverted Nikon Eclipse Ti microscope (Nikon Instruments) with the Perfect Focus System, applying an objective-type total internal reflection fluorescence (TIRF) configuration with an oil-immersion objective (Apo SR TIRF 100×, NA 1.49, Oil). Two lasers were used for excitation: 561 nm (200 mW, Coherent Sapphire) or 640 nm (150 mW, Toptica iBeam smart). The laser beam was passed through cleanup filters (ZET561/10 or ZET642/20, Chroma Technology) and coupled into the microscope objective using a beam splitter (ZT561rdc or ZT647rdc, Chroma Technology). Fluorescence light was spectrally filtered with an emission filter (ET600/50m and ET575lp or ET705/72m and ET665lp, Chroma Technology) and imaged on an electron-multiplying charge-coupled device (EMCCD) camera (Andor iXon Ultra 897, used for Figs. 1a and 3c) or sCMOS camera (Andor Zyla 4.2, used for Figs. 3b, d, and 4) without further magnification, resulting in an effective pixel size of 160 nm (EMCCD) or 130 nm (sCMOS after 2 × 2 binning).

DNA origami self-assembly. Self-assembly of DNA origami was accomplished in a one-pot reaction mix with 40 µl total volume, consisting of 10 nM scaffold strand, 100 nM folding staples, 10 nM biotinylated staples (500 nM for Fig. 2 and Supplementary Fig. 16d), and 1 µM (Figs. 1b, 2, 3b, and 4) or varying concentrations (Fig. 3c) of docking site strands (5′-staple-TTATACATCTA-3′) in folding buffer (1× TE buffer with 12.5 mM $MgCl_2$). The reaction mix was then subjected to a thermal annealing ramp using a thermocycler (Mastercycler Nexus Gradient, Eppendorf or Tetrad 2, Bio-Rad). If not otherwise noted, the reaction mix was first incubated at 80 °C for 5 min and then cooled from 60 to 4 °C in steps of 1 °C per 3.21 min and then held at 4 °C until stored at −20 °C protected from light. Samples for the measurement with varying staple excess (Fig. 3c) were purified via three rounds of PEG precipitation by adding the same volume of PEG-buffer, centrifuging at 10,000×*g* at 4 °C for 30 min, removing the supernatant, and resuspending in folding buffer. Structures for Fig. 2 were gel purified by mixing with 1× loading dye and subsequently subjected to agarose gel electrophoresis (1.5% agarose, 0.5× TAE, 10 mM $MgCl_2$, 1× SYBR Safe) at 3 V cm^{-1} for 3 h. Gel bands were extracted, crushed, filled into a Freeze 'N Squeeze column, and centrifuged for 5 min at 1000×*g* at 4 °C. Force-clamp structures were designed and assembled as described before[27]. The staple excess of the extended staple in the structure of Supplementary Fig. 16d was 100× over the scaffold.

Sample preparation. For sample preparation, a piece of coverslip and a glass slide were sandwiched together by two strips of double-sided tape (Scotch, cat. no. 665D) to form a flow chamber with inner volume of ~20 µl. First, 20 µl of biotin-labeled bovine albumin (1 mg/ml, dissolved in buffer A) was flushed into the chamber and incubated for 2 min. The chamber was then washed with 40 µl of buffer A. A volume of 20 µl of streptavidin (0.5 mg ml^{-1}, dissolved in buffer A) was then flushed through the chamber and allowed to bind for 2 min. After washing with 20 µl of buffer A and subsequently with 20 µl of buffer B, 20 µl of biotin-labeled DNA structures (~100–400 pM, see Supplementary Table 4) in buffer B were flushed into the chamber and incubated for 2 min. The chamber was washed with 40 µl of buffer B. Finally, 20 µl of the imager solution was flushed into the chamber, which was subsequently sealed with epoxy (Toolcraft, cat. no. TC-EPO5-24) before imaging.

Imaging conditions. Refer to Supplementary Table 4 for an overview of imaging conditions and Supplementary Table 5 for the imager strand sequences. Supplementary Table 3 shows the super-resolution data properties of all measurements.

Data simulation. In silico experiments were performed using the simulation module of the Picasso[18] software package. For Fig. 1c, 50 structures consisting of 12 BS spaced 20 nm apart (the "20-nm-grid" structure) were simulated with varying incorporation of staple strands (30–100%). Further simulation parameters were an image size of 128 × 128 px and an acquisition time of 50 min (15,000 frames at 200 ms integration time). For the simulation of the 3 BS and 6 BS structure of Fig. 3d, again 50 structures with the same parameters were simulated. For each simulation run, a dark time of 12.5 s and a bright time of 0.5 s were used, corresponding to 5 nM imager strand concentration at a constant association rate of 1.6×10^6 M^{-1} s^{-1}. Further simulation parameters were a pixel size of 160 nm, a detection rate of 35 photons × ms^{-1} kW^{-1} cm^{-2}, a budget of 1.5×10^6 photons, a power density of 1.5 kW × cm^{-2}, and a full width half-maximum of the point-spread-function of 309 nm.

Data analysis. First, super-resolution images were reconstructed and drift-corrected with the render module of Picasso. For the automated evaluation with our MATLAB program, individual structures were selected with Picasso's "pick similar" feature. For the experiments involving the detection of single BS (Figs. 3d and 4), structures were additionally filtered manually by using Picasso's "plot pick" feature. Structures that did not display a correct alignment pattern were discarded. An overview of all selected structures is shown in Supplementary Figs. 9, 10, 12, and 13. Localizations of selected structures were saved as *.hdf5 file and subsequently converted to a *.trace.mat, drift file and mbox file, which then could be imported into the MATLAB program.

The template of each structure was automatically generated after selection of the docking site pattern on the 2D origami map in the template tool. An image was generated by placing Gaussian distributions ($\sigma = 3$ nm, $\sigma = 2$ nm for Fig. 3c or $\sigma =$ 1 nm for the single site measurements shown in Figs. 3d and 4) of binding events on the previously defined positions.

For evaluation, a subset with n structures of all selected structures in the *.trace.mat file was used (Fig. 3b, c: $n = 500$; Fig. 3d: $n = 250$; Fig. 4: two datasets were combined and the minimum number of structures that was present for each structure type was used, $n = 186$). Next, the software aligned each structure to the structure template: the localizations of each structure were isolated and a super-resolution image of the structure was generated by calculating a 2D histogram of these localizations. The super-resolution image was rotated stepwise in a circle and in each step cross-correlated to the template image. The rotation angle with the highest correlation coefficient was determined. This rotation angle and the corresponding xy-shift were then used to transform the localization list in order to align the structure to its template. After alignment, the program counted the number of localizations in a circle with a diameter of 20 nm (Figs. 1c and 3c), 18 nm (Fig. 3b), 6 nm (Fig. 4), or 5 nm (Fig. 3d) around the predefined docking site positions of the template. The number of localizations per docking site for all

structures was displayed in a histogram within the program. This histogram was used to determine the correct detection threshold. This threshold was subsequently used to calculate the presence of each docking site for a given structure. Finally, the program displayed the percentage of detected docking sites for all evaluated structures.

For dual-channel measurements (Fig. 2), 100 structures were manually selected in the reconstructed super-resolution image from Picasso. For each selected structure, the presence or absence of both colors at each docking site was registered.

Data availability. All data supporting the findings of this study are available within the paper and its Supplementary Information. All RAW data are available upon request. The MATLAB program and source code for evaluation are available for download at http://www.jungmannlab.org. All sequences of the DNA origami structures are given in Supplementary Tables 6 and 7.

Received: 7 November 2017 Accepted: 29 March 2018
Published online: 23 April 2018

References

1. Hong, F., Zhang, F., Liu, Y. & Yan, H. DNA Origami: scaffolds for creating higher order structures. *Chem. Rev.* **117**, 12584–12640 (2017).
2. Zhang, F., Nangreave, J., Liu, Y. & Yan, H. Structural DNA nanotechnology: state of the art and future perspective. *J. Am. Chem. Soc.* **136**, 11198–11211 (2014).
3. Rothemund, P. W. K. Folding DNA to create nanoscale shapes and patterns. *Nature* **440**, 297–302 (2006).
4. Andersen, E. S. et al. Self-assembly of a nanoscale DNA box with a controllable lid. *Nature* **459**, 73–76 (2009).
5. Benson, E. et al. DNA rendering of polyhedral meshes at the nanoscale. *Nature* **523**, 441–444 (2015).
6. Dietz, H., Douglas, S. M. & Shih, W. M. Folding DNA into twisted and curved nanoscale shapes. *Science* **325**, 725–730 (2009).
7. Douglas, S. M. Self-assembly of DNA into nanoscale three-dimensional shapes. *Nature* **459**, 414–418 (2009).
8. Han, D. et al. DNA origami with complex curvatures in three-dimensional space. *Science* **332**, 342–346 (2011).
9. Liedl, T., Högberg, B., Tytell, J., Ingber, D. E. & Shih, W. M. Self-assembly of three-dimensional prestressed tensegrity structures from DNA. *Nat. Nanotechnol.* **5**, 520–524 (2010).
10. Matthies, M., Agarwal, N. P. & Schmidt, T. L. Design and synthesis of triangulated DNA origami trusses. *Nano Lett.* **16**, 2108–2113 (2016).
11. Veneziano, R. et al. Designer nanoscale DNA assemblies programmed from the top down. *Science* **352**, 1534 (2016).
12. Funke, J. J. & Dietz, H. Placing molecules with Bohr radius resolution using DNA origami. *Nat. Nanotechnol.* **11**, 47–52 (2016).
13. Kuzyk, A. et al. DNA-based self-assembly of chiral plasmonic nanostructures with tailored optical response. *Nature* **483**, 311–314 (2012).
14. Shaw, A. et al. Spatial control of membrane receptor function using ligand nanocalipers. *Nat. Methods* **11**, 841–846 (2014).
15. Steinhauer, C., Jungmann, R., Sobey, T. L., Simmel, F. C. & Tinnefeld, P. DNA origami as a nanoscopic ruler for super-resolution microscopy. *Angew. Chem. Int Ed. Engl.* **48**, 8870–8873 (2009).
16. Voigt, N. V. et al. Single-molecule chemical reactions on DNA origami. *Nat. Nanotechnol.* **5**, 200–203 (2010).
17. Wagenbauer, K. F., Wachauf, C. H. & Dietz, H. Quantifying quality in DNA self-assembly. *Nat. Commun.* **5**, 3691 (2014).
18. Myhrvold, C. et al. Barcode extension for analysis and reconstruction of structures. *Nat. Commun.* **8**, 14698 (2017).
19. Hell, S. W. et al. The 2015 super-resolution microscopy roadmap. *J. Phys. D Appl. Phys.* **48**, 443001 (2015).
20. Jungmann, R. et al. Single-molecule kinetics and super-resolution microscopy by fluorescence imaging of transient binding on DNA origami. *Nano Lett.* **10**, 4756–4761 (2010).
21. Schnitzbauer, J., Strauss, M. T., Schlichthaerle, T., Schueder, F. & Jungmann, R. Super-resolution microscopy with DNA-PAINT. *Nat. Protoc.* **12**, 1198–1228 (2017).
22. Dai, M., Jungmann, R. & Yin, P. Optical imaging of individual biomolecules in densely packed clusters. *Nat. Nanotechnol.* **11**, 798–807 (2016).
23. Jungmann, R. et al. Quantitative super-resolution imaging with qPAINT. *Nat. Methods* **13**, 439–442 (2016).
24. Seeman, N. C. DNA in a material world. *Nature* **421**, 427–431 (2003).
25. Sobczak, J.-P. J., Martin, T. G., Gerling, T. & Dietz, H. Rapid folding of DNA into nanoscale shapes at constant temperature. *Science* **338**, 1458–1461 (2012).
26. Zhang, Z. et al. Asymmetric DNA origami for spatially addressable and index-free solution-phase DNA chips. *Adv. Mater.* **22**, 2672–2675 (2010).
27. Nickels, P. C. et al. Molecular force spectroscopy with a DNA origami-based nanoscopic force clamp. *Science* **354**, 305–307 (2016).
28. Kim, D.-N., Kilchherr, F., Dietz, H. & Bathe, M. Quantitative prediction of 3D solution shape and flexibility of nucleic acid nanostructures. *Nucleic Acids Res.* **40**, 2862–2868 (2012).
29. Snodin, B. E. K. et al. Direct simulation of the self-assembly of a small DNA origami. *ACS Nano* **10**, 1724–1737 (2016).
30. Maffeo, C., Yoo, J. & Aksimentiev, A. De novo reconstruction of DNA origami structures through atomistic molecular dynamics simulation. *Nucleic Acids Res.* **44**, 3013–3019 (2016).
31. Liber, M., Tomov, T. E., Tsukanov, R., Berger, Y. & Nir, E. A bipedal DNA motor that travels back and forth between two DNA origami tiles. *Small* **11**, 568–575 (2015).
32. Tomov, T. E. et al. Rational design of DNA motors: fuel optimization through single-molecule fluorescence. *J. Am. Chem. Soc.* **135**, 11935–11941 (2013).
33. Gür, F. N., Schwarz, F. W., Ye, J., Diez, S. & Schmidt, T. L. Toward self-assembled plasmonic devices: high-yield arrangement of gold nanoparticles on DNA origami templates. *ACS Nano* **10**, 5374–5382 (2016).
34. Derr, N. D. et al. Tug-of-war in motor protein ensembles revealed with a programmable DNA origami scaffold. *Science* **338**, 662–665 (2012).
35. Chatterjee, G., Dalchau, N., Muscat, R. A., Phillips, A. & Seelig, G. A spatially localized architecture for fast and modular DNA computing. *Nat. Nanotechnol.* **12**, 920–927 (2017).
36. Ding, B. et al. Gold nanoparticle self-similar chain structure organized by DNA origami. *J. Am. Chem. Soc.* **132**, 3248–3249 (2010).
37. Endesfelder, U., Malkusch, S., Fricke, F. & Heilemann, M. A simple method to estimate the average localization precision of a single-molecule localization microscopy experiment. *Histochem. Cell Biol.* **141**, 629–638 (2014).

Acknowledgements

We thank Joerg Schnitzbauer, Thomas Schlichthaerle, Peng Yin, and William M. Shih for helpful discussions. We also thank Kimberly A. Cramer for proofreading the manuscript. This work was supported by the DFG through the Emmy Noether Program (DFG JU 2957/1-1), the SFB 1032 (Nanoagents for the spatiotemporal control of molecular and cellular reactions, project A11), the ERC through an ERC Starting Grant (MolMap, Grant agreement number 680241), the Max Planck Society, the Max Planck Foundation, and the Center for Nanoscience (CeNS) to R.J. M.T.S. acknowledges support from the International Max Planck Research School for Molecular and Cellular Life Sciences (IMPRS-LS).

Author contributions

M.T.S., F.S., and D.H. contributed equally. M.T.S. designed and performed experiments, created software, and wrote the manuscript. F.S. designed and performed experiments and wrote the manuscript. D.H. designed and performed experiments and created software. P.C.N. designed and performed experiments and wrote the manuscript. R.J. conceived of and supervised the study and wrote the manuscript.

Additional information

Supplementary Information accompanies this paper at https://doi.org/10.1038/s41467-018-04031-z.

Competing interests: The authors declare no competing interests.

Reprints and permission information is available online at http://npg.nature.com/reprintsandpermissions/

Publisher's note: Springer Nature remains neutral with regard to jurisdictional claims in published maps and institutional affiliations.

3

DNA-PAINT AND SUPER-RESOLUTION MICROSCOPY

The unique properties of DNA-PAINT make it a versatile toolbox with numerous applications for today's researchers. However, the true value of a technique comes from its adaptability. This can only be achieved when easy-to-follow protocols and tools for benchmarking and troubleshooting are provided. Additionally, impressive demonstrations of performance help spark interest and underline applicability. In our years of performing DNA-PAINT, we quickly realized the increasing interest of the scientific community to apply the method. As the training and providing support on a single user-level was very time consuming and best practice guidelines vastly improved since the initial publications, the demand for a unified reference increased.
In an attempt to meet these goals we prepared an in-depth protocol for all relevant steps to perform high-performance DNA-PAINT super-resolution microscopy. The protocol covers the creation of DNA origami test samples, in situ sample preparation, multiplexed data acquisition, data simulation, super-resolution image reconstruction and post-processing such as drift correction, molecule counting (qPAINT) and particle averaging. The protocol is meant to be completed within 1-2 days. An integral part of this protocol was the creation of an integrated software package, named Picasso. The software package allows all computational steps required for the protocol to be performed. The source code of the program was made publicly available as open source at GitHub so that the community can readily modify it for further optimization.
In order to simplify the process of getting to know the technique, I implemented a simulation module, which allows the *in silico* simulation of DNA-PAINT experiments. This enables the creation of raw data as it would originate from an experiment and thus allows the researcher to not only get acquainted with downstream processing, but also to quickly assess the feasibility of DNA-PAINT for a specific research question. The underlying fundamentals of the simulation module are presented in the next chapter. A more advanced method of benchmarking comes with the usage of DNA nanostructures that allow *in vitro* performance tests. To streamline the production of DNA origami nanostructures I employed a module that allows *designing* different patterns of DNA-PAINT docking sites on a flat, two-dimensional structure by just pointing and clicking at the respective positions on a canvas, allowing even novice users to create the desired DNA nanostructures. By first performing simulations, then working with artificial nanostructures and

ultimately performing *in situ* experiments, one can master the art of DNA-PAINT in a stepwise process.
To showcase resolution capabilities, we performed DNA origami measurements to resolve 5 nm distances. For this, we designed an 'MPI' and 'LMU'-pattern on the nanostructures and could achieve a nearest neighbor based analysis (NeNA) [46] localization precision of 1.4 nm (MPI) and 1.0 nm (LMU).

3.1 ASSOCIATED PUBLICATION P3

Super-resolution microscopy with DNA-PAINT

By

Jörg Schnitzbauer*, **Maximilian T. Strauss***, Thomas Schlichthärle, Florian Schüder, Ralf Jungmann
* *These authors contributed equally to this work*

published in

Nature Protocols (2017)

PROTOCOL

Super-resolution microscopy with DNA-PAINT

Joerg Schnitzbauer[1–3], Maximilian T Strauss[1–3], Thomas Schlichthaerle[1,2], Florian Schueder[1,2] & Ralf Jungmann[1,2]

[1]Department of Physics and Center for Nanoscience, Ludwig Maximilian University, Munich, Germany. [2]Max Planck Institute of Biochemistry, Martinsried, Germany. [3]These authors contributed equally to this work. Correspondence should be addressed to R.J. (jungmann@biochem.mpg.de).

Published online 18 May 2017; doi:10.1038/nprot.2017.024

Super-resolution techniques have begun to transform biological and biomedical research by allowing researchers to observe structures well below the classic diffraction limit of light. DNA points accumulation for imaging in nanoscale topography (DNA-PAINT) offers an easy-to-implement approach to localization-based super-resolution microscopy, owing to the use of DNA probes. In DNA-PAINT, transient binding of short dye-labeled ('imager') oligonucleotides to their complementary target ('docking') strands creates the necessary 'blinking' to enable stochastic super-resolution microscopy. Using the programmability and specificity of DNA molecules as imaging and labeling probes allows researchers to decouple blinking from dye photophysics, alleviating limitations of current super-resolution techniques, making them compatible with virtually any single-molecule-compatible dye. Recent developments in DNA-PAINT have enabled spectrally unlimited multiplexing, precise molecule counting and ultra-high, molecular-scale (sub-5-nm) spatial resolution, reaching ~1-nm localization precision. DNA-PAINT can be applied to a multitude of *in vitro* and cellular applications by linking docking strands to antibodies. Here, we present a protocol for the key aspects of the DNA-PAINT framework for both novice and expert users. This protocol describes the creation of DNA origami test samples, *in situ* sample preparation, multiplexed data acquisition, data simulation, super-resolution image reconstruction and post-processing such as drift correction, molecule counting (qPAINT) and particle averaging. Moreover, we provide an integrated software package, named Picasso, for the computational steps involved. The protocol is designed to be modular, so that individual components can be chosen and implemented per requirements of a specific application. The procedure can be completed in 1–2 d.

INTRODUCTION

For biomedical research, super-resolution microscopy is a promising tool developed in recent years, allowing optical imaging beyond the diffraction limit of light, for up to molecular-scale resolution inside cells. The significance of this group of imaging modalities is underlined by the Nobel Prize in Chemistry in 2014 'for the development of super-resolved fluorescence microscopy'. Super-resolution has been achieved by a variety of imaging modalities, most notably nonlinear structured illumination microscopy (SIM)[1], stimulated emission depletion (STED) microscopy[2], (fluorescent) photo-activated localization microscopy ((f)PALM)[3,4] and (direct) stochastic optical reconstruction microscopy ((d)STORM)[5,6]. All these techniques achieve image resolution beyond the diffraction limit by controlling the state of fluorophores such that only a small subset of them are detectable at any given time. However, super-resolution approaches can be generally divided into the following two groups according to the specific mechanism for controlling the fluorophore state[7]: (i) illumination-pattern-based (SIM and STED) and (ii) single-molecule-localization-based (PALM and STORM) methods. All these super-resolution methods have been successfully used to reveal biological insights[8–12], but each has its own advantages and difficulties. A practical advantage of both illumination-based methods is that they do not require specific fluorophores, which makes these techniques straightforward to use for biologists with conventional samples. However, instrumental implementations are typically more complex and intricate. By contrast, the branch of localization-based techniques uses stochastic blinking of specific fluorescent probes. This blinking permits them to be observed one at a time so that their spatial coordinates can be localized with subdiffraction precision[13]. Typically, this blinking is an intrinsic property of fluorescent proteins (PALM) or specific organic dyes (STORM), which can be provoked by specific excitation schemes and buffer conditions[14,15]. Although instrumentation is typically simpler for localization-based as compared with illumination-based modalities, the complexity lies in achieving suitable blinking behavior of the dyes. Troubleshooting often means testing a number of parameters such as the choice of dye, labeling density, buffer conditions and excitation illumination, making the blinking a hard-to-control phenomenon. In fact, the choice of 'well-behaving' probes is limited, and further development of substantially improved probes is complex and time-consuming. Moreover, because of the limited choice of probes with appropriate blinking kinetics, photon rates and excitation conditions, multiplexing is still difficult to implement. Furthermore, the complex photophysics of the probes impedes the predictability of blinking events so that quantitative image interpretation is error-prone. Last, owing to limited photon rates and bleaching, optimal localization precision and spatial sampling are still not achieved—the two major factors in resolution[16]. Although many biological questions could be addressed with the aforementioned techniques[8–12], researchers are still struggling with these complications to truly exploit the power of super-resolution microscopy.

A different route to single-molecule localization microscopy is PAINT[17]. Here, instead of labeling target molecules with fixed fluorophores, freely diffusing dyes[17] or dye-labeled ligands (as in uPAINT)[18] target molecules of interest by permanent or transient binding. PAINT is straightforward to implement and does not require special experimental conditions to obtain photoswitching, as long as probes are able to diffuse and reach their target molecules. However, PAINT's original implementation makes it difficult to specifically label a larger variety of biomolecules, as interactions are mainly limited to hydrophobic interactions or electrostatic coupling and are thus difficult to program.

DNA nanotechnology represents a promising tool for utilizing the advantages of the PAINT concept and establishing a programmable target–probe interaction system at the same time.

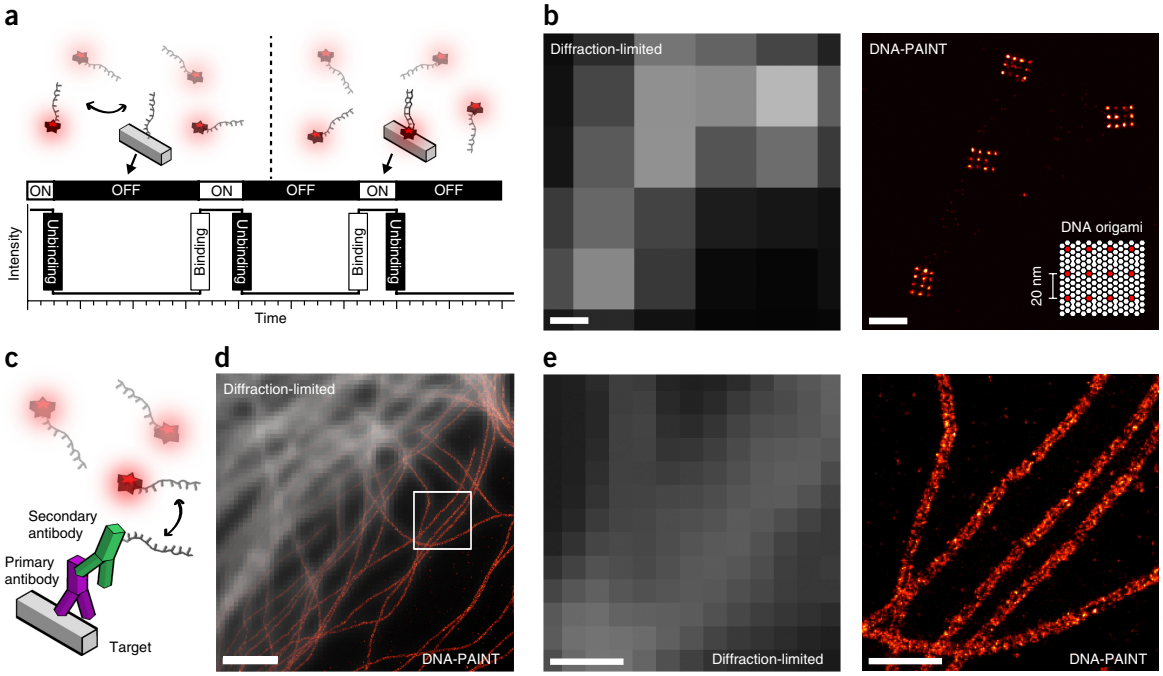

Figure 1 | DNA-PAINT. (**a**) DNA-PAINT concept. Transient binding of dye-labeled DNA strands (imagers) to their complementary target sequence (docking site) attached to a molecule of interest. The transient binding of imager strands is detected as 'blinking', illustrated by the intensity versus time trace. (**b**) Diffraction-limited (left) and super-resolved DNA-PAINT images (right) of DNA origami nanostructures. Each structure consists of 12 docking strands that are arranged in a 20-nm grid (scheme in lower right corner). (**c**) *In situ* protein-labeling strategy for DNA-PAINT using primary and DNA-conjugated secondary antibodies. (**d**) Overlay of a diffraction-limited α-tubulin image (top left) with a super-resolved DNA-PAINT image (bottom right). (**e**) Close-ups of the highlighted area in **d**, comparing diffraction-limited image (left) with DNA-PAINT super-resolved image (right). Scale bars, 100 nm (**b**), 2 μm (**d**), 500 nm (**e**).

Specifically, DNA-based PAINT (DNA-PAINT) has been developed as a straightforward approach to overcome some limitations of current localization-based super-resolution techniques[19–24]. Similar to the original PAINT concept, DNA-PAINT decouples blinking from dye photophysics, but it also adds the programmability and specificity of using DNA molecules as imaging and labeling probes. A DNA-PAINT system, illustrated in **Figure 1a**, consists of the following two components: a docking strand and an imager strand. These are short, complementary single-stranded DNA oligomers, usually 8–10 nucleotides long. Although the docking strand is fixed to a biological target of interest (e.g., using standard immunolabeling approaches with DNA-conjugated antibodies targeting proteins of interest[25] or direct hybridization of docking strands to DNA or RNA molecules), the imager strand is conjugated to an organic dye and diffuses freely in the imaging buffer. Generally, imager strands appear undetectable in the camera because they diffuse over numerous camera pixels during the duration of a single frame. However, owing to their complementary sequence, imager strands can transiently bind to docking strands. During the bound state, imager strands are fixed at the same place for an extended amount of time, allowing the camera to accumulate enough photons from the dye to be detected. The binding duration depends solely on the stability of the formed DNA duplex, and can hence be programmed at will (e.g., by modulating strand length, GC content, temperature or salinity of the imaging buffer). On the other hand, the frequency of binding events is tunable by the influx rate of imager strands (e.g., by modulating either the concentration of imager strands in the buffer or the association constant). As a result, the user has fine control over the blinking kinetics, which is independent of dye properties or illumination specifics. To date, DNA-PAINT has been used to resolve nanometer-scale structures of DNA origami (**Fig. 1b**), as well as those of cellular proteins, by conjugating docking strands to antibodies (**Fig. 1c–e**).

Advantages and limitations of the method

The properties of DNA-PAINT result in several improvements over more traditional super-resolution approaches. First, the use of DNA-based imaging probes enables high multiplexing by Exchange-PAINT[20] that is restricted only by the number of orthogonal DNA sequences, as compared with the spectrally distinct dyes used in classic multiplexing experiments. **Figure 2** illustrates the concept, procedure and results of Exchange-PAINT experiments *in vitro* and *in situ*. When tagging biological targets with orthogonal docking strand sequences, they can be probed sequentially by the respective complementary imager strands (**Fig. 2a**). Specifically, after one DNA-PAINT image has been acquired, the buffer can be exchanged to introduce a different imager strand species. Repeated imaging, washing and reintroduction of new imager strand species then allows researchers to create a multiplexed image of many biological targets. Although we have thus far demonstrated nine-target super-resolution imaging[25], multiplexing could reach thousands of species, as the only limitation is the orthogonality of DNA-PAINT sequences.

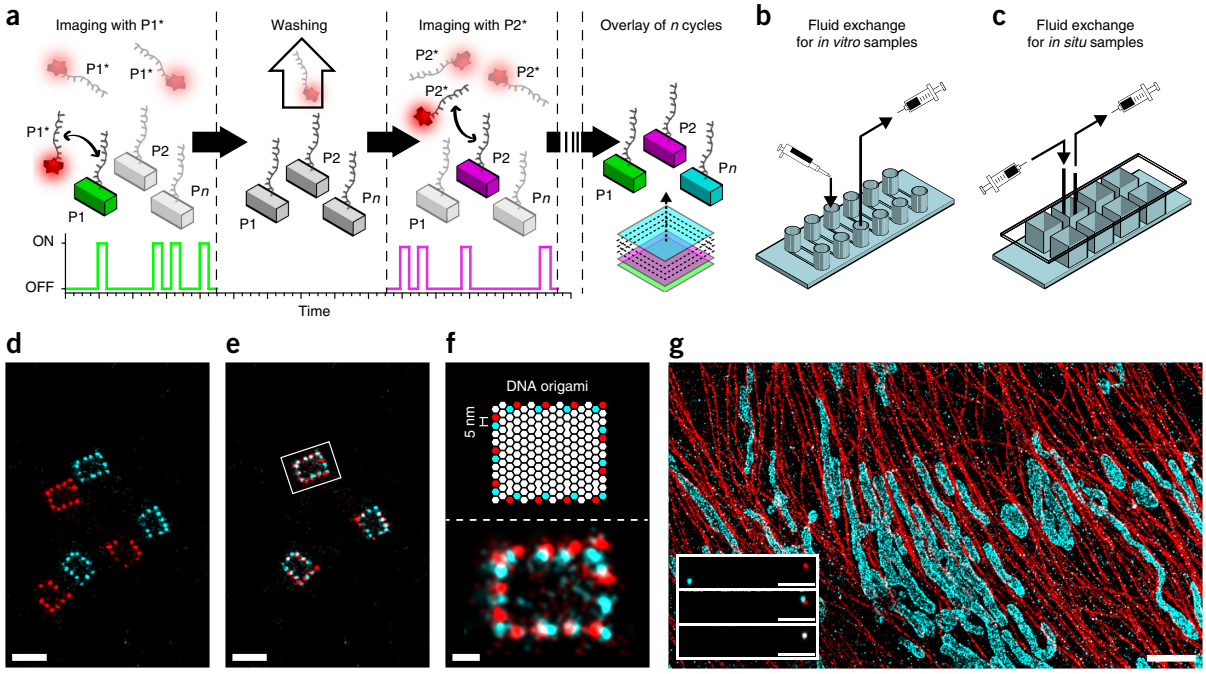

Figure 2 | Exchange-PAINT. (**a**) Schematic representation of sequential Exchange-PAINT imaging of multiple targets with orthogonal sequences using the same fluorophore. Left to right: P1* imager strands are in solution and interact with their complementary target sequence, P1. After the first acquisition round, the P1* imager strands are washed away and P2* imagers are introduced to image the next target. This is then repeated for the remaining target cycles, and pseudocolors are assigned for each respective imaging round. Last, all rounds are aligned and overlaid to form the final multiplexed Exchange-PAINT image of *n* targets. (**b**) Fluid exchange chamber for *in vitro* samples (e.g., for DNA origami imaging). Liquid is introduced by pipetting into the inlet. The outlet is attached to a syringe with a flexible tube to remove the liquid. (**c**) Fluid exchange chamber for *in situ* samples (i.e., used for *in situ* cellular imaging). Two tubes with syringes are connected to an 8-well chambered cover glass to facilitate fluid exchange. (**d**) Two rounds ('colors') Exchange-PAINT image of a frame-like DNA origami structure carrying two orthogonal docking strand species (red and cyan; see also **f**, for design schematics). (**e**) Pseudocolor image after alignment of the imaging rounds using Picasso's automated align function. (**f**) Top: DNA origami design. Bottom: Close-up (white box from **e**) of one frame-like structure. The distance between red and blue handles is ~5 nm. (**g**) *In situ* Exchange-PAINT image of protein targets α-tubulin (red) and Tom20 (cyan) with two primary and DNA-conjugated secondary antibody sandwiches. Inset: Images of one alignment marker (gold nanoparticle) in each Exchange-PAINT round without channel alignment (top), after Picasso's automated cross-correlation analysis (middle) and after manually selecting the particle as an alignment fiducial (bottom). Scale bars, 100 nm (**d**, **e**), 20 nm (**f**), 2 µm (**g**), 300 nm (**g**, insets).

Second, the predictability and tunability of DNA binding and unbinding events, combined with effectively nonexistent bleaching, allow for accurate quantitative image interpretation (i.e., counting of single molecules in an integer manner), implemented in quantitative PAINT (qPAINT)[22]. **Figure 3** depicts the qPAINT concept, procedure and results. A more detailed description of the method will be given below.

Third, DNA-PAINT simplifies the selection of suitable dyes for imaging, as the parameter space is reduced from rather complex photophysical properties (e.g., switching behavior) to basically a single parameter—the photon budget. This also means that DNA-PAINT can use a large pool of existing fluorophores that were previously not applicable to localization-based super-resolution microscopy.

Finally, by programming the binding duration, an extremely high number of photons can be detected from a single binding (or blink) event, enabling optimal localization precision. The only limitations regarding the achievable photon budget are experimental time and photobleaching during a single binding event. However, the latter can be greatly reduced by specific imaging buffer compositions, such as oxygen-scavenging systems and triplet-state quenchers[26–28]. Even if bleaching of individual dyes does occur, it has only a minimal detrimental effect overall, because of the practically infinite supply of replenishable 'fresh' imager strands from solution. All things considered, photobleaching—which is a considerable complication for all other super-resolution techniques—is eliminated as a restriction on achieving optimal sampling of the biological structure under investigation. Such optimized experimental conditions for high localization precision, combined with intricate drift correction methods, enable imaging at thus far unprecedented resolution in optical microscopy, for the first time enabling true molecular-scale resolution[23], which, to our knowledge, has not been achieved using any other super-resolution method. Example results of images with localization precisions of ~1 nm, yielding resolution better than 5 nm, and intermediate results of the applied drift correction are shown in **Figure 4**. To achieve these results, a large number of DNA origami structures were used as drift markers, considering first the whole structure, followed by the use of individual DNA-PAINT binding sites as fiducials. To eventually translate the *in vitro* ultra-resolution achievements to *in situ* samples such as fixed cells, a key challenge is the labeling

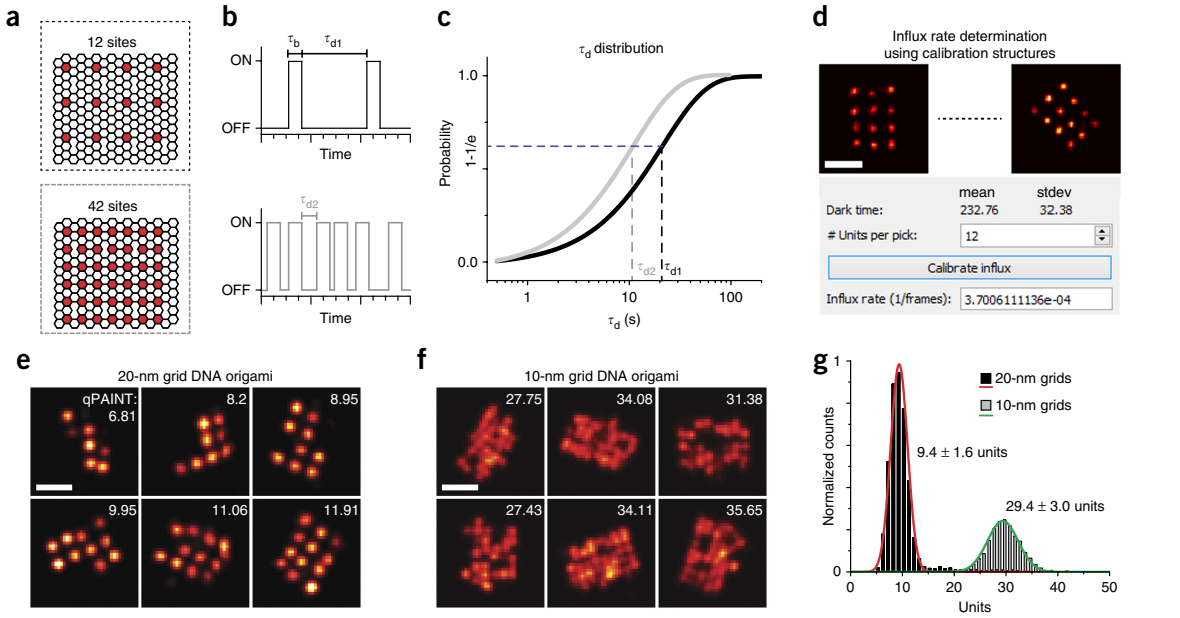

Figure 3 | qPAINT. (**a**) Design schematics for two DNA origami structures with 12 target sites spaced 20 nm apart (top, black-dotted box) and 42 binding sites spaced 10 nm apart (bottom, gray-dotted box), respectively. (**b**) DNA origami structures with 12 binding sites (top) exhibit fewer binding (blinking) events as compared with structures with 42 binding sites (bottom), resulting in longer dark times (τ_{d1}) and shorter dark times (τ_{d2}) for the 20-nm grids and 10-nm grids, respectively. (**c**) Mean dark times τ_{d1} and τ_{d2} are obtained by fitting the cumulative distribution function of the dark times. (**d**) To measure binding sites for a structure of interest, DNA origami nanostructures are used to calibrate the influx rate (here displayed as the number of blinks per frame). Visual inspection of the DNA origami defines the units (or binding sites) per pick (here only origami displaying 12 binding sites are picked for calibration, top) and can be used to calculate the influx rate (Picasso software dialog, bottom). (**e**) Visual inspection of 20-nm-grid DNA origami structures in comparison with qPAINT-predicted binding sites after calibration shows good agreement. (**f**) Visual comparison of 10-nm-grid DNA origami with predicted binding sites via qPAINT. (**g**) Histogram distribution of binding sites for 20-nm-grid structure (black and red, n = 4,210) in comparison with 10-nm-grid structure (gray and green, n = 1,818). Scale bars, 50 nm.

probe size. The size of the labeling probes introduces a linkage error and effectively limits the labeling density (because of sterical hindrance). Both these effects finally limit the achievable resolution. One way to address these issues in cells could be the use of smaller labeling agents such as nanobodies[29] or aptamers[30], rather than antibodies.

Although DNA-PAINT offers several advantages over traditional super-resolution techniques, as discussed above, we also note that there are currently limitations. One disadvantage is the fact that 'imager' strands are nonfluorogenic, with the following two implications: first, DNA-PAINT is limited to optical sectioning techniques such as total internal reflection (TIR), oblique[31] or light-sheet[32] illumination because of elevated background fluorescence originating from unbound imager strands. Second, the nonfluorogenic nature of imager strands furthermore sets an upper limit to the achievable image acquisition speed as compared with those of STED, PALM, STORM or SIM. Furthermore, DNA-PAINT applications are currently limited to fixed specimens. Live-cell imaging could be more difficult to achieve as compared with the aforementioned techniques, because of the complexity of infusing dye-labeled nucleic acid strands into living cells and the unforeseen consequences of introducing nucleic acids in general. However, we note that DNA-PAINT applications to molecules on cell surfaces such as membrane-bound receptors should be feasible even for living cells.

All in all, the DNA-PAINT imaging framework greatly reduces many technical difficulties of localization-based super-resolution microscopy and opens up possibilities for new technical development and biological applications. It will therefore allow many research groups to address their biological question with much greater efficiency. To ease the adoption of DNA-PAINT for novice and expert researchers in the super-resolution field, this protocol details the involved procedures and provides an integrated software package, named Picasso, which is specifically designed for DNA-PAINT applications. Except for data acquisition, Picasso can handle all computational efforts required in this protocol, including *in silico* data simulation, DNA origami design, and basic and advanced functionality for localization-based super-resolution microscopy.

Overview of the main procedures

The overarching goal of this protocol is to enable both novices and expert users to quickly obtain high-quality DNA-, Exchange-PAINT and qPAINT imaging data *in silico*, *in vitro* and *in situ*, without prior expertise in super-resolution microscopy. Here, we are using the term *in vitro* for DNA-PAINT studies with DNA origami structures on BSA/biotin/streptavidin-coated glass slides. By contrast, *in situ* is used to describe experiments involving fixed-cell samples. The protocol is based on several studies[19,20,22,23,25] and is arranged into four major sections, as illustrated in **Figure 5**: sample

preparation (*in vitro* and *in situ*), data acquisition, image reconstruction and image post-processing. For sa mple preparation, we describe the following two procedures: *in vitro* imaging (i.e., of DNA origami nanostructures) (Steps 1–18; **Box 1**) and *in situ* imaging (i.e., of cell samples) (Steps 19–33). Although not covered in this protocol, the procedures could be adjusted for DNA-PAINT imaging in tissue or whole organisms. Subsequently, we explain data acquisition (Steps 34–49), including a detailed procedure

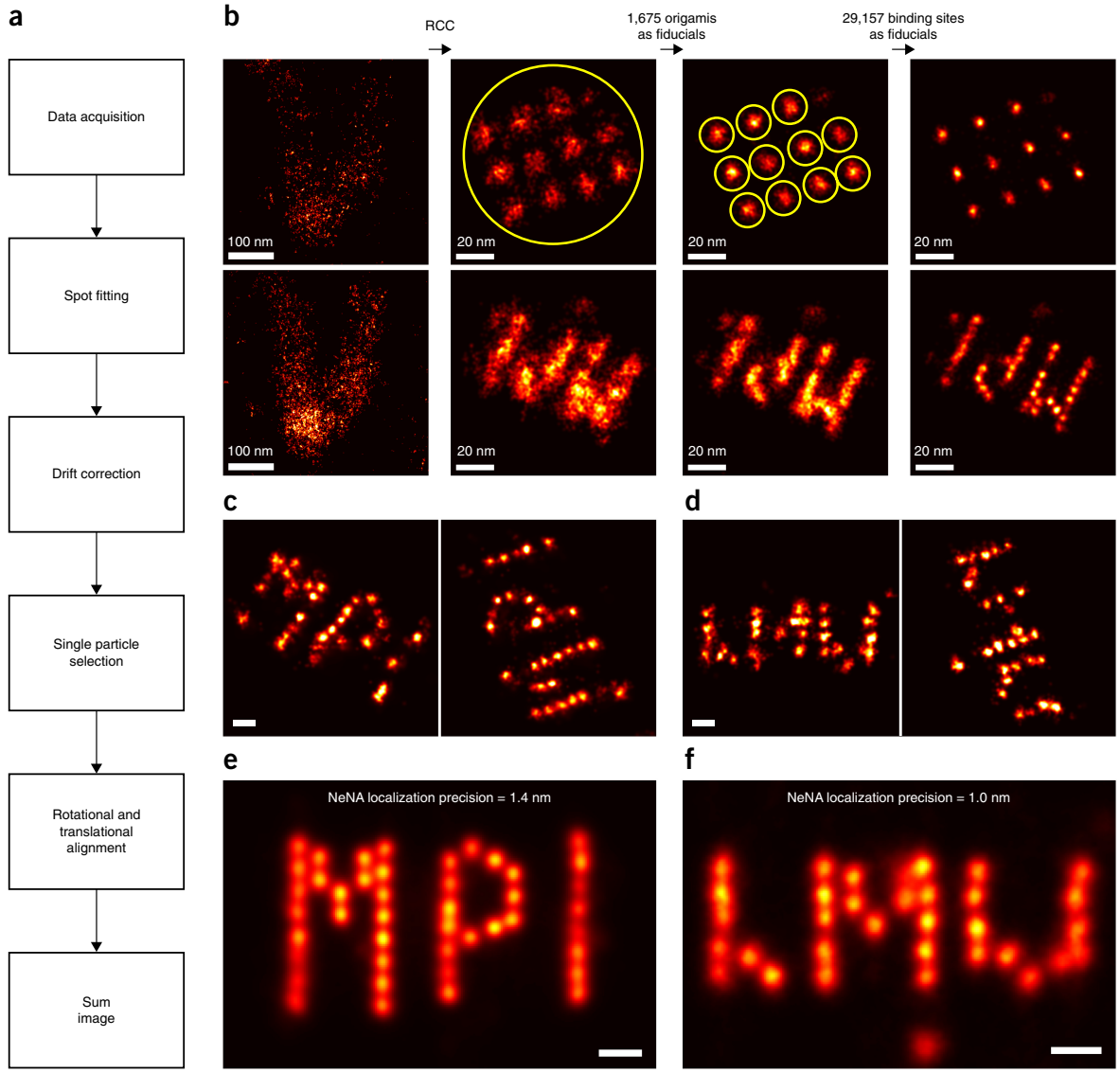

Figure 4 | 'Ultra-resolution' with DNA-PAINT. (**a**) Workflow for ultra-resolution imaging with advanced drift correction and particle averaging. (**b**) Multistage drift correction with Picasso. Top: 20-nm-grid DNA origami structures used as reference structures and drift markers. Bottom: DNA origami target structure (designed to display the letters 'MPI' (upside down) with 5-nm 'docking strand resolution') present in the same sample as the 20-nm origami. In the first drift correction stage, an RCC procedure is applied to the whole field of view (image column after RCC arrow shows results). The second step uses Picasso's semiautomated particle pick function (picked structure visualized by yellow circle) to select 1,675 DNA origami structures as fiducials for drift correction (drift for all structures is globally averaged and subtracted from the localization data). The result for this step is depicted in the third column. The third and last iteration uses the individual binding sites of the 20-nm grid for drift correction. Here, 29,157 binding sites were used as fiducial markers. The resulting image for the MPI target structures shows clearly resolved single binding sites spaced 5 nm apart. (**c**) Selection of two MPI origami after drift correction. Localization clusters of individual DNA-PAINT binding sites with a distance of ~5 nm are well resolved and circular, indicating that the residual drift is minimal and rotationally invariant. (**d**) Selection of two DNA origami, designed to show the letters 'LMU', from a different sample than in **b**,**c**,**e**, but after an analogous drift correction as shown in **b**. The images demonstrate minimal residual drift similar to that of the MPI structures shown in **c**. (**e**) Average image of 295 DNA origami with the letters 'MPI'. The mean number of localizations in individual images is 3,485 ± 1,197. All DNA-PAINT binding sites are visible, even though individual images miss binding sites because of incomplete strand incorporation, as seen in **c**. (**f**) Average image of 215 DNA origami with the letters 'LMU'. The mean number of localizations in the individual images is 2,323 ± 436. Scale bars, 10 nm (**c**–**f**).

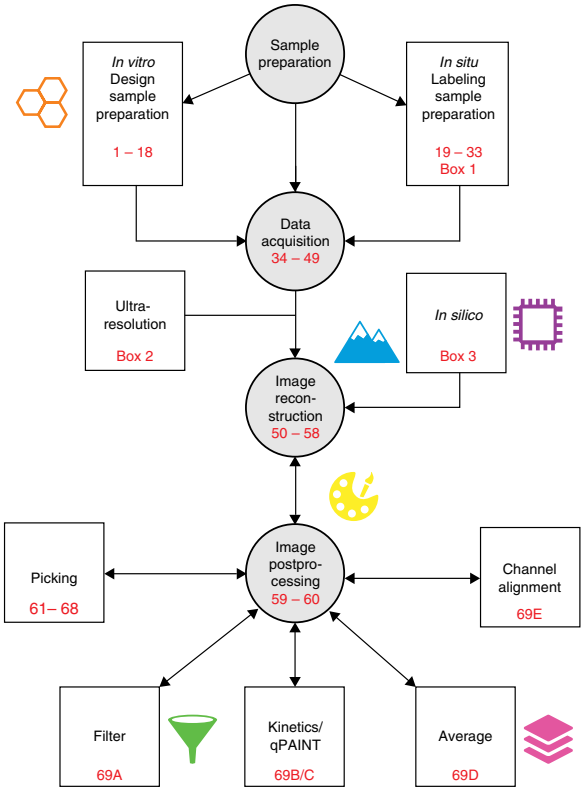

Figure 5 | DNA-PAINT protocol workflow. Starting with sample preparation, the user can perform either *in vitro* or *in situ* experiments. Next, data acquisition is performed (parameters for 'Ultra-resolution' are described in **Box 2**). The user may additionally generate DNA-PAINT data by *in silico* simulations. During image reconstruction, single-molecule fluorescence spots are localized, and resulting super-resolution images are visualized with 'Picasso: Render'. Image post-processing focuses first on drift-correction procedures. Then, special emphasis is given to analyzing the localization-based DNA-PAINT data through picking regions of interest, performing kinetic and qPAINT analysis, averaging images for ultra-resolution analysis and channel alignment for Exchange-PAINT or filtering of the localization list. Program icons indicate in which Picasso component the respective step is performed—hexagons: 'Design'; microchip: 'Simulate'; mountain peaks: 'Localize'; paint palette: 'Render'; funnel: 'Filter'; stacked layers: 'Average'. The Picasso program icons are based on contributions from the Noun Project (https://thenounproject.com)—'Design': hexagon by Creative Stall; 'Simulate': microchip by Futishia; 'Localize': mountains by Montana Rucobo; 'Filter': funnel by José Campos; 'Render': paint palette by Vectors Market; 'Average': layers by Creative Stall.

to achieve very high spatial resolution (<5 nm) with DNA-PAINT, which requires particular care in sample preparation and data acquisition (**Box 2**). Furthermore, we lay out the procedure to simulate typical DNA-PAINT data *in silico* for test and optimization purposes (**Box 3**). Then, image reconstruction is explained in two steps: fitting of single-molecule spots and subsequent rendering of the super-resolution image (Steps 50–58). Finally, we describe multiple procedures for post-processing such as drift correction (Steps 59 and 60), selection of regions of interest (Steps 61–68), filtering of localizations (Step 69A), quantitative imaging with qPAINT (Step 69B and C), particle averaging (Step 69D) and channel alignment for multiplexed images (Step 69E). Additional steps required for multiplexed imaging with Exchange-PAINT are described as optional steps in the respective sections.

One of the defining components of this protocol for DNA-PAINT is an integrated software package called Picasso, which enables researchers to quickly obtain meaningful reconstructed image results without the need of additional third-party software tools.

The Picasso software package

Like similar localization-based super-resolution methods, DNA-PAINT requires intricate data analysis. For that matter, we provide an integrated software package named 'Picasso' (free to download from http://www.jungmannlab.org). Although Picasso is suitable for any localization microscopy technique, it provides specific support for DNA-PAINT applications, e.g., qPAINT. All computational steps described in this protocol can be performed with Picasso. This includes designing of DNA origami structures and simulating typical DNA-PAINT data. After installation, Picasso is available as several stand-alone (but interlinked) modular components with graphical user interfaces. The components are named 'Design', 'Simulate', 'Localize', 'Filter', 'Render' and 'Average'. The 'Design' component allows the user to visually design rectangular 2D DNA origami structures, which we call Rothemund's rectangular origami (RRO)[33], with DNA-PAINT handles. For that matter, 'Design' autogenerates order lists and pipetting instructions. With 'Simulate', the user may generate typical DNA-PAINT raw data from *in silico* simulations. After data have been acquired or simulated, the 'Localize' component allows the user to identify and fit the coordinates of single-molecule spots. 'Picasso: Filter' offers a convenient tool to inspect the localization list, plot histograms of localization properties and filter localizations with undesired properties. Super-resolution images can be rendered and inspected with the Picasso component 'Render'. 'Picasso: Render' also offers various post-processing functions such as advanced drift correction and quantitative image evaluation by qPAINT. Last, the 'Average' module provides the functionality to perform particle averaging (i.e., rotational and translational alignment) of multiple images of the same structure. Analogous to single-particle reconstruction in the electron microscopy field, this procedure helps to improve the signal-to-noise ratio of images. Overviews of the graphical user interfaces for the 'Design', 'Simulate', 'Localize', 'Render' and 'Filter' components are shown in **Supplementary Figures 1–5**.

Although in principle a cross-platform development, we currently supply a one-click installer of Picasso for Microsoft Windows 64-bit operating systems. This single executable setup file can be downloaded from our website at http://www.jungmannlab.org. Picasso is developed in Python, and the source code is available at https://github.com/jungmannlab/picasso.

Design and preparation of DNA origami structures

As DNA-PAINT makes use of the programmability of (transient) DNA strand hybridization to enable super-resolution imaging, DNA-based objects are convenient *in vitro* test targets for imaging. Nucleic acids can serve as powerful building blocks for nanometer-scale structures based on sequence-guided self-assembly, which is the foundation of structural DNA nanotechnology[34,35]. DNA origami are complex, self-assembled, 2D or 3D structures created by annealing DNA strands of specifically designed sequences[33]. In DNA origami, a long single-stranded DNA

PROTOCOL

Box 1 | Construction of a fluid exchange chamber for *in situ* imaging

● TIMING 30 min

Procedure

For *in situ* Exchange-PAINT experiments, we recommend a simple, custom-built fluid exchange system. The lid of an 8-well chambered cover glass can be modified with one inlet and one outlet, which can be connected to imaging and washing buffer reservoirs by silicone tubing. The modified lid can be used for multiple imaging experiments, although the connected tubing should be thoroughly cleaned before reuse. Using a syringe, flush at least 3 ml (as reference for 1-m tubing with a 1.5-mm diameter; adjust accordingly) of H_2O, followed by 3 ml of 80% EtOH and finally 3 ml of H_2O, through the tubing. Follow these instructions to prepare such a lid:

1. Drill two holes with a diameter of 1.5 mm into the lid of an 8-well chambered cover glass, so that two needles can penetrate it.
2. Use a rotary tool with cutting disc or equivalent to remove the syringe connectors from two 1.2 × 40-mm needles. Alternatively, use a side cutter (although this could potentially lead to a 'less clean cut') and squeeze the channel shut. To reopen, carefully apply pressure with the side cutter at the side of the cut. Make sure that the needle is at least 2.5 cm long to be able to reach the bottom of the chambered cover glass.

! CAUTION Handle the needles with care and do not puncture yourself.

3. Cut away the sharp end of one of the needles, so the channel can reach the bottom of the wells. Carefully apply pressure to open the metallic channel of the needle at the cut side with the side cutter.

! CAUTION Handle the needles with care and do not puncture yourself.

4. Connect the cut needles to ~50 cm of tubing. Make sure that the tubing is long enough that there is enough space to handle the liquids and syringes at the microscope. To connect the tubing to the syringes, use 1.1 × 40-mm needles on the other end of the tubing.

▲ CRITICAL STEP The length of the tubing depends heavily on the accessibility of the microscope; adjust the tubing length for proper handling.

5. For imaging, fix the tubing to the microscope body via tape.

▲ CRITICAL STEP Leakage could lead to damage of the microscope. Check all tubing and connections before use.

molecule (called the 'scaffold', derived from M13mp18 single-stranded phage DNA) is folded into a desired shape by ~200 short, single-stranded DNA strands (called 'staples'). Each staple has a defined sequence and specifically binds certain parts of the scaffold together. Structures are usually assembled in a one-pot reaction using thermal annealing. After the self-assembly is completed, the scaffold is 'folded' into the desired shape with the staple strands at prescribed positions in the final origami.

The rather complex and time-consuming procedure of manually designing DNA origami structures has been markedly simplified by computer-aided design tools, such as the freely available caDNAno[36] and vHelix[37] packages, as well as by simulation programs such as CanDo[38]. Furthermore, folding protocols for structure formation are now optimized for structure yield and folding speed[39–41]. In addition, several methods for subsequent purification of DNA nanostructures from unwanted excess of staple strands are described in the literature, such as agarose gel purification[42], rate-zonal centrifugation[43] or PEG purification[44].

One of the early applications of DNA origami was its use as a microscopy standard in the form of a self-assembled nanoruler[45]. Owing to the unique positioning accuracy of DNA origami and its excellent structural integrity, the structures present an ideal platform to directly validate imaging methods and compare instrumentation. Specifically, they are a valuable tool in calibrating fluorescence and super-resolution microscopes[46].

Although it is possible to create a wide range of structures with the DNA origami technique, some are more suitable for use as a reference structure with DNA-PAINT than others. In this protocol, we use a flat, rectangular 2D DNA origami structure, adapted from the one originally described[33], here referred to as RRO. With dimensions of 90 × 70 nm and, in our case, 176 freely addressable staples arranged in a hexagonal lattice with 5-nm spacing, it is an ideal structure for DNA-PAINT imaging (see **Fig. 1b** as an example). For surface immobilization, the structure is modified with eight biotinylated staple strands that can bind to a BSA–biotin–streptavidin-coated glass surface.

'Picasso: Design' is an essential tool in this protocol that reduces all design steps to a minimum. **Figure 6** shows screenshots and outlines the procedure for creating DNA origami, from design to purification. For a detailed overview of the graphical user interface, refer to **Supplementary Figure 1**. The program displays a hexagonal lattice that serves as a canvas representing all possible staple positions available for modification in the RRO structure. It features a 'point-and-click' approach, so that the desired pattern can be made by simply 'painting' on the canvas. Clicking a hexagon will fill it with a previously selected color; each color corresponds to a built-in staple extension on the 3′-end. As all modifications are just staple extensions of the RRO structure, the core sequences are not altered, and time-consuming tasks such as altering the routing of staples or modifying their base sequence are not necessary. In addition, 'Picasso: Design' automatically calculates folding recipes for a given design based on optimized excess rates for the RRO and creates visual pipetting aids for 96-well plates so that pipetting of staple mixes is greatly facilitated. In consequence, the creation of DNA origami reference structures for DNA-PAINT can be achieved in the most straightforward way.

In situ sample preparation

A unique advantage of fluorescence microscopy, making it one of the preferred characterization tools in biological research, is its ability to interrogate biomolecules of interest, such as proteins or nucleic acids, with high efficiency and specificity. Generally, fluorescent labeling of target molecules is achieved either by

Box 2 | Ultra-resolution imaging ● TIMING ~7 h

Procedure

To achieve ultra-resolution (<5 nm), imaging conditions must be carefully adjusted. The key to higher spatial resolution is to extract more photons per frame from a blinking event while simultaneously keeping the background low. This can be achieved by optimizing the laser excitation power, as well as the fluorescence ON time (and adjusting the integration time accordingly). The background can be reduced, for example, by decreasing the imager concentration. In this case, the acquisition time should be increased to ensure proper sampling of the target structure. However, with an imager concentration that is too low, drift correction might become less accurate owing to the smaller number of localizations per frame. We also want to note that the number of drift markers in a field of view should be as high as possible, to ensure precise drift correction. One way to achieve this is to make use of the larger field of view obtainable with today's sCMOS cameras. For advanced drift correction, a 20-nm and a 10-nm grid DNA origami should be used as fiducials. Furthermore, oxygen-scavenging systems, such as the PCA/PCD/Trolox (PPT) system, allow the harvesting of more photons as they increase fluorophore stability[27]. The following steps describe in detail how to achieve ultra-resolution for imaging DNA origami structures.

1. Design and fold DNA origami structures for ultra-resolution imaging—e.g., the LMU or MPI logo. In addition, fold 20-nm and 10-nm grid DNA origami for use as drift markers (see Steps 1–17).
2. Prepare the oxygen-scavenging system PPT at least 1 h before imaging.
3. Prepare a sample with the target structure and DNA origami drift markers (see Step 18) using the following parameters:
● Origami solution ratio: 1/4 target structure (i.e. LMU or MPI logo), 1/4 20-nm drift marker, 1/4 10-nm drift marker and 1/4 Buffer B+
● Imager concentration (with PPT): 0.5 nM–1 nM.
4. Follow steps 34–48 with the following adjustments: 350 ms exposure time, 80,000 total number of frames. Set the excitation power density to ~4.5 kW/cm^2 at the sample plane.

genetically fusing a protein tag to the target[47] or by attaching an external binder molecule during a staining procedure—e.g., dye-labeled antibodies[48]. For DNA-PAINT, the labeling requirement is that a DNA docking strand is attached to the target. Although a variety of strategies could be feasible for that[29,30,49–52], this protocol focuses on immunostaining with DNA-conjugated antibodies[25]. Specifically, we describe how antibodies can be chemically modified and used for *in situ* DNA-PAINT imaging of fixed cells (Steps 19–33).

The concept of *in situ* DNA-PAINT with primary and secondary antibody labeling is shown in **Figure 1c**: imager strands from solution transiently bind to handle sites on the secondary antibody. Imaging results for *in situ* samples prepared with antibody labeling are shown in **Figure 1d,e**, displaying a gradient overlay of diffraction-limited microtubules in comparison with the reconstructed super-resolved image. Furthermore, **Figure 2g** shows DNA DBCO-labeled antibody staining of Tom20, located mainly at the outer mitochondrial membrane, and DNA thiol-labeled antibody staining of microtubules.

Various avenues are possible for attaching DNA strands to antibodies, including biotin–streptavidin linkage[20] or covalent attachment of the DNA to the antibody[22,53,54]. Although biotin–streptavidin linkage was used in the initial *in situ* DNA-PAINT demonstration[20], we here discuss a covalent attachment strategy, which was used in subsequent work[22] similar to previously reported strategies for DNA–protein conjugation[53,54]. Here, an NHS ester linker is covalently attached to amino groups on the antibody and to certain functional groups on the DNA, such as reduced thiols[22], azides[53,55], alkynes[53] or DBCO[55], for click chemistry. This results in cross-talk-free attachment, as well as smaller linker sizes between antibody and DNA strand, as compared with the biotin–streptavidin linkage[20].

Depending on the target molecules under investigation, it is furthermore important to evaluate different fixation strategies. For example, structural proteins, such as actin filaments or microtubules, can be fixed with pre-extraction and glutaraldehyde to decrease background and preserve structural integrity[56]. However, structural artifacts can arise from the various fixation strategies. For an in-depth discussion of fixation artifacts, we refer to a recent article by Whelan *et al.*[57]. DNA-PAINT was also applied to tissue samples, as was recently shown in *Drosophila* embryos[22], generally following the same procedures as described here. However, we do note that potential changes to the herein described protocol for more complex tissue samples might become necessary.

Data acquisition

A multitude of acquisition software packages are available for performing localization-based super-resolution microscopy, in particular for commercial microscope setups. In this protocol, we describe our procedures based on the freely available open-source acquisition software μManager[58]. μManager is used in a wide range of microscopy areas and offers broad device support for microscope bodies, cameras and peripherals. The Picasso software suite is specifically designed to be compatible with μManager.

Currently, two types of cameras are typically used in the field of single-molecule localization-based imaging—scientific complementary metal oxide semiconductor (sCMOS)- and electron-multiplying charge coupled device (EMCCD)-based cameras. sCMOS cameras provide better temporal resolution because of their faster readout electronics, resulting in a larger optical field of view as compared with EMCCDs under similar conditions. EMCCD cameras, in comparison, provide better quantum yields in low-light applications and thus higher signal-to-noise ratios[59]. As DNA-PAINT provides comparably higher signal-to-noise ratios (SNRs), both camera types are suitable in this context.

It has been shown that a pixel-dependent noise calibration for sCMOS cameras can improve localization precision in STORM[60]. However, for DNA-PAINT experiments—including the

PROTOCOL

Box 3 | *In silico* simulation of DNA-PAINT data ● TIMING 10–60 min

Picasso's simulation module ('Picasso: Simulate') is a tool for evaluating experimental conditions for DNA-PAINT and generating ground-truth data for test purposes. This allows systematic analysis of how different experimental parameters such as imager concentration, target density or integration time influence the imaging quality and whether the target structure can be resolved with DNA-PAINT. By default, 'Picasso: Simulate' starts with preset parameters that are typical for a DNA-PAINT experiment. Thus, meaningful raw DNA-PAINT data can be readily simulated for a given input structure without the need of a super-resolution microscope. The simulation output is a movie file in .raw format, as it would be generated during an *in vitro* DNA-PAINT experiment on a microscope.

Procedure

1. Start 'Picasso: Simulate'.
2. Define the number and type of structures that should be simulated in the group 'Structure'. Predefined grid- and circle-like structures can be readily defined by their number of columns and rows, or their diameter and the number of handles, respectively. Alternatively, a custom structure can be defined in an arbitrary coordinate system. To do so, enter comma-separated coordinates into 'Structure X' and 'Structure Y'. The unit of length of the respective axes can be changed by setting the spacing in 'Spacing X,Y'. For each coordinate point, an identifier for the docking site sequence needs to be set in 'Exchange labels' as a comma-separated list. Correctly defined points will be updated live in the 'Structure [nm]' window. Note that entries with missing *x* coordinate, *y* coordinate or exchange label will be disregarded. When a structure has been previously designed with 'Picasso: Design', it can be imported with 'Import structure from design'. A probability for the presence of a handle can be set with 'Incorporation'. By default, all structures are arranged on a grid with boundaries defined by 'Image size' in 'Camera parameters' and the 'Frame' parameter in the 'Structure' group. 'Random arrangement' distributes the structures randomly within that area, whereas 'Random orientation' rotates the structures randomly. Selecting the button 'Generate positions' will generate a list of positions with the current settings and update the preview panels. A preview of the arrangement of all structures is shown in 'Positions [Px]', whereas an individual structure is shown in 'Structure [nm]'.
3. The group 'PAINT Parameters' allows adjustment of the duty cycle of the DNA-PAINT imaging system. The mean dark time is calculated by $\tau_d = (k_{on} \cdot c)^{-1}$. The mean ON time in a DNA-PAINT system is dependent on the DNA duplex properties. For typical 9-bp imager/docking interactions, the ON time is ~500 ms. ON times can be experimentally estimated with Picasso as described in Step 69B.
4. In 'Imager Parameters', fluorophore characteristics such as PSF width and photon budget can be set. Adjusting the 'Power density' field affects the simulation analogously to changing the laser power in an experiment.
5. The 'Camera parameters' group allows the user to set the number of acquisition frames and integration time. The default image size is set to 32 pixels. As the computation time increases considerably with image size, it is recommended to simulate only a subset of the actual camera field of view.
6. Select 'Simulate data' to start the simulation. The simulation will begin by calculating the photons for each handle site of every structure and then converting it to a movie that will be saved as a .raw file, ready for subsequent localization. All simulation settings are saved and can be loaded at a later time with 'Load from previous simulation'.

? TROUBLESHOOTING

7. (Optional step for multiplexing) Multiplexed Exchange-PAINT data can be simulated by adjusting the 'Exchange Labels' setting. For each handle in the custom coordinate system ('Structure X', 'Structure Y'), an Exchange round can be specified. The different imaging rounds can be visually identified by color in the 'Structure [nm]' figure. For each round, a new movie file will be generated. By default, the simulation software detects the number of exchange rounds based on the structure definition and will simulate all multiplexing rounds with the same imaging parameters. It is possible to have different imaging parameters for each round, e.g., when using image s with different ON-times. To do so, one can simulate multiplexing rounds individually. In the 'Exchange rounds to be simulated' field, enter only the rounds that should be simulated with the current set of parameters. Change the set parameters and the multiplexing round and simulate the next data sets. Repeat until all multiplexing rounds are simulated.

ultra-resolution measurements in this protocol—we did not account for the pixel-dependent noise of our sCMOS camera. Although such calibration might also improve DNA-PAINT image quality, it was not required to achieve the ~1-nm localization precision that allowed us to resolve 5-nm spaced binding sites on DNA origami structures (**Fig. 4**).

In this protocol, we generally suggest rather long camera integration times (a few hundred milliseconds) as compared with other localization-based microscopy methods such as PALM or STORM. Typically, for localization-based super-resolution techniques, the integration time is roughly matched to the ON-time of blink events to maximize the signal-to-noise ratio of the fluorescence image. Analogously, the integration times suggested here are roughly matched to the binding kinetics of the recommended nine-base-pair DNA duplex. This allows the collection of far more photons in a single frame as compared with typical PALM or STORM experiments, thus enabling better localization precision. However, it is worth noting that the combination of slower blinking and longer integration time comes at the expense of extended total data acquisition time to detect the same number of events. Nonetheless, it is certainly possible to shorten the binding duration, integration time and thus the total acquisition time by using DNA duplexes with fewer base pairs. For example, the recommended integration time for 8-mers is only tens of milliseconds and that for 7-mers is even less. With such faster kinetics, the integration time and achievable localization precision would then be similar to those in PALM or STORM experiments. An advantage of DNA-PAINT is therefore that it gives the researcher intricate control over the desired localization precision as a trade-off for total acquisition time.

© 2017 Macmillan Publishers Limited, part of Springer Nature. All rights reserved.

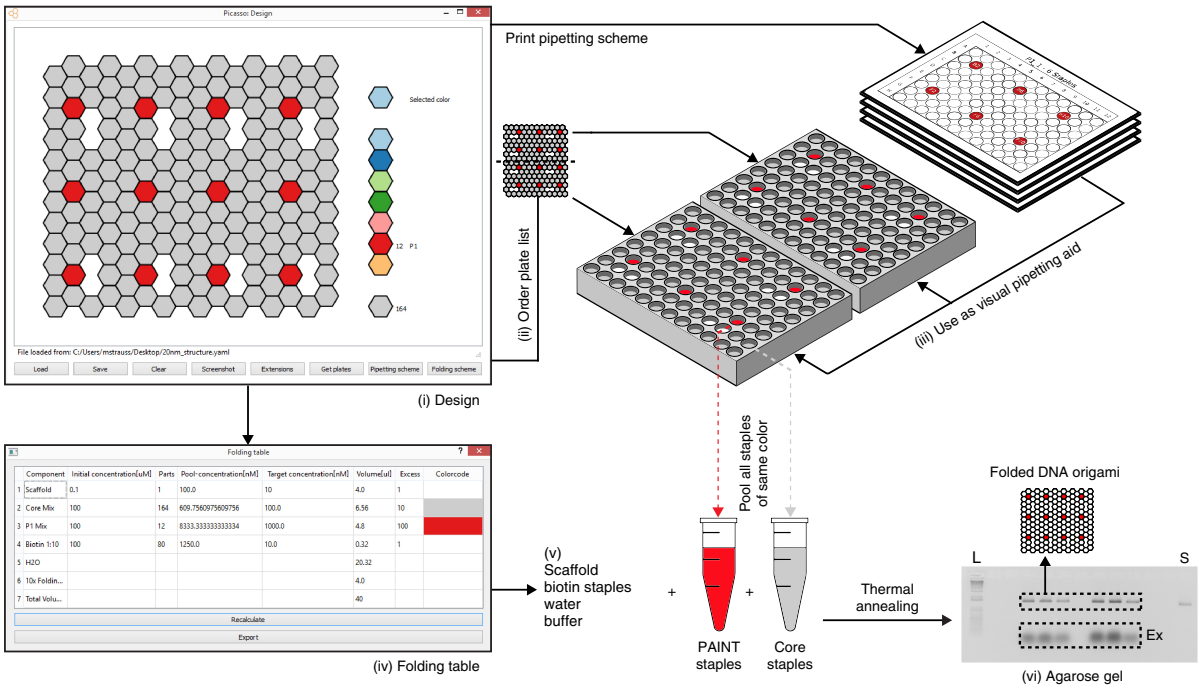

Figure 6 | Designing DNA origami structures for DNA-PAINT with 'Picasso: Design'. (i) Screenshot of the design interface displaying a 20-nm grid structure with 12 docking sites (red) selected to carry the extension P1. After design is completed, a list of plates is generated as a .csv file ready for ordering (ii). 'Picasso: Design' also creates PDF sheets that can be placed underneath the ordered 96-well plates to facilitate pipetting of staple strands (iii). The folding table (iv) gives detailed instructions for preparing components to assemble the DNA nanostructure through thermal annealing. Staple master mixes are pipetted from the plates according to the pipetting scheme. For a successful assembly process, single-stranded DNA scaffold, biotinylated staples, staple master mixes (unmodified core (gray) and docking-strand-extended (red) staples), water and folding buffer need to be mixed (v). After structures are formed (usually through thermal annealing), an agarose gel can be run for analysis or subsequent structure purification (vi). Here, a DNA ladder (L) and the scaffold strand (S) are seen as clear bands together with bands for the correctly folded DNA structures and excess staple strands (Ex). Extracted origami structures are now ready for DNA-PAINT imaging.

The number of localizations and thus the total experiment time strongly influence the resolution of a localization-based super-resolution image. Ideally, to resolve a target structure, it should be spatially probed at least at its Nyquist frequency[61]. More precisely, it has been shown that the overall image resolution for localization-based super-resolution microscopy is governed by two main factors: sampling density and localization precision[16]. In the same work, it was demonstrated that longer acquisition times increase spatial resolution of the reconstructed image because of increased spatial sampling up to the point at which image resolution is solely limited by localization precision. As the molecule density of a target structure might be unknown, it is often necessary to evaluate a range of acquisition times to determine how many frames are sufficient to represent the structure with the desired resolution. *In silico* simulations of localization-based super-resolution imaging can be a practical method of assaying a large number of data acquisition parameters such as the total acquisition time[62], reducing the need for time-consuming experiments. The Picasso software package comes with a module for simulating DNA-PAINT data, thus providing the tools for this approach. A more detailed discussion of the 'Picasso: Simulate' module follows below. Finally, we want to provide an exemplary thought-experiment as a guide to estimating appropriate acquisition lengths t. Consider an imager concentration c of 10 nM and a probe association rate k_{on} of 10^6 $(Ms)^{-1}$. This leads to a mean time in between binding events (or dark time τ_d) for a single site of 100 s according to $\tau_d = (k_{on} \times c)^{-1}$. For an ~98% probability (P) of any single binding site being visited at least once, a total imaging time of $t = 4 \times \tau_d = 400$ s is required, according to $P = 1 - e^{-t/\tau_d}$. To achieve multiple binding events per site resulting in a decent image quality, we recommend a total imaging time of ~33 min.

In silico simulation of DNA-PAINT data

A fundamental challenge in single-molecule localization microscopy is to systematically design, optimize and validate super-resolution experiments. *In silico* simulations provide a convenient way to address this challenge. Software packages such as SuReSim generate a ground truth model and simulate localization microscopy data using parameters matching an experimental microscope setup[62]. Similar to this approach, the Picasso software suite can simulate localization data with its 'Simulate' component, which is specifically tailored to DNA-PAINT. In a graphical user interface, shown in **Figure 7** and **Supplementary Figure 2**, simulation parameters can be set for the type of target structure, DNA-PAINT kinetics, dye properties and hypothetical data acquisition settings such as integration time and total number of acquisition frames.

PROTOCOL

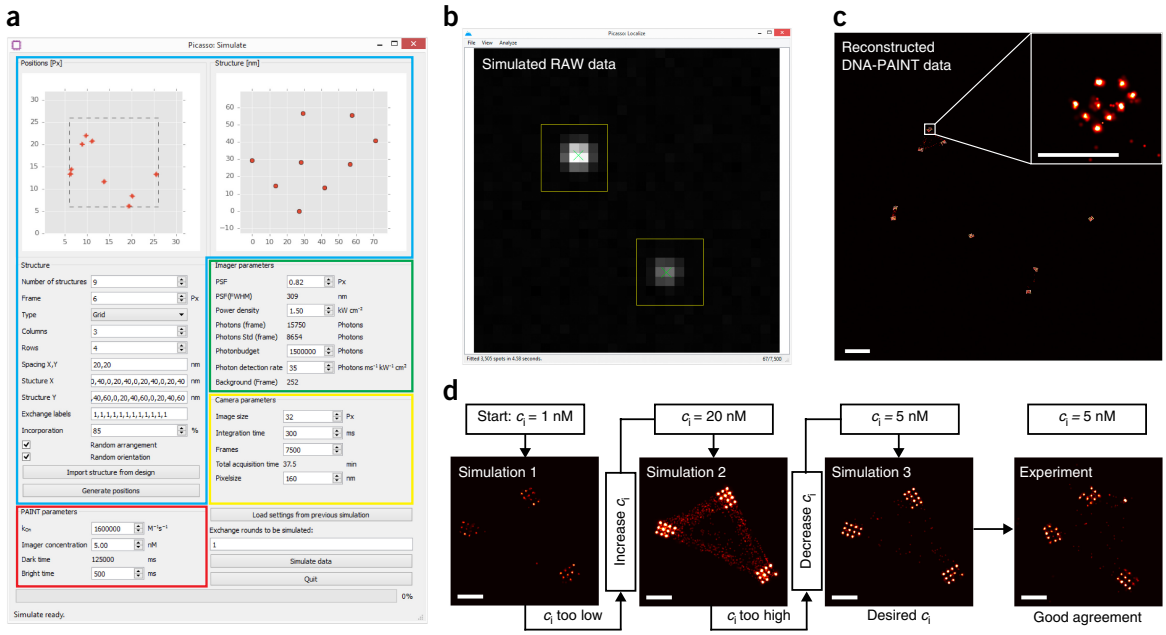

Figure 7 | Simulating DNA-PAINT raw data from DNA origami-like structures. (**a**) Overview of the graphical user interface for 'Picasso: Simulate'. A DNA-PAINT simulation can be defined by parameters in four categories, indicated by colored frames: 'Structure' (blue), PAINT parameters (red), 'Imager parameters' (green) and 'Camera parameters' (yellow). Two overview plots are shown in the upper row. 'Positions [Px]' shows the arrangement of individual structures within the field of view and 'Structure [nm]' shows the positions of DNA-PAINT binding sites in an individual structure. The positions of binding sites in individual structures can be defined in the 'Structure' section by (i) importing RRO structures designed with 'Picasso: Design', (ii) using predefined geometric shapes (circles, grids), or (iii) manually entering coordinates. In the 'PAINT parameters' section, kinetic parameters for DNA-duplex formation can be set. Imager-related properties (PSF width, laser power, photon budget, photon detection rate and background) are defined in the 'Imager parameters' section. Last, acquisition settings, such as image size, integration time, number of frames and pixel size can be set in the 'Camera parameters' section. (**b**) Example of simulated raw DNA-PAINT data in 'Picasso: Localize' after spot identification and fitting. The simulation program simulates blinking events as if they were acquired with a microscope. (**c**) Reconstructed DNA-PAINT image from data generated with 'Picasso: Simulate'. The overview of all structures corresponds to the 'Positions [Px]' window shown in **a**. A close-up shows the structure that is presented in the 'Structure [nm]' window in **a**. (**d**) Example of an iterative process for optimizing DNA-PAINT experiments with simulations. A DNA origami structure is simulated with an imager concentration of 1 nM (Simulation 1). The simulation shows that the concentration is too low, because features of the structure are not clearly visible. Consequently, in a next iteration, data are simulated with a higher concentration, here 20 nM (Simulation 2). Now the simulation reveals that the imager concentration chosen is too high, resulting in 'cross-talk' localizations between the structures. Such cross-talk arises when two imagers bind simultaneously to nearby structure sites. Their diffraction-limited images spatially overlap and are falsely identified as a single event with a fitted center coordinate in between the two true positions. For the next iteration, the imager concentration is decreased to 5 nM. The resulting simulation shows structures with clear features and no inter-structure cross-talk. Hence, the 5 nM imager concentration was chosen to perform a DNA-PAINT experiment (Experiment), which in turn is in good agreement with the simulation. Scale bars, 500 nm (**c**), 100 nm (**c** inset, **d**).

The simulated imaging targets are nanometer-sized 2D structures (similar to RROs) on which the positions of DNA-PAINT handles can be defined. These handles serve as a ground truth model for localization events. On the basis of the values set for DNA-PAINT kinetics, the simulation algorithm will calculate a kinetic series of ON- and OFF-events over the total acquisition time for each handle.

The duration of an ON-event is calculated by random selection from an exponential distribution defined by a mean ON-time. This time can be either determined experimentally (i.e., using Picasso's kinetic analysis tool; see Step 69B) or estimated by the number of base pairs in the imager/docking strand duplex[19]. The length of an OFF-event is generated accordingly. Here, the mean OFF-time is calculated from the user-defined binding rate constant and the imager concentration[19].

The user-defined integration time of the simulated camera is used as a sampling window to calculate how long an imager was bound during each frame. To emulate experimental results, the simulation randomly selects a photon detection rate for each binding event from a normal distribution. The mean and standard deviation of this normal distribution increase linearly with the user-definable laser power density according to experimentally determined coefficients. For each frame (or fraction of a frame) in which the binding event occurs, the detected number of photons is then selected randomly from a Poisson distribution. The mean of this Poisson distribution is equal to the mean expected photon number for the binding event duration within this frame (photon detection rate × duration). In addition, the simulation considers an upper-limit for detected photons from a single binding event, based on a user-defined photon budget per fluorophore.

After the number of photons for all binding events in each frame is calculated, photons are distributed around the center position of their handle by a user-adjustable 2D normal distribution, representing the microscope's point spread function (PSF).

This results in a list of all photon positions for each frame, which is converted to an image by calculating a 2D histogram. Poissonian noise is added to each frame specified by the background level. Finally, the frames are exported as a raw movie file. The default values for all parameters were estimated from calibration experiments on our TIR fluorescence (TIRF) setup described in the EQUIPMENT section. The imager sequence for calibration experiments was CTAGATGTAT (P1), which was labeled with a Cy3B dye that was excited by a 561-nm laser.

Super-resolution image reconstruction

After a movie of DNA-PAINT data has been acquired (either *in silico*, *in vitro* or *in situ*), single-molecule spots must be identified and fitted to find their center position with subpixel accuracy. These routines are performed with Picasso's 'Localize' component. An overview of the graphical user interface with identified and fitted localizations is shown in **Supplementary Figure 3**, as well as screenshots of parameter dialogs.

A multitude of spot identification algorithms have been developed and applied to localization-based super-resolution microscopy[63]. In 'Picasso: Localize', spot identification makes use of the image gradient to minimize the impact of nonhomogeneous background. First, local maxima are detected by identifying pixels with highest count in their local neighborhood. This local neighborhood is defined by a square box around the pixel with a user-defined side length. Then, the net gradient (G_{net}) is calculated for each box around a local maximum pixel by

$$G_{net} = \sum_{box} g_i \cdot \mathbf{u}_i$$

where the sum is taken over all pixels of the box, g_i is the central difference gradient at pixel i and $\mathbf{u}_i$ is a unit vector originating at pixel i and pointing toward the center pixel of the box. Hence, the net gradient of a spot is the sum of intensity flowing toward the spot center, which is roughly proportional to the number of signal photons. A user-defined minimum threshold for the net gradient defines whether a spot will be further considered for fitting or disregarded.

After spots have been identified by the net gradient method, their box serves as input for a maximum likelihood fitting procedure[64]. Although a plethora of spot-fitting algorithms have been published and used for localization microscopy[63], we chose to implement the maximum likelihood algorithm because it achieves theoretically minimum uncertainty at the Cramer-Rao lower bound with good computational performance. However, it is critical to this fitting algorithm that the camera images be converted correctly to photons, because the algorithm incorporates the Poisson noise statistics inherent to light detection. In 'Picasso: Localize', the user can set the required parameters for converting camera counts to photons. One result of the maximum likelihood fitting is the Cramer-Rao lower bound (CRLB) for each spot. The localization precision is then obtained by calculating the square root of the CRLB.

Finally, super-resolution images are rendered with the 'Picasso: Render' component based on a list of subpixel spot center coordinates (see **Supplementary Fig. 4** for an interface overview). The super-resolution image is a pixel image with arbitrary pixel size, although super-resolution pixels that are too large result in insufficient spatial sampling and a potential loss in resolution. We define the ratio of super-resolution image pixels to camera pixels as the 'oversampling' parameter. In Picasso, the oversampling can be set either manually or automatically according to how far the user zooms into the image. In the dynamic case, each computer display pixel corresponds to one pixel of the super-resolution image.

Picasso offers several rendering modes for the super-resolution image. The basic option is to use no 'Blur', in which case the super-resolution image is merely a 2D histogram of localization coordinates[65]. The second option is 'One-Pixel-Blur', in which the 2D histogram is convolved with a Gaussian probability density function of volume and standard deviation equal to one. The third option, 'Global Localization Precision', is similar to the 'One-Pixel-Blur'. However, the standard deviation of the Gaussian kernel is set to the median localization precision of all localization coordinates. In the fourth option, 'Individual Localization Precision', each localization is added to the super-resolution image as a Gaussian probability density with volume equal to one and standard deviation equal to the individual coordinate localization precision[3]. For the localization-precision-based representation methods ('Global' and 'Individual Localization Precision'), a minimum blur width can be defined by the user, so that the blur width is equal to the localization precision, unless the precision is smaller than the set minimum blur width.

Picasso furthermore allows for contrast adjustment of the super-resolution image based on the density of localizations in one super-resolution image—i.e., the number of localizations per pixel (or in the case of 'blurred' images, the sum of probability densities from localizations at each pixel).

Drift correction

A critical post-processing step for localization-based super-resolution imaging is to compensate for stage drift that occurred during data acquisition. In fact, with intricate drift correction methods, extremely high resolution (well below 5 nm) can be achieved[23]. After such post-processing steps, drift is almost completely removed as a factor for resolution degradation. Consequently, localization precision and structure sampling are the only remaining factors that determine image quality. Even so, localization precision can be greatly optimized, because DNA-PAINT decouples dye photophysics from blinking, and particle averaging (described below) allows reducing of the effects of undersampling the structure of interest.

Picasso offers two major routes for drift correction: (i) using the localization events themselves and (ii) using specific fiducials in the sample. The localization-events-based drift correction is an implementation of a redundant cross-correlation (RCC) algorithm[66] in which localizations are split and rendered into multiple super-resolution images according to their temporal appearance in the movie. Image cross-correlation of all resulting super-resolution images then yields the spatial shift between temporal movie segments from which the drift is interpolated. Another conventional way for compensating drift in localization-based super-resolution microscopy is by using fiducial markers[3]. Such fiducial markers are luminescent and typically observed in the same emission channel as the fluorescent signal. Commonly used fiducials are gold nanoparticles, quantum dots and fluorescently dyed microspheres. With Picasso, localizations from such fiducial markers can be selected and used for drift correction, as the localizations can be assumed to originate from a single

point-like source. Recent developments in extremely high resolution in DNA-PAINT applications have used a large number of DNA origami as fiducial markers[23]. When using hundreds of DNA origami structures as markers, their intrinsic size does not affect the drift estimation because of their random rotational orientation. In the same work, an additional drift correction step was applied by selecting single DNA-PAINT binding sites as drift markers. Similar to the case of whole DNA origami, a large number of binding sites (usually several thousands) are required, as each individual site does not comprise sufficient localizations to interpolate the drift for each movie frame accurately. Although DNA origami and their DNA-PAINT binding sites are excellent choices, this type of fiducial-based drift estimation is not limited to these structures. It is feasible to use any distinctly visible landmarks in the image as fiducial markers—for example, protein clusters such as the nuclear pore complex.

In this protocol, we recommend subsequent applications of drift correction by RCC and, if available, fiducial-based correction with DNA origami markers followed by fiducial-based correction with single DNA-PAINT binding sites as markers. Example results after each drift correction step of such a process are shown in **Figure 4b**. In the final images, drift is almost completely eliminated as a factor in image resolution. This is corroborated by the fact that the spread of imaged DNA-PAINT binding sites is similar to the estimated localization precision by nearest neighbor analysis (NeNA)[67].

Multiplexing

One major benefit of DNA-PAINT is its straightforward extension to multiplexed imaging. Here, the simplest implementation is to use spectrally distinct dyes coupled to orthogonal imager sequences[68]. Unlike other multiplexed localization-based super-resolution techniques[69], no photo-switching of dyes is necessary, and thus it is rather simple to find compatible spectrally distinct fluorophores[68] (i.e., Atto488, Cy3B and Atto655).

However, one major drawback of spectral multiplexing is the limited number of distinguishable dyes in the visible spectrum. This limitation can be overcome with Exchange-PAINT[20]. Here, the unique programmability of DNA-PAINT docking and imager strands is used to enable spectrally unlimited multiplexing by sequentially applying orthogonal imager strands (carrying the same dye) to targets of interest.

In each imaging round, only one imager species is present in solution for one target. After acquisition, the imager is washed out and the imager for the next round is introduced. This is then repeated for the total number of targets. A multicolor image is achieved by assigning a pseudocolor to each imaging round and stacking the acquisitions on top of each other, which is depicted in **Figure 2a**.

Preparation of samples for Exchange-PAINT is similar to that for singleplex experiments, only that an open chamber allowing for fluid exchange is used as displayed in **Figure 2b**,**c**.

To create multicolor images, Picasso automatically assigns pseudocolors when several data sets are loaded. Different imaging rounds potentially comprise an offset with respect to each other because of instrumentation drift during data acquisition. However, alignment procedures can detect and correct for such image offsets.

Picasso offers cross-correlation or fiducial-based alignment algorithms. When images share features as reference points, such as DNA origami or the general cell shape, the cross-correlation can align images with high precision—e.g., sub-5-nm channel alignment, as demonstrated in **Figure 2d–f**. When few reference points are available, e.g., for *in situ* imaging of different cell targets, alignment markers or drift fiducials can be added to the sample and used in Picasso's alignment procedure.

A distinct advantage of Exchange-PAINT over spectral multiplexing is that for each imaging round the same dye is used, and thus misalignment and inhomogeneous image warping due to chromatic aberrations are avoided. This allows for very precise channel alignment and makes Exchange-PAINT ideal for colocalization studies to assess spatial proximity and possible molecular interactions. Such results are illustrated in the *in situ* example in **Figure 2g**, in which the morphology of the mitochondrial network and the spatial relationship to microtubules is studied. It shows how mitochondria are embedded in the microtubule network, as described in previous work[70].

Quantitative imaging with qPAINT

Most super-resolution studies to date harness their exquisite sub-diffraction spatial resolution to address challenges in the biological sciences by structural imaging. However, although still challenging, counting integer numbers of biomolecules when localization precision is insufficient to spatially resolve them can bring further insight into biological systems[8,71,72]. To achieve this, researchers began using the spatiotemporal information of single-molecule localization microscopy data sets beyond just binning localization events for visualization. The basic concept involves extracting molecule numbers by evaluating the kinetics of the blinking behavior of photoswitchable molecules[73–75]. Most of these counting techniques use rather complex modeling of the dye photophysics, in some cases combined with spatiotemporal clustering[72–76]. However, incumbent techniques have certain limitations that prevent them from achieving the highest accuracy and precision over a wide range of molecular densities in resolution-limited areas. These limitations generally lead to overcounting or undercounting artifacts, because the dyes typically have environmentally sensitive photophysics that are hard to predict and model. Furthermore, distinct dyes behave differently even under similar experimental conditions, which severely complicates multiplexed quantitative imaging. In addition, inhomogeneous excitation and photoactivation intensities due to uneven illumination across a sample can lead to inaccurate quantification as well. Last, dyes typically bleach over the course of an experiment, which deteriorates quantification accuracy and precision.

Recently, DNA-PAINT has been used to achieve precise and accurate counting—because of its independence from dye photophysics and immunity to photobleaching—in an implementation called qPAINT[22]. In contrast to the traditional approach of fixing blinking dyes to the target molecule, DNA-PAINT creates target 'blinking' by transient binding of dye-labeled imager strands to complementary docking strands on the target. As opposed to dye photoswitching, DNA hybridization kinetics is more predictable. Hence, combined with the effective absence of photobleaching, qPAINT can extract molecule numbers with high precision and accuracy.

Figure 3 illustrates the procedure and results of a typical qPAINT experiment. Using Picasso's quantification capabilities, we now provide users with an integrated software solution for calibrating and quantifying molecule numbers in DNA-PAINT data sets. qPAINT relies on the fact that mean dark times for a given influx rate of imager strands ($\xi = k_{on} \times c$) are dependent

only on the number of docking strands (and thus biomolecules) in an area of interest. To illustrate this, we compare two DNA origami structures, carrying 12 or 42 binding sites in 20-nm and 10-nm grid arrangements, respectively (**Fig. 3a**). A schematic representation of their respective intensity vs. time traces is shown in **Figure 3b**. By plotting the cumulative distribution function of both dark time distributions, we can obtain mean dark times for the two structures (**Fig. 3c**). To translate these dark times to actual numbers of binding sites (or units), the influx rate per unit needs to be calibrated. This can be achieved with DNA origami structures in which binding sites can be visually identified (see **Fig. 3d**, 20-nm grid structures displaying 12 binding sites). In Picasso, users can now select these calibration structures displaying a known number of units (or binding sites in this case) and calibrate the probe influx rate for subsequent quantification of target molecules of interest in the same data set (**Fig. 3d**).

The results for a typical qPAINT experiment post calibration are illustrated in **Figure 3e–g**. 20-nm DNA origami grid structures can be used to compare visually counted numbers of spots with qPAINT results, which are in good agreement (**Fig. 3e**). Note that not all DNA origami carry all binding sites, because typical staple incorporation efficiencies are <100%. qPAINT allows binding-site identification on 10-nm DNA origami grid structures, in which single sites are not clearly identifiable (**Fig. 3f**).

Finally, Picasso allows users to quickly obtain statistics from qPAINT data sets using its integrated 'Pick' and 'Pick similar' tools. **Figure 3g** illustrates the resulting number of binding-site distributions for 20-nm and 10-nm DNA origami grid structures in a single sample. The average number of binding sites is in excellent agreement with expectations. For 20-nm structures, the incorporation efficiency is ~78%, whereas it is slightly lower for 10-nm grid structures at 70%. This, however, is to be expected, as staple incorporation efficiency should be lower for larger numbers of modified staple strands in DNA origami structures.

Filtering localizations

After identification and fitting of single-molecule spots, filtering the list of localizations might improve super-resolution image quality[3,5,6,69,70,77]. Only after fitting a single-molecule spot, are properties such as spot width or an accurate estimation of the number of photons available. Hence, spot identification itself may not reliably rule out false-spot detections. A typical filtering procedure is to remove localizations with spot widths that are too small or too large. Ideally the spot width matches that of the microscope's PSF. Therefore, if the spot width is, for example, too big, it is likely that the spot originates from two closeby and overlapping events. The resulting fit coordinate will be between the two correct center positions and should therefore be disregarded. Another example of filtering is to remove localizations with a number of photons or a localization precision that is too low. After such filtering, the super-resolution image quality can improve, because only high-precision localizations remain. Picasso's 'Filter' component provides a convenient, visually guided way to filter localizations based on histograms of their properties. An overview of its graphical user interface, as well as screenshots of filtering procedures in progress, is shown in **Supplementary Figure 5**. We recommend studying histograms of localization properties and joint histogram maps of two localization properties with the goal of identifying the true signal population and removing false populations or outliers. An overview of localization properties saved by Picasso is shown in the **Supplementary Manual**.

Particle averaging

When imaging a structure that appears multiple times in the field of view, aligning the individual images on top of each other and 'summing them up' can generate an 'average' image with improved image quality[23,78]. Such a procedure is analogous to the particle averaging often applied for structural biology in single-particle electron microscopy[79] and has already been successfully applied to localization-based super-resolution microscopy[80,81]. Although, strictly speaking, we do not create an 'averaged' but rather a 'sum image' from all localizations, we here will continue to use the notion of averaging as a historical term from the electron microscopy field. 'Averaging' primarily increases the image signal-to-noise ratio, which translates for localization microscopy to the proportion of true, high-precision localizations (signal) to false or imprecise localizations (noise). Hence, structure sampling, a major factor for image resolution[16], can be improved by the averaging procedure. This is exemplified by the individual and average images of two RRO DNA origami structures in **Figure 4c–f**, showing the letters 'MPI' and 'LMU'. The average image comprises a greatly enhanced signal-to-noise ratio as compared with images of individual structures. Moreover, even though some binding sites are missing in individual structures, averaging could reconstruct all binding sites and resolve their ~5-nm distances well.

Picasso offers a graphical user interface for averaging multiple images of the same structure with the 'Average' component. The underlying algorithm does not require a reference and is based on a traditional procedure borrowed from single-particle electron microscopy[82]. Briefly, the individual images are first translationally aligned on top of each other by overlaying the center of mass of localizations. Then, several iterations of rotational and refined translational alignment are applied. In each iteration, an average image is constructed by pooling all localizations and rendering them on a super-resolution pixel grid. Then, localizations from each individual structure are rotated over 360 degrees in small steps and rendered as a super-resolution image for each rotational step. The angular step size is dynamically chosen so that the rotation distance at twice the root mean square (RMS) deviation of all localizations from their center of mass matches the size of a super-resolution pixel. Each rotated image is cross-correlated with the average image of the current iteration, and the maximum value and position of the cross-correlation are recorded. Finally, the localizations of an individual structure are rotated and translated according to the rotation and translation with the highest cross-correlation value. In the next iteration, a new improved average image can be generated from the now updated localization coordinates. After a certain number of iterations, the average image will converge—i.e., the pixel values will not change after an iteration. At this point, the algorithm can be stopped, and the new localization list is saved.

Averaging results, as shown in **Figure 4e,f**, rely on experimental conditions and post-processing steps that are specifically aimed at ultra-resolution. In particular, intricate drift correction as described above is a key contribution. Experimental conditions for ultra-resolution are described in **Box 2**; refer to **Supplementary Figures 6–9** for structure design.

PROTOCOL

MATERIALS

REAGENTS

! CAUTION All reagents can be potentially hazardous and should be handled only by trained personnel.

DNA labeling

- PBS, pH 7.2 (Life Technologies, cat. no. 20012-019)
- 0.5 M EDTA, pH 8.0 (Ambion, cat. no. AM9261) **! CAUTION** EDTA may cause eye and skin irritation; avoid breathing the dust or fumes.
- DMF (Thermo Fisher Scientific, cat. no. 20673) **! CAUTION** DMF is a toxic and flammable liquid; protect your eyes and skin, and avoid breathing the dust or fumes. It may also damage fertility and cause harm to the unborn child. Handle it under a chemical hood.
- AffiniPure Donkey Anti-Rat IgG (Jackson ImmunoResearch, cat. no. 712-005-150)
- AffiniPure Donkey Anti-Rabbit IgG (Jackson ImmunoResearch, cat. no. 711-005-152)
- AffiniPure Goat Anti-Mouse IgG (Jackson ImmunoResearch, cat. no. 115-005-003)

Antibody labeling via maleimide-PEG2-succinimidyl ester

- Maleimide-PEG2-succinimidyl ester (Sigma-Aldrich, cat. no. 746223)
- No-Weigh Format DTT (Thermo Fisher Scientific, cat. no. 20291) **! CAUTION** This compound causes skin and respiratory pathway irritation, as well as serious eye irritation. It is toxic if swallowed and causes long-term damage to aquatic life.
- Micro BCA Protein Assay Kit (Thermo Fisher Scientific, cat. no. 23235)
- Thiol-DNA (P1 handle: Thiol-TTATACATCTA; MWG Eurofins)
- Thiol-DNA (P3 handle: Thiol-TTTCTTCATTA; MWG Eurofins)

Antibody labeling via DBCO-sulfo-NHS ester

- DBCO-sulfo-NHS ester (Jena Bioscience, cat. no. CLK-A124-10)
- Azide-DNA (Biomers.net) P1 Handle: Azide-TTATACATCTA
- Azide-DNA (Biomers.net) P3 Handle: Azide-TTTCTTCATTA

Immunofixation and cell imaging

- 8-well chambered cover glasses (Eppendorf, cat. no. 0030742036 or Thermo Fisher Scientific, cat. no. 155409)
- BSA (Sigma-Aldrich, cat. no. A4503-10g)
- Triton X-100 (Carl Roth, cat. no. 6683.1) **! CAUTION** This compound is toxic if swallowed, and it can cause serious eye damage.
- 0.22-µm sterile filters (Merck/EMD Millipore, cat. no. SLGS033SS)
- Sodium chloride (Ambion, cat. no. AM9759) **! CAUTION** Sodium chloride may cause skin and eye irritation, and it may be harmful if inhaled or swallowed.
- Sodium borohydride (Carl Roth, cat. no. 4051.1) **! CAUTION** This compound reacts in a volatile manner with H_2O, is toxic if swallowed and can cause serious skin damage. Handle it under a chemical hood.
- 16% (vol/vol) Paraformaldehyde (Electron Microscopy Sciences, cat. no. 15710) **! CAUTION** This compound is flammable, a carcinogen and toxic if swallowed; avoid breathing the fumes or dust. It can cause serious eye, skin or respiratory pathway irritation. Handle it under a chemical hood.
- 25% (vol/vol) Glutaraldehyde (SERVA, cat. no. 23115.01) **! CAUTION** Glutaraldehyde is toxic if swallowed; it causes serious skin damage, and acute and chronic toxicity in aquatic life. Avoid breathing the fumes or dust. Wear protective equipment and handle the compound under a chemical hood.
- α-Tubulin (YL1/2) antibody (Thermo Fisher Scientific, cat. no. MA1-80017)
- α-Tubulin (DM1A) mouse antibody (Cell Signaling, cat. no. 3873S)
- Tom20 (FL-145) rabbit antibody (Santa Cruz, cat. no. sc-11415)
- DNA-labeled secondary antibodies and imager kit (Ultivue, cat. no. U10001)
- Imager strand (P1-Cy3B: CTAGATGTAT-Cy3B; Eurofins Genomics)
- Imager strand (P3-Atto655: GTAATGAAGA-Atto655; Eurofins Genomics)
- Imager strand (P3-Cy3B: GTAATGAAGA-Cy3B; Eurofins Genomics)

Cell culture

- PBS, pH 7.2 (Thermo Fisher Scientific, cat. no. 20012-019)
- MEM (Thermo Fisher Scientific, cat. no. 31095-052)
- Eagle's Minimum Essential Medium (EMEM; ATCC, cat. no. 30-2003)
- L-Glutamine (Thermo Fisher Scientific, cat. no. 25030-149)
- Non-essential amino acids (Thermo Fisher Scientific, cat. no. 11140-035)
- FBS (Thermo Fisher Scientific, cat. no. 10500-064)
- Penicillin–streptomycin (P/S; Thermo Fisher Scientific, cat. no. 15140-122) **! CAUTION** It may damage fertility and cause harm to the unborn child. Avoid breathing fumes or dust.
- Trypsin-EDTA (Thermo Fisher Scientific, cat. no. 25300-054)
- HELA cell line (Leibniz Institute DSMZ: Catalogue of Human and Animal Cell Lines (http://www.dsmz.de), cat. no. ACC-57) **! CAUTION** The cell lines used in your research should be regularly checked to ensure that they are authentic and they are not infected with mycoplasma.
- BS-C-1 cell line (ATCC, cat. no. CCL-26) **! CAUTION** The cell lines used in your research should be regularly checked to ensure that they are authentic and they are not infected with mycoplasma.

DNA origami folding

- Staple strands, modified and unmodified (Eurofins Genomics)
- M13 bacteriophage ssDNA scaffold p7249 (New England BioLabs, cat. no. N4040S)
- Tris, pH 8.0, 1 M (Ambion, cat. no. AM9856) **! CAUTION** Tris can cause skin and serious eye irritation.
- EDTA, pH 8.0, 0.5 M (Ambion, cat. no. AM9261) **! CAUTION** EDTA may cause eye and skin irritation; avoid breathing the dust or fumes.
- Water (Gibco, cat. no. 10977-035)
- Magnesium, 1 M (Ambion, cat. no. AM9530G)
- Agarose (Biomol, cat. no. 01280.100)
- 50× TAE Buffer (Fluka Analytical, cat. no. 67996-10L-F)
- SYBR safe DNA gel stain (Invitrogen, cat. no. SS33102) **! CAUTION** Protect your eyes and avoid breathing the dust, fumes or mist; it causes eye, skin and respiratory irritation.
- DNA gel loading dye (Thermo Fisher Scientific, cat. no. R0611)
- DNA ladder (Invitrogen, cat. no. 10787-018)

***In vitro* sample preparation**

- Protocatechuic acid (PCA; Sigma-Aldrich, cat. no. 37580-25G-F) **! CAUTION** PCA causes skin, respiratory pathway and serious eye irritation. Avoid breathing the dust, fumes or mist.
- Protocatechuate 3,4-dioxygenase (PCD; Sigma-Aldrich, cat. no. P8279-25UN)
- Trolox (Sigma-Aldrich, cat. no. 238813-1G) **! CAUTION** Trolox causes skin, respiratory pathway and serious eye irritation. Avoid breathing the dust, fumes or mist.
- NaOH (VWR, cat. no. 31627.290) **! CAUTION** NaOH causes serious skin and eye damage; avoid breathing the dust, fumes or mist. Wear protective equipment.
- Methanol (Sigma-Aldrich, cat. no. 32213-2.5L) **! CAUTION** Methanol is a flammable liquid, and it is toxic upon ingestion and skin contact; avoid breathing the dust, fumes or mist.
- Potassium chloride (Carl Roth, cat. no. 6781.1)
- Glycerol (Sigma-Aldrich, cat. no. 65516-500ml)
- Isopropanol (Carl Roth, cat. no. 33539-2.5L-R) **! CAUTION** Vapor and liquid phases are easily flammable, and the compound causes heavy eye irritation.
- Epoxy Glue (Toolcraft, cat. no. TC-EPO5-24)
- Albumin, biotin-labeled bovine (Sigma-Aldrich, cat. no. A8549-10MG)
- Streptavidin (Thermo Fisher Scientific, cat. no. S888)
- Tween 20 (Sigma-Aldrich, cat. no. p2287)

EQUIPMENT

- Thermocycler (Mastercycler Nexus Gradient; Eppendorf, cat. no. 6331000017)
- 10-liter Tank (Carl Roth, cat. no. K653.1)
- Sub-cell GT system gel chamber (Bio-Rad, cat. nos. 170 4401-4406 and 170 4481-4486)
- PowerPac basic power supply (Bio-Rad, cat. no. 1645050)
- Microwave (Severin, cat. no. 7891)
- Erlenmeyer flask, 250 ml (Carl Roth, cat. no. NY87.1)
- Razor blade (Carl Roth, cat. no. CK07.1)
- Visi-blue light transilluminator (UVP, cat. no. 95-0461-02)
- Centrifuge 5430R (Eppendorf, cat. no. 5428000414)
- NanoDrop 2000c (Thermo Fisher Scientific, cat. no. ND-2000c)
- Shaker (GFL, cat. no. 3015)
- Biological safety cabinet (HeraSafe; Thermo Electron Corporation, cat. no. 51022482)
- Water purification system (PURELAB classic; ELGA LabWater, cat. no. CLXXUVFM2)
- Incubator (Heracell 240; Thermo Fisher Scientific, cat. no. 51026333)
- Pipetboy acu 2 (Integra, cat. no. 155017)
- Eppendorf Research plus 0.1–2.5 µl pipette (Eppendorf, cat. no. 3120000011)
- Eppendorf Research plus 0.5–10 µl pipette (Eppendorf, cat. no. 3120000020)
- Eppendorf Research plus 2–20 µl pipette (Eppendorf, cat. no. 3120000038)
- Eppendorf Research plus 10–100 µl pipette (Eppendorf, cat. no. 3120000046)

- Eppendorf Research plus 20–200 µl pipette (Eppendorf, cat. no. 3120000054)
- Eppendorf Research plus 100–1000 µl pipette (Eppendorf, cat. no. 3120000062)
- Multipette M4 pipette (Eppendorf, cat. no. 4982000314)
- Eppendorf Research plus, 8-channel, 0.5–10 µl pipette (Eppendorf, cat. no. 3122000019)
- Gel imager (Typhoon FLA 9500; GE, cat. no. 28996943)
- Side cutter (Hoffmann Group, cat. no. 725310)
- Amicon spin filters, 3 kDa (Merck/EMD Millipore, cat. no. UFC500396)
- Amicon spin filters, 100 kDa (Merck/EMD Millipore, cat. no. UFC510096)
- Nap5 columns (GE Healthcare, cat. no. 17-0853-02)
- Zeba desalting spin columns (Thermo Fisher Scientific, cat. no. 89882)
- Amicon spin filters, 100 kDa (Merck/EMD Millipore, cat. no. UFC510096)
- NORM-JECT 2-ml syringe (Henke Sass Wolf, cat. no. 4020-000V0)
- NORM-JECT 10-ml syringe (Henke Sass Wolf, cat. no. 4100-000V0)
- NORM-JECT 20-ml syringe (Henke Sass Wolf, cat. no. 4200-000V0)
- FINE-JECT Needle, 1.2 × 40 mm (Henke Sass Wolf, cat. no. 4710012040)
- FINE-JECT Needle, 1.1 × 40 mm (Henke Sass Wolf, cat. no. 4710011040)
- Silicon tubing, inner diameter = 0.5 mm, outer diameter = 1 mm (GM GmbH, cat. no. 35605)
- T75 Flasks (Falcon, cat. no. 353136)
- 10-ml Serological pipettes (Greiner Bio-One, cat. no. 607180)
- 5-ml Serological pipettes (Greiner Bio-One, cat. no. 606180)
- 2-ml Serological pipettes (Falcon, cat. no. 357507)
- Glass Pasteur pipettes (Brand, cat. no. 747720)
- 90-nm Gold particles (prepared in house[83])
- DNA LoBind Tube, 0.5 ml (Eppendorf, cat. no. 0030 108.035)
- PCR tubes (Trefflab, cat. no. 96.09852.9.01)
- Freeze 'N Squeeze columns (Bio-Rad, cat. no. 732-6165)
- Aluminum foil (VWR, cat. no. 391-1257)
- 1.5-ml Eppendorf tubes (Eppendorf, cat. no. 0030 120.086)
- 15-ml Falcon tubes (Falcon, cat. no. 352096)
- 50-ml Falcon tubes (Falcon, cat. no. 352070)
- ibidi sticky-Slide VI 0.4 (ibidi, cat. no. 80608)
- High-precision cover glasses 18 × 18 mm, no. 1.5H (Marienfeld, cat. no. 0107032)
- High-precision cover glasses 24 × 60 mm, no. 1.5H (Marienfeld, cat. no. 0107242)
- Microscopy slide (Thermo Fisher Scientific, cat. no. 10756991)
- Double-sided adhesive tape (Scotch, cat. no. 665D)
- Weighing paper (VWR International, cat. no. 12578-121)

TIRF super-resolution setup

- Optical air table (Newport, cat. no. RS4000-46-12)
- Inverted fluorescence microscope (Nikon, Ti Eclipse with Perfect Focus System)
- XY Stage (Physik Instrumente, cat. no. M-545.2MN)
- Lenses and mirrors (Thorlabs)
- Filter cubes (Chroma Technology, cat. nos. TRF49904-NK, TRF49909-NK, TRF49914-NK)
- Oil-immersion objective, 100× Apo SR TIRF objective, numerical aperture (NA) = 1.49, working distance (WD) = 0.12 (Nikon)
- Immersion oil, refractive index (n) = 1.515 (23 °C), (Nikon, Type A)
- sCMOS camera (Hamamatsu Orca Flash 4.0 V2)
- EMCCD camera (Andor, iXon Ultra, model no. DU-897)
- Excitation laser, 488 nm, 200 mW (Toptica iBeam smart, model no. 488-S-HP)
- Excitation laser, 561 nm, 200 mW (Coherent Sapphire, model no. 561-200 CW CDRH)
- Excitation laser, 640 nm, 150 mW (Toptica, iBeam smart, model no. 640-S)
- Microscopy slide thermal power sensor (Thorlabs, model no. S170C)
- Digital power meter (Thorlabs, model no. PM100D)
- Acquisition computer: a computer used to acquire microscope data with the µManager software package[58]. See EQUIPMENT SETUP for hardware requirements.
- Analysis computer: a computer with a Microsoft Windows 64-bit operating system. See EQUIPMENT SETUP for hardware requirements.
- Analysis software: our analysis software package 'Picasso' can be downloaded from our website at http://www.jungmannlab.org.

REAGENT SETUP

Pre-extraction buffer The pre-extraction buffer consists of 0.4% (vol/vol) glutaraldehyde and 0.25% (vol/vol) Triton X-100 in 1× PBS at pH 7.2. It can be stored at −20 °C for 12 months.

Enhanced microtubule fixative The enhanced microtubule fixative consists of 3% (vol/vol) glutaraldehyde in 1× PBS at pH 7.2, and it can be stored at −20 °C for 12 months.

Standard fixative The standard fixative consists of 3% (vol/vol) paraformaldehyde and 0.1% (vol/vol) glutaraldehyde in 1× PBS at pH 7.2. It can be stored at −20 °C for 12 months.

Blocking solution The blocking solution contains 3% (wt/vol) BSA and 0.2% (vol/vol) Triton X-100 in 1× PBS at pH 7.2, and it must be filter-sterilized. It can be stored at 4 °C for up to 6 weeks.

Antibody dilution solution The antibody dilution solution contains 3% (wt/vol) BSA in 1× PBS at pH 7.2, and it must be filter-sterilized. It can be stored at 4 °C for up to 6 weeks.

DTT solution The DTT solution consists of 250 mM DTT, 1.5 mM EDTA and 0.5× PBS, pH 7.2. It must be freshly prepared for the reduction of the thiolated DNA.

BCA mix The BCA mix includes 500 µl of reagent A, 500 µl of reagent B and 25 µl of reagent C (from the Micro BCA Protein Assay Kit), and it must be freshly prepared.

HeLa cell medium The HeLa cell medium consists of MEM, 10% (vol/vol) FCS, 1% (vol/vol) P/S, 2 mM L-glutamine and 1× non-essential amino acids. HeLa cell medium can be stored at 4 °C for up to 4 months.

BSC1 cell medium The BSC1 cell medium consists of EMEM, 10% (vol/vol) FCS and 1% (vol/vol) P/S.

Cross-linker aliquots Cross-linkers should be divided into aliquots at a concentration of 10 mg/ml in DMF, and they can be stored at −80 °C for up to 12 months.

Buffer A Buffer A consists of 10 mM Tris-HCl and 100 mM NaCl at pH 8.0, and it can be stored at room temperature (RT; 21 °C) for 6 months.

Buffer A+ Buffer A+ consists of 10 mM Tris-HCl, 100 mM NaCl and 0.05% (vol/vol) Tween 20 at pH 8.0, and it can be stored at RT for 6 months.

Buffer B Buffer B consists of 5 mM Tris-HCl, 10 mM $MgCl_2$ and 1 mM EDTA at pH 8.0, and it can be stored at RT for 6 months.

Buffer B+ Buffer B+ consists of 5 mM Tris-HCl, 10 mM $MgCl_2$, 1 mM EDTA and 0.05 % (vol/vol) Tween 20 at pH 8.0, and it can be stored at RT for 6 months.

Buffer C Buffer C consists of 1× PBS at pH 7.2 supplemented with additional 500 mM NaCl, and it can be stored at RT for up to 6 months.

Exchange washing buffer Exchange washing buffer consists of Buffer B+ for *in vitro* samples and of 1× PBS, pH 7.2, for *in situ* samples; it can be stored at RT for 6 months.

100× Trolox solution 100× Trolox solution consists of 100 mg of Trolox, 430 µl of methanol and 345 µl of NaOH (1 M) in 3.2 ml of H_2O. It should be divided into 20-µl portions in PCR tubes and can be stored at −20 °C for up to 6 months.

40× PCA solution 40× PCA solution consists of 154 mg of PCA in 10 ml of water, adjusted to pH 9.0 with NaOH. The solution should be divided into 20-µl aliquots in PCR tubes and can be stored at −20 °C for up to 6 months.

100× PCD solution 100× PCD solution consists of 9.3 mg of PCD and 13.3 ml of buffer (50% glycerol stock in 50 mM KCl, 1 mM EDTA and 100 mM Tris–HCl, pH 8.0). It should be divided into 20-µl aliquots in PCR tubes and can be stored at −20 °C for up to 6 months.

Oxygen-scavenging system PPT solution PPT solution consists of a 1:1:1 ratio of 1× PCA/1× PCD/1× Trolox. Mix with imaging buffer at least 1 h before imaging.

Imager solution For *in vitro* samples, the imager solution consists of 1× Buffer B+, optional scavenger system PPT solution (1× Buffer B+, 1× PCA, 1× PCD, 1× Trolox) and a fluorophore-labeled DNA strand. For *in situ* samples, the imager solution consists of 1× Buffer C, optional scavenger system PPT solution (1× Buffer C, 1× PCA, 1× PCD, 1× Trolox) and a fluorophore-labeled DNA strand. The concentration range for the fluorophore-labeled DNA strand is highly target dependent, but it ranges between 100 pM and 10 nM. The solution should always be freshly prepared.

10× Folding buffer 10× folding buffer consists of 125 mM $MgCl_2$, 100 mM Tris and 10 mM EDTA at pH 8.0, and it can be stored at RT for up to 6 months.

Gel buffer Gel buffer consists of 1× TAE buffer, and it can be stored at RT for 1 year.

Gel running buffer Gel running buffer consists of 1× TAE buffer and 12.5 mM $MgCl_2$, and it can be stored at RT for up to 1 year.

BSA–biotin stock BSA–biotin stock contains 10 mg/ml BSA–biotin in Buffer A, and it should be divided into 20-µl aliquots. It can be stored at −20 °C for up to 6 months.

PROTOCOL

BSA–biotin solution BSA–biotin solution contains 1 mg/ml BSA–biotin in Buffer A+ and should be freshly prepared. It can be stored for up to 3 d at 4 °C.

Streptavidin stock Streptavidin stock contains 10 mg/ml streptavidin in Buffer A and should be divided into 10-µl aliquots. It can be stored at −20 °C for up to 6 months.

Streptavidin solution Streptavidin solution contains 0.5 mg/ml streptavidin in Buffer A+ and should be freshly prepared. It can be stored for up to 3 d at 4 °C.

Staple strands Staple strands can be ordered in different purity grades. High-purity salt-free purification is sufficient for standard staples; however, we recommended ordering modified staples, such as those with fluorophores or biotins, HPLC or PAGE purified. Staple strands for nanostructures should be ordered in 96-well plates (0.2 ml) to facilitate the handling and creation of master mixes with the help of multipipettes. To keep the manual handling to a minimum, the staples should be ordered prediluted at a concentration of 100 µM in H_2O. The plates can be stored at −20 °C for at least 12 months.

EQUIPMENT SETUP

Acquisition computer The following computer system was used for all data acquisition in this protocol: Dell Precision T7910, Dual Intel Xeon Processor E5-2620 v3 at 2.4 GHz (12 cores), 32 GB RAM, four 2 TB HDD configured in a Hardware RAID 0, Windows 7 Professional 64-bit operating system. ▲ **CRITICAL** A RAID 0 setup is optimized for fast input/output. For long-term data storage, users are advised to use data storage facilities with daily backup available to research groups at universities or research institutes.

Acquisition software As image acquisition software, install µManager, an open-source software[58] that can be downloaded from https://micro-manager.org. Follow the installation instructions and set up the software to control the microscope equipment.

Analysis computer We do recommend performing all postacquisition steps with Picasso on a separate analysis workstation. The hardware requirements depend on the specific file size of the data set to be analyzed. Generally, the most important factors are the number of available CPU cores and RAM. The following system was used for all analyses in this protocol: Dell Precision T7910, Dual Intel Xeon CPU E5-2680 v3 at 2.5 GHz (24 cores), 256 GB RAM and four 2 TB HDD configured in a Hardware RAID 0, Windows Server 2012 R2 64-bit operating system. ▲ **CRITICAL** A RAID 0 setup is optimized for fast input/output. For long-term data storage, users are advised to use data storage facilities with daily backup available to research groups at universities or research institutes.

Analysis software Download the 'Picasso' installer available at our website (http://www.jungmannlab.org). Follow the installation instructions. Multiple Picasso components will appear as shortcuts in a start menu subfolder named 'Picasso'.

Power density calibration Determine the laser power at the sample by placing the microscopy slide thermal power sensor with immersion oil on the sample holder. The power density is then calculated as an average density over the illuminated area. See **Supplementary Table 1** for an exemplary calibration on our microscope.

Fluid exchange chamber To prepare a fluid exchange chamber for *in situ* imaging, see **Box 1**.

PROCEDURE

Design of DNA nanostructures ● TIMING 1 h

1| Start 'Picasso: Design', which displays a canvas of a hexagonal lattice, representing the staple strand positions (**Fig. 6**) in a 2D RRO[33].

2| Design a pattern of DNA-PAINT binding sites by clicking on the canvas hexagons. Clicking on a hexagon will change its color and marks the respective staple to be extended with an external sequence. Each color corresponds to a specific extension that may be defined later. The default state without an external extension is indicated by a gray hexagon. The center-to-center distance between two hexagons is ~5 nm on the DNA origami. To change the 'current color', click on a colored hexagon in the color palette to the right. Clicking on a hexagon with a currently selected color will reset the 'current color' to the unmarked state (gray). Click 'Clear' to reset all hexagons in the lattice. The eight white double-hexagons within the structure are placeholders for biotinylated staples for surface attachment and are not intended for modification. In total, the structure consists of 176 staples available for modification.

3| Click 'Save' to save the design. Progress can be saved at any time and loaded at a later point by selecting 'Load'. A screenshot of the design can be saved by clicking on 'Screenshot'.

4| Click on 'Extensions' to specify the extensions corresponding to each color. A table with all the colors present in the design will open. A selection of commonly used DNA-PAINT handles can be obtained via the dropdown menu in the 'Preselection' column. This list can be extended by modifying 'paint_sequences.csv' in the subfolder 'picasso' of the Picasso install directory. See **Supplementary Table 2** for a table of the default sequences. Alternatively, define a custom 'Shortname' and 'Extension' by entering them in the table. After defining all colors used in the canvas, select 'OK' to confirm the extensions. The display will update with the 'Shortname'. The sequence specified will be added to the 3'-end of the staple and will point out of the structure (away from the cover glass). For a full list of all unmodified core staples, refer to **Supplementary Table 3**.

5| Once the design step is complete, the sequences for the corresponding structure need to be obtained. Click on 'Get plates' to generate a staple list for ordering. As an RRO origami structure consists of 184 staples, the staples in the list are arranged in two 96-well plates, so that each well corresponds to a position on the hexagonal lattice. It is possible to export only the sequences of a particular structure (in total, two plates) or to get a list of plates for which all possible positions are extended with all extensions used in the design. This is particularly useful in the case in which different origami designs with different extensions and patterns will be tested, so all staples are ready to be mixed and matched for subsequent design iterations. The software will export the list in .csv format, so that the file can be used for direct ordering at your favorite oligo synthesis company. Choose high-purity salt-free purification and order oligonucleotides in solution with a

© 2017 Macmillan Publishers Limited, part of Springer Nature. All rights reserved.

concentration of 100 µM in H_2O (see also Reagent Setup). Store the .csv file in a folder so that the program can later create pipetting schemes based on your plate stock. In addition, order the biotinylated staples (for cover glass attachment of the DNA origami) that can be found in **Supplementary Table 4**.

■ **PAUSE POINT** Typically, synthesis of unmodified oligonucleotides at a commercial vendor will take between 2 and 10 working days.

Folding of DNA structures ● TIMING 6–7 h

6| Once all sequences are obtained, staples with the same extension are pooled together from plates and place in microcentrifuge tubes as stock mixes. Picasso will generate a visual pipetting aid to help identify which staples need to be pooled together in a separate microcentrifuge tube. To so initiate this, select 'Pipetting scheme' and select the folder with all previously generated plates. 'Picasso: Design' will search in all .csv files in that folder for sequences that are needed for the design. Note that only .csv files that contain staple lists (that were generated with 'Get plates' in 'Picasso: Design') should be present in that folder. A list will be generated with all necessary sequences and the visual pipetting aid in .pdf format for the origami stock mixes. The dimensions of the printed pipetting scheme match those of typical 96-well plates, so that wells that need to be pipetted can be easily identified.

▲ **CRITICAL STEP** If the software does not find all sequences that are needed in the plate list, it will display an error message but still compile the pipetting aid and the staple list. Missing staples are indicated by 'NOT FOUND' in the list.

7| Print out the pipetting aid and place a transparent 96-well plate above it. Pool staples according to their color and the pipetting aid for stock mixes in microcentrifuge tubes. The volume of each staple that is needed when pooling can be estimated considering the final amount of structures. When folding, i.e., 40 µl of DNA origami with a 10-nM final scaffold concentration (enough for ~80 DNA-PAINT experiments), the amount of staples needed is ~0.04 µl for each core staple and ~0.4 µl for each extended staple. As pipetting precision decreases with small volumes, pipette at least 1 µl per staple when pooling for mixes. Avoid contamination of the plates, do not talk while pipetting and cover the plates whenever possible. Seal the plates immediately after use. Store mixes at –20 °C in tubes for up to 12 months.

8| Select 'Folding Scheme' to generate a table with a folding protocol. Adjust the initial concentrations in the table according to the ordered stocks and click 'Recalculate', if applicable. The software will automatically calculate the concentration of a strand in a staple mix depending on the number of staples in the mix. Adjust 'Excess' or 'Total Volume' to your needs and mix all items on the folding scheme list in the calculated quantities. Refer to **Supplementary Table 5** for n exemplar folding table.

9| Use a thermocycler and fold the origami mix using the following thermal gradient:

Cycle number	Parameters
1	80 °C
2–57	60 °C–4 °C, 3 min 12 s per °C
58	Hold at 4 °C

■ **PAUSE POINT** The structures can be stored at 4 °C for up to 1 week or at –20 °C in DNA LoBind Tubes for long-term storage (at least several months).

Purification of DNA nanostructures ● TIMING ~3.5 h

10| Purify the DNA nanostructures using your favorite method. Several methods for purification of DNA nanostructures, such as Gel[42], rate-zonal centrifugation[43] and PEG[44], are described in the literature. For DNA-PAINT, it is possible in most cases to use the structures without purification, as excess staple strands will be washed out of the flow chamber.

▲ **CRITICAL STEP** When folding DNA origami for the first time, it is recommended to run an agarose gel to confirm the folding (**Fig. 6**). Typically, well-folded monomeric structures will appear as a single sharp gel band (upper highlighted area in the gel in **Fig. 6**) together with a faster migrating band consisting of excess staple strands (lower highlighted area in the gel in **Fig. 6**).

■ **PAUSE POINT** The structures can be stored at 4 °C for up to 1 week or at –20 °C in DNA LoBind Tubes for at least 1 year.

11| Prepare a solution of 1.8 g of agarose in 120 ml of gel buffer in an Erlenmeyer flask (1.5% (wt/vol)).

PROTOCOL

12| Use a microwave to heat up and completely solubilize the agarose solution by stirring the flask in between the heating phases.
! CAUTION Use heat-resistant gloves when handling the hot flask to avoid burns.

13| If no agarose particle traces are visible anymore, let the solution cool for 1 min, and add 1.5 ml of 1M $MgCl_2$ and 14 µl of Sybr Safe.
! CAUTION Avoid inhaling solutions with Sybr Safe.

14| Pour the solution into a gel chamber, add an appropriate comb and let it solidify for 45 min.

15| Load the gel with the DNA origami structures. Prepare two lanes for a DNA ladder and scaffold (same concentration as origami) as reference. Mix the origami solution with loading dye (20 µl of folded DNA Origami + 5 µl of loading dye) and run the gel in running buffer at 90 V for 90 min at 4 °C or on ice.

16| Acquire an image using a gel imager for documentation.

17| Cut out the origami band with a razor blade on a blue-light transilluminator table. The origami band should appear as a distinct band with a slight shift as compared with the scaffold. Excess staples will have created a broader band that traveled further. Crush the gel piece with a pestle, transfer it to a Freeze 'N Squeeze column, and spin it for 6 min at 1,000*g* at 4 °C. Keep the flow-through and discard the filter.
? TROUBLESHOOTING
■ PAUSE POINT The origami can be stored at 4 °C for 1 week or at –20 °C in LoBind tubes for long-term storage.

Preparation of DNA origami for DNA-PAINT imaging ● TIMING ~45 min
18| There are two options for preparing microscopy slides. See option A for the preparation in a custom-built flow chamber that will be sealed after immobilization of structures and addition of imager solution. For Exchange-PAINT experiments that require fluid exchange, see option B for preparation in an open chamber. The process of making custom-built chambers is also depicted in **Supplementary Figure 10**.

(A) Immobilization in a custom-built chamber

(i) Clean the microscopy slide and the cover glass with isopropanol and dry it with lab wipes.
(ii) Prepare a flow chamber by taping two stripes of double-sided adhesive tape ~8 mm apart on the microscopy slide and form a flow chamber by placing a cover glass on top. The resulting channel will have a volume of ~20–30 µl. Use a pipette tip and press the cover glass firmly against the sticky tape. The sticky tape will appear darker when the cover glass is in good contact.
▲ **CRITICAL STEP** Do not use excessive force, as the glass may break.
(iii) Remove excess adhesive tape by pulling the tape over the edges of the cover glass.
(iv) Fill the chamber with 20 µl of BSA–Biotin solution (1 mg/ml) and incubate it for 2 min.
(v) Wash the channel with 40 µl of Buffer A+ by holding the tip of a folded lab wipe on one end of the channel and simultaneously pipetting in washing buffer on the other side. The capillary forces of the tissue will suck the liquid out of the chamber, whereas the pipetting will introduce additional volume. Control the flow by variation of pipetting speed and tissue pressure.
▲ **CRITICAL STEP** Avoid bubbles by keeping an even flow. Do not let the chamber dry out. Practice with an empty slide and water if necessary.
(vi) Add 20 µl of streptavidin solution (0.5 mg/ml) to the channel and incubate it for 2 min.
(vii) Wash the channel with 40 µl of Buffer A+.
(viii) Wash the channel with 40 µl of Buffer B+.
(ix) Add 20 µl of (5 µl of gel-purified DNA origami and 15 µl of Buffer B+) origami solution and incubate for 2 min.
? TROUBLESHOOTING
(x) Wash the channel with 40 µl of Buffer B+.
(xi) Add 20 µl of imager solution to the channel.
▲ **CRITICAL STEP** Imager concentration has a critical role in proper acquisition of DNA-PAINT data. For *in vitro* samples, consider an ~5 nM imager concentration for a DNA nanostructure with 12 binding sites as a start value.
(xii) (Optional) For spectral multiplexing, use 2 different DNA sequences with spectrally distinct fluorophores, such as Cy3B and Atto655.
(xiii) Use epoxy glue to seal the chamber. Pour the glue on a piece of weighing paper, mix with a pipette tip and distribute the glue evenly on the edges of the cover glass. Once the chamber is sealed, place the pipette tip standing up in the remaining epoxy to later evaluate the glue dryness.

(xiv) Wait for ~15 min for the epoxy to dry. The drying process can be evaluated by checking the pipette tip in the epoxy. Once the epoxy is completely dry, the pipette tip should stick. The sample is now ready for imaging.
▲ CRITICAL STEP Wait until the epoxy is completely dry to avoid glue contamination of the microscope objective.

(B) Immobilization in a 6-channel ibidi sticky-Slide

(i) Clean the cover glass (24 × 60 mm) with isopropanol and dry it with lab wipe.
(ii) Attach the cover glass upside down to the sticky-Slide and press it with the help of a pipette tip against the cover glass.
(iii) Add 80 µl of BSA–biotin solution to the channel. Tilt the slide slightly to ensure that the chamber is completely filled and incubate it for 5 min.
(iv) Wash the channel with 180 µl of Buffer A+ by pipetting the solution into one opening and pipetting out 180 µl from the opposing opening.
(v) Incubate 40 µl of streptavidin solution twice for 5 min.
(vi) Wash the channel with 180 µl of Buffer A+.
(vii) Wash the channel with 180 µl of Buffer B+.
(viii) Icubate the DNA origami solution (20 µl of gel-purified DNA origami + 60 µl of Buffer B+) for 20 min.
? TROUBLESHOOTING
(ix) Wash the channel two times with 100 µl of Buffer B+.
(x) Add Imager strand solution to the sample for imaging.
▲ CRITICAL STEP Imager concentration has a critical role in proper acquisition of DNA-PAINT data. For *in vitro* samples, consider ~5 nM for DNA nanostructures with 12 binding sites as a start value. (Optional) For spectral multiplexing, use two different DNA sequences with spectrally distinct fluorophores, such as Cy3B and Atto655.
(xi) Put the lid back on the chamber. The sample is now ready for imaging.

Sample preparation for *in situ* samples

19| Generate DNA-conjugated secondary antibodies. Here, two methods are presented: option A describes the use of a maleimide-PEG2-succinimidyl ester cross-linker, which links free amino groups on the protein to reduced thiolated DNA[22], and option B describes the use of a DBCO-sulfo-NHS ester, which binds to amino groups on the protein and via copper-free click chemistry to an azide-modified DNA strand[55]. The copper-free click chemistry allows for conjugation of multiple antibody species in parallel, whereas the attachment via Maleimide chemistry is more cost-effective, considering the DNA components. The reduction of the thiol group and the subsequent purification of the DNA from DTT using the Nap-5 column is time-consuming and time-critical. Long waiting times will lead to disulfide bridging of the DNA strands. The copper-free click chemistry in comparison does not have such a time-consuming and time-critical step in regard to the reagent stability, and therefore allows for parallel labeling of the antibodies. Alternatively, DNA-labeled antibodies can also be obtained from Ultivue (http://www.ultivue.com).

(A) DNA labeling of antibodies via maleimide-PEG2-succinimidyl ester for cellular labeling ● TIMING 1 d 1 h

(i) To reduce the thiolated DNA for the Maleimide reaction, mix 30 µl of 1-mM thiolated DNA with 70 µl of freshly prepared DTT solution and incubate the mixture on a shaker for 2 h at RT covered with aluminum foil.
(ii) Concentrate the antibody using Amicon spin filters (100 kDa). Wash the filters with 1× PBS for 10 min at 14,000*g* at 4 °C. Discard the flow-through, add 300 µl of antibody solution and spin at 14,000*g* for 5 min at 4 °C. Discard the flow-through and invert the spin filter in an empty tube. Spin for 6 min at 1,000*g* at 4 °C. Adjust the volume to 100 µl with 1× PBS, and measure the concentration with the NanoDrop spectrophotometer. Keep the antibody on ice. The final concentration should be >1.5 mg/ml.
(iii) Prepare the cross-linker solution in 1× PBS and add it to the antibody in a 10:1 molar ratio. Incubate the solution for 90 min at 4 °C on a shaker covered in aluminum foil. Start the reaction 1 h after the DNA reduction step was started.
▲ CRITICAL STEP The desired amount of cross-linker must be no more than 5 µl in volume in order to avoid adding too much of DMF or diluting the antibody further.
(iv) 20 min before the DNA reduction step is completed, start to equilibrate a Nap-5 column with ddH_2O filled to the top three times. Add DNA–DTT solution to the column and immediately add 400 µl of ddH_2O. After 400 µl has passed through, add 1 ml of ddH_2O and start collecting fractions immediately. Collect three drops in the first four tubes, two drops in the following four and one drop in the last eight tubes. Starting from the last collected tube, add 25 µl of BCA mix to the tubes. If DTT is still present, the solution turns purple. Discard those tubes. If no color change is visible anymore, discard the next tube as well and measure the concentration of the remaining fractions via the NanoDrop spectrophotometer. Pool the fractions with the highest concentrations. The highest fractions will have a DNA concentration between 200 and 800 ng/µl.
▲ CRITICAL STEP If DTT is still present in the DNA solution, it will interfere with the Maleimide reaction.

PROTOCOL

(v) Concentrate the reduced DNA using Amicon spin filters (3 kDa). Wash the filter with 1× PBS for 30 min at 14,000*g* at 4 °C. Discard the flow-through and add the pooled fractions of reduced DNA to the filter. Centrifuge for 30 min at 14,000*g* at 4 °C and discard the flow-through. Invert the spin filter in an empty new tube and spin for 6 min at 1,000*g* at 4 °C. Measure the concentration with the NanoDrop spectrophotometer; the DNA should have a concentration >700 ng/µl.

(vi) After the antibody–cross-linker reaction has completed, use a Zeba desalting column to remove the linker. Remove the storage solution by centrifugation at 1,500*g* for 1 min at 4 °C. Mark the side where the resin slid up, and perform the subsequent centrifugation steps in the same orientation. Wash the Zeba column with 300 µl of PBS and centrifuge it at 1,500*g* for 1 min at 4 °C. Dry the bottom of the column and use a fresh 1.5-ml tube. Add the antibody–cross-linker solution to the Zeba column, and spin at 1,500*g* for 2 min at 4 °C. Discard the Zeba column, retain the flow-through and measure the concentration with the NanoDrop spectrophotometer. The antibody concentration should be > 1.5 mg/ml.

(vii) Incubate a 10:1 molar ratio of thiolated DNA to antibody overnight on a shaker covered in aluminum foil in a cold room.

(viii) Remove excess DNA by Amicon spin filtration (100 kDa). For this, wash the filters with 1× PBS for 10 min at 14,000*g* at 4 °C. Discard the flow-through, add antibody–DNA solution, add 300 µl PBS and spin at 14,000*g* for 5 min at 4 °C. Discard the flow-through and invert the spin filter into an empty tube. Spin the solution for 6 min at 1,000*g* at 4 °C. Adjust the volume to 100 µl with 1× PBS, and measure the concentration with the NanoDrop spectrophotometer. The peak signal should be shifted toward 260 nm from 280 nm, and the concentration should be >5 mg/ml because of the stronger absorbance of DNA. Keep the antibody on ice and store it at 4 °C for a maximum of 6 months.
? TROUBLESHOOTING

(B) Labeling via DBCO-sulfo-NHS ester ● TIMING 4 h

(i) Concentrate the antibody using Amicon spin filters (100 kDa). For this, wash the filters with 1× PBS for 10 min at 14,000*g* at 4 °C. Discard the flow-through, add 300 µl of antibody solution and spin at 14,000*g* for 5 min at 4 °C. Discard the flow-through and invert the spin filter in an empty tube. Spin for 6 min at 1,000*g* at 4 °C. Adjust the volume to 100 µl with 1× PBS, and measure the concentration with the NanoDrop spectrophotometer. Keep the antibody on ice. The final concentration should be >1.5 mg/ml.

(ii) Prepare 5 µl of cross-linker solution in 1× PBS so that the final solution after addition of 100 µl of the antibody contains a 10:1 molar ratio of cross-linker to antibody. Incubate the solution for 90 min at 4 °C on a shaker covered in aluminum foil.

(iii) After the antibody–cross-linker reaction is completed, use a Zeba desalting column to remove the linker. Remove the storage solution by centrifugation at 1,500*g* for 1 min at 4 °C. Mark the side where the resin slid up, and perform the subsequent centrifugation steps in the same orientation. Wash the Zeba column with 300 µl of 1× PBS at 1,500*g* for 1 min at 4 °C. Dry the bottom of the column and use a fresh 1.5-ml tube. Add antibody–cross-linker solution to the Zeba column and spin it at 1,500*g* for 2 min at 4 °C. Discard the Zeba column, retain the flow-through and measure the concentration on the NanoDrop spectrophotometer. The antibody concentration should be >1.5 mg/ml.

(iv) Create a 15:1 molar ratio of DNA to antibody and incubate the solution for 1 h at RT on a shaker covered in aluminum foil.

(v) Remove the excess DNA by Amicon spin filtration (100 kDa). For this, wash the filters with 1× PBS for 10 min at 14,000*g* at 4 °C. Discard the flow-through, add antibody-DNA solution, add 300 µl of 1× PBS and spin at 14,000*g* for 5 min at 4 °C. Discard the flow-through and invert the spin filter in an empty tube. Spin for 6 min at 1,000*g* at 4 °C. Adjust the volume to 100 µl with 1× PBS, and measure the concentration with the NanoDrop spectrophotometer. The peak signal should be shifted toward 260 nm from 280 nm, and the concentration should be >5 mg/ml because of the stronger absorbance of DNA.
? TROUBLESHOOTING
■ PAUSE POINT Keep the antibody on ice and store it at 4 °C for a maximum of 6 months.

Immunofixation of cells ● TIMING 2.5 d

▲ CRITICAL In Steps 20–33, we describe procedures for immunofixation optimized for DNA-PAINT super-resolution microscopy. Fixation strategies depend on the target of interest, as well as on the antibody-recognition motifs[57].

20| Seed 30,000 cells in 8-well chambered cover glasses, and let them grow overnight at 37 °C and 5% CO_2 in an incubator.

21| After 24 h, the cells are ready to be fixed.

22| In this step, fixative is added to the cells; this can be performed in two ways: option A, an optimized protocol for maximum preservation of cellular cytoskeletal structures (recommended for imaging microtubules) and option B, a standard protocol.

© 2017 Macmillan Publishers Limited, part of Springer Nature. All rights reserved.

(A) Optimized microtubule fixation

(i) Pre-extract the cells with prewarmed (37 °C for 10 min) pre-extraction buffer for 90 s.

(ii) Remove the extraction buffer and fix the cells for 15 min in prewarmed enhanced microtubule fixative.

(B) Standard fixation

(i) Fix the cells in standard fixative for 15 min.

23| Aspirate the fixative solution and reduce the sample with 1 mg/ml sodium borohydride for 7 min.
▲ **CRITICAL STEP** Sodium borohydride must be prepared just before application to the sample and is very volatile.

24| Wash the chamber four times (1 × 20 s, 3 × 5 min) with 1× PBS at pH 7.2.

25| Block and permeabilize the cell sample in blocking buffer for 90 min at RT.

26| Dilute the primary antibody according to supplier instructions in antibody dilution buffer, and incubate the sample at 4 °C overnight on a rocking platform.

27| Wash the sample three times for 5 min in 1× PBS.

28| Dilute DNA-labeled secondary antibody (5–50 µg/ml) in antibody dilution buffer, and apply it to the sample for 60 min. (Optional) For multiplexing experiments, use different secondary antibodies with orthogonal DNA handles; see **Supplementary Table 2** for recommended sequences.

29| Wash the sample three times for 5 min in 1× PBS.

30| Dilute 90-nm gold particles at a 1:10 ratio in PBS as fiducial markers and incubate for 5 min on the cell sample.

31| Wash the sample three times for 5 min in 1× PBS.

32| Add a target-specific imager solution to the sample.
▲ **CRITICAL STEP** Imager concentration has a critical role in proper acquisition of DNA-PAINT data. The concentration should be adjusted for the target (hence docking strand) density. For microtubules, we recommend starting with a 500 pM imager strand concentration and adjusting as necessary.

33| (Optional) For multiplexed Exchange-PAINT experiments, place the exchange lid with the connected tubing on the chambered cover glass.

Data acquisition ● TIMING 10 min to 10 hours

▲ **CRITICAL** The following section describes the procedure for performing DNA-PAINT experiments using imager sequences labeled with Cy3B fluorophores. As the SNR for DNA-PAINT is rather high, both CCD or sCMOS cameras are suitable for imaging. The procedure is written for use of an iXon Ultra DU-897 EMCCD camera, although electron-multiplying is not necessary. Considerations in regard to acquisition of images with ultra-high resolution are described in **Box 2**. For test purposes, raw DNA-PAINT data can also be simulated *in silico* with 'Picasso: Simulate' (see **Box 3** for procedure details).

34| Place the sample on the microscope stage, and move the objective up until the immersion oil touches the sample.

35| (Optional) For multiplexing with Exchange-PAINT, attach tubing with syringes to the exchange chamber. Consider using an ~15-ml syringe volume of exchange buffer per exchange round for *in situ* exchange experiments, and ~1 ml of exchange buffer per exchange round for *in vitro* experiments. For *in situ* experiments, additionally attach tubing to the chamber inlet. Put the connected syringes into plastic trays to avoid accidental fluid spills. The syringes should be at the same level as the chamber to avoid liquid exchange, as they are communicating vessels.
▲ **CRITICAL STEP** Handle liquids extremely carefully if they are close to the microscope. Improper handling and leakage can lead to damage of delicate microscope components.

36| Start µManager, select the configuration file for the camera and select 'Ok'. The main window of µManager will open.

37| Set 'Exposure [ms]' with regard to the following considerations: exposure times for DNA-PAINT experiments are dependent on the imager length and concentration, the imaging buffer and the docking strand density of the target structure. Typical

© 2017 Macmillan Publishers Limited, part of Springer Nature. All rights reserved.

PROTOCOL

exposure times for 9-bp DNA duplexes are hundreds of milliseconds, and those for 8-bp DNA duplexes are tens of milliseconds, as they have a shorter ON-time. For the samples used in **Figure 1**, an exposure time of 300 ms for *in vitro* (Buffer B+) and 200 ms for *in situ* (Buffer C) samples was used. 'Picasso: Simulate' can be used to determine ideal exposure times for given sample parameters. As a general rule of thumb, camera integration times should be matched to mean ON-times of DNA-PAINT imager/docking duplexes for best performance; these can be experimentally determined using Picasso (see Step 69B). Refer to **Supplementary Table 6** for the acquisition settings used for the images in this protocol.

38| Open 'Tools' > 'Device Property Browser'.

39| Set the camera parameters: set 'Output_Amplifier' to 'Conventional', set 'Region of Interest' to 'Full Image', set 'Frame Transfer' to 'On', set 'PixelType' to '16bit', set 'ReadMode' to 'Image' and set 'Camera shutters' to 'Open'.

40| Click on 'Live' in the main window, and the 'Snap/Live' window will appear. Select 'Autostretch' in the contrast settings. The 'Snap/Live' window should show background noise.

41| Set the laser to a low power density of 0.25 kW/cm^2 at the sample plane (refer to the calibration as performed in the Equipment Setup), and open the laser shutter.
? TROUBLESHOOTING

42| Focus the image.
▲ CRITICAL STEP A focused image should show blinking diffraction-limited spots, each representing the binding and unbinding of an imager strand to its target. Adjust the contrast by dragging the black and white triangles in the 'Contrast' window if needed. For prefocusing, preferably use a focus-lock system such as the Nikon Perfect Focus System or, in case of *in situ* samples, prefocus with the bright-field image.
? TROUBLESHOOTING

43| Increase the laser power to a power density of ~ 2.5 kW/cm^2 at the sample plane.

44| Adjust the laser incident angle. When starting in an epifluorescence configuration, increase the angle until total internal reflection occurs. Continue until no more light is reflected and the signal decreases. Then, go back by decreasing the angle and optimize the SNR. When imaging structures beyond the TIRF illumination range, decrease the incident angle—potentially moving to oblique (HILO) illumination[31]—just until the structure of interest is properly illuminated. Keeping the incident angle as high as possible limits out-of-focus excitation above the target structure, which is particularly critical for DNA-PAINT, as free imager strands in solution increase background and therefore affect imaging quality adversely.

45| In the device manager, adjust the 'Readout Mode' to the frequency with the lowest readout noise possible for the currently selected integration time. This is usually the lowest frequency at which the readout time does not exceed the exposure time. The readout time will be displayed in 'ReadoutTime' and should be shorter than the 'Exposure' time. Please double-check that the field 'ActualInterval-ms', which denotes the true duration between two frames, does not exceed the exposure time.

46| Click on 'Multi-D-Acq.' in the main window to open the 'Multi-Dimensional Acquisition' window. Activate 'Time points' and set the 'Number' to the number of frames to be acquired—e.g., 7,500 for *in vitro* samples and 15,000 for *in situ* samples. These exemplar numbers for total acquisition frames are suggestions for initial experiments and may have to be adjusted according to the specific experiment. For a detailed discussion of optimal acquisition time, refer to Nieuwenhuizen *et al.*[16] and respective sections in the introduction of this protocol.

47| Set the interval to '0' and 'ms'. Set 'Acquisition Order' to 'Time'. Activate 'Save images' and set a destination filename and folder.

48| Select 'Acquire!' to start the acquisition. A live image will pop up. The progress of the acquisition can be followed on the upper left corner.
? TROUBLESHOOTING

49| *(Optional) Multiplexed image acquisition.* There are two methods for performing multiplexed target acquisition with DNA-PAINT. Spectral multiplexing (option A) uses spectrally distinct fluorophores, whereas Exchange-PAINT multiplexing

© 2017 Macmillan Publishers Limited, part of Springer Nature. All rights reserved.

(option B) uses (typically) the same fluorophore attached to orthogonal DNA species that are sequentially supplied to the sample. With Exchange-PAINT, only one species is present in the imager buffer in each multiplexing round, and it will be washed out afterward. Option A provides a relatively fast workflow for imaging multiple targets by imaging in multiple emission channels. Option B has almost no limitation in multiplexing but requires a fluid exchange system. In addition, option B provides the capability of using the most favorable fluorophore for all targets. Refer to **Supplementary Table 7** for a list of dye recommendations for DNA-PAINT.

(A) Spectral multiplexing

(i) Perform Steps 34–48 for the first fluorophore.
▲ **CRITICAL STEP** To reduce photodamage, start acquisition with the dye that has the longest excitation wavelength, and then proceed to those with shorter wavelengths.
(ii) After acquisition of the first imager species, change the laser line and the filter set on the microscope to match the next wavelength.
(iii) Click on 'Live' in the main window of µManager and adjust the TIRF angle if necessary.
(iv) Adjust the file name in the 'Multi-Dimensional Acquisition' window.
(v) Select 'Acquire!' to start a new acquisition.
(iv) (Optional) Repeat the procedure for any other spectrally distinct imager species in solution.

(B) Exchange multiplexing

(i) Perform Steps 34–48 to acquire a movie for the first imager species.
(ii) Click on 'Live' in the main window and adjust the contrast so that individual blinking events are visible. Deselect 'Autostretch'. It is important to keep the contrast to determine when all imagers are washed out.
(iii) Apply several washing steps while observing the 'Live/Snap' window until no more blinking events are visible. One washing step consists of filling the chamber by adding exchange buffer (for *in vitro* imaging use ~180 µl, and for *in situ* imaging use 1 ml) to the inlet and then removing the same volume from the outlet. For *in situ* imaging a total of ~15 ml and for *in vitro* imaging a total of ~1 ml of exchange buffer will be needed per exchange round.
▲ **CRITICAL STEP** Do not remove all liquid from the chamber; it should never dry out. Perform liquid exchange slowly to avoid introducing air bubbles into the chamber or disturbing the sample.
? TROUBLESHOOTING
(iv) After washing, introduce a new imager solution into the chamber. For *in vitro* samples, simply pipette the required amount into the chamber and remove the same amount from the outlet. For *in situ* samples, empty the inlet tubing by disconnecting the empty syringe and pumping air through it. Connect a new 2-ml syringe with a new imager solution and fill the chamber.
(v) While introducing the new imager, the 'Live/Snap' window should show reappearing blinking events.
(vi) Adjust the filename in the 'Multi-Dimensional Acquisition' window.
(vii) Select 'Acquire!' to start a new acquisition.
(viii) (Optional) Repeat the procedure for subsequent imaging rounds.

Image reconstruction ● TIMING 5–30 min

50| *Identification and fitting of single-molecule spots*. In 'Picasso: Localize', open a movie file by dragging the file into the window or by selecting 'File' > 'Open'. If the movie is split into multiple µManager .tif files, open only the first file. Picasso will automatically detect the remaining files according to their file names.

51| Adjust the image contrast (select 'View' > 'Contrast') so that the single-molecule spots are clearly visible.

52| To adjust spot identification and fit parameters, open the 'Parameters' dialog (select 'Analyze' > 'Parameters').

53| In the 'Identification' group, set the 'Box side length' to the rounded integer value of $6 \times \sigma + 1$, where σ is the standard deviation of the PSF. In an optimized microscope setup, σ is one pixel, and the respective 'Box side length' should be set to 7. The value of 'Min. net gradient' specifies a minimum threshold above which spots should be considered for fitting. The net gradient value of a spot is roughly proportional to its intensity, independent of its local background. By checking 'Preview', the spots identified with the current settings will be marked in the displayed frame. Adjust 'Min. net gradient' to a value at which only spots are detected (no background).

54| In the 'Photon conversion' group, adjust 'EM Gain', 'Baseline', 'Sensitivity' and 'Quantum Efficiency' according to your camera specifications and the experimental conditions. Set 'EM Gain' to 1 for conventional output amplification. 'Baseline' is

PROTOCOL

the average dark camera count. 'Sensitivity' is the conversion factor (electrons per analog-to-digital (A/D) count) and 'Quantum Efficiency' should be set according to the average emission wavelength.
▲ CRITICAL STEP These parameters are critical to converting camera counts to photons correctly. The quality of the upcoming maximum likelihood fit strongly depends on a Poisson photon noise model, and thus on the absolute photon count.

For simulated data, generated with 'Picasso: Simulate' as described in **Box 3** and **Figure 7**, set the parameters as follows: 'EM Gain' = 1, 'Baseline' = 0, 'Sensitivity' = 1, 'Quantum Efficiency' = 1.

55| From the menu bar, select 'Analyze' > 'Localize (Identify & Fit)' to start spot identification and fitting in all movie frames. The status of this computation is displayed in the window's status bar. After completion, the fit results will be saved in a new file in the same folder as the movie, in which the filename is the base name of the movie file with the extension '_locs.hdf5'. Furthermore, information about the movie and analysis procedure will be saved in an accompanying file with the extension '_locs.yaml'; this file can be inspected using a text editor.

56| *Rendering of the super-resolution image*: In 'Picasso: Render', open a movie file by dragging a localization file (ending with '.hdf5') into the window or by selecting 'File' > 'Open'. The super-resolution image will be rendered automatically. A region of choice can be zoomed into by a rectangular selection using the left mouse button. The 'View' menu contains more options for zooming and panning.

57| (Optional) Adjust rendering options by selecting 'View' > 'Display Settings'. The field 'Oversampling' defines the number of super-resolution pixels per camera pixel. The contrast settings 'Min. Density' and 'Max. Density' define at which number of localizations per super-resolution pixel the minimum and maximum color of the colormap should be applied.

58| (Optional) For multiplexed image acquisition, open HDF5 localization files from other channels subsequently. Alternatively, drag and drop all HDF5 files to be displayed simultaneously.

Image post-processing: drift correction ● TIMING seconds to minutes
59| Picasso offers two procedures to correct for drift: an RCC algorithm[66] (option A), and use of specific structures in the image as drift markers[23] (option B). Although option A does not require any additional sample preparation, option B depends on the presence of either fiducial markers or inherently clustered structures in the image. On the other hand, option B often supports more precise drift estimation and thus allows for higher image resolution. To achieve the highest possible resolution (ultra-resolution), we recommend consecutive applications of option A and multiple rounds of option B. The drift markers for option B can be features of the image itself (e.g., protein complexes or DNA origami) or intentionally included markers (e.g., DNA origami or gold nanoparticles). When using DNA origami as drift markers, the correction is typically applied in two rounds: first, with whole DNA origami structures as markers, and, second, using single DNA-PAINT binding sites as markers. In both cases, the precision of drift correction strongly depends on the number of selected drift markers.

(A) Redundant cross-correlation drift correction

(i) In 'Picasso: Render', select 'Postprocess' > 'Undrift by RCC'.
(ii) A dialog will appear asking for the segmentation parameter. Although the default value, 1,000 frames, is a sensible choice for most movies, it might be necessary to adjust the segmentation parameter of the algorithm, depending on the total number of frames in the movie and the number of localizations per frame[66]. A smaller segment size results in better temporal drift resolution but requires a movie with more localizations per frame.
(iii) After the algorithm finishes, the estimated drift will be displayed in a pop-up window and the display will show the drift-corrected image.

(B) Marker-based drift correction

(i) In 'Picasso: Render', pick drift markers as described in Steps 61–64. Use the 'Pick similar' option (Step 65) to automatically detect a large number of drift markers similar to a few manually selected ones.
▲ CRITICAL STEP If the structures used as drift markers have an intrinsic size larger than the precision of individual localizations (e.g., DNA origami, large protein complexes), it is critical to select a large number of structures. Otherwise, the statistic for calculating the drift in each frame (the mean displacement of localization to the structure's center of mass) is not valid.
(ii) Select 'Postprocess; > 'Undrift from picked' to compute and apply the drift correction.

60| (Optional) Save the drift-corrected localizations by selecting 'File' > 'Save localizations'.

© 2017 Macmillan Publishers Limited, part of Springer Nature. All rights reserved.

Picking of regions of interest ● TIMING **5–30 min**

61| *Manual selection*. Open 'Picasso: Render' and load the localization HDF5 file to be processed.

62| Switch the active tool by selecting 'Tools' > 'Pick'. The mouse cursor will now change to a circle.

63| Set the size of the pick circle by adjusting the 'Diameter' field in the tool settings dialog ('Tools' > 'Tools Settings').

64| Pick regions of interest using the circular mouse cursor by clicking the left mouse button. All localizations within the circle will be selected for further processing.

65| *(Optional) Automated region of interest selection*. Select 'Tools' > 'Pick similar' to automatically detect and pick structures that have similar numbers of localizations and RMS deviation (RMSD) from their center of mass than already-picked structures. The upper and lower thresholds for these similarity measures are the respective standard deviations of already-picked regions, scaled by a tunable factor. This factor can be adjusted using the field 'Tools' > 'Tools Settings' > 'Pick similar ± range'. To display the mean and standard deviation of localization number and RMSD for currently picked regions, select 'View' > 'Show info' and click 'Calculate info below'.

66| *(Optional) Exporting of pick information*. All localizations in picked regions can be saved by selecting 'File' > 'Save picked localizations'. The resulting HDF5 file will contain a new integer column 'group' indicating to which pick each localization is assigned.

67| (Optional) Statistics about each pick region can be saved by selecting 'File' > 'Save pick properties'. The resulting HDF5 file is not a localization file. Instead, it holds a data set called 'groups' in which the rows show statistical values for each pick region.

68| (Optional) The picked positions and diameter itself can be saved by selecting 'File' > 'Save pick regions'. Such saved pick information can also be loaded into 'Picasso: Render' by selecting 'File' > 'Load pick regions'.

Additional post-processing steps

69|Depending on the experimental goals, a variety of post-processing steps may be used. To filter localizations based on their properties, for example to remove localizations below a certain photon threshold, use option A. For investigating the statistics of DNA-PAINT binding kinetics and how to count DNA-PAINT binding sites with qPAINT[22], use options B and C, respectively. Option D describes the procedure to generate an average image of multiple structures. Finally, option E describes the procedure to align images from multiplexed experiments.

(A) Filtering of localizations ● TIMING **5–10 min**

(i) Open a localization HDF5 file in 'Picasso: Filter' by dragging it into the main window or by selecting 'File' > 'Open'. The displayed table shows the properties of each localization in rows. Each column represents one property (e.g., coordinates, number of photons); see the **Supplementary Manual** for details.

(ii) To display a histogram from values of one property, select the respective column in the header and select 'Plot' > 'Histogram' (Ctrl + h). 2D histograms can be displayed by selecting two columns (press Ctrl to select multiple columns) and then selecting 'Plot' > '2D Histogram' (Ctrl + d).

(iii) Left-click and hold the mouse button down to drag a selection area in a 1D or 2D histogram. The selected area will be shaded in green, as shown in **Supplementary Figure 5b**,**c**. Each localization event with histogram properties outside the selected area is immediately removed from the localization list.

(iv) Save the filtered localization table by selecting 'File' > 'Save'.

(B) Analysis of blinking kinetics ● TIMING **5–60 min**

(i) In 'Picasso: Render', pick regions of interest as described in Steps 61–65.

(ii) Select 'View' > 'Show info'.

(iii) In the opened dialog, click 'Calculate info below'. The mean and standard deviation per pick of several values will be calculated and displayed. The 'Length' row describes the blinking 'ON' time (τ_b) and the 'Dark time' row describes the blinking 'OFF' time (τ_d).

(iv) Click 'Histograms' to open a new window showing histograms for the picked region's kinetics.

(v) (Optional) Individual values for each picked region can be obtained by exporting the data. Select 'File' > 'Save pick properties'. The saved HDF5 file will contain a data set called 'groups', in which each row corresponds to one pick region.

PROTOCOL

(C) Counting of molecule numbers with qPAINT ● TIMING 5–60 min

(i) In 'Picasso: Render', pick calibration regions as described in Steps 61–64. Typically, calibration regions are regions with a known number of binding sites. Do not use the option 'Pick similar' (Step 65), as this may bias the calibration.

(ii) Select 'View' > 'Show info' and click 'Calculate info below'.

(iii) Set '# Units per pick' to the number of units to which the counting should be calibrated. Typically, one unit is equal to one DNA-PAINT binding site, but other user-defined units might be suitable too. This could, i.e., be useful in the case in which calibration is performed on single antibodies, which can carry multiple docking strands for protein quantification using qPAINT. The final counting result will be reported in number of units. For example, if the calibration regions contain 12 binding sites and the counting result should be reported in 'number of binding sites', then '# Units per pick' should be to be set to 12.

(iv) Click 'Calibrate influx' for an estimation of the influx rate from the calibration regions kinetics. The influx rate will be displayed in the respective field. As an alternative to the experimental calibration, the influx rate (ξ) can be theoretically calculated via $\xi = k_{on} \times c$ if the ON rate (k_{on}) and imager concentration (c) are known. In that case, enter the influx rate manually into the respective field.

(v) Select 'Tools' > 'Clear picks' to remove the calibration pick selections.

(vi) Pick structures of interest (Steps 61–65) from which the unknown number of units should be determined.

(vii) In the 'Info' dialog, click 'Calculate info below'. The mean number of units per picked region will be displayed in the '# Units' row, as calculated from the currently displayed influx rate.

(viii) (Optional) The individual number of units for each picked region can be obtained by exporting pick property data. Select 'File' > 'Save pick properties'. The saved HDF5 file will contain a data set called 'groups', which holds statistics about each pick region as rows, including a column for the unit number ('n_units').

(D) Particle averaging ● TIMING 10–30 min

(i) In 'Picasso: Render', pick structures to be averaged as in Steps 61–65.

(ii) Save the picked localizations by selecting 'File' > 'Save picked localizations'.

(iii) Load the resulting file with picked localizations into 'Picasso: Average' by selecting 'File' > 'Open' or dragging and dropping it into the window.

(iv) 'Picasso: Average' will immediately perform a translational alignment of the picked structures and display an average image. Rotational and refined translational alignment will follow in the next steps.

(v) Select 'Process' > 'Parameters' and adjust the 'Oversampling' parameter. We recommend choosing the highest number at which the average image still appears smooth. High oversampling values result in substantial computational time. Hence, it might be useful to first use low oversampling to generate a less-refined average image and perform a second averaging step with higher oversampling for optimized resolution.

(vi) Adjust the number of average iterations in the 'Iterations' field. In most cases, a value of 10 is more than sufficient. If you are unsure about the computational time of the process, choose one iteration as a starting point. More iterations can be added later by repeating the processing steps. After a certain number of iterations, the average image will converge, meaning that it will not change with more iterations.

(vii) Select 'Process' > 'Average' to perform particle averaging with the current oversampling for the set number of iterations. This step can be repeated with different settings. The program will use the current average image as a starting point.

(viii) Once the average image has converged, save the transformed localizations by selecting 'File' > 'Save'. The resulting HDF5 localization file contains the aligned localizations in the center of the movie dimensions. It can be loaded like any other HDF5 localization file into 'Picasso: Render'.

(E) Aligning of channels from multiplexed experiments ● TIMING 5–10 min

(i) To align images from multiplexed data acquisition, the images need to share some features as reference points. Such reference features can be the cell shape for *in situ* images (typically, background is higher inside the cell) or overlapping clusters (for example, on the same DNA origami). If alignment results are ambiguous or not satisfying because of the lack of inherent reference features, drift or alignment markers should be included and imaged in all channels.

(ii) In 'Picasso: Render' display all HDF5 localization files to be aligned.

(iii) (Optional) If the reference features are too weak to create proper alignment, they can be selected manually, as described in Steps 61–65. Ensure that within a picked region the reference structures of all channels are included.

(iv) Select 'Postprocess' > 'Align'.

(v) (Optional) Export the aligned localizations by selection 'File' > 'Save localizations'.

? TROUBLESHOOTING

Troubleshooting advice can be found in **Table 1**.

© 2017 Macmillan Publishers Limited, part of Springer Nature. All rights reserved.

TABLE 1 | Troubleshooting table.

Steps	Problem	Possible reason	Solution
Sample preparation			
Step 17	There is no band visible on the gel	Depending on the used final scaffold concentration, the bands can appear very faint on the blue-light transilluminator table and seem difficult to excise	To improve brightness of the sample band, use a more sensitive DNA stain such as SYBR Gold, or increase scaffold concentration
	The structure does not fold	Thermal gradients have an important role during the assembly process of DNA nanostructures. However, the rectangle 2D origami design shows extremely robust folding behavior and forms with high yield within ~75 min	Different temperature gradients between 15 and 72 h can be used to improve folding performance. Prepare fresh staple stocks for the origami structure with particular focus on correct magnesium concentration and staple excess
Step 18A(ix), 18B(viii)	There are not enough DNA origami structures on the surface	Depending on the purification method, different origami concentrations are obtained—e.g., the size of the excised gel band will influence the concentration after the Freeze 'N Squeeze column purification step	Compensate for this by incubating with a higher origami concentration and/or increased incubation time. Concentration adjustment can be estimated by counting the number of targets on the surface and interpolating to the desired density. A good sample density can be achieved by incubation with 125–500 pM of origami. Typical concentrations after gel purification are between 1 and 2 nM, and those after PEG purification are approximately 8–10 nM. Alternatively, the DNA origami solution can be incubated longer (up to 45 min)
Step 19A(viii), 19B(v)	After purification, there still seem to be free DNA strands in solution	The DNA strands might not be completely filtered out by the spin columns, which are optimized for protein concentration	For further purification of DNA-labeled antibodies, use size-exclusion column chromatography to remove the free DNA (with a Superdex 75/200)
	Not enough DNA strands are attached to the antibodies	Not enough cross-linker or DNA was used	For more DNA handles attached to the antibodies, use larger excess of cross-linker (40×) and DNA (30×). However, please note that an increased DNA-to-antibody ratio might lead to reduced binding affinity of antibodies or increased off-target binding
Data acquisition			
Step 41	Poor data quality	Laser power not adjusted to sample	To achieve the best possible data quality, it is important to extract the largest possible number of photons from a single binding (blinking) event of the fluorophores. A good indicator of a suitable laser power setting can be estimated by measuring the bright time versus laser power. Increase laser power until the bright time decreases. What happens is that imager strands start to bleach while they are still bound to docking strands. This should be the upper limit of your laser power setting. When a laser power meter is available, a good reference value for power densities in DNA-PAINT experiments using, i.e., Cy3B as dye and 561-nm laser excitation is 1–6 kW/cm^2
Step 42	The focal plane is difficult to find	Focusing was not performed in bright-field mode, or the immersion oil was not in contact with the cover glass.	For cellular samples, focusing should be performed in bright-field. For DNA nanostructures, the immersion oil on the objective should touch the cover glass; use oblique illumination and then slowly raise the objective until the surface of the cover glass is reached. Monitor the approach in 'Live' mode. Reaching the cover glass will be visible via an increase in fluorescence and appearance of diffraction-limited blinking spots. Add fluorescent beads that have increased brightness to find the focal plane, if necessary

(continued)

PROTOCOL

TABLE 1 | Troubleshooting table (continued).

Steps	Problem	Possible reason	Solution
Step 48	The sample drifts in xy and/or focus is lost during image acquisition	Setup not equilibrated	Before image acquisition, allow the sample to 'equilibrate' on the microscope for 5–15 min. Adjust room temperature to maintain a constant ambient temperature to avoid additional thermal drift of microscope and stage components
Step 49B(iii)	The imager strands are difficult to wash away	Cellular samples are highly cross-linked through the fixation process. Imager strands might be trapped in the cross-linked network	We recommend incubating with the washing solution for 3 min so that the imager strands can diffuse into the large reservoir. In addition, washing with gentle flow can be effective
Box 3, step 6	The simulation of a DNA-PAINT data set takes a long time	The time required to simulate data sets is dependent on the number of structures, imager concentration, frames and image size	As computation time increases with image size, it is recommended to avoid exceeding an image size of 64 × 64 pixels. A simulation with the standard settings should take <1 min on the described analysis computer

● TIMING

Steps 1–5, design of DNA nanostructures: 1 h
Steps 6–9, folding of DNA nanostructures: 6–7 h
Steps 10–17, purification of DNA nanostructures: ~3.5 h
Step 18, preparation of DNA origami for DNA-PAINT imaging: 45 min
Step 19A, preparation of DNA-labeled antibodies using maleimide-PEG2-succinimidyl ester: 1 d and 1 h
Step 19B, labeling via DBCO-sulfo-NHS ester: 4 h
Steps 20–33, immunofixation of cells: 2.5 d
Steps 34–49, data acquisition: 10 min to 10 h; for each multiplexing round ~20 min–2 h
Steps 50–58, image reconstruction: 5–30 min
Steps 59 and 60, drift correction: seconds to minutes
Steps 61–68, picking of regions of interest: 5–30 min
Step 69A, filtering of localizations: 5–10 min
Step 69B, analysis of blinking kinetics with qPAINT: 5–60 min
Step 69C, counting of molecule numbers with qPAINT: 5–60 min
Step 69D, particle averaging: 10–30 min
Step 69E, aligning of channels for multiplexed experiments: 5–10 min
Box 1, construction of a fluid exchange chamber for *in situ* imaging: 30 min
Box 2, ultra-resolution imaging: ~7 h
Box 3, *in silico* simulation of DNA-PAINT: 10–60 min

ANTICIPATED RESULTS

Examples of single-color DNA-PAINT super-resolution images can be found in **Figure 1**. Panel **b** presents an image of a DNA origami with a three-by-four grid of binding sites, as designed with 'Picasso: Design'. Measured distances between individual binding sites are in good agreement with the designed origami. Panels **d** and **e** show a DNA-PAINT image of microtubules *in situ*, immunolabeled with primary and secondary antibodies. Hollow microtubule structures, observed here as two parallel lines because of the 2D projection, are characteristic for a high labeling density and localization precision.

Expected results for multiplexed DNA-PAINT experiments by Exchange-PAINT are shown in **Figure 2**. Panels **d**, **e** and **f** show *in vitro* DNA origami imaged with multiple 'Exchange' rounds before (**d**) and after (**e**,**f**) alignment. The image after alignment shows that the DNA nanostructure is in good agreement with the designed pattern of binding sites. *In situ* Exchange-PAINT images of microtubules and Tom20, which localizes to mitochondria, are shown in panel **g**. The inset in panel **g** shows gold particles imaged in both rounds and demonstrates the alignment steps for the two images. The gold particles colocalize after the alignment procedure, and the different channels do not comprise any cross talk between them.

Results for counting DNA-PAINT binding sites via quantitative PAINT (qPAINT) can be found in **Figure 3**. Visual inspection of individual origami structures shows they match the predicted binding sites from the qPAINT analysis.

Expected results for ultra-resolution imaging, including the intermediate steps for drift correction and a final image from averaging multiple structures, can be seen in **Figure 4**. Key features of a successful ultra-resolution experiment are very high NeNA localization precision (~1 to 1.5 nm) and the ability to visually separate individual binding sites spaced 5 nm apart on the origami structures.

Note: Any Supplementary Information and Source Data files are available in the online version of the paper.

ACKNOWLEDGMENTS We thank B. Rieger, S.S. Agasti, S. Strauss, D. Haas, J.B. Woehrstein and E. Woehrstein for helpful discussions. This work was supported by the German Research Foundation (DFG) through an Emmy Noether Fellowship (DFG JU 2957/1-1), the European Research Council (ERC) through an ERC Starting Grant (MolMap, grant agreement no. 680241), the Max Planck Society, the Max Planck Foundation and the Center for Nanoscience (CeNS). M.T.S. acknowledges support from the International Max Planck Research School for Molecular and Cellular Life Sciences (IMPRS-LS). T.S. acknowledges support from the DFG through the Graduate School of Quantitative Biosciences Munich (QBM). F.S. acknowledges support from the DFG through the SFB 1032 (Nanoagents for the spatiotemporal control of molecular and cellular reactions).

AUTHOR CONTRIBUTIONS J.S. and M.T.S. contributed equally to this work. J.S. designed and developed the Picasso software suite. M.T.S. developed 'Picasso: Design' and 'Simulate' and performed *in vitro* experiments. T.S. developed antibody labeling strategies and performed *in situ* experiments. F.S. performed ultra-resolution experiments. R.J. conceived the study and supervised the project. All authors contributed to the writing of the manuscript.

COMPETING FINANCIAL INTERESTS The authors declare competing financial interests: details are available in the online version of the paper.

1. Gustafsson, M.G.L. Nonlinear structured-illumination microscopy: wide-field fluorescence imaging with theoretically unlimited resolution. *Proc. Natl. Acad. Sci. USA* **102**, 13081–13086 (2005).
2. Hell, S.W. & Wichmann, J. Breaking the diffraction resolution limit by stimulated emission: stimulated-emission-depletion fluorescence microscopy. *Opt. Lett.* **19**, 780–782 (1994).
3. Betzig, E. *et al.* Imaging intracellular fluorescent proteins at nanometer resolution. *Science* **313**, 1642–1645 (2006).
4. Hess, S.T., Girirajan, T.P.K. & Mason, M.D. Ultra-high resolution imaging by fluorescence photoactivation localization microscopy. *Biophys. J.* **91**, 4258–4272 (2006).
5. Rust, M.J., Bates, M. & Zhuang, X. Sub-diffraction-limit imaging by stochastic optical reconstruction microscopy (STORM). *Nat. Methods* **3**, 793–795 (2006).
6. Heilemann, M. *et al.* Subdiffraction-resolution fluorescence imaging with conventional fluorescent probes. *Angew. Chem. Int. Ed. Engl.* **47**, 6172–6176 (2008).
7. Hell, S.W. Far-field optical nanoscopy. *Science* **316**, 1153–1158 (2007).
8. Sengupta, P. *et al.* Probing protein heterogeneity in the plasma membrane using PALM and pair correlation analysis. *Nat. Methods* **8**, 969–975 (2011).
9. Xu, K., Zhong, G. & Zhuang, X. Actin, spectrin, and associated proteins form a periodic cytoskeletal structure in axons. *Science* **339**, 452–456 (2012).
10. Honigmann, A. *et al.* Phosphatidylinositol 4,5-bisphosphate clusters act as molecular beacons for vesicle recruitment. *Nat. Struct. Mol. Biol.* **20**, 679–686 (2013).
11. Li, D. *et al.* ADVANCED IMAGING. Extended-resolution structured illumination imaging of endocytic and cytoskeletal dynamics. *Science* **349**, aab3500 (2015).
12. Galiani, S. *et al.* Super-resolution microscopy reveals compartmentalization of peroxisomal membrane proteins. *J. Biol. Chem.* **291**, 16948–16962 (2016).
13. Hell, S.W. *et al.* The 2015 super-resolution microscopy roadmap. *J. Phys. D Appl. Phys.* **48**, 443001 (2015).
14. Huang, B., Bates, M. & Zhuang, X. Super-resolution fluorescence microscopy. *Annu. Rev. Biochem.* **78**, 993–1016 (2009).
15. Lippincott-Schwartz, J., Jennifer, L.-S. & Patterson, G.H. Photoactivatable fluorescent proteins for diffraction-limited and super-resolution imaging. *Trends Cell Biol.* **19**, 555–565 (2009).
16. Nieuwenhuizen, R.P.J. *et al.* Measuring image resolution in optical nanoscopy. *Nat. Methods* **10**, 557–562 (2013).
17. Sharonov, A. & Hochstrasser, R.M. Wide-field subdiffraction imaging by accumulated binding of diffusing probes. *Proc. Natl. Acad. Sci. USA* **103**, 18911–18916 (2006).
18. Giannone, G. *et al.* Dynamic superresolution imaging of endogenous proteins on living cells at ultra-high density. *Biophys. J.* **99**, 1303–1310 (2010).
19. Jungmann, R. *et al.* Single-molecule kinetics and super-resolution microscopy by fluorescence imaging of transient binding on DNA origami. *Nano Lett.* **10**, 4756–4761 (2010).
20. Jungmann, R. *et al.* Multiplexed 3D cellular super-resolution imaging with DNA-PAINT and Exchange-PAINT. *Nat. Methods* **11**, 313–318 (2014).
21. Iinuma, R. *et al.* Polyhedra self-assembled from DNA tripods and characterized with 3D DNA-PAINT. *Science* **344**, 65–69 (2014).
22. Jungmann, R. *et al.* Quantitative super-resolution imaging with qPAINT. *Nat. Methods* **13**, 439–442 (2016).
23. Dai, M., Jungmann, R. & Yin, P. Optical imaging of individual biomolecules in densely packed clusters. *Nat. Nanotechnol.* **11**, 798–807 (2016).
24. Schlichthaerle, T., Strauss, M.T., Schueder, F., Woehrstein, J.B. & Jungmann, R. DNA nanotechnology and fluorescence applications. *Curr. Opin. Biotechnol.* **39**, 41–47 (2016).
25. Agasti, S. *et al.* DNA-barcoded labeling probes for highly multiplexed Exchange-PAINT imaging. *Chem. Sci.* (2017) http://dx.doi.org/10.1039/c6sc05420j.
26. Rasnik, I., McKinney, S.A. & Ha, T. Nonblinking and long-lasting single-molecule fluorescence imaging. *Nat. Methods* **3**, 891–893 (2006).
27. Aitken, C.E., Marshall, R.A. & Puglisi, J.D. An oxygen scavenging system for improvement of dye stability in single-molecule fluorescence experiments. *Biophys. J.* **94**, 1826–1835 (2008).
28. Ha, T. & Tinnefeld, P. Photophysics of fluorescent probes for single-molecule biophysics and super-resolution imaging. *Annu. Rev. Phys. Chem.* **63**, 595–617 (2012).
29. Ries, J., Kaplan, C., Platonova, E., Eghlidi, H. & Ewers, H. A simple, versatile method for GFP-based super-resolution microscopy via nanobodies. *Nat. Methods* **9**, 582–584 (2012).
30. Opazo, F. *et al.* Aptamers as potential tools for super-resolution microscopy. *Nat. Methods* **9**, 938–939 (2012).
31. Tokunaga, M., Imamoto, N. & Sakata-Sogawa, K. Highly inclined thin illumination enables clear single-molecule imaging in cells. *Nat. Methods* **5**, 159–161 (2008).
32. Legant, W.R. *et al.* High-density three-dimensional localization microscopy across large volumes. *Nat. Methods* **13**, 359–365 (2016).
33. Rothemund, P.W.K. Folding DNA to create nanoscale shapes and patterns. *Nature* **440**, 297–302 (2006).
34. Seeman, N.C. Nucleic acid junctions and lattices. *J. Theor. Biol.* **99**, 237–247 (1982).
35. Seeman, N.C. An overview of structural DNA nanotechnology. *Mol. Biotechnol.* **37**, 246–257 (2007).
36. Douglas, S.M. *et al.* Rapid prototyping of 3D DNA-origami shapes with caDNAno. *Nucleic Acids Res.* **37**, 5001–5006 (2009).
37. Benson, E. *et al.* DNA rendering of polyhedral meshes at the nanoscale. *Nature* **523**, 441–444 (2015).
38. Kim, D.-N., Kilchherr, F., Dietz, H. & Bathe, M. Quantitative prediction of 3D solution shape and flexibility of nucleic acid nanostructures. *Nucleic Acids Res.* **40**, 2862–2868 (2012).
39. Douglas, S.M. *et al.* Self-assembly of DNA into nanoscale three-dimensional shapes. *Nature* **459**, 414–418 (2009).
40. Martin, T.G. & Dietz, H. Magnesium-free self-assembly of multi-layer DNA objects. *Nat. Commun.* **3**, 1103 (2012).
41. Sobczak, J.-P.J., Martin, T.G., Gerling, T. & Dietz, H. Rapid folding of DNA into nanoscale shapes at constant temperature. *Science* **338**, 1458–1461 (2012).
42. Bellot, G., Gaëtan, B., McClintock, M.A., Chenxiang, L. & Shih, W.M. Recovery of intact DNA nanostructures after agarose gel–based separation. *Nat. Methods* **8**, 192–194 (2011).
43. Lin, C., Perrault, S.D., Kwak, M., Graf, F. & Shih, W.M. Purification of DNA-origami nanostructures by rate-zonal centrifugation. *Nucleic Acids Res.* **41**, e40 (2013).
44. Stahl, E., Martin, T.G., Praetorius, F. & Dietz, H. Facile and scalable preparation of pure and dense DNA origami solutions. *Angew. Chem. Int. Ed. Engl.* **53**, 12735–12740 (2014).
45. Steinhauer, C., Jungmann, R., Sobey, T.L., Simmel, F.C. & Tinnefeld, P. DNA origami as a nanoscopic ruler for super-resolution microscopy. *Angew. Chem. Int. Ed. Engl.* **48**, 8870–8873 (2009).
46. Schmied, J.J. *et al.* DNA origami–based standards for quantitative fluorescence microscopy. *Nat. Protoc.* **9**, 1367–1391 (2014).
47. Dean, K.M. & Palmer, A.E. Advances in fluorescence labeling strategies for dynamic cellular imaging. *Nat. Chem. Biol.* **10**, 512–523 (2014).

© 2017 Macmillan Publishers Limited, part of Springer Nature. All rights reserved.

PROTOCOL

48. Dempsey, G.T., Vaughan, J.C., Chen, K.H., Bates, M. & Zhuang, X. Evaluation of fluorophores for optimal performance in localization-based super-resolution imaging. *Nat. Methods* **8**, 1027–1036 (2011).
49. Mikhaylova, M. *et al.* Resolving bundled microtubules using anti-tubulin nanobodies. *Nat. Commun.* **6**, 7933 (2015).
50. Los, G.V. *et al.* HaloTag: a novel protein labeling technology for cell imaging and protein analysis. *ACS Chem. Biol.* **3**, 373–382 (2008).
51. Keppler, A., Pick, H., Arrivoli, C., Vogel, H. & Johnsson, K. Labeling of fusion proteins with synthetic fluorophores in live cells. *Proc. Natl. Acad. Sci. USA* **101**, 9955–9959 (2004).
52. Wang, L., Xie, J. & Schultz, P.G. Expanding the genetic code. *Annu. Rev. Biophys. Biomol. Struct.* **35**, 225–249 (2006).
53. Schweller, R.M. *et al.* Multiplexed *in situ* immunofluorescence using dynamic DNA complexes. *Angew. Chem. Int. Ed. Engl.* **51**, 9292–9296 (2012).
54. Ullal, A.V. *et al.* Cancer cell profiling by barcoding allows multiplexed protein analysis in fine-needle aspirates. *Sci. Transl. Med.* **6**, 219ra9 (2014).
55. Gong, H. *et al.* Simple method to prepare oligonucleotide-conjugated antibodies and its application in multiplex protein detection in single cells. *Bioconjug. Chem.* **27**, 217–225 (2016).
56. Xu, K., Babcock, H.P. & Zhuang, X. Dual-objective STORM reveals three-dimensional filament organization in the actin cytoskeleton. *Nat. Methods* **9**, 185–188 (2012).
57. Whelan, D.R. & Bell, T.D.M. Image artifacts in single molecule localization microscopy: why optimization of sample preparation protocols matters. *Sci. Rep.* **5**, 7924 (2015).
58. Edelstein, A.D. *et al. J. Biol. Methods* **1**, 10 (2014).
59. Beier, H.T. & Ibey, B.L. Experimental comparison of the high-speed imaging performance of an EM-CCD and sCMOS camera in a dynamic live-cell imaging test case. *PLoS One* **9**, e84614 (2014).
60. Huang, F. *et al.* Video-rate nanoscopy using sCMOS camera–specific single-molecule localization algorithms. *Nat. Methods* **10**, 653–658 (2013).
61. Shroff, H., Galbraith, C.G., Galbraith, J.A. & Betzig, E. Live-cell photoactivated localization microscopy of nanoscale adhesion dynamics. *Nat. Methods* **5**, 417–423 (2008).
62. Venkataramani, V., Herrmannsdörfer, F., Heilemann, M. & Kuner, T. SuReSim: simulating localization microscopy experiments from ground truth models. *Nat. Methods* **13**, 319–321 (2016).
63. Sage, D. *et al.* Quantitative evaluation of software packages for single-molecule localization microscopy. *Nat. Methods* **12**, 717–724 (2015).
64. Smith, C.S., Joseph, N., Rieger, B. & Lidke, K.A. Fast, single-molecule localization that achieves theoretically minimum uncertainty. *Nat. Methods* **7**, 373–375 (2010).
65. Egner, A. *et al.* Fluorescence nanoscopy in whole cells by asynchronous localization of photoswitching emitters. *Biophys. J.* **93**, 3285–3290 (2007).
66. Wang, Y. *et al.* Localization events-based sample drift correction for localization microscopy with redundant cross-correlation algorithm. *Opt. Express* **22**, 15982–15991 (2014).
67. Endesfelder, U., Malkusch, S., Fricke, F. & Heilemann, M. A simple method to estimate the average localization precision of a single-molecule localization microscopy experiment. *Histochem. Cell Biol.* **141**, 629–638 (2014).
68. Lin, C. *et al.* Submicrometre geometrically encoded fluorescent barcodes self-assembled from DNA. *Nat. Chem.* **4**, 832–839 (2012).
69. Bates, M., Huang, B., Dempsey, G.T. & Zhuang, X. Multicolor super-resolution imaging with photo-switchable fluorescent probes. *Science* **317**, 1749–1753 (2007).
70. Huang, B., Jones, S.A., Brandenburg, B. & Zhuang, X. Whole-cell 3D STORM reveals interactions between cellular structures with nanometer-scale resolution. *Nat. Methods* **5**, 1047–1052 (2008).
71. Shin, J.Y. *et al.* Visualization and functional dissection of coaxial paired SpoIIIE channels across the sporulation septum. *Elife* **4** (2015).
72. Puchner, E.M., Walter, J.M., Kasper, R., Huang, B. & Lim, W.A. Counting molecules in single organelles with superresolution microscopy allows tracking of the endosome maturation trajectory. *Proc. Natl. Acad. Sci. USA* **110**, 16015–16020 (2013).
73. Lee, S.-H., Shin, J.Y., Lee, A. & Bustamante, C. Counting single photoactivatable fluorescent molecules by photoactivated localization microscopy (PALM). *Proc. Natl. Acad. Sci. USA* **109**, 17436–17441 (2012).
74. Rollins, G.C., Shin, J.Y., Bustamante, C. & Pressé, S. Stochastic approach to the molecular counting problem in superresolution microscopy. *Proc. Natl. Acad. Sci. USA* **112**, E110–8 (2015).
75. Nieuwenhuizen, R.P.J. *et al.* Quantitative localization microscopy: effects of photophysics and labeling stoichiometry. *PLoS One* **10**, e0127989 (2015).
76. Sengupta, P., Jovanovic-Talisman, T. & Lippincott-Schwartz, J. Quantifying spatial organization in point-localization superresolution images using pair correlation analysis. *Nat. Protoc.* **8**, 345–354 (2013).
77. Juette, M.F. *et al.* Three-dimensional sub-100 nm resolution fluorescence microscopy of thick samples. *Nat. Methods* **5**, 527–529 (2008).
78. Broeken, J. *et al.* Resolution improvement by 3D particle averaging in localization microscopy. *Methods Appl. Fluoresc.* **3**, 014003 (2015).
79. Cheng, Y., Yifan, C., Nikolaus, G., Penczek, P.A. & Thomas, W. A primer to single-particle cryo-electron microscopy. *Cell* **161**, 438–449 (2015).
80. Szymborska, A. *et al.* Nuclear pore scaffold structure analyzed by super-resolution microscopy and particle averaging. *Science* **341**, 655–658 (2013).
81. Loschberger, A. *et al.* Super-resolution imaging visualizes the eightfold symmetry of gp210 proteins around the nuclear pore complex and resolves the central channel with nanometer resolution. *J. Cell Sci.* **125**, 570–575 (2012).
82. Penczek, P., Radermacher, M. & Frank, J. Three-dimensional reconstruction of single particles embedded in ice. *Ultramicroscopy* **40**, 33–53 (1992).
83. Perrault, S.D. & Chan, W.C.W. Synthesis and surface modification of highly monodispersed, spherical gold nanoparticles of 50-200 nm. *J. Am. Chem. Soc.* **131**, 17042–17043 (2009).

3.2 SIMULATION OF SINGLE MOLECULE FLUORESCENCE DATA

In the previous chapter, I introduced the DNA-PAINT protocol and the software package Picasso. In the following section, I will present the fundamentals of the simulation module of Picasso.
The simulation of single-molecule fluorescence data from a known ground-truth allows straightforward benchmarking and feasibility analysis of experiments. In recent years, several simulation packages have been developed for use in super-resolution microscopy, notably SuReSim [48], TestStorm [49] and the SOFI Simulation Tool [50], that are specifically targeted for optimization purposes such as understanding imaging parameters and interpret imaging artifacts.

- **SuReSim** starts from ground-truth structure data and allows to either simulate 3D localizations or raw movie stacks to explore how changing experimental parameters can affect potential imaging outcomes.
- **TestStorm** is a MATLAB based simulation software for the generation of test data stacks. It contains advanced physical models such as scalar and vector-based point spread functions, polarization sensitive detection, drift, spectral crosstalk and structured background.
- **SOFI Simulation Tool** is intended as a simple qualitative comparison of simulated super-resolution optical fluctuation imaging (SOFI) images. It incorporates SOFI and STORM algorithms and displays and describes the SOFI image processing steps in a tutorial-like fashion.

In principle, all software packages use the same fundamental approach for simulating fluorescence data - Monte Carlo methods. In the following section, we will discuss how they can be used as a tool for performing experiments *in silico* and how they are implemented in the simulation module in the Picasso software package.

3.2.1 *The Monte Carlo method*

Kroese et al. define a Monte Carlo simulation as *the generation of random objects or processes by means of a computer* that in many cases *simply involves random sampling from certain probability distributions* [51].
An illustrative way on how Monte Carlo methods or random sampling can be used to solve problems numerically is the approximation of π. Here, a widely used example solves this problem geometrically by drawing random X, Y values in the range of $[0, 1]$ that define points in the XY-Plane. These points will be randomly distributed in a unit

square. By defining a quarter circle with radius 1, one can easily use the circle equation to determine whether each point is within the circle or not. Assuming that the points are randomly distributed, the ratio of points within the circle to the number of points within the square can be used to approximate the ratio of their areas:

$$\frac{n_{Circle}}{n_{Square}} \approx \frac{A_{Circle}}{A_{Square}} = \frac{r^2\pi}{4 \cdot r^2}.$$

Ultimately this gives a direct estimate of π:

$$\pi \approx 4 \cdot \frac{n_{Circle}}{n_{Square}}.$$

In the following sections, it will be discussed how the typical processes within a fluorescence experiment can be modeled by Monte Carlo Methods.

3.2.2 *Simulation outline*

The workflow to perform a simulation with the Picasso module consists of the following steps:

1. Set handle positions to define a ground-truth model
2. Simulate kinetic traces for each handle
3. Sample the kinetic trace with the integration time window
4. Calculate the number of photons that are emitted and detected in each frame and handle
5. Simulate photon emission in 2D
6. Collect photons with a virtual camera and convert into a movie

3.2.3 *Simulate kinetic traces*

As already mentioned in Chapter 1 the additional information that is needed to super-resolve a target molecule with a stochastic super-resolution approach is taken from the time domain. Therefore, it is imperative that a fluorescence signal originating from the target molecule is time-dependent. When experiencing a stepwise-like switching from an ON- to an OFF-state the target is blinking. The time dependency can be described by average ON- and OFF-times and their underlying distribution functions. In the case of DNA-PAINT, the blinking behavior is caused by DNA hybridization.

Starting from the foundations presented in the introductory chapter, a DNA-PAINT system can be described as pseudo–first-order reaction with association rate (k_{ON}) and dissociation rate (k_{OFF}):

$$A + B \underset{k_{OFF}}{\overset{k_{ON}}{\rightleftharpoons}} C.$$

The two rates define the average time being in the respected states: $\tau_B = \frac{1}{k_{OFF}}$ and $\tau_D = \frac{1}{k_{ON} \cdot c}$. The dwell time distribution for τ_B and τ_D follows an exponential distribution [21]. Therefore, in order to simulate a DNA-PAINT kinetic trace, we can draw a random OFF-time and ON-time from the respective exponential distributions and concatenate them. This process is repeated until the desired trace length is achieved. Refer to Figure 8 for an exemplary trace and the respective probability distributions.

Each exponential distribution can be defined by its mean dwell time. For τ_B this is exponentially dependent from the number of nucleotides of the imager-handle-duplex that is bound to the surface. As a rule of thumb, τ_B increases one order of magnitude for each bp added. Reported values for a 9 bp interaction are 0.625 s and 5 s for a 10 bp interaction [21].
When knowing the association rate k_{ON} and imager concentration c, τ_D can be directly calculated:

$$\tau_D = \frac{1}{k_{ON} \cdot c}.$$

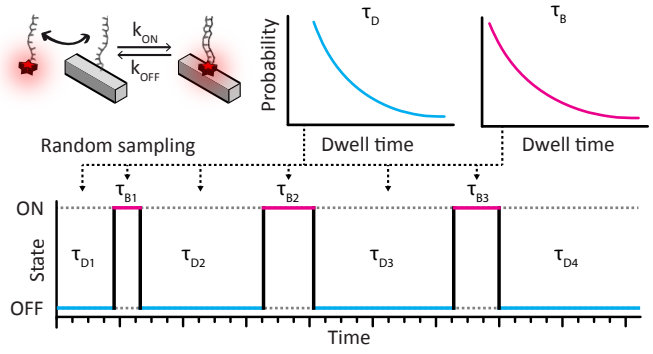

Figure 8: Simulation of a kinetic trace from a DNA-PAINT system. The DNA-PAINT system can be described as the binding and unbinding of imager strands in solution to the target handle that is attached to the target molecule. The association and dissociation rate define the average dwell times, which follow an exponential probability distribution. A DNA-PAINT kinetic trace can be simulated by randomly sampling ON- and OFF-times from said distributions and concatenating them to a kinetic trace.

For algorithmic simplicity, the simulation module of Picasso always starts with an OFF-event. Therefore it is necessary to have at least several binding events when wanting to accurately analyze kinetic traces.

3.2.4 *Simulating photon emission and acquisition*

Once the kinetic trace of a handle is generated, the next step is to simulate photon emission. For this, the spatial distribution of a given number of photons around their center position needs to be estimated. As discussed in Chapter 1, light that is traveling from a point-like source through the microscope will be imaged as an Airy-Disc pattern that can be approximated with a Gaussian function.
Therefore, the photon emission can be simulated by using a 2D-Gaussian emitter with its mean being the handle position $\overline{x}, \overline{y}$. Here, the σ of the Gaussian is defined by the PSF of the imaging system. When simulating the emission of n photons, we can draw their positions from a normal distribution $\mathcal{N}$ for x and y:

$$x_{0..n}, y_{0..n} \sim \mathcal{N}(\overline{x}, \sigma^2), \mathcal{N}(\overline{y}, \sigma^2).$$

While this approach achieves a high precision because it considers individual photons, it is computationally expensive for large photon numbers. In the latter case, individual photons will not be statistically significant and computation can be sped up by e.g. directly simulating pixel intensities.
To calculate how many photons are emitted and detected in each frame, one needs to sample the kinetic trace, specifically the ON-times with the integration time. Depending on the time point of hybridization and dissociation of the imager strand to the handle, the imager is in an ON-state and thus emits photons for either a full frame or a fraction thereof. Next, we assume a photon emission rate that is constant for the field of view (FOV) and laser-power dependent, a normally distributed photon detection rate and a Poissonian model for the photon detection. We use this model in the following algorithm to calculate the photon numbers:

First, a photon detection rate $\dot{n}$ is drawn from a normal distribution $\mathcal{N}$:

$$\dot{n} \sim \mathcal{N}(\mu, \sigma^2).$$

Subsequently, the kinetic trace is used to determine the binding duration Δt for the for each frame, which can be used to calculate the number of photons $n_{emitted}$ that are being emitted:

$$n_{emitted} = \dot{n} \cdot \Delta t.$$

Lastly, the number of photons that are detected within that frame $n_{detected}$ is modeled to follow a Poissonian distribution $\mathcal{P}$:

$$n_{detected} \sim \mathcal{P}(n_{emitted}).$$

This last step takes into account that the exact moment of photon emission is uncertain. As this follows a Poissonian distribution it is to note that for large photon numbers this last step will not be of significance. As an example, for 100 photons, the resulting standard deviation is only 10%, for 1000 it is 3.2%.
The average lifetime of a fluorophore is considered with the idea of a maximum *photon-budget*, a maximum number of photons that are emitted by a fluorophore before it bleaches.
After knowing the number of photons that are being simulated in each frame, the Gaussian emitter can be used to simulate photon positions for each handle and each frame. Lastly, photon lists need to be converted to a 2D image by creating a 2D-Histogram. Poissonian image noise is added to each frame.
To consider camera saturation, pixel values are capped at the bit-depth of the image ($2^{16} - 1$ for 16 bit). All images are concatenated to create a movie file.

3.2.5 *Parameters and background model*

In order to create realistic *in silico* simulations, simulation parameters need to be matched to real-life experiments. The first set of parameters can be used from an existing experimental setup, such as the pixel size of the microscope camera. Other parameters are changed depending on the experiment, such as imager concentration and integration time. To create exact simulation results, it is essential to identify parameters that affect the imaging resolution. For typical DNA-PAINT imaging acquisitions, localizations have high photon numbers. The imaging performance is thus mainly defined by the laser power and imager concentration, which determines the background level.
To have a background model that can be used to estimate the background B for different parameters, I implemented the following equation:

$$B = (C_{Laser} + C_{Imager} \cdot c) \cdot I_{Laser} \cdot \Delta t.$$

It contains two constants, one reflecting the background arising from increasing imager concentration C_{Imager}, the other from increasing laser power C_{Laser}. The nested multiplications arise from the following considerations:

- The background has to be zero if the laser power I_{Laser} or the integration time Δt is zero.
- If the no imager $c = 0$ is present, there will still be signal arising from background fluorescence that scales with laser power and integration time.

The constants were experimentally determined by measuring slides with buffer and the respective imager concentration and fitting to the background equation.
Based on the calculated background model, Poissonian noise is added to each frame.

3.2.6 *In silico simulations of biological processes*

A first showcase on how to use the simulation tool was within a collaborative project with the group of Ralf Jacob of the Philipps University Marburg. They studied the molecular mechanism to recruit galectin-3 into multivesicular bodies for polarized exosomal secretion [52]. GSDIM super-resolution light microscopy was employed and a key question here was whether this approach would be capable of distinguishing the principal stages of the three-stage recruiting mechanism – binding, budding, and scission. In order to test the feasibility of the GSDIM-approach, I first analyzed the experimental data and iterated through several simulation settings to create a model that matches the experimental data. To model the different recruiting stages I created three models of multivesicular bodies with spheres. Figure 9 shows a comparison of experimental data and the *in silico* data of the simulation model. The simulation data was used to support the hypothesis that the GSDIM approach would, in principle be, capable of observing the stages of the recruiting mechanism.

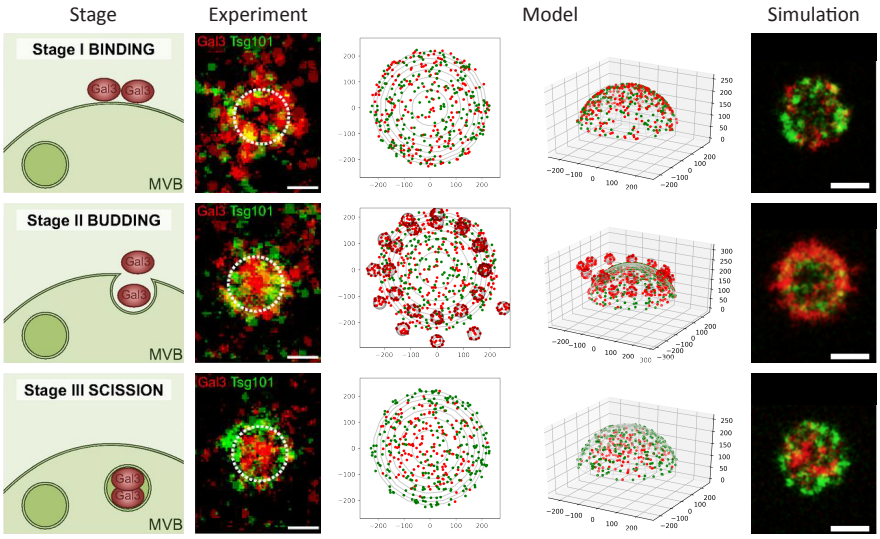

Figure 9: Simulation of the three-stage recruiting mechanism of multivesicular bodies (MVBs). The three stages are depicted on the left side. Experimental data for the three stages was acquired and used to estimate imaging performance. A simulation model was created to simulate the process of binding with having MVBs in different distances. Images show several structures together as 'Average Intensity'. Scale bars: 250 nm. Image adapted from [52].

4

ADVANCES IN DNA-PAINT

As previous chapters elucidated, DNA-PAINT exhibits several features that make this technique particularly useful for biologists. Amongst these are high resolution, the capability to count molecules from their kinetic signature and the possibility to attach DNA-PAINT handles to antibodies for biological imaging. In this chapter, I will introduce some key developments in the field of DNA-PAINT that aim to further increase the use case of DNA-PAINT for the biological sciences. First, a method to further improve resolution via sequential imaging termed RESI. Second, imaging conditions that allow the absolute counting of molecules in unresolvable spots. Third, the use of SNAP-tag as an improved label for biological imaging.

4.1 RESOLUTION ENHANCEMENT VIA SEQUENTIAL IMAGING: RESI

The achievable resolution of current super-resolution techniques is steadily increasing. When Stefan Hell proposed his STED microscope in 1994, he theoretically estimated it to be capable of resolving 35 nm. With the latest advance in STED - MINFLUX nanoscopy, which was presented in 2016, he demonstrated localization precisions of $\approx 1\,\text{nm}$ for particle tracking and was able to resolve 6 nm distances on DNA origami nanostructures [18].
Earlier in the same year, Mingjie Dai et al. demonstrated localization precisions of $< 1\,\text{nm}$ and resolved 5 nm distances on DNA origami [53] using DNA-PAINT.
While these results are impressive benchmarks that prove the potential of super-resolution techniques to enter the resolution domain of electron microscopy, they are typically achieved in environments that can be precisely controlled. Imaging of biological systems - in contrast to DNA nanostructures - comes with several traits that negatively influence imaging performance so that comparable resolution values have yet to be demonstrated.
After all, even for super-resolution techniques, every imaging system will exhibit a certain achievable resolution limit. This poses a fundamental limitation when one wants to investigate a biological structure that is well below this boundary.
Here, I propose the idea of RESI – resolution enhancement via sequential imaging, which uses the unique multiplexing capability of DNA-PAINT to push this microscopy technique further to resolve structures beyond its nominal resolution.

When imaging a target structure with DNA-PAINT, an imager strand in solution will bind to the corresponding handle strand at the target structure and can be localized. Depending on the number of photons emitted in relation to the background signal (SNR) a localization will exhibit a certain localization precision σ. As each binding event can last several frames, the localizations of several frames that belong to one binding can be *linked* or *merged*, into one localization with higher localization precision. Assuming that each localization has the same localization precision, the localization precision of the merged localization will increase with the square root of the number of localizations that are merged. This is commonly known as the standard error of the mean:

$$\overline{\sigma} = \frac{\sigma}{\sqrt{n}}.$$

One of the unique properties of DNA-PAINT is that, in contrast to other SMLM techniques, the target will not *bleach* in a conventional sense. Usually, a fluorophore is attached to the target, and after harvesting the full photon budget, no more photons can be exploited for increasing the localization precision. For DNA-PAINT, the fluorophore of an imager may bleach, but for the next binding event a new imager with a fresh fluorophore from solution will attach to the target strand and can be exploited. It is, therefore, possible to not only link localizations from one binding event but also from several binding events to ultimately perform unlimited sampling of a single binding site. Fitting of infinite localizations yields in principle an unlimited localization precision for the detection of the binding site.

One should note, however, that this can only be done when single binding sites can be identified. The fitting of localizations that come from a dense cluster of binding sites that do not allow unambiguous identification is not possible. Therefore, the increase in localization precision itself does not directly translate to a higher possible resolution.

To use this increased localization precision to increase resolution, we use the multiplexing capabilities of DNA-PAINT. Here, we can use orthogonal sequences to label the same target. By imaging each sequence sequentially, each imaging round will have decreased labeling density as only a fraction of all targets are imaged, allowing the unique identification of individual binding sites.

This principle can be exemplified when imaging a line structure that has 12 labels in close enough proximity that they cannot be individually resolved (see Figure 10). When alternating the labels with orthogonal sequences and splitting the image acquisition into four imaging rounds, the labeling density is decreased by a factor of 4. From an initial label distance of 5 nm that was not resolvable, the distance in each round is 20 nm which is long enough to be resolved. The individual localizations can be unambiguously attributed to a single binding site. For each

imaging step, orthogonal imagers are introduced into the system and washed out after image acquisition. Finally, all reconstructed imaging rounds are overlayed, and the resulting image now resolves the individual handle positions.

4.1.1 *Precision, accuracy and resolution*

The previous subsection already used the terms *resolution* and *precision*. To increase clarity on how these concepts are used in this thesis, they will be discussed as follows:
In general, the ability of a system to measure entities is characterized by its precision and accuracy. Precision refers to the occurrence of random errors while accuracy refers to systematic errors. Accuracy in the literal sense means how *accurate* the system is in determining the true value, therefore refers to the difference between true value and observation. In contrast, precision refers to the spread that occurs when performing the experiment several times.
In the context of super-resolution imaging, the term accuracy would describe how far the determined position deviates from the actual position of the target structure. Evidently, for experimental data, the ground truth is not a parameter that can be directly determined. Here, DNA origami structures can be used as a nanoscopic ruler to approximate the underlying true positions. Additionally, the size of the label and linker that are needed for fluorescence microscopy will add a linkage error to the true center position. In that sense, we will neglect accuracy and use the localization precision as a quantitative parameter to

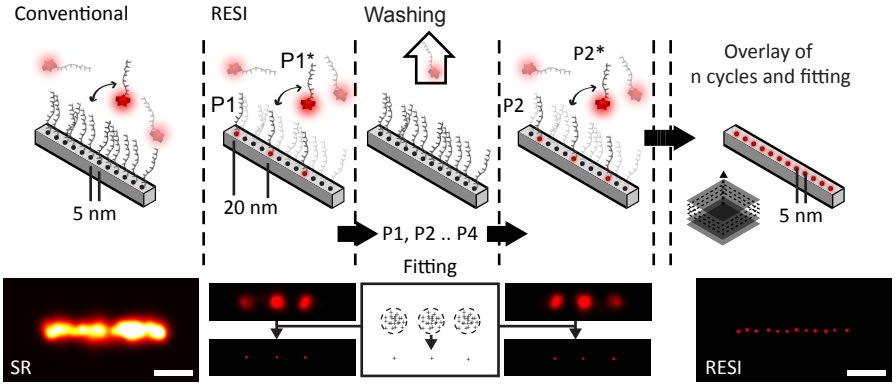

Figure 10: Left side: Conventional super-resolution microscopy will be limited by its imaging resolution, handles that are too close cannot be resolved. Right side: RESI approach. Sequential labeling and imaging can decrease the labeling density of the sample. This allows identification of single binding sites, fitting of individual localizations and subsequent localization precision increase. Each sequential imaging round will be overlayed to create a RESI image with increased resolution.

compare the performance of different imaging methods.
When having a number of localizations, the localization precision can be approximated by a 2D Gaussian distribution with defined σ. The average distance $E|x|$ to the true center position, also known as the average absolute deviation, or mean absolute deviation can then be calculated as follows:

$$\frac{E|x|}{\sigma} = \sqrt{\frac{2}{\pi}} \approx 0.798.$$

Therefore, when the standard deviation of the localization precision is known one can estimate the average distance (and hence the error) to the center of the emitter.
In the context of this thesis, we use the term *resolution* to refer to whether two spots in close proximity can be distinguished or not. Specifically, the idea of FWHM$\approx 2.3548 \cdot \sigma$ is being used.

4.1.2 *Increasing localization precision*

As already introduced, the localization precision $\overline{\sigma}$ that can be achieved when fitting several localization scales with the inverse square root of their quantity. As the number of localizations that occur are dependent on the imaging time t, imager concentration c and k_{on}, and as the initial localization precision is dependent on the imager concentration $\sigma(c)$ the increase in precision can be described as follows:

$$\overline{\sigma} = \frac{\sigma(c)}{\sqrt{c \cdot \frac{1}{k_{on}} \cdot t}}.$$

Accordingly, there are two ways to increase $\overline{\sigma}$ for a given σ: (1) to increase imaging time and (2) to increase imager concentration. Because of the different SNR, an increase of imager concentration not only increases the sampling rate but also decreases the localization precision. Assuming that the background increases linearly with imager concentration while having a square root dependency for precision, it becomes clear that the determining factor for increasing localization precision is an increase in imaging time.
While in principle the increase of localization precision is unlimited, possible practical limitations can occur, e.g., when DNA hybridization is exhausted that results in deactivation of the binding site or the bleaching of all imager strands in solution which would require buffer exchange.

4.1.3 *Localizations and binding events*

Another technicality that needs to be considered is the distinction of localizations and binding events in terms of localization precision. Depending on the chosen integration time a binding event can either span over one or several frames. When assuming a constant photon emission rate over the binding duration a localization with higher localization precision will be split into i localizations with lower localization precision. Theoretically, this will not affect the final localization precision as the localization precision scales with the square root of the number of photons. Note that $\frac{\sigma}{\sqrt{n}} = \frac{\sigma \cdot \sqrt{i}}{\sqrt{n \cdot i}}$. However, additional noise that arises from increasing the sampling rate (i.e., shot noise or higher readout noise when using a higher readout frequency) will make fewer localizations preferable. Additionally, decreasing the integration time will decrease the resolution in the first place and therefore reduces the fraction of localizations that can be identified as belonging to only one binding site.
As the number of binding events can be directly estimated from the kinetic parameters of the measurement, we can easily use it to calculate the final localization precision. Accordingly, one can estimate the localization precision of a single binding event σ_B by determining the average number of localizations per event. This is approximately the ratio of ON-time to the integration time Δt:

$$\sigma_B \approx \sigma \cdot \frac{\Delta t}{\tau_B}.$$

4.1.4 *Deterministic and stochastic labeling*

In the example of the line structures, the orthogonal labels were intentionally placed so that the distance between the same sequence is maximized. This labeling approach is referred to as *deterministic labeling*. This can only be obtained when one has precise control of the position of target sequences for a given target. While this can readily be achieved for programmable DNA nanostructures such as DNA origami, this is typically not the case for biological samples. To reduce the labeling density here, the target structure can be labeled stochastically, which refers to the random labeling of the same target with orthogonal targets.
The probability that two labels will be within a distance that is not resolvable while also having the same sequence and thus will not be separable decreases with the number of labels. As these binding sites cannot be unambiguously identified, they cannot be used for RESI. One can think of a *virtual* labeling efficiency E_v to describe the fraction of points that can be used for resolution increase. E_v will be a function

of the target density ρ, the number of orthogonal sequences S and the initial resolution σ:

$$E_v = E_v(\rho, S, \sigma).$$

As for an experimental setup, one will need to estimate the required labeling efficiency and resolution for the specific research question. Approximating ρ to be the number N of particles in a 2D space with the area A, on average, each particle will occupy an area of $a^2 = \frac{A}{N}$ with side length a. Therefore, there is a square-root dependency for the average particle to particle distance and the labeling density. In other words, if one wants to push a given labeling density so that the resulting average distance of points is half in order to increase the resolution, one will need at least four orthogonal sequences S:

$$\overline{a} \sim \sqrt{S} \rightarrow \overline{\sigma} \sim \sqrt{S}.$$

4.1.5 *Testcase DNA origami*

In order to test the feasibility of RESI, flat rectangular DNA origami nanostructures (RRO) were used for benchmarking.
As an initial step, a line pattern was designed to measure the potential resolution increase. The line consists of eight handles, each 10 nm apart. The handles were alternated with orthogonal sequences, X61 (TT-TCCTCAATT) and X70 (TT-TCAATATCT) so that the effective distance in each imaging round was 20 nm. Additional sequence identification marker handles were placed in opposing corners of the structure. Refer to Figure 11 for a schematic of the structure and the experimental results. For the assessment of resolution it was found that analyzing single structures is not ideal for several reasons: First, depending on the Gaussian illumination profile of the microscope, the power density will vary and will decrease towards the edges, leading to a resolution gradient. Second, as the binding and unbinding of DNA-PAINT is a statistical process, there will be variance in sampling for individual samples. Lastly, structures can exhibit deformations and missing handles. Ultimately the determined resolution from two structures from the same measurement may differ. To address this, I chose to make the comparison in resolution increase more quantitative by picking several structures to create a sum image, and estimated an average resolution by fitting Gaussians to the resulting profiles. For the alignment of the picked structures to the sum image, I consider both rounds simultaneously so that they can be aligned although not having overlapping

staple positions.

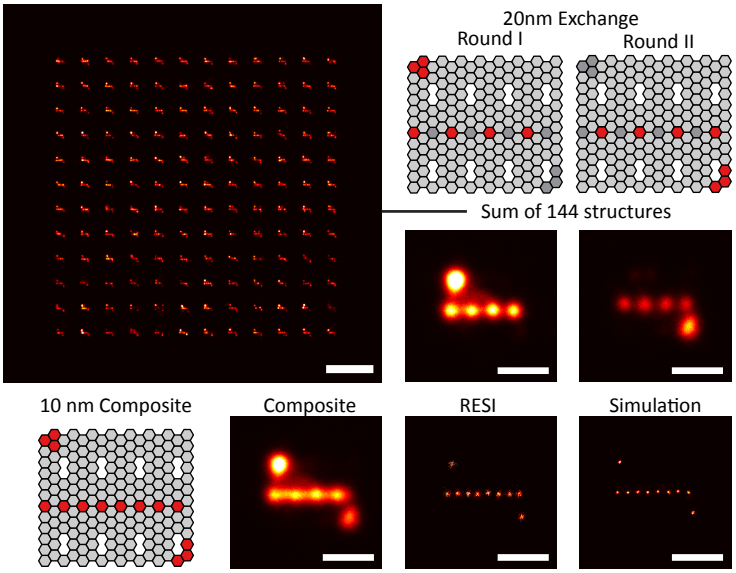

Figure 11: 2x Exchange RESI measurement: A line structure was designed that exhibited 20 nm distances per round and 10 nm in the composite. From the field of view, 144 structures were selected, and the resolution in each imaging round was determined. The mean resolution per round was 13.54 nm, making it impossible to resolve the 10 nm distances. This becomes evident in the sum image of the composite. After RESI reconstruction, an average resolution of 3.15 nm was achieved, enough to clearly resolve the 10 nm distances. The origami measurement was validated with *in-silico* simulations that showed a similar resolution increase.

As a second step, *in silico* simulations were performed to assess the potential resolution increase for the given structure. For this, simulation conditions were matched to the final experimental conditions. The imaging parameters were fine-tuned so that the overall imaging resolution of the system was worse than 10 nm so that one is unable to resolve the designed line pattern. A total of $n = 49$ line structures were picked from the field of view and aligned on top of each other to form a sum image. Displaying only one round at a time and fitting the resulting spots with Gaussians can be used to determine an average resolution. In the simulation case, it was determined to be 10.96 nm. After fitting an average of $N = 32$ binding events (114 localizations), the resulting average resolution after RESI was 1.85 nm, resulting in an effective resolution increase of 5.9.
Here, the resolution increase is roughly the square root of the number of binding events ($\sqrt{32} = 5.66$):

$$\sigma_{RESI} \approx \sigma \cdot \sqrt{N}.$$

For the experimental data, determined NeNA values (FWHM) for the X61 round were 11.54 nm and the X70 round 19.59 nm, well above 10 nm. A total of $n = 144$ line structures were picked from the field of view and aligned on top of each other to form a sum image as previously done with the simulation data. When displaying a composite image, meaning that both rounds are displayed at the same time, it is evident that the imaging resolution is not sufficient to resolve individual binding sites. Refer to Figure 12 for experimental data. In contrast, the sum images of the individual rounds show the binding sites. Note that the different intensity arises from deviations in sampling.
Fitting of the four peaks resulted in the in a mean resolution (FWHM) of 13.54 nm (13.08 nm for X61 and 13.97 nm for X70). The FWHM for the reconstructed RESI dataset was 3.15 nm, resulting in a resolution increase of 4.3.
Kinetic analysis revealed an average of 77 binding events for X61 (604 localizations) and 33 binding events for X70 (207 localizations). Again, the resolution increase is in the order of the square root of the number of binding events ($\sqrt{33} = 5.74, \sqrt{77} = 8.77$).
Giving the achievable FWHM resolution of 3.15 nm it should also be possible to resolve the 5 nm hexagonal pattern on a DNA origami.
To test this, the line structure pattern was decorated with two additional sequences, X68 (TT-ATCAATCTT) and X72 (TT-TTAAATCCT) to decrease the composite distance to 5 nm while keeping the distance of 10 nm per round. Again, 144 structures were selected and evaluated for RESI. The composite image of all structures shows that the original resolution of the imaging system is not able to resolve the individual distances while the RESI reconstructed data clearly resolves the 5 nm hexagonal zig-zag pattern that arises from the hexagonal pattern arrangement. This highlights how RESI can be used to increase the imaging resolution via sequential imaging and fitting.

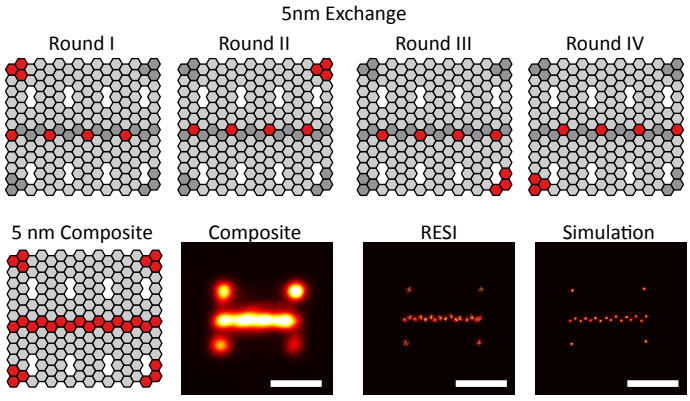

Figure 12: 4x Exchange RESI measurement: The addition of two additional exchange rounds scales the effective distance down to 5 nm. Using RESI, an imaging system with less than 10 nm could resolve distances below 5 nm.

4.2 COUNTING ABSOLUTE MOLECULE NUMBERS

In the previous section, recent developments in terms of the achievable resolution in super-resolution microscopy were discussed. Researchers are now capable of resolving structures with nanoscale resolution. However, counting molecules in complexes and specifically determining absolute copy numbers of proteins in localization data that cannot be resolved remains challenging. In this section, I will introduce absolute qPAINT, which explores the imaging conditions of classical qPAINT to be able to count absolute handle numbers. Ultimately, together with site-specific, stoichiometric 1:1 labeling this will allow counting absolute protein copy numbers. I benchmarked measurement conditions to use absolute qPAINT using DNA nanostructures and nuclear pore complexes.

4.2.1 *Requirements for absolute counting*

Classical qPAINT is a capable technique to extract quantitative information from repetitive hybridization events. When knowing the influx rate of an imaging system, it is possible to estimate handle numbers given a kinetic trace. In order to push qPAINT to be able to count absolute molecule numbers, it is not only necessary to find a stoichiometric 1:1 label but also to optimize imaging conditions so that populations can

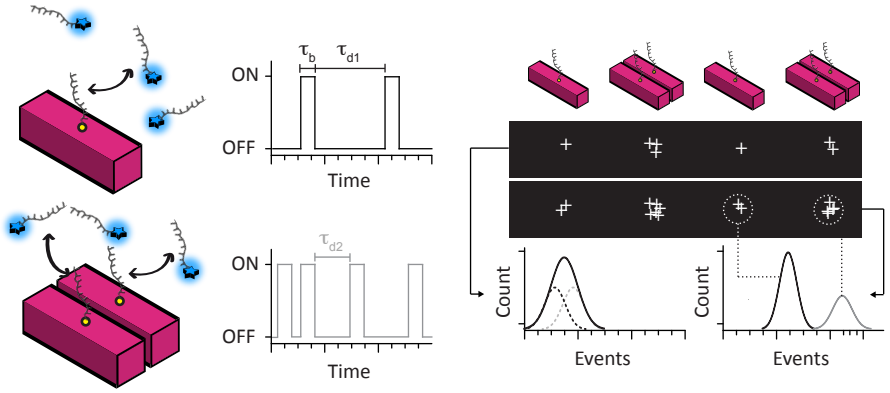

Figure 13: Concept of absolute qPAINT. Left side: Repetitive hybridization of fluorophore-labeled imager strands not only can be used for super-resolution microscopy but also yields quantitative information. While a single binding site in an unresolvable spot will be visited with a certain frequency, the frequency for two binding sites in close proximity will be double because of statistical independence. Right side: When analyzing the number of binding events, short image acquisitions will exhibit too little binding events to unambiguously distinguish monomers from dimers. For acquisitions that are long enough the distribution of binding events will show two populations making the distinction of absolute copy numbers possible.

be unambiguously identified. A useful benchmark to assess the counting capabilities of DNA-PAINT is to test whether one can distinguish a monomer from a dimer. While a single binding site will be visited with a certain frequency, the frequency for two binding sites in close proximity will be doubled because of statistical independence. While the frequency can be measured through several ways, e.g., by measuring dark-times, calculating their mean or fitting them to a cumulative distribution and taking the inverse, it is useful to simply count the number of binding events as a parameter for the frequency. For short image acquisitions, the populations of the number of binding events arising from the two populations will overlap. A distinction and unambiguous identification are thus not possible. However, for acquisitions that are long enough, the difference in kinetics will be better sampled, and the populations can be separated.
The fundamental requirements for the imaging conditions can be estimated when considering the prerequisite that the probability distribution of the number of binding events of a monomer $P(X_1)$ should not overlap with the probability distribution of a dimer $P(X_2)$:

$$P(X_1) \cap P(X_2) = \varnothing.$$

Assuming that this probability distribution is Poissonian, the σ of a population is equal to the square root of the average number n of binding events:

$$\sigma = \sqrt{n}.$$

As the Poissonian can be approximated with a Gaussian for large n, we expect that for an interval of 3σ we have 99.7% coverage of all observed number of binding events. Hence in order to have almost no overlap between two populations, the distance between the mean number of events of each distribution $n_2 - n_1$ needs to be at least the sum of $3\sigma_1$ and $3\sigma_2$. When distinguishing a monomer from a dimer $2 \cdot n_1 = n_2$ the distance is n_1 and therefore:

$$3 \cdot \sqrt{n_1} + 3 \cdot \sqrt{2n_1} \geq n_1 \Rightarrow n \geq 52.46.$$

Consequently, the average number of binding events per site that needs to be detected is at least 53. Given a typical imager concentration of $c = 2.5\,\mathrm{nM}$ and a $k_{on} = 1.6 \cdot 10^6$ this would translate to ≈ 217 minutes of image acquisition. The theoretical assumptions can be validated by *in silico* simulation of a sample with each 100 single and double binding

sites for an imaging duration of 45000 frames at 300 ms integration time (225 minutes) with above imaging conditions. Examining the number of binding events reveals two distinct peaks at 49 ± 6.2 and 96.7 ± 8.6 binding events. Refer to Figure 14 for the simulated distribution. Similiar, for 2σ and a coverage of 95%, this would be $n_1 = 23.31$ with an imaging time of ≈ 96 minutes.

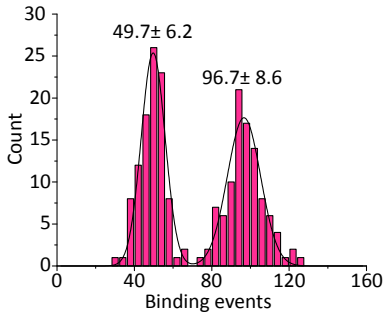

Figure 14: Simulation of imaging parameters for double peak detection. A total of each 100 single and double binding sites were simulated with the following imaging parameters: Imager concentration $c = 2.5\,\text{nM}$, $k_{on} = 1.6 \cdot 10^6$ and a total acquisition time of 225 minutes (45000 frames at 300 ms integration time). As expected from theoretical considerations two distinct peaks at 49 ± 6.2 and 96.7 ± 8.6 binding events can be identified.

While the principle requirement for absolute counting is just a sufficiently long imaging time with respect to the imager concentration, the optimization of imaging conditions needs careful tuning. Typically, performance increase for qPAINT will come at the cost of imaging resolution. In the following, several imaging parameters are qualitatively discussed on how they affect the performance in different regimes.

- *Laserpower:* Laserpower needs to be sufficiently high to be able to detect single-molecule binding events. For high-resolution imaging, one wants to exploit the full photon budget of the fluorophore, hence typically high laser powers in combination with oxygen scavenging systems are used. However, for kinetic measurements, lower laser powers are preferred as it will minimize the induction of photo effects that affect the stability of the acquisition.

- *Imager concentration:* Low imager concentrations will decrease the background and thus increase the localization precision. However, they also decrease the sampling and therefore requires longer imaging times for accurate qPAINT.

- *Integration time:* While for high-resolution acquisition the integration time is ideally in the range of the ON-time of the imager to increase SNR, for qPAINT measurements, smaller integration times are preferred as they have increased time-sampling. However, the integration time needs to be sufficiently high to collect enough photons to enable single-molecule detection. Refer to Figure 15 for a simulation of the effect of integration time and resolution as well as the relative error introduced for the determination of kinetic parameters. In general, longer integration times will lead to an overestimation of ON-times, while integration times that are too short will lead to an underestimation. As OFF-times are typically much larger than the integration times they experience little variation.

- *Photostabilizing buffers:* The usage of photostabilizing buffers may increase photon yield and may reduce free radicals in solution as unwanted bleaching is prevented, however as most buffers use enzymatic reactions they are time critical.

Therefore, it is required to find the matching imaging conditions for the specific target. A fundamental question here is how good the imaging resolution and the qPAINT resolution should be. As for the measurements that follow I chose imaging parameters of 10 mW (measured before the backport of the microscope) for a 561 nm laser, 2.5 nM imager concentration with Cy3b, 200 ms integration time for 60.000 frames with Buffer C).

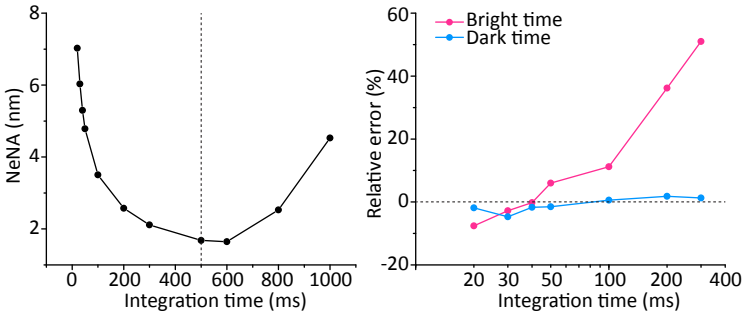

Figure 15: Simulation on the effect of integration time on resolution and determination of dark and bright time. A total of 100 binding sites with a bright time of 500 ms, dark time of 12 500 ms and an imaging duration of 1 h were simulated. Left: Influence on the achievable resolution. Analyzing the NeNA parameter as a measure for resolution reveals a local optimum for resolution when matching the integration time to the bright time. Right: Influence on bright and dark time determination. For small integration times, the reduced photon count can cause binding events not to be detected, resulting in an underestimation of the bright time. For integration times that are too large, the bright time will be overestimated. In contrast, the dark time shows little variation as it is much larger than the integration time and is thus measured with adequate sampling. Therefore, for the accurate determination of bright and dark times, it is advisable to choose the shortest integration time that still has sufficient photons to detect single-molecule binding events.

4.2.2 *Absolute counting on DNA origami*

To benchmark the capability of DNA-PAINT for absolute counting, I tested the theoretical assumptions with DNA origami nanostructures. Here, I mimicked a monomer/dimer structure by decorating a flat sheet origami structure with DNA-PAINT docking sites. Two diagonal corners contain one binding site while the other two contain two binding sites. After image acquisition and reconstruction, individual origami structures were identified, and the binding sites in their corners were selected. A histogram of the number of binding events for 4455 binding sites is shown in Figure 16. Here, a bimodal distribution with two peaks at 65 ($\sigma = 15$) and 114 ($\sigma = 14$) is visible, clearly demonstrating the distinction of monomer and dimer-population.

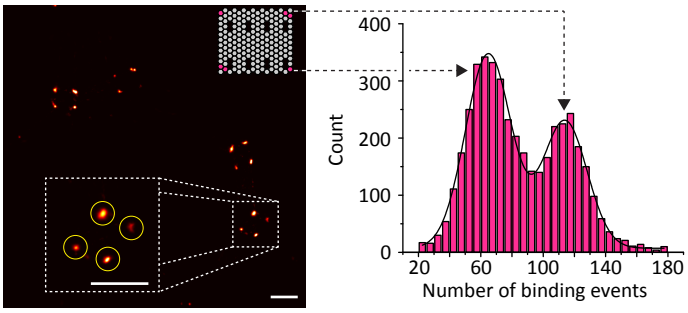

Figure 16: Absolute qPAINT for DNA origami: DNA origami structures containing two docking sites in two opposing corners and one in the other two were imaged with DNA-PAINT and imaging conditions that are optimized for absolute qPAINT measurements. (Left side). Picking the corners of each origami (yellow circles in inset) and counting the number of binding events yielded a bimodal distribution with peaks at 65 and 114, allowing the unique identification of the respective populations. Scale bars: 100 nm.

4.3 SNAP-TAG FOR BIOLOGICAL IMAGING

One major reason why the remarkable achievements in resolution cannot be directly translated to imaging cellular components is that the current labeling approaches are limited by either large label sizes (e.g., antibodies) or the sparse availability of small and efficient binders. The first labels that enabled DNA-PAINT imaging of biological targets were formed by reacting biotinylated docking strands with streptavidin and incubating them with biotinylated antibodies. When using primary and secondary antibodies, an additional linkage error of 10-15 nm is introduced.

Here, a potential solution is the use of self-labeling tags such as SNAP, which has a molecular weight of 19.4 kDa. SNAP-tag is a mutant of the DNA repair protein O^6-alkylguanine-DNA alkyltransferase that reacts with benzylguanine (BG). This allows specific and rapid covalent binding of the SNAP-tag with a synthetic probe. Expansion of the SNAP-tag labeling method to DNA-PAINT is feasible, as BG-modified oligos are readily commercially available, and additionally allow stoichiometric 1:1 labeling. However, the use of SNAP-tag requires genetic engineering of cell lines.

The nuclear pore complex (NPC) is of great interest for super-resolution imaging. NPCs act as gatekeepers within a cell and are responsible for the exchange of components between the nucleus and cytoplasm they play an important role in an organism. They have been studied extensively by electron-microscopy methods over the last decades. Today's models assume a double-ring structure composed of nuclear and cytoplasmic ring. Each ring consists of an inner and outer ring which are formed by the arrangement of a so-called *Y-complex* in an eightfold symmetry. The Y-complex consists of several nucleoporins. Individual nucleoporins in the outer rings are laterally shifted to the ones in the inner rings, here a distance of $\approx 12\,\text{nm}$ for NUP107 is expected. For the architecture of NUP107, one expects a radial diameter of $\approx 100\,\text{nm}$ and a z-distance between the double-rings of $\approx 50\,\text{nm}$. Consequently, resolving the double-ring structure is an impressive benchmark for an imaging method.

Refer to Figure 17 for a reaction scheme and a structural overview of the nuclear pore complex.

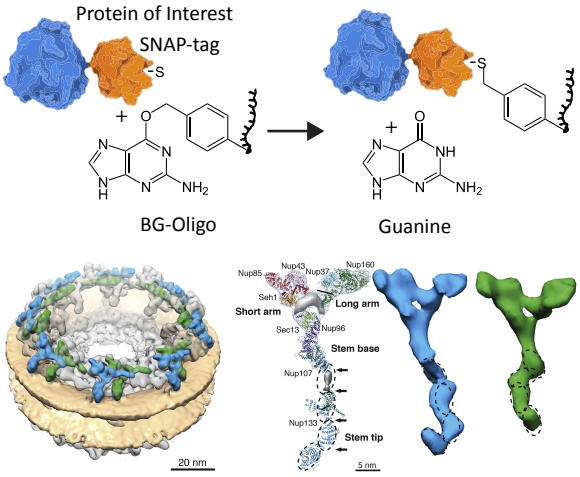

Figure 17: SNAP-Tag and nuclear pore complex. Upper panel: Schematic of the SNAP-tag labeling reaction. The protein of interest is fused to a SNAP-tag. Using a BG-oligo, a DNA-PAINT docking site can be fused to the SNAP-tag. Image adapted from [54] and [55]. Lower panel: Overview of the double-ring structure of a nuclear pore with eightfold symmetry. Individual Nucleoporines form the so-called Y-Complex (right side) and arrange in an inner and outer ring on the nuclear pore. For NUP107, one expects a radial diameter of $\approx 100\,\mathrm{nm}$ and a z-distance between the double-rings of $\approx 50\,\mathrm{nm}$. For neighboring NUP107 on the inner and outer ring, a distane of $\approx 12\,\mathrm{nm}$ is estimated. Images reproduced with permission from [56].

4.3.1 *Labeling efficiceny*

A critical point when imaging biological targets is the achievable labeling efficiency. As one knows the symmetrical structure of NUPs from electron microscopy, they can be used for straightforward determination of labeling efficiency. For a fully assembled NUP, a total of 32 NUP107 are expected, of which 16 are in each the cytoplasmic and nuclear ring. Each ring itself consists out of an inner and outer ring with each eight NUP107 that are arranged in an eightfold symmetry. As neighboring NUPs on the inner and outer ring are in close proximity, they might not be resolved, depending on the resolution of the imaging system. Each observed cluster then, can either have one or two handles. In order to assess the influence of labeling efficiency on the cluster distribution and hence the final representation when being imaged, I simulated the labeling fraction with respect to the labeling efficiency using Monte Carlo methods. The distribution is displayed in Figure 18. Evidently, for low labeling efficiency, the majority of NUP107 will not be imaged, and most of the unresolved spots will be single. For higher labeling efficiencies, the fraction of labeled NUPs will increase causing more and more to be labeled twice.

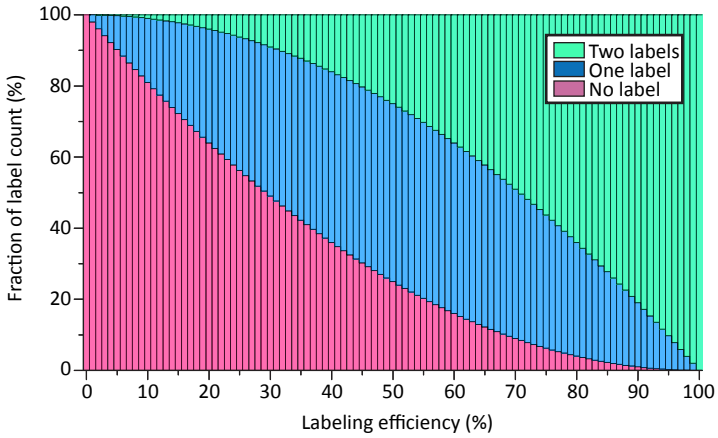

Figure 18: Influence of the labeling efficiency and the labeling fraction. The labeling efficiency will have a tremendous impact on the expected label distribution for an unresolved spot. For low labeling efficiency, the majority of NUP107 will not be imaged, and if a cluster is detected, it is very likely to be single NUP107. For higher labeling efficiencies, the fraction of labeled NUPs will increase and more and more will be labeled twice.

4.3.2 *Absolute counting of NUP107*

In a previous section, I demonstrated measurement conditions that allow absolute counting of binding sites for DNA origami. SNAP-tag permits extending this concept for cellular applications. For this, NUP107, a protein in the nuclear pore complex was targeted via the SNAP-tag label. This label allows stochiometric 1:1 labeling of the target NUP107.
As the arrangement of the NUP107 is in the form of a 3D double-ring structure with the rings being $\approx$ 50 nm apart, the previously used approach used for DNA origami of picking individual binding sites in 2D is not possible, as binding sites can overlap in z. To overcome this, I used measurement conditions that not only can resolve the double-ring structure in 3D but also perform absolute counting. For picking in 3D, a k-means clustering algorithm was implemented. In brief, it randomly places a given number of cluster centers within the 3D space and assigns each localization to the closest cluster. Then, the center of mass for each cluster is used to update the cluster center. The algorithm is repeated until convergence. Once all localizations are attributed to a cluster, they can be used for downstream kinetic analysis (i.e., counting).

With the chosen imaging parameters of 10 mW (measured before the backport of the microscope) for a 561 nm laser, 2.5 nM imager concentration with Cy3b, 200 ms integration time at 60.000 frames with Buffer C it was possible to identify NPCs and individual NUP107 clusters, arranged in eightfold symmetry. An NPC average with assumed eight-fold symmetry shows that the double ring structure can be well separated (See Figure 19).
For qPAINT evaluation, I picked 104 NPCs and used k-means clustering to identify individual NUP107. For this, the number of clusters for k-means was manually set, and outliers were removed. For all NPCs a total of 499 clusters were detected. The resolution of the measurement was determined with the NeNA parameter to be 13.78 nm (FWHM), which is close to the expected inner-to-outer-ring distance of 12 nm of two neighboring NUP107. However, as the exact linker position is not known, the actual distance and whether they can be resolved remains ambiguous, leaving the possibility to either expect 32 or 16 clusters within each ring for the given imaging conditions. Evaluation of the number of binding events showed a unimodal distribution with a mean value of 58 binding events ($\sigma = 19$). The distribution overlapped with the monomer peak of the origami measurement, suggesting that each cluster consists of a single binding site.
The number of clusters in each NPCs can be translated into a labeling efficiency of either $\approx 30\%$ when assuming that one should resolve all 32 clusters or $\approx 15\%$ for the 16 cluster case. A comparison with the label-

ing chart of Figure 18 reveals that the probability of detecting single clusters is ≈ 82% (30% labeling) or ≈ 91% (15% labeling), which are in good agreement with the observed unimodal distribution. Refer to Figure 19 for schematics of cluster analysis and experimentally determined distribution.

Arguably, the true power of absolute counting comes when being able to determine the number of absolute molecules in an unresolvable spot. While the unimodal distribution demonstrates that quantitative labeling and absolute counting can be achieved using SNAP-tag and DNA-PAINT, ideally one wants to count multiple copy numbers. To demonstrate this, it would be necessary to image nucleoporins that are closer together and well below the resolution limit. Additionally, an increase in labeling efficiency is needed, so that the dimer population is sufficiently large. To obtain an equally sized dimer population, a labeling efficiency of 67% would be required.

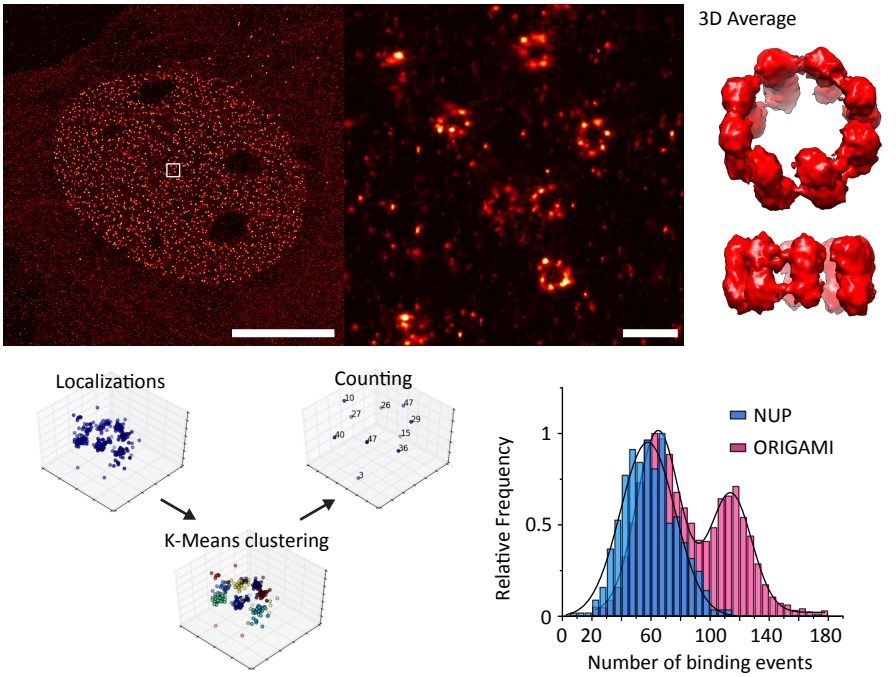

Figure 19: Absolute qPAINT for NUP107 with SNAP-tag: To test the feasibility of absolute counting in a cellular context, NUP107 was labeled with SNAP-tag and measured with absolute qPAINT measurement conditions. Upper panel: Left shows an overview of a nucleus with NPCs and labeled nucleoporin NUP107. The middle image is a zoom-in that shows individual NPCs and their localization clusters in 2D. The right panel shows an average of several nuclear pores in 3D, showing that the double ring structure can be resolved. For the creation of the average, an eight-fold symmetry was assumed. Lower panel: To evaluate the data, 104 nuclear pore complexes were picked and analyzed via a k-means clustering algorithm in 3D. It allows attributing a localization to each cluster and subsequent kinetic analysis. The number of binding events followed a unimodal distribution with a fitted mean of 58 binding events. Also shown is the bimodal distribution from the previous DNA origami measurement, overlapping with the monomer distribution of the origami, indicating that each NUP107 cluster contains a single binding site. Scale bars: Overview 10 µm, zoom-in 100 nm.

5

OUTLOOK

The technological advancements presented in this thesis highlight the beneficial interplay of DNA nanotechnology and fluorescence microscopy. Not only can DNA nanotechnology be used to improve fluorescence methods but also to obtain a greater understanding of DNA nanotechnology itself. DNA nanotechnology can provide a constant in an environment that is typically determined by nature's variability.
As for DNA-PAINT, imaging of the nuclear pore complex gives an outlook on how this technique can be a valuable tool for today's biologists. Major advantages of this method are high resolution, and the ability to perform absolute counting while also retaining multiplexing capabilities. With DNA-PAINT reaching the resolution domain of electron microscopy methods but still having the benefits of single-molecule fluorescence microscopy, the potential for structural biology applications becomes evident.
One major challenge that needs to be addressed will be finding appropriate labels for highly multiplexed experiments. The ideal probe will be small in size, has a known quantitative stoichiometry, exhibits high labeling efficiency and can be readily created for a multitude of targets. While SNAP-tag has proven to be a useful small stoichiometric label to create high-resolution images, it necessitates cell line engineering and poses a bottleneck.
Currently, the advantages of DNA-PAINT come at the price of rather long image acquisition times at high power densities, effectively limiting it to the imaging of fixed cells. Here, further technological advances will be required to make this technology applicable to live-cell imaging.
Additional challenges will arise when considering downstream data processing. As more and more data is acquired, powerful computational tools will be required to generate meaningful insight. Here, the recent advancements in computer science regarding machine learning should be applied to alleviate future data processing.
Ultimately, future research questions will require a combination of several skillsets: biologists, physicists, chemists, engineers and computer scientists - and will truly be an interdisciplinary effort.

A

APPENDIX

A.1 SUPPORTING INFORMATION FOR ASSOCIATED PUBLICATION P1

Supporting Information

Sub–100-nm metafluorophores with digitally tunable optical properties self-assembled from DNA

By

Johannes B. Woehrstein*, **Maximilian T. Strauss***, Luvena L. Ong, Bryan Wei, David Y. Zhang, Ralf Jungmann°, Peng Yin°
* *These authors contributed equally to this work*
° *Co-corresponding authors*

published in

Science Advances (2017)

Science Advances
AAAS

advances.sciencemag.org/cgi/content/full/3/6/e1602128/DC1

Supplementary Materials for

Sub–100-nm metafluorophores with digitally tunable optical properties self-assembled from DNA

Johannes B. Woehrstein, Maximilian T. Strauss, Luvena L. Ong, Bryan Wei, David Y. Zhang, Ralf Jungmann, Peng Yin

Published 21 June 2017, *Sci. Adv.* **3**, e1602128 (2017)
DOI: 10.1126/sciadv.1602128

This PDF file includes:

- table S8. Triggered assembly sequences.
- protocol S1. DNA origami self-assembly.
- protocol S2. Microscopy sample preparation.
- protocol S3. Triggered assembly on surface.
- protocol S4. Triggered assembly in solution and gel assay.
- Materials
- Optical setup
- Software section

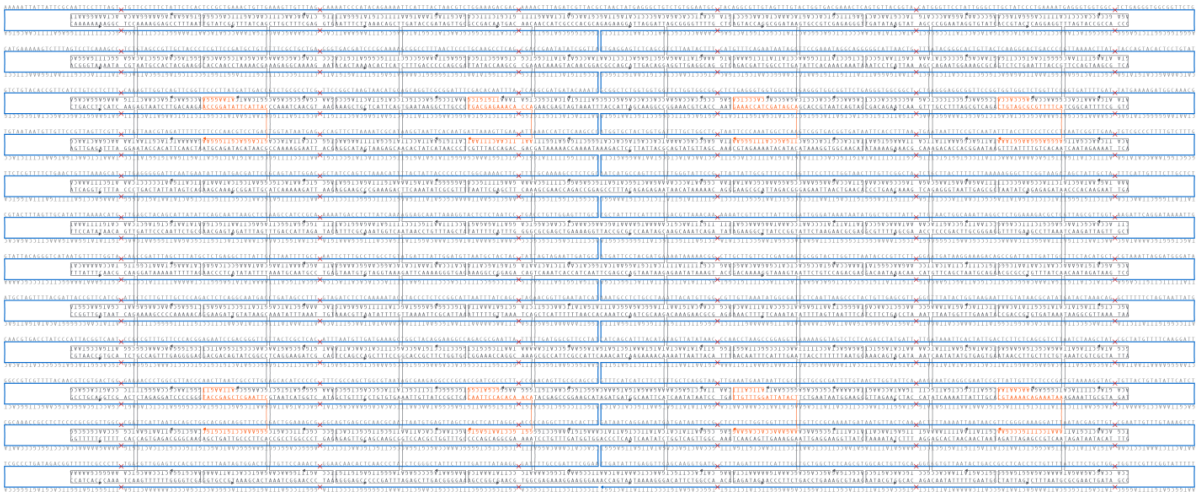

fig. S1. caDNAno DNA origami design. Circular DNA scaffold (blue) is routed in horizontal loops to form 24 parallel helices. Staple strands (gray) connect parts of the scaffold and form the rectangle. Eight strands are biotinylated on the 5'-end (orange). Most gray staples' 3' and 5'-ends are on the same DNA origami face. However, Biotin and dye functionalizations are intended to protrude on opposite faces. With the help of adjacent staples, the orange staples are shifted by one helix. This switches the 3' and 5'-ends to the opposite face. Red crosses define base-skips, which are required to prevent the DNA origami from twisting.

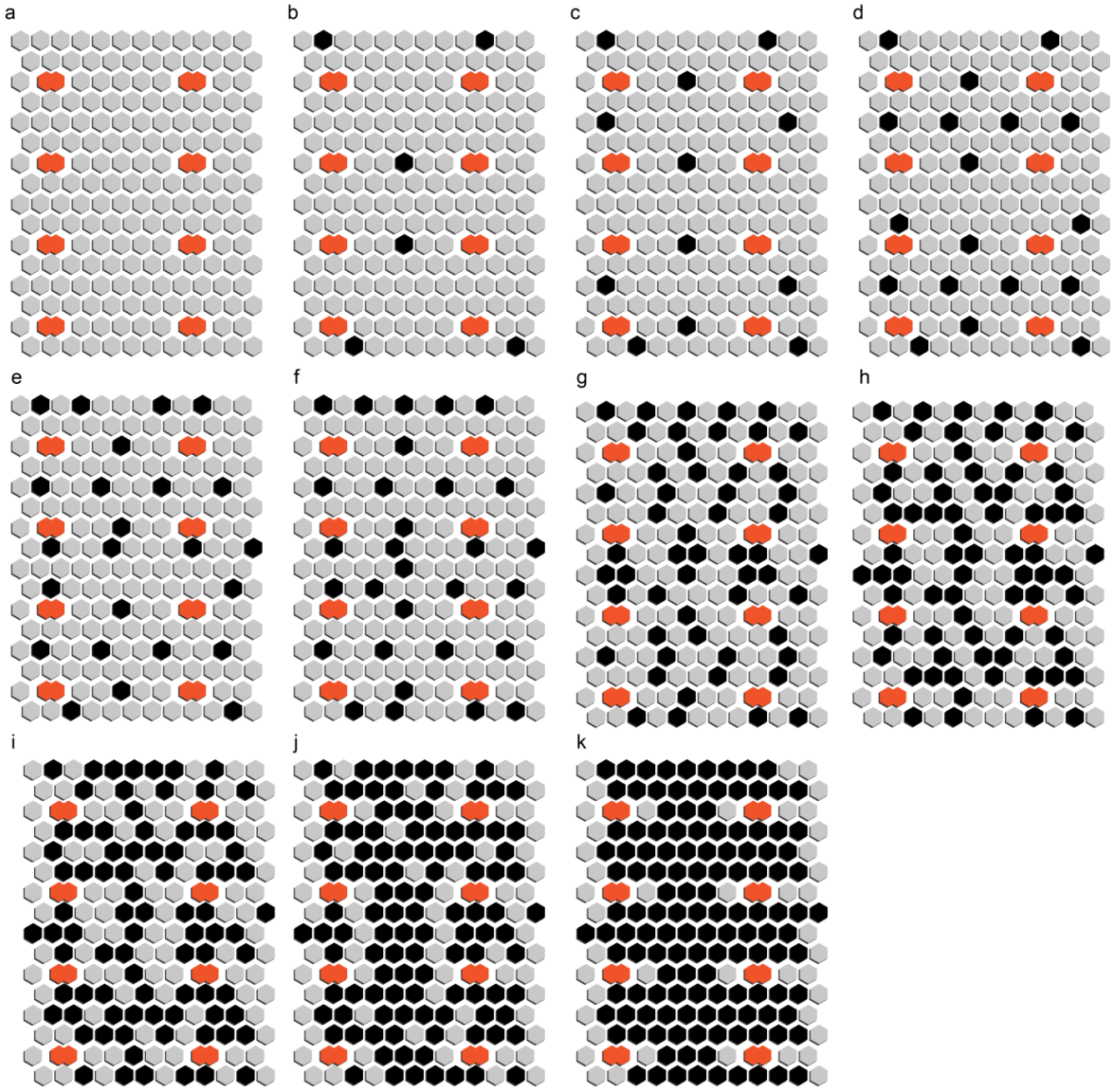

fig. S2. Schematic DNA origami staple layouts of single-color metafluorophores (6 to 132). Hexagons represent 3'-ends of all 176 staples, compare to figure S1. Orange shapes represent biotinylated staple strands, protruding on the opposite face. Black hexagons represent staples with 3'-handle extension, see table S3. Pattern is the same for Atto 647N, Cy3 and Atto 488. (**a**) is a not functionalized structure, corresponding to the caDNAno layout. (**b**) 6, (**c**) 12, (**d**) 18, (**e**) 24, (**f**) 30, (**g**) 54, (**h**) 72, (**i**) 84, (**j**) 108 and (**k**) 132 dyes attached.

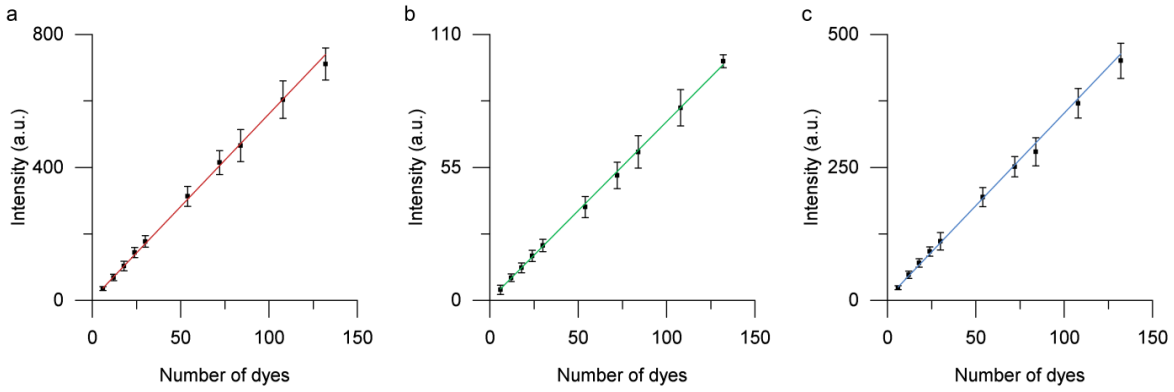

fig. S3. Linear dependence of intensity on the number of dyes per DNA origami (calibrated). From 6 to 132 dyes per DNA origami, the intensity scales linearly for (**a**) Atto 647N, (**b**) Cy3 and (**c**) Atto 488. Investigated samples are identical to those in Figure 1 of the main text. However, samples contained the structure of interest and additionally a second DNA origami with a significantly different dye count as reference. This allows comparison and calibration of measured intensities and thereby reduces sample-to-sample variations. Corresponding data in Figure 1 of the main text is not calibrated.

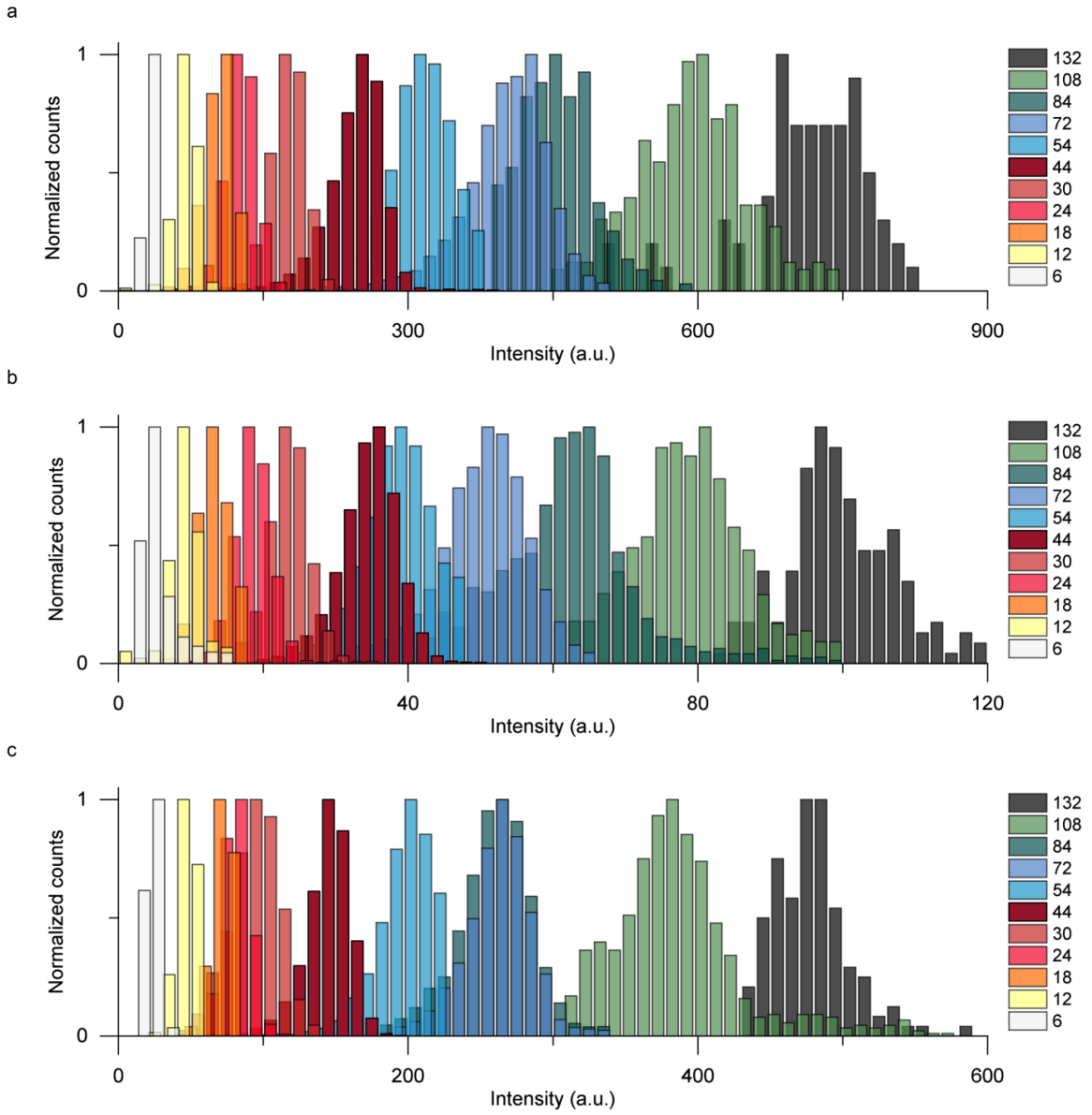

fig. S4. Intensity distributions for 6 to 132 dyes. Data corresponds to figure S3, where mean and standard deviation of the distributions are plotted. (**a**) Atto 647N. (**b**) Cy3. (**c**) Atto 488. Investigated samples contained the structure of interest and a second DNA origami with a significantly different dye count as reference. Reference intensity distributions are not shown.

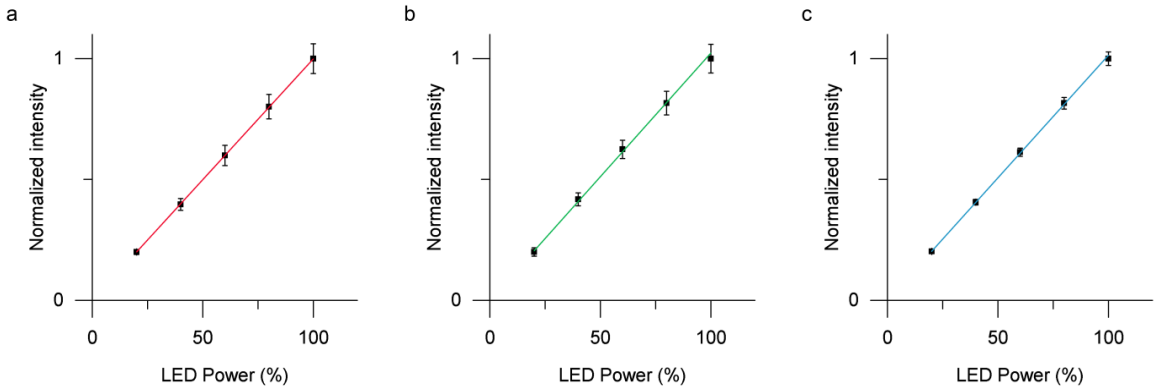

fig. S5. Excitation power variation. The measured intensity of a 30 dye metafluorophore scales linear with the applied excitation intensity for (**a**) Atto 647N, (**b**) Cy3 and (**c**) Atto 488. More than 12,000 metafluorophores were evaluated per data point. Camera integration times were constant at 10 s. All subsequent measurements throughout this study were performed at 60 %.

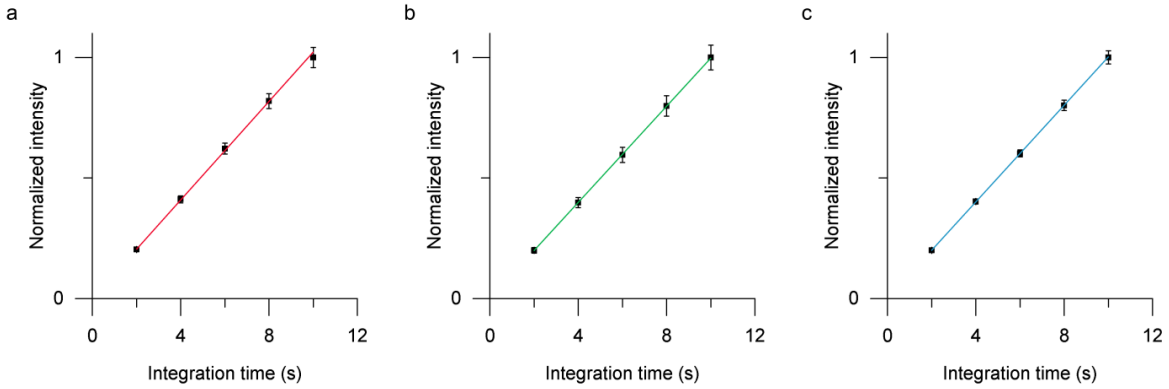

fig. S6. Integration time variation. DNA origami-based metafluorophore recordings were measured using a Hamamatsu ORCA Flash 4.0 sCMOS camera. Integration times were varied from 2 s to 10 s per recording and show a linear increase in intensity of a 30 dye metafluorophore for (**a**) Atto 647N, (**b**) Cy3 and (**c**) Atto 488 at 60 % excitation intensity. More than 12,000 metafluorophores were evaluated per data point.

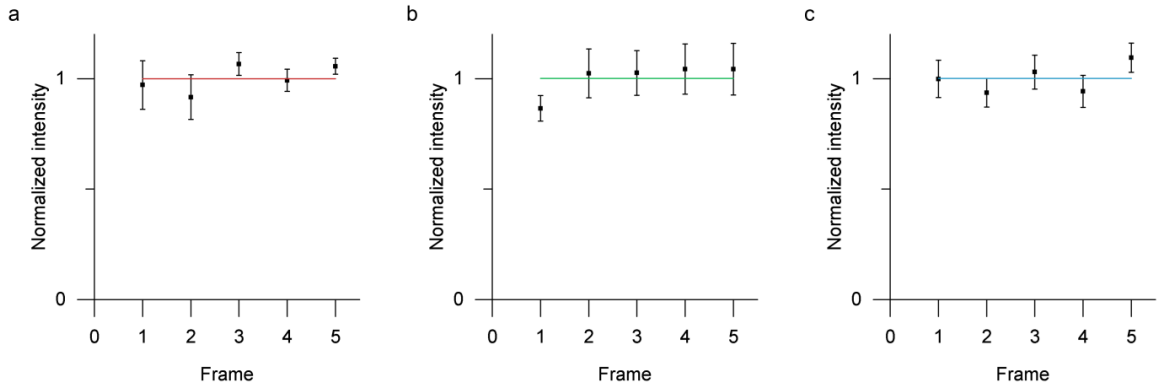

fig. S7. Refocusing performance. While repeated focusing attempts may lead to imaging in different focal planes, different focal planes may yield different intensities of a single target. The same samples, containing DNA origami based metafluorophores with 30 dyes, were imaged and refocused five times for (**a**) Atto 647N, (**b**) Cy3 and (**c**) Atto 488. Plots are normalized to the average value (colored line).

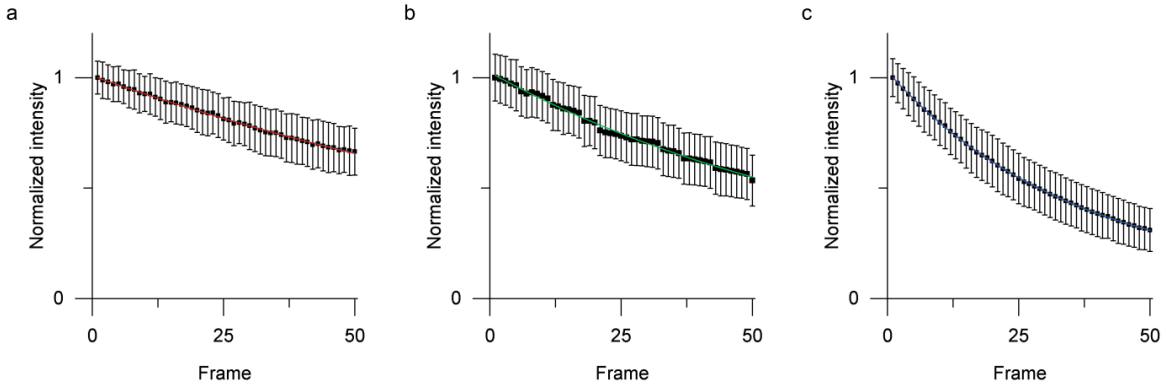

fig. S8. Photostability. Repeated recording of the same area causes photobleaching of the dyes. The measured intensity drops exponentially. Measurements were performed at 60 % excitation power and integration times of 10 s per frame on a 30 dye DNA origami metafluorophore for (**a**) Atto 647N (-0.77 %), (**b**) Cy3 (-1.37 %) and (**c**) Atto 488 (-2.80 % per acquisition) on the Zeiss Axio Observer microscope.

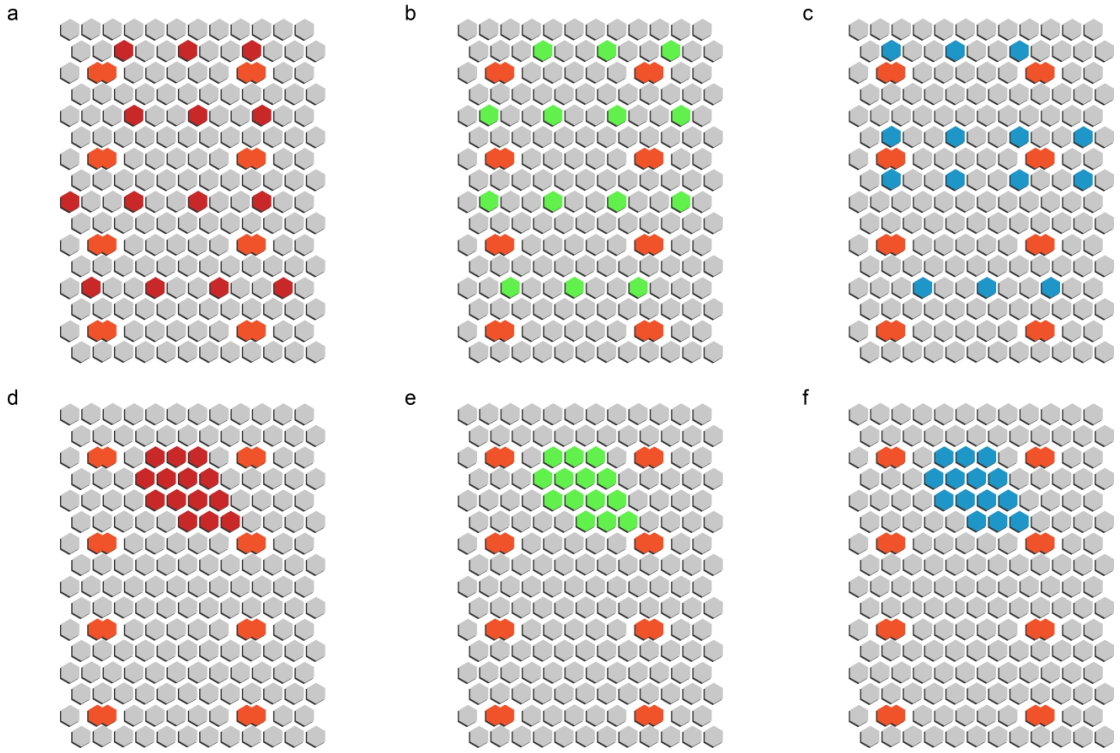

fig. S9. Schematic DNA origami staple layouts of self-quenching study. (**a** to **c**) Sparse dye patterning on DNA origami with ~15 nm dye-to-dye distance, for Atto 647N (red), Cy3 (green) and Atto 488 (blue). (**d** to **f**) Dense dye patterning on DNA origami with ~5 nm dye-to-dye distance, for Atto 647N (red), Cy3 (green) and Atto 488 (blue).

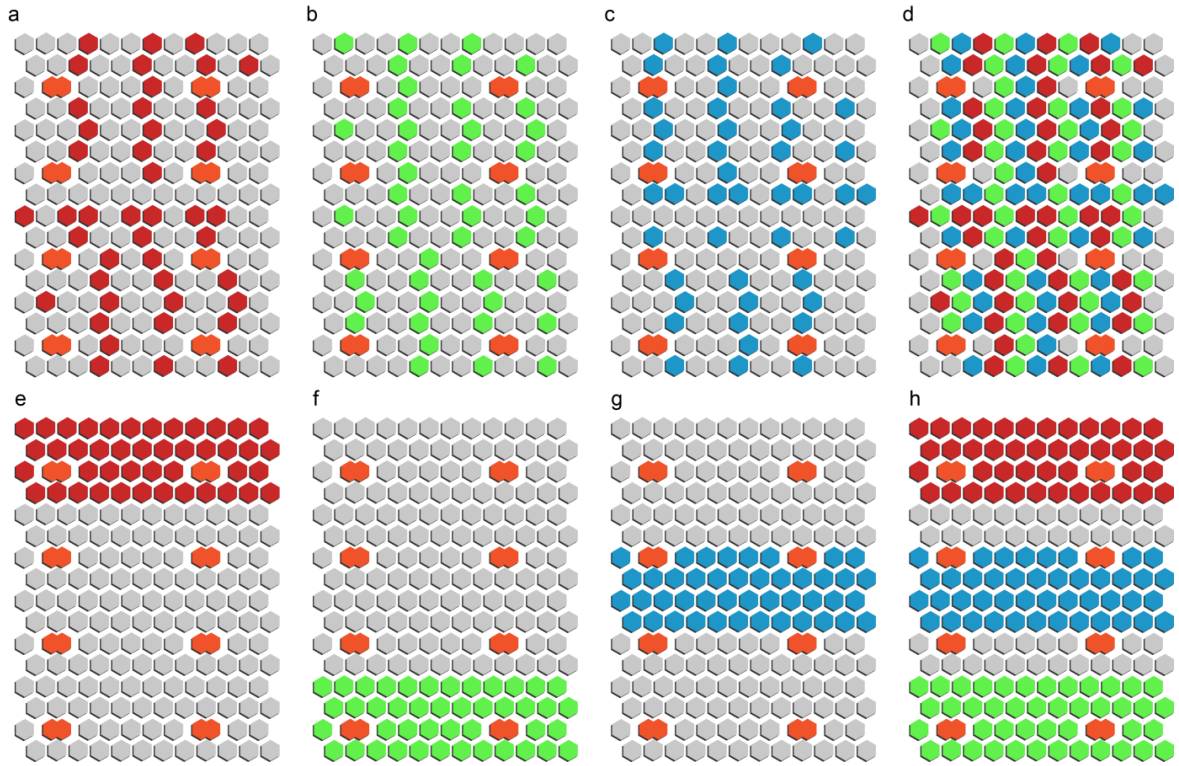

fig. S10. FRET investigation dye patterning (random and column-wise). (**a** to **d**) Mixed dye patterns, corresponding to Figure 2 (a-c) of the main text. (**e** to **h**) Column-wise dye pattern with inter-color spacing > 10 nm, corresponding to figure 2 (d-f) of the main text.

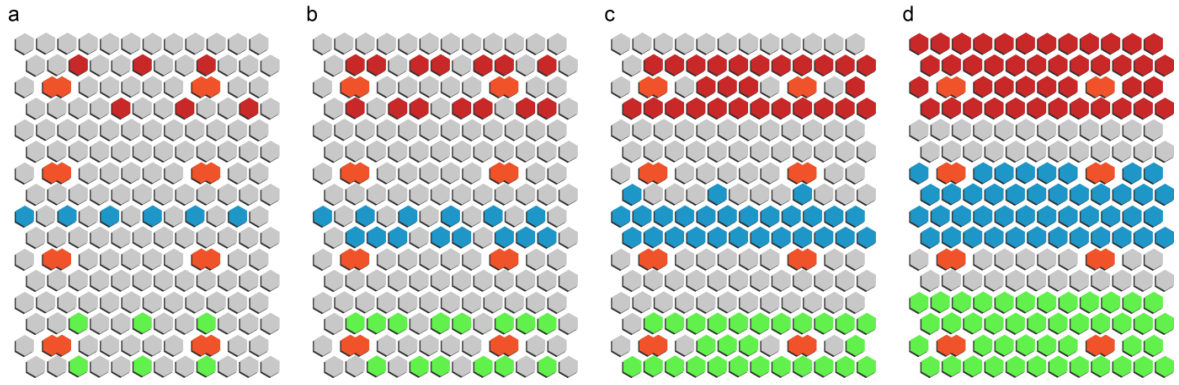

fig. S11. Intensity barcode dye patterns. The column-wise dye pattern separates distinct dyes > 10 nm and thus prevents FRET. (**a**) 6, (**b**) 14, (**c**) 27 and (**d**) 44 dyes attached per color. These layouts were used to independently control brightness levels for all three colors in the barcode studies.

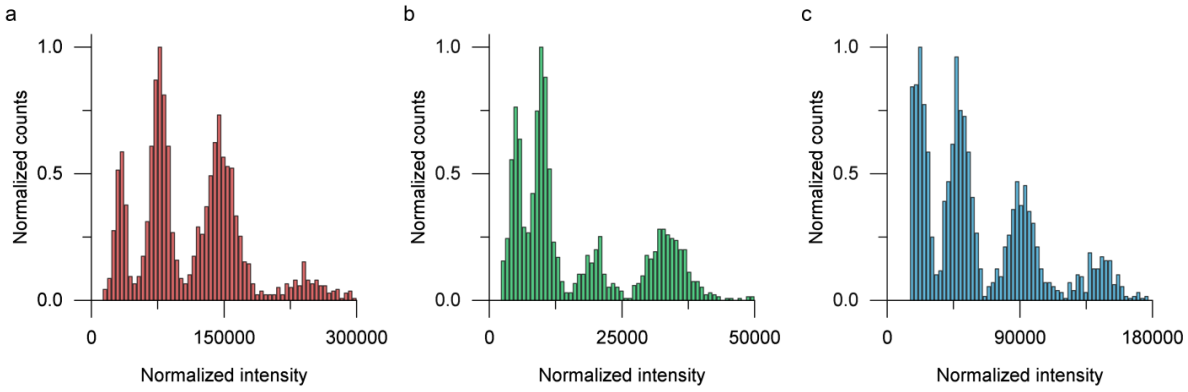

fig. S12. Intensity distributions for 124 barcodes in one sample. Exemplary intensity distributions of 25 distinct metafluorophores combined in one sample for (**a**) Atto 647N, (**b**) Cy3 and (**c**) Atto 488. Four levels (corresponding to 6, 14, 27 and 44 dyes) are clearly distinguishable. Overlapping regions in between peaks were identified (see software section) and barcodes displaying corresponding intensities were classified as unqualified.

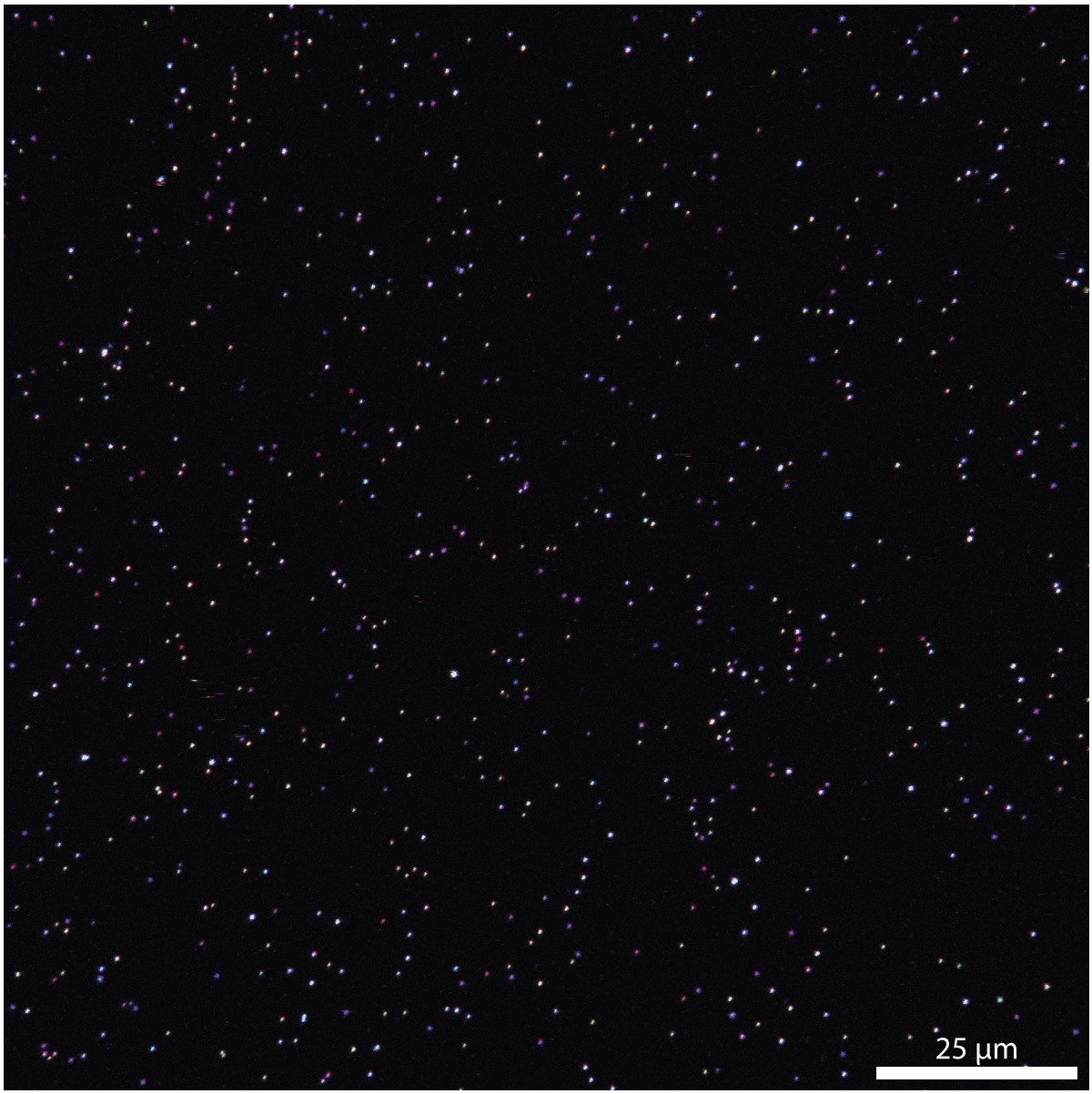

fig. S13. Exemplary fluorescent image of nucleic acid detection. Three-color confocal image of the nucleic acid detection experiment. Eight different barcodes were used (see table S7), six of them specifically tethered to the glass surface by synthetic DNA targets. Note that the fluorescent image (and thus the data analysis) is comparable to the image in Fig. 3b. Identifying all barcodes yields the first data set (i.e. the green bars) in figure S14b.

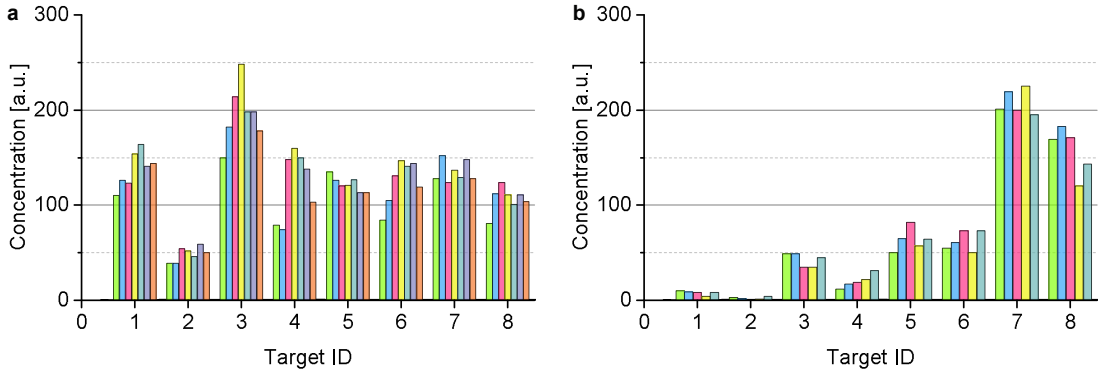

fig. S14. DNA detection calibration. (**a**) Eight DNA targets (See table S7) have been added to a detection assay at the same designed concentration (12.5 pM). Due to imperfect initial determination of target concentration and subsequent pipetting errors, the different targets are not detected with the same frequency. However, this target-to-target variation is constant between samples. By normalizing the average of each target to a reference target (here Target ID '3'), a calibration table can be produced. This allows the normalization of future measurements with the same targets. (**b**) Counted metafluorophores from the same experiment as shown in Fig. 4c, before normalization. In contrast to (a), targets have been added at different concentrations: 0 pM (targets 1 and 2), 1.5 pM (targets 3 and 4), 4.5 pM (targets 5 and 6) and 13.5 pM (targets 7 and 8). Since targets 1 and 2 have been omitted, the corresponding detections represent non-specifically bound metafluorophores and false-positives.

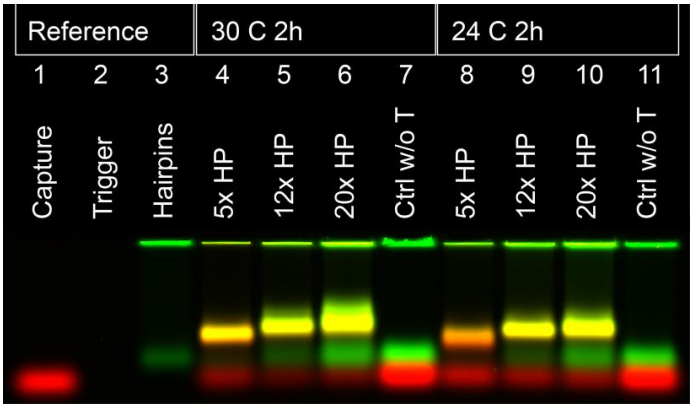

fig. S15. Triggered assembly formation gel assay. See 'triggered assembly gel assay protocol' for details. Capture strands (CAP) are labeled with Alexa 647 (red), hairpins (HP) with Cy3 (green). Trigger strands (T) are unlabeled. Lane 1 (1 pmol CAP) and 3 (12 pmol) serve as reference for CAP and HP migration speeds. Lanes 4 - 7 show reactions performed at 30 C, lanes 8 - 11 at 24 C, respectively (1 pmol CAP each).
Control lanes 7 and 11 are missing the (T) strand, thereby inhibiting triangle formation. Lanes only show CAP and HP bands, in agreement with the reference bands.
Assembly reactions in lanes 5 and 9 had 12 fold excess of HP strands over CAP strands (10.9 over T) and triangles (10 HP per triangle) are formed as indicated by the strong band migrating slower than the reference bands. The presence of a CAP reference band indicates that not all CAP strands formed a triangle. Since HP strands are in slight stoichiometric excess in regards to the triangles, a weak HP band is notable.
Lanes 6 and 10 contain reactions with higher HP excess. Product bands appear to migrate slightly slower than the product bands in lane 5 and 9, indicating only marginally increased triangle size.
Reactions in lanes 4 and 8 were had insufficient HP to fully assemble a triangle (<5 of 10 strands). Lanes show a faster product band than the corresponding 12x and 20x lanes, implying only partly assembled triangles. The green HP band is very weak, indicating complete usage of HP strands.

table S1. DNA origami staple sequences. The colors match those in the caDNAno layout shown in fig. S1. The first column denotes the staples position according to the caDNAno layout. The first digit indicates the helix the 5'-end is located on (y-coordinate), the succeeding number in brackets marks the number of base pairs the 5'-end is away from the boundary (x-coordinate). The second pair of numbers corresponds to the 3'-end in similar fashion.

Position	Sequence	Color	Description
0[111]1[95]	TAAATGAATTTTCTGTATGGGATTAATTTCTT		Structure strand
0[143]1[127]	TCTAAAGTTTTGTCGTCTTTCCAGCCGACAA		Structure strand
0[175]0[144]	TCCACAGACAGCCCTCATAGTTAGCGTAACGA		Structure strand
0[207]1[191]	TCACCAGTACAAACTACAACGCCTAGTACCAG		Structure strand
0[239]1[223]	AGGAACCCATGTACCGTAACACTTGATATAA		Structure strand
0[271]1[255]	CCACCCTCATTTTCAGGGATAGCAACCGTACT		Structure strand
0[47]1[31]	AGAAAGGAACAACTAAAGGAATTCAAAAAAA		Structure strand
0[79]1[63]	ACAACTTTCAACAGTTTCAGCGGATGTATCGG		Structure strand
1[128]4[128]	TGACAACTCGCTGAGGCTTGCATTATACCAAGCGCGATGATAAA		Structure strand
1[160]2[144]	TTAGGATTGGCTGAGACTCCTCAATAACCGAT		Structure strand
1[192]4[192]	GCGGATAACCTATTATTCTGAAACAGACGATTGGCCTTGAAGAGCCAC		Structure strand
1[224]3[223]	GTATAGCAAACAGTTAATGCCCAATCCTCA		Structure strand
1[256]4[256]	CAGGAGGTGGGGTCAGTGCCTTGAGTCTCTGAATTTACCGGGAACCAG		Structure strand
1[32]3[31]	AGGCTCCAGAGGCTTTGAGGACACGGGTAA		Structure strand
1[64]4[64	TTTATCAGGACAGCATCGGAACGACACCAACCTAAAACGAGGTCAATC		Structure strand
1[96]3[95]	AAACAGCTTTTTGCGGGATCGTCAACACTAAA		Structure strand
10[111]8[112]	TTGCTCCTTTCAAATATCGCGTTTGAGGGGGT		Structure strand
10[143]9[159]	CCAACAGGAGCGAACCAGACCGGAGCCTTTAC		Structure strand
10[175]8[176]	TTAACGTCTAACATAAAAACAGGTAACGGA		Structure strand
10[207]8[208]	ATCCCAATGAGAATTAACTGAACAGTTACCAG		Structure strand
10[239]8[240]	GCCAGTTAGAGGGTAATTGAGCGCTTTAAGAA		Structure strand
10[271]8[272]	ACGCTAACACCCACAAGAATTGAAAATAGC		Structure strand
10[47]8[48]	CTGTAGCTTGACTATTATAGTCAGTTCATTGA		Structure strand
10[79]8[80]	GATGGCTTATCAAAAAGATTAAGAGCGTCC		Structure strand
11[128]13[127]	TTTGGGGATAGTAGTAGCATTAAAAGGCCG		Structure strand
11[160]12[144]	CCAATAGCTCATCGTAGGAATCATGGCATCAA		Structure strand
11[192]13[191]	TATCCGGTCTCATCGAGAACAAGCGACAAAAG		Structure strand
11[224]13[223]	GCGAACCTCCAAGAACGGGTATGACAATAA		Structure strand
11[256]13[255]	GCCTTAAACCAATCAATAATCGGCACGCGCCT		Structure strand
11[32]13[31]	AACAGTTTTGTACCAAAAACATTTTATTTC		Structure strand
11[64]13[63]	GATTTAGTCAATAAAGCCTCAGAGAACCCTCA		Structure strand
11[96]13[95]	AATGGTCAACAGGCAAGGCAAAGAGTAATGTG		Structure strand
12[111]10[112]	TAAATCATATAACCTGTTTAGCTAACCTTTAA		Structure strand
12[143]11[159]	TTCTACTACGCGAGCTGAAAAGGTTACCGCGC		Structure strand
12[175]10[176]	TTTTATTTAAGCAAATCAGATATTTTTTGT		Structure strand
12[207]10[208]	GTACCGCAATTCTAAGAACGCGAGTATTATTT		Structure strand
12[239]10[240]	CTTATCATTCCCGACTTGCGGGAGCCTAATTT		Structure strand

12[271]10[272]	TGTAGAAATCAAGATTAGTTGCTCTTACCA		Structure strand
12[47]10[48]	TAAATCGGGATTCCCAATTCTGCGATATAATG		Structure strand
12[79]10[80]	AAATTAAGTTGACCATTAGATACTTTTGCG		Structure strand
13[128]15[127]	GAGACAGCTAGCTGATAAATTAATTTTTGT		Structure strand
13[160]14[144]	GTAATAAGTTAGGCAGAGGCATTTATGATATT		Structure strand
13[192]15[191]	GTAAAGTAATCGCCATATTTAACAAAACTTTT		Structure strand
13[224]15[223]	ACAACATGCCAACGCTCAACAGTCTTCTGA		Structure strand
13[256]15[255]	GTTTATCAATATGCGTTATACAAACCGACCGT		Structure strand
13[32]15[31]	AACGCAAAATCGATGAACGGTACCGGTTGA		Structure strand
13[64]15[63]	TATATTTTGTCATTGCCTGAGAGTGGAAGATT		Structure strand
13[96]15[95]	TAGGTAAACTATTTTTGAGAGATCAAACGTTA		Structure strand
14[111]12[112]	GAGGGTAGGATTCAAAAGGGTGAGACATCCAA		Structure strand
14[143]13[159]	CAACCGTTTCAAATCACCATCAATTCGAGCCA		Structure strand
14[175]12[176]	CATGTAATAGAATATAAAGTACCAAGCCGT		Structure strand
14[207]12[208]	AATTGAGAATTCTGTCCAGACGACTAAACCAA		Structure strand
14[239]12[240]	AGTATAAAGTTCAGCTAATGCAGATGTCTTTC		Structure strand
14[271]12[272]	TTAGTATCACAATAGATAAGTCCACGAGCA		Structure strand
14[47]12[48]	AACAAGAGGGATAAAAATTTTTAGCATAAAGC		Structure strand
14[79]12[80]	GCTATCAGAAATGCAATGCCTGAATTAGCA		Structure strand
15[128]18[128]	TAAATCAAAATAATTCGCGTCTCGGAAACCAGGCAAAGGGAAGG		Structure strand
15[160]16[144]	ATCGCAAGTATGTAAATGCTGATGATAGGAAC		Structure strand
15[192]18[192]	TCAAATATAACCTCCGGCTTAGGTAACAATTTCATTTGAAGGCGAATT		Structure strand
15[224]17[223]	CCTAAATCAAAATCATAGGTCTAAACAGTA		Structure strand
15[256]18[256]	GTGATAAAAAGACGCTGAGAAGAGATAACCTTGCTTCTGTTCGGGAGA		Structure strand
15[32]17[31]	TAATCAGCGGATTGACCGTAATCGTAACCG		Structure strand
15[64]18[64]	GTATAAGCCAACCCGTCGGATTCTGACGACAGTATCGGCCGCAAGGCG		Structure strand
15[96]17[95]	ATATTTTGGCTTTCATCAACATTATCCAGCCA		Structure strand
16[111]14[112]	TGTAGCCATTAAAATTCGCATTAAATGCCGGA		Structure strand
16[143]15[159]	GCCATCAAGCTCATTTTTTAACCACAAATCCA		Structure strand
16[175]14[176]	TATAACTAACAAAGAACGCGAGAACGCCAA		Structure strand
16[207]14[208]	ACCTTTTTATTTTAGTTAATTTCATAGGGCTT		Structure strand
16[239]14[240]	GAATTTATTTAATGGTTTGAAATATTCTTACC		Structure strand
16[271]14[272]	CTTAGATTTAAGGCGTTAAATAAAGCCTGT		Structure strand
16[47]14[48]	ACAAACGGAAAAGCCCCAAAAACACTGGAGCA		Structure strand
16[79]14[80]	GCGAGTAAAAATATTTAAATTGTTACAAAG		Structure strand
17[160]18[144]	AGAAAACAAAGAAGATGATGAAACAGGCTGCG		Structure strand
17[224]19[223]	CATAAATCTTTGAATACCAAGTGTTAGAAC		Structure strand
17[32]19[31]	TGCATCTTTCCCAGTCACGACGGCCTGCAG		Structure strand
17[96]19[95]	GCTTTCCGATTACGCCAGCTGGCGGCTGTTTC		Structure strand
18[111]16[112]	TCTTCGCTGCACCGCTTCTGGTGCGGCCTTCC		Structure strand
18[143]17[159]	CAACTGTTGCGCCATTCGCCATTCAAACATCA		Structure strand
18[175]16[176]	CTGAGCAAAAATTAATTACATTTTGGGTTA		Structure strand
18[207]16[208]	CGCGCAGATTACCTTTTTTAATGGGAGAGACT		Structure strand
18[239]16[240]	CCTGATTGCAATATATGTGAGTGATCAATAGT		Structure strand

18[271]16[272]	CTTTTACAAAATCGTCGCTATTAGCGATAG		Structure strand
18[47]16[48]	CCAGGGTTGCCAGTTTGAGGGGACCCGTGGGA		Structure strand
18[79]16[80]	GATGTGCTTCAGGAAGATCGCACAATGTGA		Structure strand
19[160]20[144]	GCAATTCACATATTCCTGATTATCAAAGTGTA		Structure strand
19[224]21[223]	CTACCATAGTTTGAGTAACATTTAAAATAT		Structure strand
19[32]21[31]	GTCGACTTCGGCCAACGCGCGGGGTTTTTC		Structure strand
19[96]21[95]	CTGTGTGATTGCGTTGCGCTCACTAGAGTTGC		Structure strand
2[111]0[112]	AAGGCCGCTGATACCGATAGTTGCGACGTTAG		Structure strand
2[143]1[159]	ATATTCGGAACCATCGCCCACGCAGAGAAGGA		Structure strand
2[175]0[176]	TATTAAGAAGCGGGGTTTTGCTCGTAGCAT		Structure strand
2[207]0[208]	TTTCGGAAGTGCCGTCGAGAGGGTGAGTTTCG		Structure strand
2[239]0[240]	GCCCGTATCCGGAATAGGTGTATCAGCCCAAT		Structure strand
2[271]0[272]	GTTTTAACTTAGTACCGCCACCCAGAGCCA		Structure strand
2[47]0[48]	ACGGCTACAAAAGGAGCCTTTAATGTGAGAAT		Structure strand
2[79]0[80]	CAGCGAAACTTGCTTTCGAGGTGTTGCTAA		Structure strand
20[111]18[112]	CACATTAAAATTGTTATCCGCTCATGCGGGCC		Structure strand
20[143]19[159]	AAGCCTGGTACGAGCCGGAAGCATAGATGATG		Structure strand
20[175]18[176]	ATTATCATTCAATATAATCCTGACAATTAC		Structure strand
20[207]18[208]	GCGGAACATCTGAATAATGGAAGGTACAAAAT		Structure strand
20[239]18[240]	ATTTTAAAATCAAAATTATTTGCACGGATTCG		Structure strand
20[271]18[272]	CTCGTATTAGAAATTGCGTAGATACAGTAC		Structure strand
20[47]18[48]	TTAATGAACTAGAGGATCCCCGGGGGGTAACG		Structure strand
20[79]18[80]	TTCCAGTCGTAATCATGGTCATAAAAGGGG		Structure strand
21[120]23[127]	CCCAGCAGGCGAAAAATCCCTTATAAATCAAGCCGGCG		Structure strand
21[160]22[144]	TCAATATCGAACCTCAAATATCAATTCCGAAA		Structure strand
21[184]23[191]	TCAACAGTTGAAAGGAGCAAATGAAAAATCTAGAGATAGA		Structure strand
21[224]23[223]	CTTTAGGGCCTGCAACAGTGCCAATACGTG		Structure strand
21[248]23[255]	AGATTAGAGCCGTCAAAAAACAGAGGTGAGGCCTATTAGT		Structure strand
21[32]23[31]	TTTTCACTCAAAGGGCGAAAAACCATCACC		Structure strand
21[56]23[63	AGCTGATTGCCCTTCAGAGTCCACTATTAAAGGGTGCCGT		Structure strand
21[96]23[95]	AGCAAGCGTAGGGTTGAGTGTTGTAGGGAGCC		Structure strand
22[111]20[112]	GCCCGAGAGTCCACGCTGGTTTGCAGCTAACT		Structure strand
22[143]21[159]	TCGGCAAATCCTGTTTGATGGTGGACCCTCAA		Structure strand
22[175]20[176]	ACCTTGCTTGGTCAGTTGGCAAAGAGCGGA		Structure strand
22[207]20[208]	AGCCAGCAATTGAGGAAGGTTATCATCATTTT		Structure strand
22[239]20[240]	TTAACACCAGCACTAACAACTAATCGTTATTA		Structure strand
22[271]20[272]	CAGAAGATTAGATAATACATTTGTCGACAA		Structure strand
22[47]20[48]	CTCCAACGCAGTGAGACGGGCAACCAGCTGCA		Structure strand
22[79]20[80]	TGGAACAACCGCCTGGCCCTGAGGCCCGCT		Structure strand
23[128]23[159]	AACGTGGCGAGAAAGGAAGGGAAACCAGTAA		Structure strand
23[160]22[176]	TAAAAGGGACATTCTGGCCAACAAAGCATC		Structure strand
23[192]22[208]	ACCCTTCTGACCTGAAAGCGTAAGACGCTGAG		Structure strand
23[224]22[240]	GCACAGACAATATTTTTGAATGGGGTCAGTA		Structure strand
23[256]22[272]	CTTTAATGCGCGAACTGATAGCCCCACCAG		Structure strand

23[32]22[48]	CAAATCAAGTTTTTTGGGGTCGAAACGTGGA		Structure strand
23[64]22[80]	AAAGCACTAAATCGGAACCCTAATCCAGTT		Structure strand
23[96]22[112]	CCCGATTTAGAGCTTGACGGGGAAAAAGAATA		Structure strand
3[160]4[144]	TTGACAGGCCACCACCAGAGCCGCGATTTGTA		Structure strand
3[224]5[223]	TTAAAGCCAGAGCCGCCACCCTCGACAGAA		Structure strand
3[32]5[31]	AATACGTTTGAAAGAGGACAGACTGACCTT		Structure strand
3[96]5[95]	ACACTCATCCATGTTACTTAGCCGAAAGCTGC		Structure strand
4[111]2[112]	GACCTGCTCTTTGACCCCCAGCGAGGGAGTTA		Structure strand
4[143]3[159]	TCATCGCCAACAAAGTACAACGGACGCCAGCA		Structure strand
4[175]2[176]	CACCAGAAAGGTTGAGGCAGGTCATGAAAG		Structure strand
4[207]2[208]	CCACCCTCTATTCACAAACAAATACCTGCCTA		Structure strand
4[239]2[240]	GCCTCCCTCAGAATGGAAAGCGCAGTAACAGT		Structure strand
4[271]2[272]	AAATCACCTTCCAGTAAGCGTCAGTAATAA		Structure strand
4[47]2[48]	GACCAACTAATGCCACTACGAAGGGGGTAGCA		Structure strand
4[79]2[80]	GCGCAGACAAGAGGCAAAAGAATCCCTCAG		Structure strand
5[160]6[144]	GCAAGGCCTCACCAGTAGCACCATGGGCTTGA		Structure strand
5[224]7[223]	TCAAGTTTCATTAAAGGTGAATATAAAAGA		Structure strand
5[32]7[31]	CATCAAGTAAAACGAACTAACGAGTTGAGA		Structure strand
5[96]7[95]	TCATTCAGATGCGATTTTAAGAACAGGCATAG		Structure strand
6[111]4[112]	ATTACCTTTGAATAAGGCTTGCCCAAATCCGC		Structure strand
6[143]5[159]	GATGGTTTGAACGAGTAGTAAATTTACCATTA		Structure strand
6[175]4[176]	CAGCAAAAGGAAACGTCACCAATGAGCCGC		Structure strand
6[207]4[208]	TCACCGACGCACCGTAATCAGTAGCAGAACCG		Structure strand
6[239]4[240]	GAAATTATTGCCTTTAGCGTCAGACCGGAACC		Structure strand
6[271]4[272]	ACCGATTGTCGGCATTTTCGGTCATAATCA		Structure strand
6[47]4[48]	TACGTTAAAGTAATCTTGACAAGAACCGAACT		Structure strand
6[79]4[80]	TTATACCACCAAATCAACGTAACGAACGAG		Structure strand
7[120]9[127]	CGTTTACCAGACGACAAAGAAGTTTTGCCATAATTCGA		Structure strand
7[160]8[144]	TTATTACGAAGAACTGGCATGATTGCGAGAGG		Structure strand
7[184]9[191]	CGTAGAAAATACATACCGAGGAAACGCAATAAGAAGCGCA		Structure strand
7[224]9[223]	AACGCAAAGATAGCCGAACAAACCCTGAAC		Structure strand
7[248]9[255]	GTTTATTTTGTCACAATCTTACCGAAGCCCTTTAATATCA		Structure strand
7[32]9[31]	TTTAGGACAAATGCTTTAAACAATCAGGTC		Structure strand
7[56]9[63]	ATGCAGATACATAACGGGAATCGTCATAAATAAAGCAAAG		Structure strand
7[96]9[95]	TAAGAGCAAATGTTTAGACTGGATAGGAAGCC		Structure strand
8[111]6[112]	AATAGTAAACACTATCATAACCCTCATTGTGA		Structure strand
8[143]7[159]	CTTTTGCAGATAAAAACCAAAATAAAGACTCC		Structure strand
8[175]6[176]	ATACCCAACAGTATGTTAGCAAATTAGAGC		Structure strand
8[207]6[208]	AAGGAAACATAAAGGTGGCAACATTATCACCG		Structure strand
8[239]6[240]	AAGTAAGCAGACACCACGGAATAATATTGACG		Structure strand
8[271]6[272]	AATAGCTATCAATAGAAAATTCAACATTCA		Structure strand
8[47]6[48]	ATCCCCCTATACCACATTCAACTAGAAAAATC		Structure strand
8[79]6[80]	AATACTGCCCAAAAGGAATTACGTGGCTCA		Structure strand
9[128]11[127]	GCTTCAATCAGGATTAGAGAGTTATTTTCA		Structure strand

9[160]10[144]	AGAGAGAAAAAAATGAAAATAGCAAGCAAACT		Structure strand
9[192]11[191]	TTAGACGGCCAAATAAGAAACGATAGAAGGCT		Structure strand
9[224]11[223]	AAAGTCACAAAATAAACAGCCAGCGTTTTA		Structure strand
9[256]11[255]	GAGAGATAGAGCGTCTTTCCAGAGGTTTTGAA		Structure strand
9[32]11[31]	TTTACCCCAACATGTTTTAAATTTCCATAT		Structure strand
9[64]11[63]	CGGATTGCAGAGCTTAATTGCTGAAACGAGTA		Structure strand
9[96]11[95]	CGAAAGACTTTGATAAGAGGTCATATTTCGCA		Structure strand
4[63]6[56]	Biotin – ATAAGGGAACCGGATATTCATTACGTCAGGACGTTGGGAA – 3’		5’-Biotin modification
4[127]6[120]	Biotin – TTGTGTCGTGACGAGAAACACCAAATTTCAACTTTAAT – 3’		5’-Biotin modification
4[191]6[184]	Biotin – CACCCTCAGAAACCATCGATAGCATTGAGCCATTTGGGAA – 3’		5’-Biotin modification
4[255]6[248]	Biotin – AGCCACCACTGTAGCGCGTTTTCAAGGGAGGGAAGGTAAA – 3’		5’-Biotin modification
18[63]20[56]	Biotin – ATTAAGTTTACCGAGCTCGAATTCGGGAAACCTGTCGTGC – 3’		5’-Biotin modification
18[127]20[120]	Biotin – GCGATCGGCAATTCCACACAACAGGTGCCTAATGAGTG – 3’		5’-Biotin modification
18[191]20[184]	Biotin – ATTCATTTTTGTTTGGATTATACTAAGAAACCACCAGAAG – 3’		5’-Biotin modification
18[255]20[248]	Biotin – AACAATAACGTAAAACAGAAATAAAAATCCTTTGCCCGAA – 3’		5’-Biotin modification

table S2. M13mp18 scaffold sequence.

TTCCCTTCCTTTCTCGCCACGTTCGCCGGCTTTCCCCGTCAAGCTCTAAATCGGGGGCTCCCTTTAGGGTTCCGATTTAGTGCTTTACGGCACCTCGACCCCAAAAAAC
TTGATTTGGGTGATGGTTCACGTAGTGGGCCATCGCCCTGATAGACGGTTTTTCGCCCTTTGACGTTGGAGTCCACGTTCTTTAATAGTGGACTCTTGTTCCAAACTGG
AACAACACTCAACCCTATCTCGGGCTATTCTTTTGATTTATAAGGGATTTTGCCGATTTCGGAACCACCATCAAACAGGATTTTCGCCTGCTGGGGCAAACCAGCGTGG
ACCGCTTGCTGCAACTCTCTCAGGGCCAGGCGGTGAAGGGCAATCAGCTGTTGCCCGTCTCACTGGTGAAAAGAAAAACCACCCTGGCGCCCAATACGCAAACCGCCTC
TCCCCGCGCGTTGGCCGATTCATTAATGCAGCTGGCACGACAGGTTTCCCGACTGGAAAGCGGGCAGTGAGCGCAACGCAATTAATGTGAGTTAGCTCACTCATTAGGC
ACCCCAGGCTTTACACTTTATGCTTCCGGCTCGTATGTTGTGTGGAATTGTGAGCGGATAACAATTTCACACAGGAAACAGCTATGACCATGATTACGAATTCGAGCTC
GGTACCCGGGGATCCTCTAGAGTCGACCTGCAGGCATGCAAGCTTGGCACTGGCCGTCGTTTTACAACGTCGTGACTGGGAAAACCCTGGCGTTACCCAACTTAATCGC
CTTGCAGCACATCCCCCTTTCGCCAGCTGGCGTAATAGCGAAGAGGCCCGCACCGATCGCCCTTCCCAACAGTTGCGCAGCCTGAATGGCGAATGGCGCTTTGCCTGGT
TTCCGGCACCAGAAGCGGTGCCGGAAAGCTGGCTGGAGTGCGATCTTCCTGAGGCCGATACTGTCGTCGTCCCCTCAAACTGGCAGATGCACGGTTACGATGCGCCCAT
CTACACCAACGTGACCTATCCCATTACGGTCAATCCGCCGTTTGTTCCCACGGAGAATCCGACGGGTTGTTACTCGCTCACATTTAATGTTGATGAAAGCTGGCTACAG
GAAGGCCAGACGCGAATTATTTTTGATGGCGTTCCTATTGGTTAAAAAATGAGCTGATTTAACAAAAATTTAATGCGAATTTTAACAAAATATTAACGTTTACAATTTA
AATATTTGCTTATACAATCTTCCTGTTTTTGGGGCTTTTCTGATTATCAACCGGGGTACATATGATTGACATGCTAGTTTTACGATTACCGTTCATCGATTCTCTTGTT
TGCTCCAGACTCTCAGGCAATGACCTGATAGCCTTTGTAGATCTCTCAAAAATAGCTACCCTCTCCGGCATTAATTTATCAGCTAGAACGGTTGAATATCATATTGATG
GTGATTTGACTGTCTCCGGCCTTTCTCACCCTTTTGAATCTTTACCTACACATTACTCAGGCATTGCATTTAAAATATATGAGGGTTCTAAAAATTTTTATCCTTGCGT
TGAAATAAAGGCTTCTCCCGCAAAAGTATTACAGGGTCATAATGTTTTTGGTACAACCGATTTAGCTTTATGCTCTGAGGCTTTATTGCTTAATTTTGCTAATTCTTTG
CCTTGCCTGTATGATTTATTGGATGTTAATGCTACTACTATTAGTAGAATTGATGCCACCTTTTCAGCTCGCGCCCCAAATGAAAATATAGCTAAACAGGTTATTGACC
ATTTGCGAAATGTATCTAATGGTCAAACTAAATCTACTCGTTCGCAGAATTGGGAATCAACTGTTATATGGAATGAAACTTCCAGACACCGTACTTTAGTTGCATATTT
AAAACATGTTGAGCTACAGCATTATATTCAGCAATTAAGCTCTAAGCCATCCGCAAAAATGACCTCTTATCAAAAGGAGCAATTAAAGGTACTCTCTAATCCTGACCTG
TTGGAGTTTGCTTCCGGTCTGGTTCGCTTTGAAGCTCGAATTAAAACGCGATATTTGAAGTCTTTCGGGCTTCCTCTTAATCTTTTTGATGCAATCCGCTTTGCTTCTG
ACTATAATAGTCAGGGTAAAGACCTGATTTTTGATTTATGGTCATTCTCGTTTTCTGAACTGTTTAAAGCATTTGAGGGGGATTCAATGAATATTTATGACGATTCCGC
AGTATTGGACGCTATCCAGTCTAAACATTTTACTATTACCCCCTCTGGCAAAACTTCTTTTGCAAAAGCCTCTCGCTATTTTGGTTTTTATCGTCGTCTGGTAAACGAG
GGTTATGATAGTGTTGCTCTTACTATGCCTCGTAATTCCTTTTGGCGTTATGTATCTGCATTAGTTGAATGTGGTATTCCTAAATCTCAACTGATGAATCTTTCTACCT
GTAATAATGTTGTTCCGTTAGTTCGTTTTATTAACGTAGATTTTTCTTCCCAACGTCCTGACTGGTATAATGAGCCAGTTCTTAAAATCGCATAAGGTAATTCACAATG
ATTAAAGTTGAAATTAAACCATCTCAAGCCCAATTTACTACTCGTTCTGGTGTTTCTCGTCAGGGCAAGCCTTATTCACTGAATGAGCAGCTTTGTTACGTTGATTTGG
GTAATGAATATCCGGTTCTTGTCAAGATTACTCTTGATGAAGGTCAGCCAGCCTATGCGCCTGGTCTGTACACCGTTCATCTGTCCTCTTTCAAAGTTGGTCAGTTCGG
TTCCCTTATGATTGACCGTCTGCGCCTCGTTCCGGCTAAGTAACATGGAGCAGGTCGCGGATTTCGACACAATTTATCAGGCGATGATACAAATCTCCGTTGTACTTTG
TTTCGCGCTTGGTATAATCGCTGGGGGTCAAAGATGAGTGTTTTAGTGTATTCTTTTGCCTCTTTCGTTTTAGGTTGGTGCCTTCGTAGTGGCATTACGTATTTTACCC
GTTTAATGGAAACTTCCTCATGAAAAAGTCTTTAGTCCTCAAAGCCTCTGTAGCCGTTGCTACCCTCGTTCCGATGCTGTCTTTCGCTGCTGAGGGTGACGATCCCGCA
AAAGCGGCCTTTAACTCCCTGCAAGCCTCAGCGACCGAATATATCGGTTATGCGTGGGCGATGGTTGTTGTCATTGTCGGCGCAACTATCGGTATCAAGCTGTTTAAGA
AATTCACCTCGAAAGCAAGCTGATAAACCGATACAATTAAAGGCTCCTTTTGGAGCCTTTTTTTTGGAGATTTTCAACGTGAAAAAATTATTATTCGCAATTCCTTTAG
TTGTTCCTTTCTATTCTCACTCCGCTGAAACTGTTGAAAGTTGTTTAGCAAAATCCCATACAGAAAATTCATTTACTAACGTCTGGAAAGACGACAAAACTTTAGATCG
TTACGCTAACTATGAGGGCTGTCTGTGGAATGCTACAGGCGTTGTAGTTTGTACTGGTGACGAAACTCAGTGTTACGGTACATGGGTTCCTATTGGGCTTGCTATCCCT
GAAAATGAGGGTGGTGGCTCTGAGGGTGGCGGTTCTGAGGGTGGCGGTTCTGAGGGTGGCGGTACTAAACCTCCTGAGTACGGTGATACACCTATTCCGGGCTATACTT
ATATCAACCCTCTCGACGGCACTTATCCGCCTGGTACTGAGCAAAACCCCGCTAATCCTAATCCTTCTCTTGAGGAGTCTCAGCCTCTTAATACTTTCATGTTTCAGAA
TAATAGGTTCCGAAATAGGCAGGGGGCATTAACTGTTTATACGGGCACTGTTACTCAAGGCACTGACCCCGTTAAAACTTATTACCAGTACACTCCTGTATCATCAAAA
GCCATGTATGACGCTTACTGGAACGGTAAATTCAGAGACTGCGCTTTCCATTCTGGCTTTAATGAGGATTTATTTGTTTGTGAATATCAAGGCCAATCGTCTGACCTGC
CTCAACCTCCTGTCAATGCTGGCGGCGGCTCTGGTGGTGGTTCTGGTGGCGGCTCTGAGGGTGGTGGCTCTGAGGGTGGCGGTTCTGAGGGTGGCGGCTCTGAGGGAGG
CGGTTCCGGTGGTGGCTCTGGTTCCGGTGATTTTGATTATGAAAAGATGGCAAACGCTAATAAGGGGGCTATGACCGAAAATGCCGATGAAAACGCGCTACAGTCTGAC
GCTAAAGGCAAACTTGATTCTGTCGCTACTGATTACGGTGCTGCTATCGATGGTTTCATTGGTGACGTTTCCGGCCTTGCTAATGGTAATGGTGCTACTGGTGATTTTG
CTGGCTCTAATTCCCAAATGGCTCAAGTCGGTGACGGTGATAATTCACCTTTAATGAATAATTTCCGTCAATATTTACCTTCCCTCCCTCAATCGGTTGAATGTCGCCC
TTTTGTCTTTGGCGCTGGTAAACCATATGAATTTTCTATTGATTGTGACAAAATAAACTTATTCCGTGGTGTCTTTGCGTTTCTTTTATATGTTGCCACCTTTATGTAT
GTATTTTCTACGTTTGCTAACATACTGCGTAATAAGGAGTCTTAATCATGCCAGTTCTTTTGGGTATTCCGTTATTATTGCGTTTCCTCGGTTTCCTTCTGGTAACTTT
GTTCGGCTATCTGCTTACTTTTCTTAAAAAGGGCTTCGGTAAGATAGCTATTGCTATTTCATTGTTTCTTGCTCTTATTATTGGGCTTAACTCAATTCTTGTGGGTTAT
CTCTCTGATATTAGCGCTCAATTACCCTCTGACTTTGTTCAGGGTGTTCAGTTAATTCTCCCGTCTAATGCGCTTCCCTGTTTTTATGTTATTCTCTCTGTAAAGGCTG
CTATTTTCATTTTTGACGTTAAACAAAAAATCGTTTCTTATTTGGATTGGGATAAATAATATGGCTGTTTATTTTGTAACTGGCAAATTAGGCTCTGGAAAGACGCTCG
TTAGCGTTGGTAAGATTCAGGATAAAATTGTAGCTGGGTGCAAAATAGCAACTAATCTTGATTTAAGGCTTCAAAACCTCCCGCAAGTCGGGAGGTTCGCTAAAACGCC
TCGCGTTCTTAGAATACCGGATAAGCCTTCTATATCTGATTTGCTTGCTATTGGGCGCGGTAATGATTCCTACGATGAAAATAAAAACGGCTTGCTTGTTCTCGATGAG
TGCGGTACTTGGTTTAATACCCGTTCTTGGAATGATAAGGAAAGACAGCCGATTATTGATTGGTTTCTACATGCTCGTAAATTAGGATGGGATATTATTTTTCTTGTTC
AGGACTTATCTATTGTTGATAAACAGGCGCGTTCTGCATTAGCTGAACATGTTGTTTATTGTCGTCGTCTGGACAGAATTACTTTACCTTTTGTCGGTACTTTATATTC
TCTTATTACTGGCTCGAAAATGCCTCTGCCTAAATTACATGTTGGCGTTGTTAAATATGGCGATTCTCAATTAAGCCCTACTGTTGAGCGTTGGCTTTATACTGGTAAG
AATTTGTATAACGCATATGATACTAAACAGGCTTTTTCTAGTAATTATGATTCCGGTGTTTATTCTTATTTAACGCCTTATTTATCACACGGTCGGTATTTCAAACCAT
TAAATTTAGGTCAGAAGATGAAATTAACTAAAATATATTTGAAAAAGTTTTCTCGCGTTCTTTGTCTTGCGATTGGATTTGCATCAGCATTTACATATAGTTATATAAC
CCAACCTAAGCCGGAGGTTAAAAAGGTAGTCTCTCAGACCTATGATTTTGATAAATTCACTATTGACTCTTCTCAGCGTCTTAATCTAAGCTATCGCTATGTTTTCAAG
GATTCTAAGGGAAAATTAATTAATAGCGACGATTTACAGAAGCAAGGTTATTCACTCACATATATTGATTTATGTACTGTTTCCATTAAAAAAGGTAATTCAAATGAAA
TTGTTAAATGTAATTAATTTTGTTTTCTTGATGTTTGTTTCATCATCTTCTTTTGCTCAGGTAATTGAAATGAATAATTCGCCTCTGCGCGATTTTGTAACTTGGTATT
CAAAGCAATCAGGCGAATCCGTTATTGTTTCTCCCGATGTAAAAGGTACTGTTACTGTATATTCATCTGACGTTAAACCTGAAAATCTACGCAATTTCTTTATTTCTGT
TTTACGTGCAAATAATTTTGATATGGTAGGTTCTAACCCTTCCATTATTCAGAAGTATAATCCAAACAATCAGGATTATATTGATGAATTGCCATCATCTGATAATCAG
GAATATGATGATAATTCCGCTCCTTCTGGTGGTTTCTTTGTTCCGCAAAATGATAATGTTACTCAAACTTTAAAATTAATAACGTTCGGGCAAAGGATTTAATACGAG
TTGTCGAATTGTTTGTAAAGTCTAATACTTCTAAATCCTCAAATGTATTATCTATTGACGGCTCTAATCTATTAGTTGTTAGTGCTCCTAAAGATATTTTAGATAACCT
TCCTCAATTCCTTTCAACTGTTGATTTGCCAACTGACCAGATATTGATTGAGGGTTTGATATTTGAGGTTCAGCAAGGTGATGCTTTAGATTTTTCATTTGCTGCTGGC
TCTCAGCGTGGCACTGTTGCAGGCGGTGTTAATACTGACCGCCTCACCTCTGTTTTATCTTCTGCTGGTGGTTCGTTCGGTATTTTTAATGGCGATGTTTTAGGGCTAT
CAGTTCGCGCATTAAAGACTAATAGCCATTCAAAAATATTGTCTGTGCCACGTATTCTTACGCTTTCAGGTCAGAAGGGTTCTATCTCTGTTGGCCAGAATGTCCCTTT
TATTACTGGTCGTGTGACTGGTGAATCTGCCAATGTAAATAATCCATTTCAGACGATTGAGCGTCAAAATGTAGGTATTTCCATGAGCGTTTTTCCTGTTGCAATGGCT
GGCGGTAATATTGTTCTGGATATTACCAGCAAGGCCGATAGTTTG

table S3. Fluorescently labeled DNA sequences.

Label	Handle
5' - GTGATGTAGGTGGTAGAGGAA – Atto 647N	staple – TTCCTCTACCACCTACATCAC – 3′
5' - TATGAGAAGTTAGGAATGTTA - Cy3	staple - TAACATTCCTAACTTCTCATA – 3′
5' - CGAGTTTAGGAGAGATGGTAA – Atto 488	staple - TTACCATCTCTCCTAAACTCG – 3′

table S4. Intensity barcode subset (25 of 124).

Barcode-No	RED	GRN	BLU	Subset No
1	6	0	0	
2	14	0	0	
3	27	0	0	
4	44	0	0	
5	0	6	0	
6	6	6	0	1
7	14	6	0	
8	27	6	0	
9	44	6	0	
10	0	14	0	
11	6	14	0	
12	14	14	0	
13	27	14	0	2
14	44	14	0	
15	0	27	0	
16	6	27	0	3
17	14	27	0	
18	27	27	0	
19	44	27	0	
20	0	44	0	
21	6	44	0	
22	14	44	0	
23	27	44	0	4
24	44	44	0	5
25	0	0	6	
26	6	0	6	
27	14	0	6	
28	27	0	6	6
29	44	0	6	7

30	0	6	6	
31	6	6	6	
32	14	6	6	
33	27	6	6	
34	44	6	6	
35	0	14	6	
36	6	14	6	
37	14	14	6	
38	27	14	6	
39	44	14	6	
40	0	27	6	
41	6	27	6	
42	14	27	6	
43	27	27	6	
44	44	27	6	
45	0	44	6	
46	6	44	6	
47	14	44	6	
48	27	44	6	
49	44	44	6	
50	0	0	14	
51	6	0	14	
52	14	0	14	
53	27	0	14	
54	44	0	14	
55	0	6	14	
56	6	6	14	
57	14	6	14	
58	27	6	14	8
59	44	6	14	
60	0	14	14	9
61	6	14	14	10
62	14	14	14	
63	27	14	14	
64	44	14	14	11
65	0	27	14	
66	6	27	14	
67	14	27	14	12
68	27	27	14	
69	44	27	14	13
70	0	44	14	

71	6	44	14	
72	14	44	14	
73	27	44	14	14
74	44	44	14	15
75	0	0	27	
76	6	0	27	
77	14	0	27	
78	27	0	27	
79	44	0	27	16
80	0	6	27	
81	6	6	27	
82	14	6	27	17
83	27	6	27	
84	44	6	27	
85	0	14	27	
86	6	14	27	
87	14	14	27	18
88	27	14	27	
89	44	14	27	19
90	0	27	27	20
91	6	27	27	
92	14	27	27	
93	27	27	27	
94	44	27	27	
95	0	44	27	
96	6	44	27	
97	14	44	27	21
98	27	44	27	
99	44	44	27	
100	0	0	44	
101	6	0	44	
102	14	0	44	
103	27	0	44	22
104	44	0	44	
105	0	6	44	23
106	6	6	44	
107	14	6	44	
108	27	6	44	
109	44	6	44	
110	0	14	44	
111	6	14	44	

112	14	14	44	
113	27	14	44	
114	44	14	44	
115	0	27	44	
116	6	27	44	
117	14	27	44	
118	27	27	44	
119	44	27	44	
120	0	44	44	24
121	6	44	44	25
122	14	44	44	
123	27	44	44	
124	44	44	44	

table S5. Intensity barcode subset (12 of 64).

Barcode-No	RED	GRN	BLU	Subset No
1	6	6	6	
2	14	6	6	
3	27	6	6	
4	44	6	6	
5	6	14	6	1
6	14	14	6	
7	27	14	6	
8	44	14	6	
9	6	27	6	
10	14	27	6	
11	27	27	6	2
12	44	27	6	
13	6	44	6	
14	14	44	6	3
15	27	44	6	
16	44	44	6	
17	6	6	14	
18	14	6	14	
19	27	6	14	4
20	44	6	14	
21	6	14	14	
22	14	14	14	5
23	27	14	14	
24	44	14	14	6
25	6	27	14	
26	14	27	14	
27	27	27	14	
28	44	27	14	
29	6	44	14	
30	14	44	14	
31	27	44	14	
32	44	44	14	
33	6	6	27	
34	14	6	27	
35	27	6	27	
36	44	6	27	
37	6	14	27	
38	14	14	27	

39	27	14	27	
40	44	14	27	
41	6	27	27	
42	14	27	27	
43	27	27	27	7
44	44	27	27	
45	6	44	27	8
46	14	44	27	
47	27	44	27	
48	44	44	27	9
49	6	6	44	
50	14	6	44	
51	27	6	44	
52	44	6	44	
53	6	14	44	
54	14	14	44	
55	27	14	44	
56	44	14	44	10
57	6	27	44	
58	14	27	44	11
59	27	27	44	
60	44	27	44	
61	6	44	44	12
62	14	44	44	
63	27	44	44	
64	44	44	44	

table S6. Intensity barcode subset (5 of 20).

Barcode-No	RED	GRN	BLU	Subset No
1	44	14	14	
2	14	44	14	1
3	14	14	44	
4	44	44	14	
5	44	14	44	2
6	14	44	44	
7	44	44	44	
8	14	14	14	
9	44	44	0	
10	44	0	44	3
11	0	44	44	
12	14	14	0	
13	14	0	14	
14	0	14	14	4
15	44	14	0	
16	44	0	14	
17	0	44	14	
18	14	44	0	5
19	14	0	44	
20	0	14	44	

table S7. DNA detection sequences and corresponding barcodes.

Target	Sequence	Barcode (RED-GRN-BLU)
1	5′ – GCAGTTTCCGACCGATATAGT TTT CGGTTGTACTGTGACCGATTC – 3′	14-44-14
2	5′ – TAGAGTCCAAGAGTCCTCGTT TTT CGGTTGTACTGTGACCGATTC – 3′	14-44-44
3	5′ – GGTTAAGGTCAACATCGTCTC TTT CGGTTGTACTGTGACCGATTC – 3′	14-14-14
4	5′ – CATGTCAGGAGATTTTCAGCC TTT CGGTTGTACTGTGACCGATTC – 3′	14-14-44
5	5′ – TACCCTATCTGAGTGAGTAGC TTT CGGTTGTACTGTGACCGATTC – 3′	44-14-14
6	5′ – CTTCCCGTTATGACAAGATGG TTT CGGTTGTACTGTGACCGATTC – 3′	44-14-44
7	5′ – CCCTAGTGCTTTTGGAGAAAC TTT CGGTTGTACTGTGACCGATTC – 3′	44-44-14
8	5′ – GGACACGGTATTCCTAATTCG TTT CGGTTGTACTGTGACCGATTC – 3′	44-44-44

table S8. Triggered assembly sequences.

Description	Sequence
Capture	Alexa 647 – CTCCTCGCCCTTGCTCACCAT – Biotin
Trigger	5′ – ATGGTGAGCAAGGGCGAGGAG … CCTCACCTCTACTCCCACCCACACGCACCCTC CCTCACCTCTACTCCCACCCACACGCACCCTC … CCTCACCTCTACTCCCACCCACACGCACCCTC CCTCACCTCTACTCCCACCCACACGCACCCTC – 3′
Hairpin	Cy3 – TCCCACCCACACGCACCCTC CCTCACCTCTAC … GAGGGTGCGTGTGGGTGGGA GTAGAGGTGAGG – 3′

protocol S1. DNA origami self-assembly.

Self-assembly was performed in a one-pot reaction with 20 µl total volume containing 10 nM scaffold strand (M13mp18), 100 nM folding staples and 150 nM biotinylated strands, 100 nM strands with dye-handle extension and 225 nM fluorescently-labeled anti-handles in folding buffer (1×TAE Buffer with 12.5 mM $MgCl_2$). The solution was heatshocked at 65 °C for 5 min to remove eventual secondary structures and subsequently cooled to 4 °C over the course of 1 h. DNA origami were purified by agarose gel electrophoresis (1.5 % agarose, 1×TAE Buffer with 12.5 mM $MgCl_2$) at 4.5 V/cm for 1.5 h, on ice. Gel bands were cut, crushed and filled into a 'Freeze 'N Squeeze' column and spun for 5 min at 1000×g at 4 °C.

protocol S2. Microscopy sample preparation.

Clean coverslip (No. 1.5, 18×18 mm^2, ≈0.17 mm thick) and microscopy slide (3×1 $inch^2$, 1 mm thick) with Isopropanol.
Build flow chamber by sandwiching two strips of sticky tape between coverslip and glass slide, ~ 20 µl volume.

Incubate 2 min with 20 µl 1 mg/ml BSA-Biotin in Buffer A (see Materials).
Rinse with 40 µl Buffer A.
Incubate 2 min with 20 µl 0.5 mg/ml Streptavidin in Buffer A.
Rinse with 40 µl Buffer A.
Rinse with 40 µl Buffer B (see Materials).
Incubate for 2 min with 20 µl ~300 pM DNA origami based metafluorophores.
Rinse with 40 µl Buffer B.

Seal chamber with epoxy.

protocol S3. Triggered assembly on surface.

Capture (CAP) and trigger (T) strands were annealed in a thermocycler directly before adding to the sample at 1 µM in 1x TAE with 12.5 mM $MgCl_2$ with 0.05% Tween20 (85 °C for 5 min, gradient from 85 °C to 10 °C in 15 min).
Hairpin (HP) strands were annealed in a thermocycler directly before adding to the sample at 1 µM in 1x TAE with 12.5 mM $MgCl_2$ (85 °C for 5 min, gradient from 85 °C to 10 °C in 15 min).

Build flow chamber with 3x sticky tape height, ~ 60 µl volume.
Incubate 2 min with 60 µl 1 mg/ml BSA-Biotin in Buffer A.
Rinse with 120 µl Buffer A.
Incubate 2 min with 60 µl 0.5 mg/ml Streptavidin in Buffer A.
Rinse with 120 µl Buffer A.
Rinse with 120 µl 1x TAE with 12.5mM $MgCl_2$ with 0.05% Tween-20.
Incubate 1 min with 60 µl 25 pM annealed CAP-T duplexes in 12.5mM $MgCl_2$ with 0.05% Tween-20.
Rinse with 120 µl 1x TAE with 12.5mM $MgCl_2$ with 0.05% Tween-20.
Incubate for 2 min with 60 µl 100 pM DNA origami standards.
Rinse with 120 µl 1x TAE with 12.5mM $MgCl_2$ with 0.05% Tween-20.

Incubate for 20 min with 60 µl 30 nM annealed HP.
Rinse with 120 µl 1x TAE with 12.5mM $MgCl_2$ with 0.05% Tween-20.
Repeat HP incubation 3 times.

Seal chamber.

protocol S4. Triggered assembly in solution and gel assay.

Triggered assembly of triangles for the gel assay was performed in a one-pot reaction. Capture strands (CAP), trigger strands (T) and fluorescently labeled hairpins (HP) were added in varying stoichiometric ratios to a total volume of 40 µl. CAP strands were at a final concentration of 100 nM, T strands at 110 nM and HP strands at 550 nM (5x), 1.325 µM (12x) or 2.2 µM (20x). Strands were diluted in 1x TAE with 12.5 mM MgCl2. HP strands were annealed in a thermocycler directly before adding to the triggered assembly reaction at 10 µM in 1x TAE with 12.5 mM $MgCl_2$ (85 C for 5 min, gradient from 85 C to 10 C in 15 min). The control sample did not contain the T strand but HP strands at 1.325 µM (12x). Assembly was performed in low retention PCR tubes at either 30 C or at 24 C for 2 h each.
Gel electrophoresis was performed using a 2% agarose gel in 1x TAE with 12.5 mM $MgCl_2$, with 4.5 V/cm for 3 h on ice.
Gel was scanned with a Typhoon scanner.

Materials

Unmodified DNA oligonucleotides were purchased from Integrated DNA Technologies. Fluorescently modified DNA oligonucleotides were purchased from Biosynthesis. Streptavidin was purchased from Invitrogen (Catalog number: S-888). Albumin, biotin labeled bovine (BSA-biotin) was obtained from Sigma Aldrich (Catalog Number: A8549). Glass slides and coverslips were purchased from VWR. M13mp18 scaffold was obtained from New England Biolabs. 'Freeze N Squeeze' columns were ordered from Bio-Rad.

Two buffers were used for sample preparation and imaging:

Buffer A (10 mM Tris-HCl, 100 mM NaCl, 0.05 % Tween-20, pH 8).

Buffer B (5 mM Tris-HCl, 10 mM $MgCl_2$, 1 mM EDTA, 0.05 % Tween-20, pH 8).

Optical setup

DNA origami-based metafluorophore imaging was performed on a Zeiss Axio Observer Z1 Inverted Fluorescence Microscope with Definite Focus and a Zeiss Colibri LED illumination system (ATTO 488: 470 nm, Cy3: 555 nm, ATTO 647N: 625 nm). We used a Zeiss Plan-apochromat (63x/1.40 Oil) oil-immersion objective and a Hamamatsu Orca-Flash 4.0 sCMOS camera.

ATTO 488: Zeiss filter set 38: (BP 470/40, FT 495, BP 525/50).

Cy3: Zeiss Filter Set 43 (BP 545/25, FT 570, BP 605/70).

ATTO 647N: Zeiss filter set 50 (BP 640/30, FT 660, BP 690/50).

Triggered assembly imaging was carried out on an inverted Nikon Eclipse Ti microscope using a Nikon TIRF illuminator with an oil-immersion objective (CFI Apo TIRF 100×, numerical aperture (NA) 1.49, oil).

Lasers: 488 nm (200 mW nominal, Coherent Sapphire), 561 nm (200 mW nominal, Coherent Sapphire) and 647 nm (300 mW nominal, MBP Communications).

Camera: iXon X3 DU-897 EMCCD (Andor Technologies)

Excitation filters: (ZT488/10, ZET561/10 and ZET640/20, Chroma Technology)

Multiband beam splitter: (ZT488rdc/ZT561rdc/ZT640rdc, Chroma Technology)

Emission filters: (ET525/50m, ET600/50m and ET700/75m, Chroma Technology)

Multiplexed nucleic acid detection was performed on a Zeiss LSM 780 confocal laser scanning microscope equipped with a ZEISS Plan-APO 63x/NA1.46 oil immersion objective and a GaAsP array for detection.

Lasers: 458 nm (Argon), 561 nm (DPSS), 647 nm (HeNe).

Software section

Spot detection, intensity analysis

After image acquisition, spot-detection was performed using a custom LabVIEW script. Here, 2D Gaussians were fitted within a 10x10 px^2 area around the center of the spots. The volume of the 2D Gaussian is proportional to the photon count and is thereby defined as intensity. Finally, one obtains a molecule-list with both, spatial coordinates and corresponding intensity values.

Barcode identification

All intensity values were plotted as a histogram and the local maxima (peaks) were fitted with Gaussians. Based on the intersections of these fits, the distinct intensity-level intervals could be determined.
Non-overlapping regions in between two peaks had to be identified and barcodes with a corresponding intensity had to be classified as qualified. To identify the overlapping interval between two peaks, the height of the intersection (x counts) of the corresponding fits was determined. By determining the intersections of the two Gaussians with half the height of their intersection ($x/2$ counts), the overlapping interval and boundaries for barcode levels were defined. Additionally, spots that did not meet the criteria of the robust subsets were removed (e.g. removal of barcodes that do not have three colors for the 64-subset.).

After removing the spots that did not qualify, the intensity values in the molecule-list were replaced with barcode-level indicators. Individual barcodes were identified by combining spots from the three molecule-lists (corresponding to the three recorded colors), which are in close proximity (i.e. < 500 nm).

Triggered assembly

Triggered assembly evaluation was performed by determining spot coordinates and spot intensities as described above. Colocalizations of red (Alexa 647) and green (Cy3) spots were grouped as triangles and blue (Atto 488) and green (Cy3) colocalizations as DNA origamis. Plotting the two groups together resulted in Figure 6c of the main test.

A.2 SUPPORTING INFORMATION FOR ASSOCIATED PUBLICATION P2

Supporting Information

Quantifying absolute addressability in DNA origami with molecular resolution

By

Maximilian T. Strauss*, **Florian Schüeder***, **Daniel Haas***, P. Nickels, Ralf Jungmann

** These authors contributed equally to this work*

published in

Nature Communications (2018)

Reprinted from [45].

Supplementary Information

Quantifying Absolute Addressability in DNA origami with Molecular Resolution

Maximilian T. Strauss, Florian Schueder, Daniel Haas, Philipp C. Nickels, and Ralf Jungmann

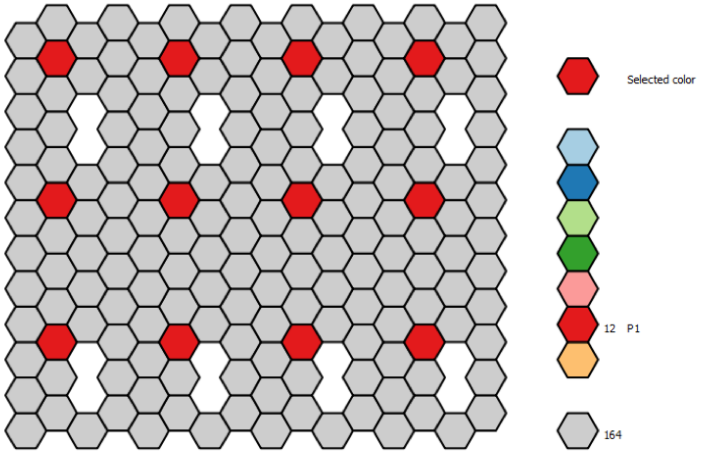

Supplementary Figure 1 | 20-nm DNA origami grid structure. Each hexagon represents a single staple, colored hexagons indicate a single staple extension at the 3'-end for DNA-PAINT probing.

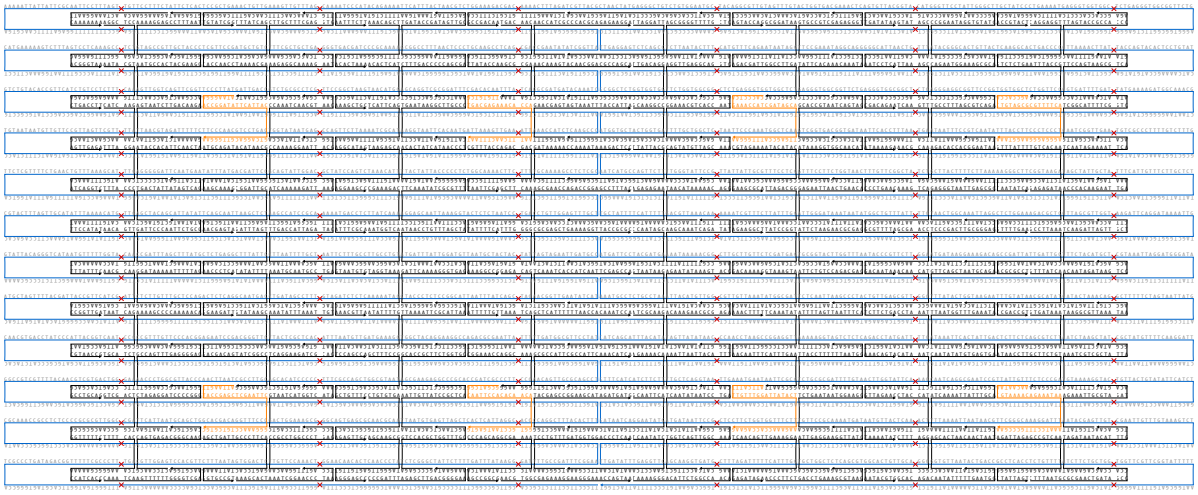

Supplementary Figure 2 | caDNAno overview of the rectangular origami structure. Blue: scaffold, black: unmodified staples, orange: biotinylated staples. For strand modification details see Supplementary Table 6.

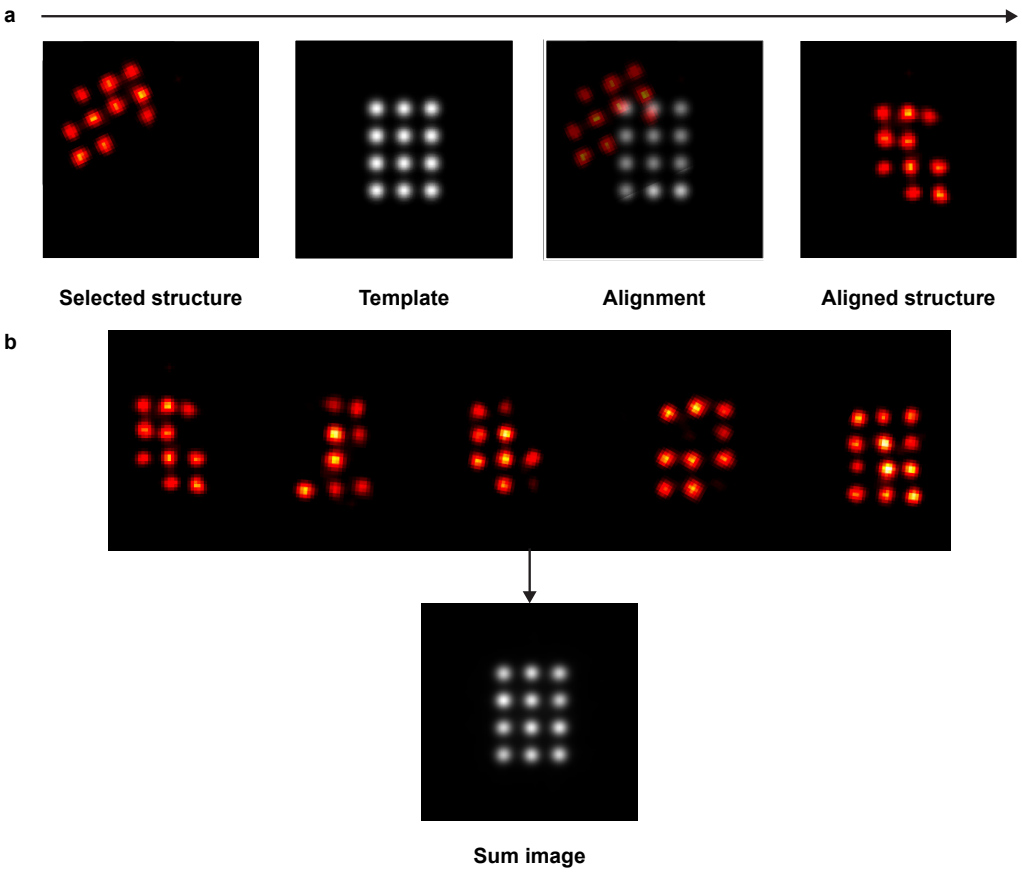

Supplementary Figure 3 | Overview of alignment procedure. **a**, DNA origami nanostructures are selected from the reconstructed DNA-PAINT super-resolution image. All selected structures are randomly orientated. A template is generated from the structure design. The selected structure is rotated stepwise and cross-correlated to the template. By selecting the angle where the correlation is maximised, the correct rotation angle can be obtained. The localisation data is rotated by the determined angle and corresponding shift, and the structure is aligned. **b**, Several aligned structures are stacked on top of each other to create a sum image which can be used for detection analysis.

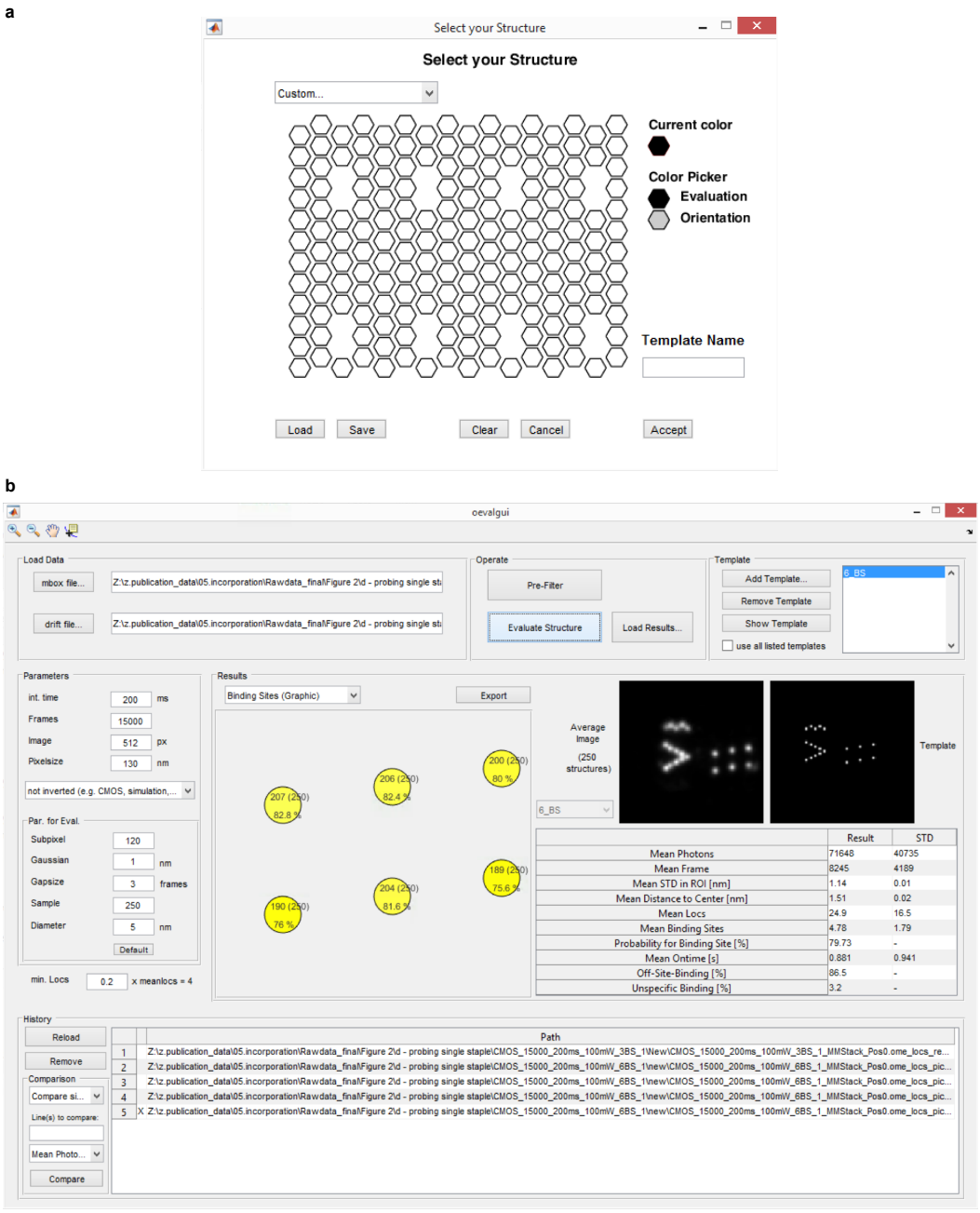

Supplementary Figure 4 | Interface of analysis software. **a**, Structure selection dialog. The analysis software features an interface where a structural template for the rectangular origami can be defined by clicking on hexagons. The software distinguishes between evaluation handles which will be evaluated and orientation handles which will be used in the template generation for the cross-correlation but not in the evaluation **b**, Main window. The main window features a display of the template, the sum image and detection statistics for the loaded dataset. Parameters for cross-correlation and thresholding can be set.

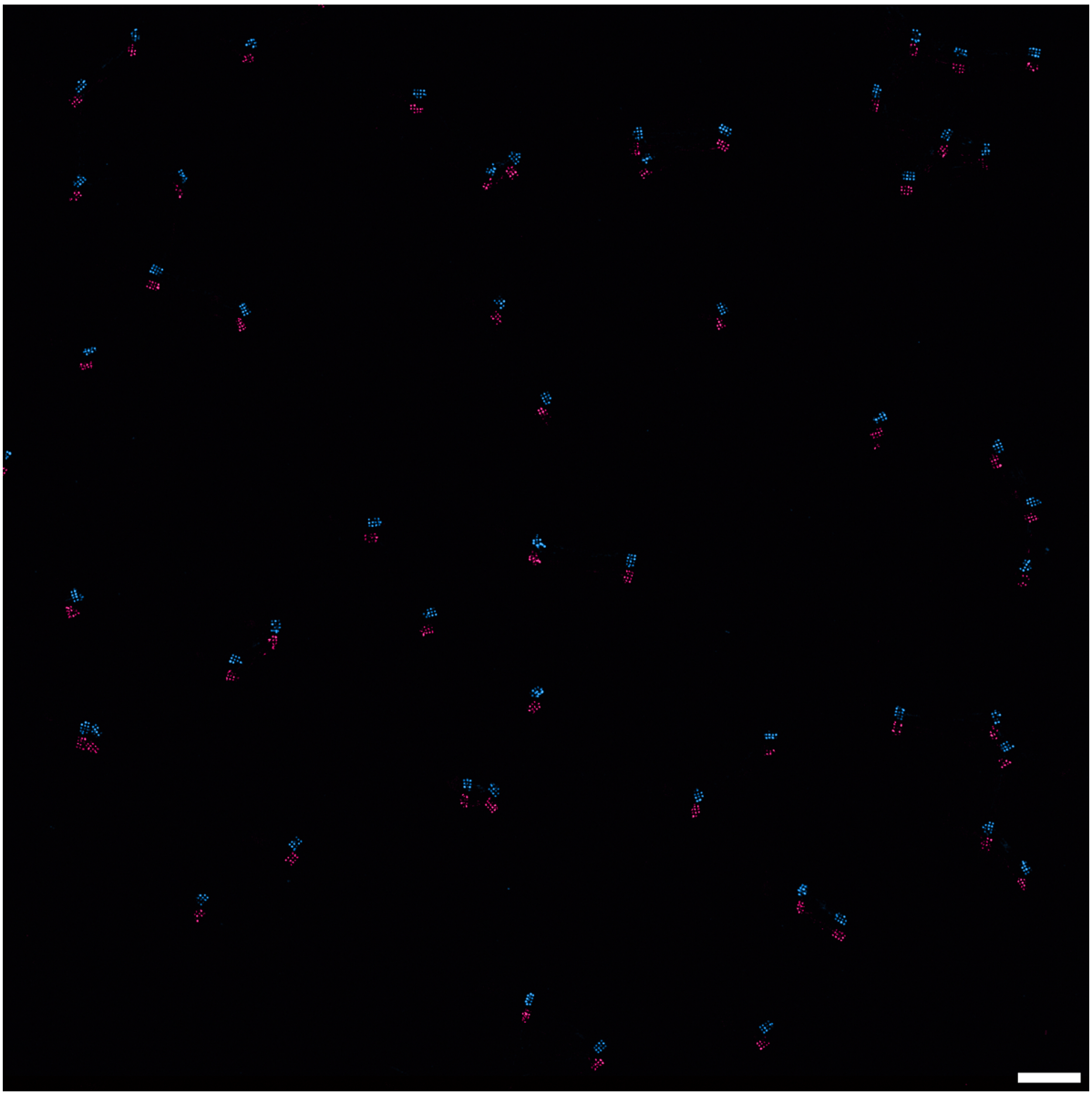

Supplementary Figure 5 | Overview image for Fig. 2. The two channels, red (Atto647N - 3') and blue (Cy3b - 5') are shifted to each other to allow better identification. Scale bar, 500 nm.

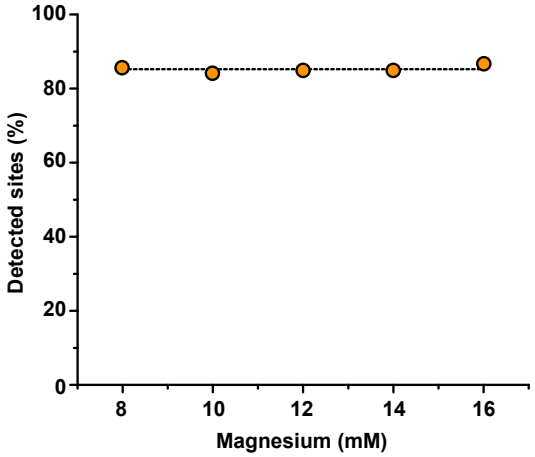

Supplementary Figure 6 | Influence of Magnesium in folding buffer on staple detection. DNA origami structures were folded at different Magnesium concentrations with a 3h folding ramp (60 to 4 °C). Modified staples had a 100× excess over Scaffold. Average detection (dashed line): 85.2%

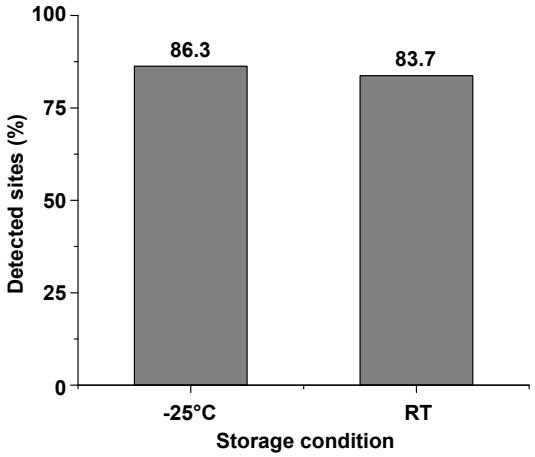

Supplementary Figure 7 | Influence of storage conditions on detection values. DNA origami structures were folded, PEG-purified and kept at room temperature and -25 °C for 58 days.

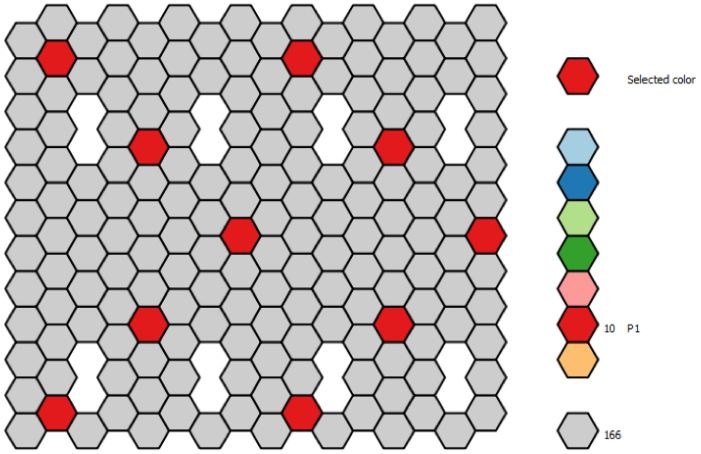

Supplementary Figure 8 | 'Arrow'-shaped DNA origami grid with 10 binding sites used in Fig. 3c Each hexagon represents a single staple, colored hexagons indicate a single staple extension at the 3'-end for DNA-PAINT probing.

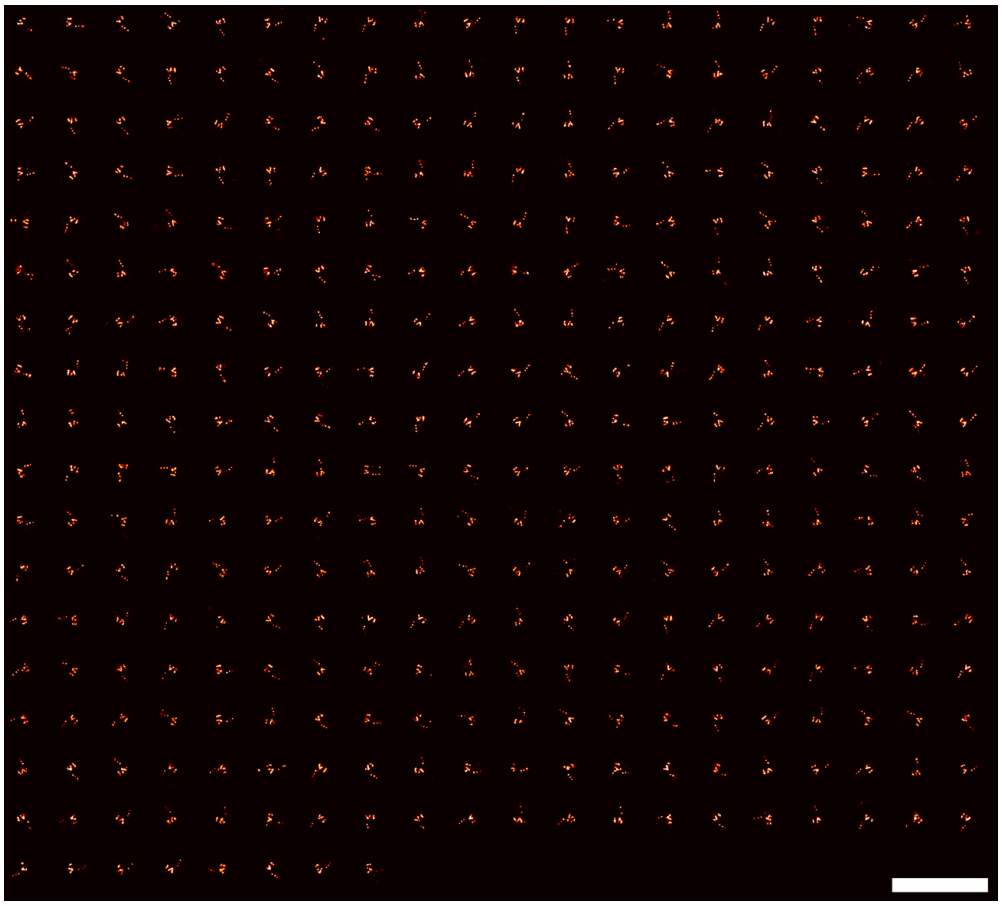

Supplementary Figure 9 | Overview of DNA-PAINT images used for quantification in Fig. 3d. 348 3BS structures are shown. Scale bar, 500 nm

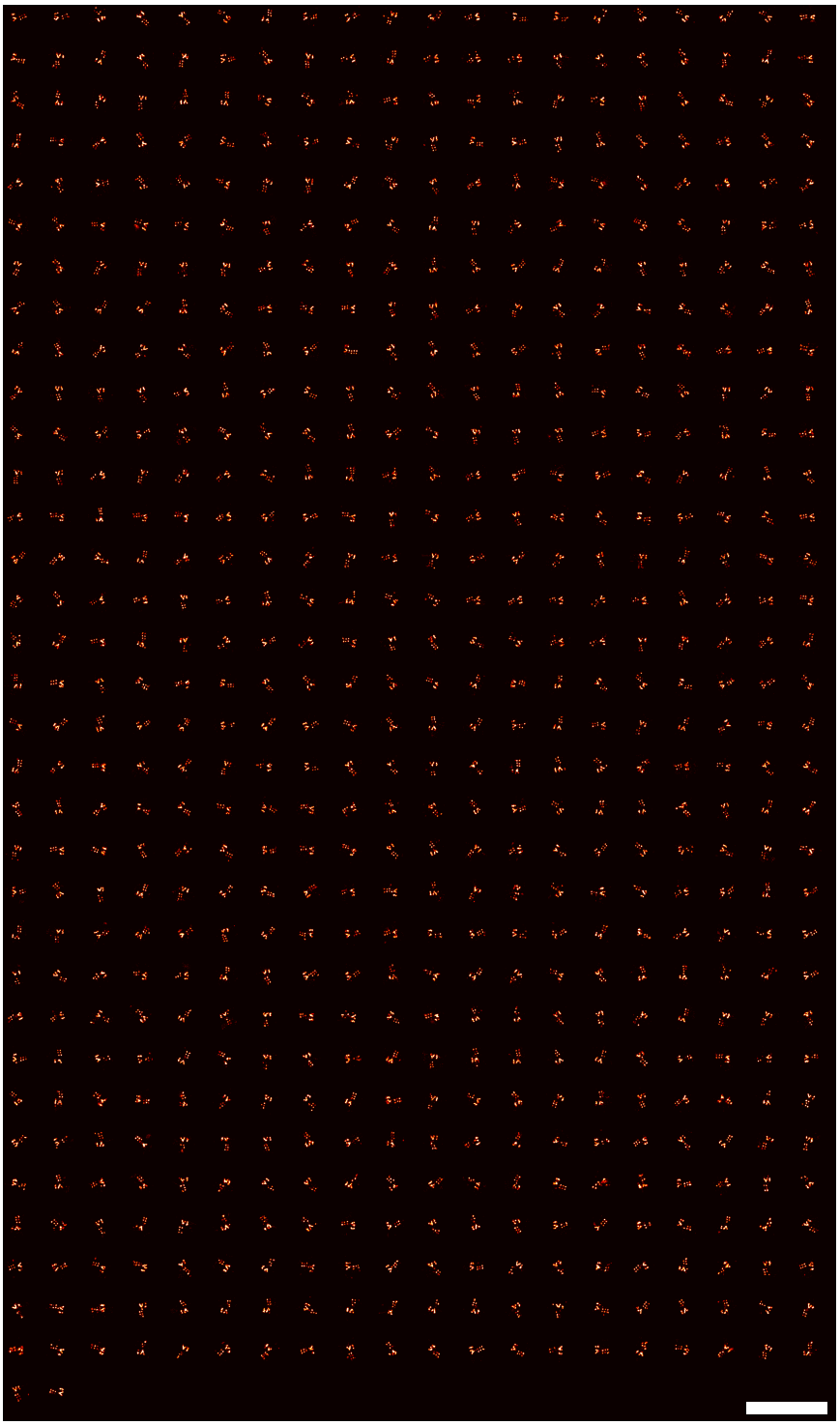

Supplementary Figure 10 | Overview of DNA-PAINT images used for quantification in Fig. 3d. 662 6BS structures are shown. Scale bar: 500 nm

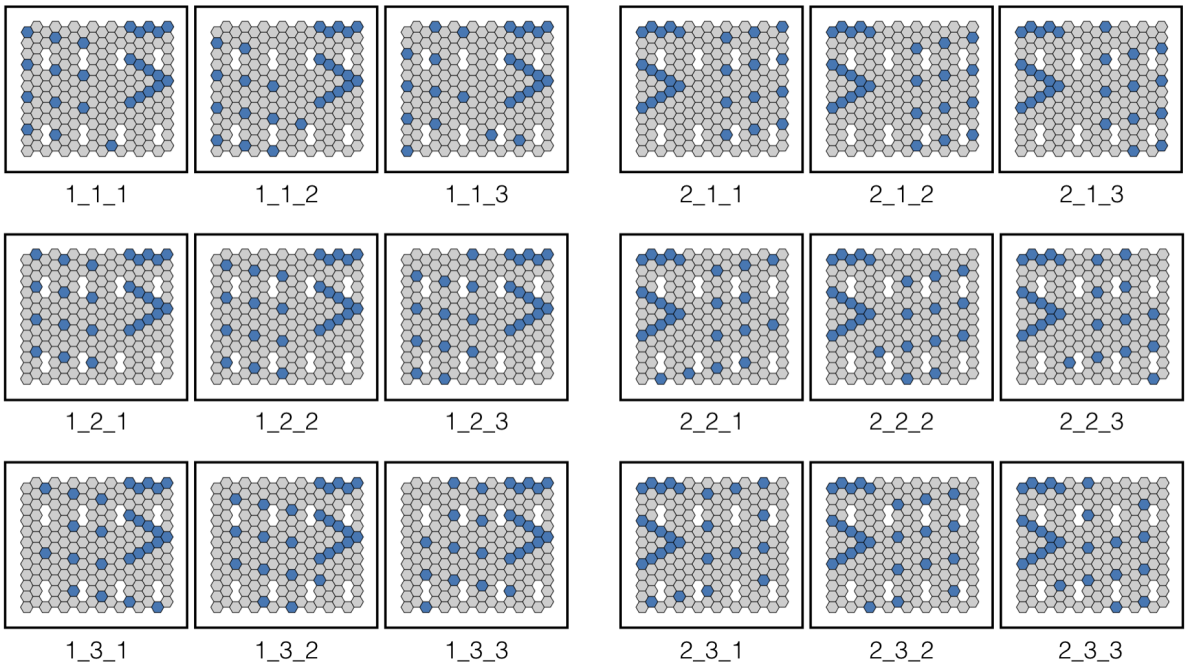

Supplementary Figure 11 | Overview of 18 DNA origami structures used for the heatmap in Fig. 4. The origami is divided into two sides, containing an orientation marker (arrow pattern) and staple positions to be probed.

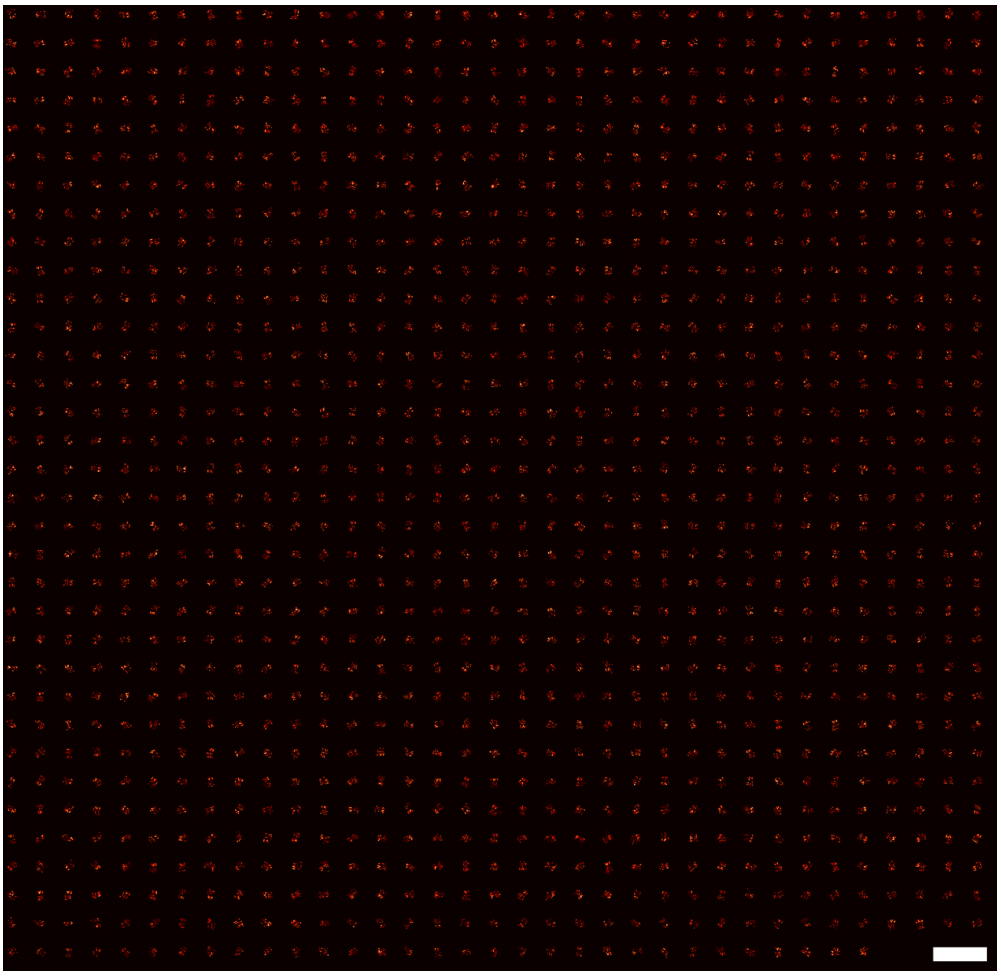

Supplementary Figure 12 | Overview of DNA-PAINT images used for quantification in Fig. 4, Dataset 1. 1186 structures are shown. The measurement contains all 18 origami structures. Scale bar: 500 nm

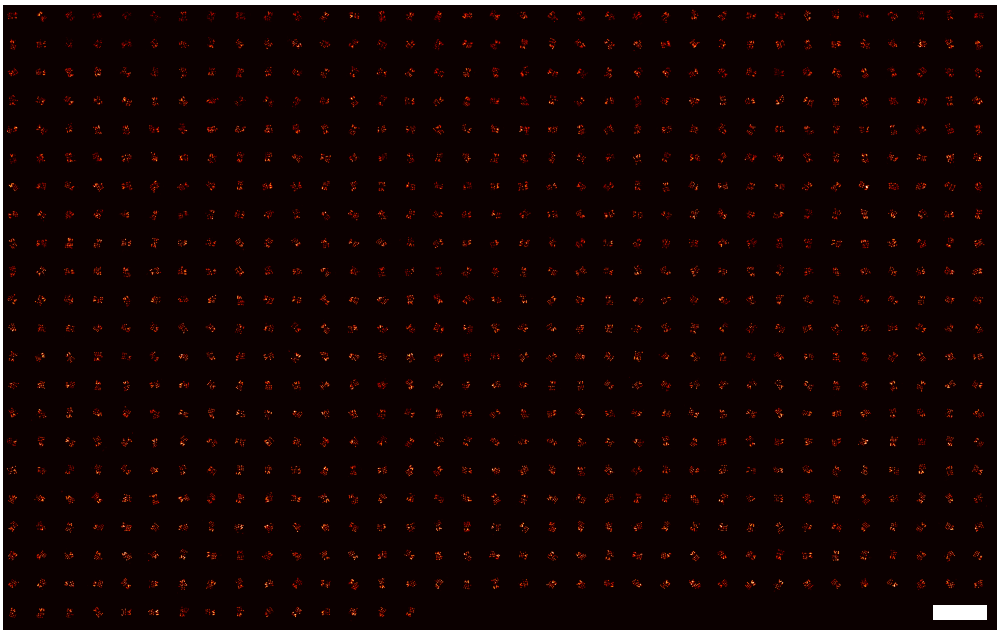

Supplementary Figure 13 | Overview of DNA-PAINT images used for quantification in Fig. 4, Dataset 2. 750 structures are shown. The measurement contains all 18 origami structures. Scale bar, 500 nm.

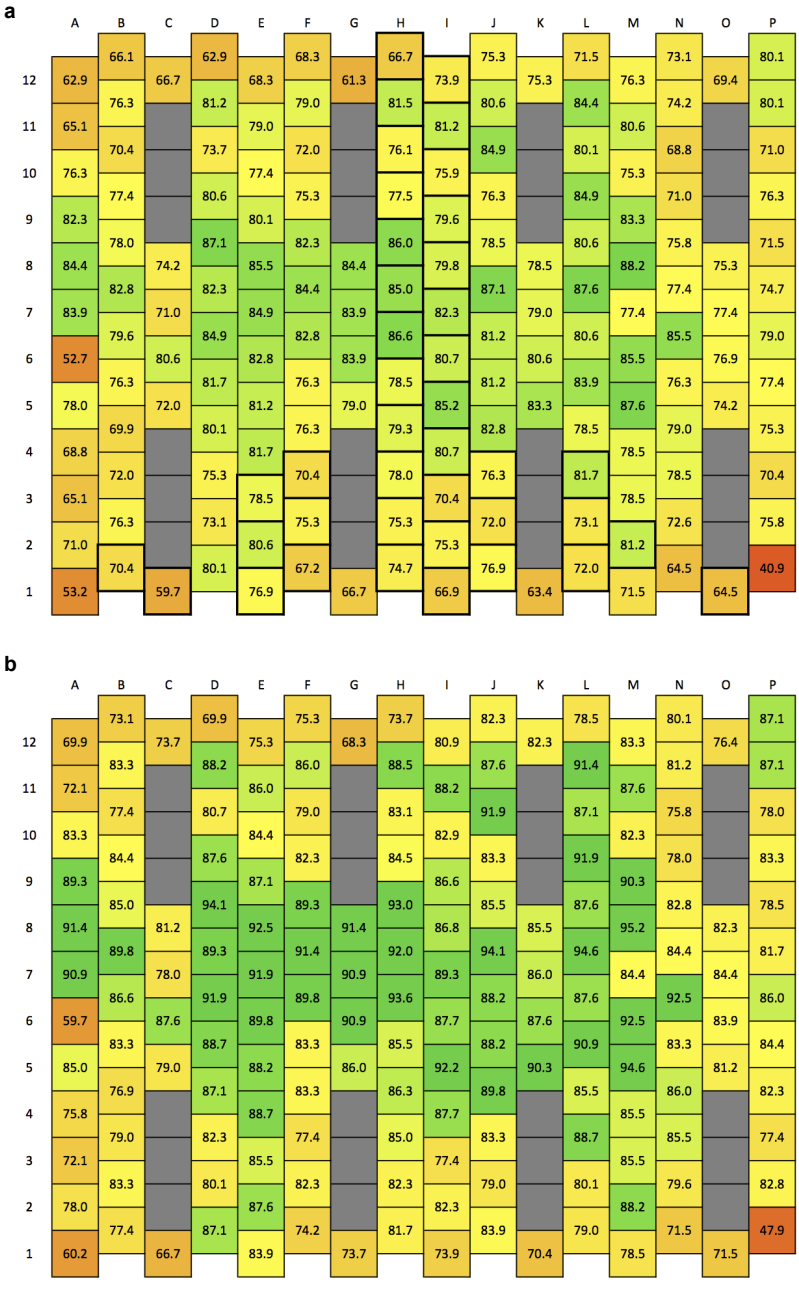

Supplementary Figure 14 | Detection and incorporation heatmap. a, The heatmap shows detection values for each probed position. **b**, The detection values can be translated to incorporation values by adding an offset of 7 % (as determined to be the 3'-error (see Figure 2) to generate an incorporation heatmap.

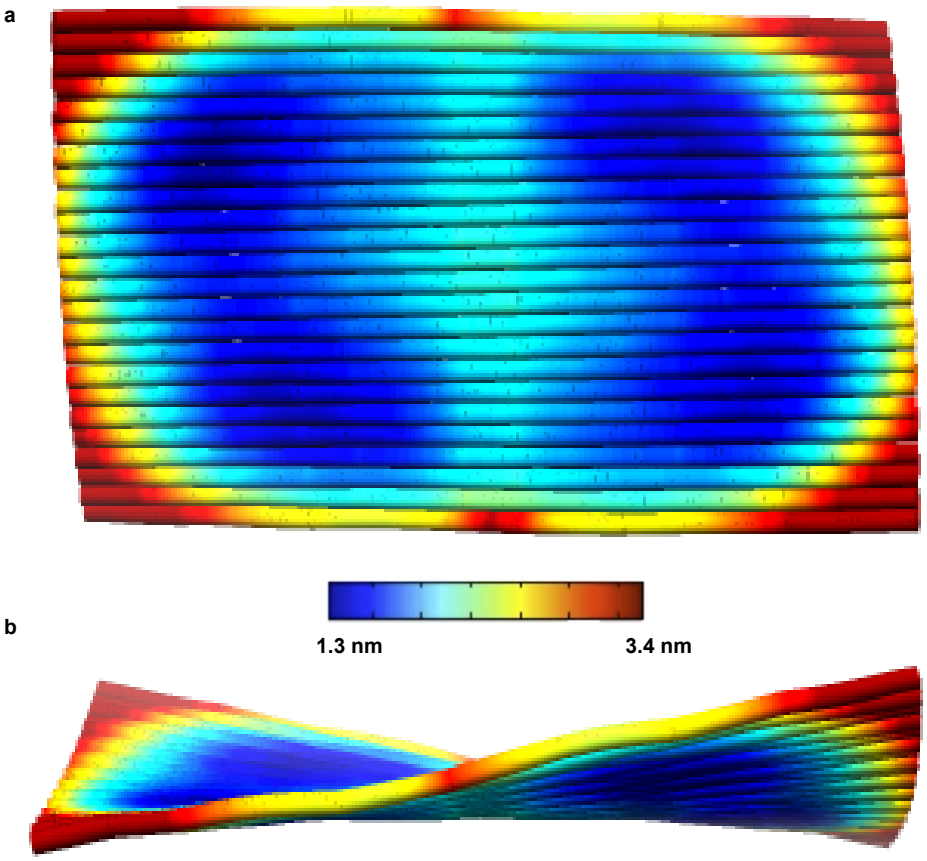

Supplementary Figure 15 | CanDo simulation of RMS fluctuations. a, Top view. The CanDo simulations show little thermal fluctuations in the center of the rectangular structure. Fluctuations with the highest magnitude can be found at the corners and edges. **b**, Side view. The side view shows the twisting of the DNA origami structure.

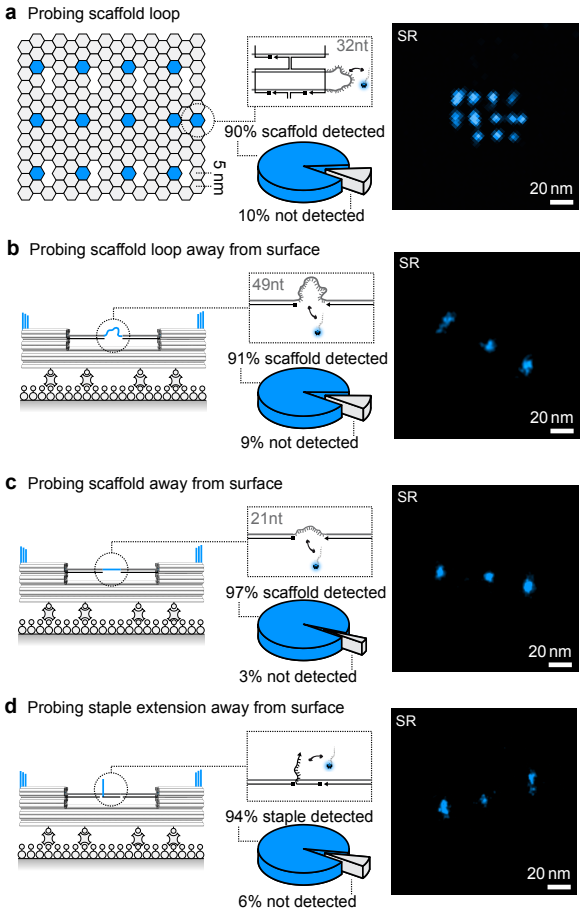

Supplementary Figure 16 | Scaffold and staple detection experiments. a, Probing the scaffold loop close to the surface yields a 90% detection efficiency. **b**, Probing a scaffold stretch (49 nt, similar to the loop of the flat origami) away from the surface yields a 91% detection efficiency. **c**, Probing a shorter scaffold stretch (21 nt, more ideally accessible) away from the surface yields a 97% detection efficiency **d**, Probing a staple extension away from the surface yields a 94% detection efficiency.

Supplementary Table 1 | Fit of Michaelis-Menten saturation curve

Name	Value	Standard Error
Formula	y = Vmax * x / (Km + x)	
Adj. R-Square	0.9805	
Vmax	83.13349	0.39929
Km	1.47056	0.11358

Supplementary Table 2 | Overview of related studies and their incorporation values. For (1) and (2) we estimated the incorporated for a single staple by considering the decay in 6 steps. For (1) this was from 100% to 74%, for (2) to 42%. For (3) we estimated the incorporation with the given probability of 98.7% that a particle is present being bound to three strands and backcalculation to one strand.

Reference	Structure and attachment	Incorporation
Jungmann et al. 2010	Streptavidin/Biotin	83%
Derr et al. 2012	Motor Protein	80%
Tomov et al. 2013	Hairpin Walker	95% (1)
Voigt et al. 2010	Streptavidin/Biotin	84%
Liber et al. 2015	Walker	86.50% (2)
Guer et al. 2016	Gold Nanoparticle Attachment	76.50% (3)
Jungmann et al. 2016	qPAINT	85%
Chatterjee et al. 2017	DNA Computing	92.5%/83%

Supplementary Table 3 | Super-resolution data properties

Measurement	NeNA
Fig 2: Atto647N	2.256 nm
Fig 2: Cy3b	1.616 nm
Fig 3: Annealing	10min: 1.573 nm 1h: 1.508 nm 3h: 1.664 nm 12h: 1.534 nm 3d: 1.768 nm
Fig 3: Excess	10x: 2.752 nm 20x: 2.144 nm 50x: 2.112 nm 100x: 2.72 nm 523x: 2.096 nm
Fig 3: 3 BS	4.017 nm
Fig 3: 6 BS	1.365 nm
Fig 4: Heatmap	1.495 nm / 1.469 nm

Supplementary Table 4 | Imaging conditions

Figure	Name	Origami	Excess	Folding Buffer	Folding Ramp	Purification	c(Origami)	Buffer	Imager	c(Img)-nM	Laserpower	Power density (kW/cm-2)	Int (ms)	Frames	Camera	ROI (px)
1 d	Simulations	20nm	-	-	-	-	50 structures	-	-	5		1.5	200	15000	160nm Px	128
2	5' - 3' Experiment	20nm	100	1x FB	80-4, 10min	Gel	17/100	B+/PPT	P1*	1		561 nm @ ~1.37	300	15000	EMCCD	256
2	5' - 3' Experiment	20nm	100	1x FB	80-4, 10min	Gel	17/100	B+/PPT	P9	1		640 nm @ ~1.97	300	15000	EMCCD	256
3	Folding Ramps	Arrow	100	1x FB	80-4, 10min	none	2/100	O+/PPT	P1	5	100	561 nm ~4.2	200	15000	sCMOS	512
			100	1x FB	80-4, 1h	none	2/100	O+/PPT	P1	5	100	561 nm ~4.2	200	15000	sCMOS	512
			100	1x FB	80-4, 3h	none	2/100	O+/PPT	P1	5	100	561 nm ~4.2	200	15000	sCMOS	512
			100	1x FB	80-4, 12h	none	2/100	O+/PPT	P1	5	100	561 nm ~4.2	200	15000	sCMOS	512
			100	1x FB	80-4, 3d	none	2/100	O+/PPT	P1	5	100	561 nm ~4.2	200	15000	sCMOS	512
3	Excess	20nm	10	1x FB	60to4,3h	PEG	3/100	O+	P1	5	70	561 nm @ ~2.9	300	7500	EMCCD	256
			20	1x FB		PEG	3/100	O+	P1	5	70	561 nm @ ~2.9	300	7500	EMCCD	256
			50	1x FB		PEG	2/100	O+	P1	5	70	561 nm @ ~2.9	300	7500	EMCCD	256
			100	1x FB		PEG	2/100	O+	P1	5	70	561 nm @ ~2.9	300	7500	EMCCD	256
			523.3	1x FB		PEG	2/100	O+	P1	5	70	561 nm @ ~2.9	300	7500	EMCCD	256
3d	Simulations	20nm	-	-	-	-	50 structures	-	-	5		1.5	200	15000	160nm Px	128
4	Heatmap	1_1_1	100	1x FB	60to4,3h	none	18x 0.2/100	O+/PPT	P1	2	100	561 nm ~4.2	###	##	CMOS	###
		1_1_2	100	1x FB		none										
		1_1_3	100	1x FB		none										
		1_2_1	100	1x FB		none										
		1_2_2	100	1x FB		none										
		1_2_3	100	1x FB		none										
		1_3_1	100	1x FB		none										
		1_3_2	100	1x FB		none										
		1_3_3	100	1x FB		none										
		2_1_1	100	1x FB		none										
		2_1_2	100	1x FB		none										
		2_1_3	100	1x FB		none										
		2_2_1	100	1x FB		none										
		2_2_2	100	1x FB		none										
		2_2_3	100	1x FB		none										
		2_3_1	100	1x FB		none										
		2_3_2	100	1x FB		none										
		2_3_3	100	1x FB		none										
SI	Magnesium	Arrow	100	1x FB (8mM $MgCl_2$)	60to4,3h	none	2/100	O+/PPT	P1	5	100	561 nm ~4.2	200	15000	sCMOS	512
			100	1x FB (10mM $MgCl_2$)		none	2/100	O+/PPT	P1	5	100	561 nm ~4.2	200	15000	sCMOS	512
			100	1x FB (12mM $MgCl_2$)		none	2/100	O+/PPT	P1	5	100	561 nm ~4.2	200	15000	sCMOS	512
			100	1x FB (14mM $MgCl_2$)		none	2/100	O+/PPT	P1	5	100	561 nm ~4.2	200	15000	sCMOS	512
			100	1x FB (16mM $MgCl_2$)		none	2/100	O+/PPT	P1	5	100	561 nm ~4.2	200	15000	sCMOS	512
SI 16	Scaffold Loop (a)	20nm	100	1x FB	80-4, 10min	Gel	17/100	B+/PPT	P9	1		640 nm @ ~1.97	300	15000	EMCCD	256
	Force Clamp (b,c,d)	Force Clamp	100	1x FB	Refer to Paper	Gel	500pM	B+/PPT	P1	5	70	561 nm @ ~2.9	200	15000	sCMOS	512

Supplementary Table 5 | Used DNA-PAINT sequences

Shortname	Docking sequence	Imager sequence	Experiment
P1	TT ATACATCTA	CTAGATGTAT-Cy3b	Fig 3/4
P1*	TT ATACATCTA	Cy3b-CATCCTAATT	Fig 2
P9	TT AATTAGGAT	CATCCTAATT-Atto647N	Fig 2

Supplementary Table 6 | List of core staples

Position	Name	Sequence
A1	21[32]23[31]BLK	TTTTCACTCAAAGGGCGAAAAACCATCACC
B1	23[32]22[48]BLK	CAAATCAAGTTTTTTGGGGTCGAAACGTGGA
C1	21[56]23[63]BLK	AGCTGATTGCCCTTCAGAGTCCACTATTAAAGGGTGCCGT
D1	23[64]22[80]BLK	AAAGCACTAAATCGGAACCCTAATCCAGTT
E1	21[96]23[95]BLK	AGCAAGCGTAGGGTTGAGTGTTGTAGGGAGCC

F1	23[96]22[112]BLK	CCCGATTTAGAGCTTGACGGGGAAAAAGAATA
G1	21[120]23[127]BLK	CCCAGCAGGCGAAAAATCCCTTATAAATCAAGCCGGCG
H1	21[160]22[144]BLK	TCAATATCGAACCTCAAATATCAATTCCGAAA
I1	23[128]23[159]BLK	AACGTGGCGAGAAAGGAAGGGAAACCAGTAA
J1	23[160]22[176]BLK	TAAAAGGGACATTCTGGCCAACAAAGCATC
K1	21[184]23[191]BLK	TCAACAGTTGAAAGGAGCAAATGAAAAATCTAGAGATAGA
L1	23[192]22[208]BLK	ACCCTTCTGACCTGAAAGCGTAAGACGCTGAG
M1	21[224]23[223]BLK	CTTTAGGGCCTGCAACAGTGCCAATACGTG
N1	23[224]22[240]BLK	GCACAGACAATATTTTTGAATGGGGTCAGTA
O1	21[248]23[255]BLK	AGATTAGAGCCGTCAAAAAACAGAGGTGAGGCCTATTAGT
P1	23[256]22[272]BLK	CTTTAATGCGCGAACTGATAGCCCCACCAG
A2	19[32]21[31]BLK	GTCGACTTCGGCCAACGCGCGGGGTTTTTC
B2	22[47]20[48]BLK	CTCCAACGCAGTGAGACGGGCAACCAGCTGCA
D2	22[79]20[80]BLK	TGGAACAACCGCCTGGCCCTGAGGCCCGCT
E2	19[96]21[95]BLK	CTGTGTGATTGCGTTGCGCTCACTAGAGTTGC
F2	22[111]20[112]BLK	GCCCGAGAGTCCACGCTGGTTTGCAGCTAACT
H2	19[160]20[144]BLK	GCAATTCACATATTCCTGATTATCAAAGTGTA
I2	22[143]21[159]BLK	TCGGCAAATCCTGTTTGATGGTGGACCCTCAA
J2	22[175]20[176]BLK	ACCTTGCTTGGTCAGTTGGCAAAGAGCGGA
L2	22[207]20[208]BLK	AGCCAGCAATTGAGGAAGGTTATCATCATTTT
M2	19[224]21[223]BLK	CTACCATAGTTTGAGTAACATTTAAAATAT
N2	22[239]20[240]BLK	TTAACACCAGCACTAACAACTAATCGTTATTA
P2	22[271]20[272]BLK	CAGAAGATTAGATAATACATTTGTCGACAA
A3	17[32]19[31]BLK	TGCATCTTTCCCAGTCACGACGGCCTGCAG
B3	20[47]18[48]BLK	TTAATGAACTAGAGGATCCCCGGGGGGTAACG
D3	20[79]18[80]BLK	TTCCAGTCGTAATCATGGTCATAAAAGGGG
E3	17[96]19[95]BLK	GCTTTCCGATTACGCCAGCTGGCGGCTGTTTC
F3	20[111]18[112]BLK	CACATTAAAATTGTTATCCGCTCATGCGGGCC
H3	17[160]18[144]BLK	AGAAAACAAAGAAGATGATGAAACAGGCTGCG
I3	20[143]19[159]BLK	AAGCCTGGTACGAGCCGGAAGCATAGATGATG
J3	20[175]18[176]BLK	ATTATCATTCAATATAATCCTGACAATTAC
L3	20[207]18[208]BLK	GCGGAACATCTGAATAATGGAAGGTACAAAAT
M3	17[224]19[223]BLK	CATAAATCTTTGAATACCAAGTGTTAGAAC
N3	20[239]18[240]BLK	ATTTTAAAATCAAAATTATTTGCACGGATTCG
P3	20[271]18[272]BLK	CTCGTATTAGAAATTGCGTAGATACAGTAC
A4	15[32]17[31]BLK	TAATCAGCGGATTGACCGTAATCGTAACCG
B4	18[47]16[48]BLK	CCAGGGTTGCCAGTTTGAGGGGACCCGTGGGA
C4	15[64]18[64]BLK	GTATAAGCCAACCCGTCGGATTCTGACGACAGTATCGGCCGCAAGGCG

D4	18[79]16[80]BLK	GATGTGCTTCAGGAAGATCGCACAATGTGA
E4	15[96]17[95]BLK	ATATTTTGGCTTTCATCAACATTATCCAGCCA
F4	18[111]16[112]BLK	TCTTCGCTGCACCGCTTCTGGTGCGGCCTTCC
G4	15[128]18[128]BLK	TAAATCAAAATAATTCGCGTCTCGGAAACCAGGCAAAGGGAAGG
H4	15[160]16[144]BLK	ATCGCAAGTATGTAAATGCTGATGATAGGAAC
I4	18[143]17[159]BLK	CAACTGTTGCGCCATTCGCCATTCAAACATCA
J4	18[175]16[176]BLK	CTGAGCAAAAATTAATTACATTTTGGGTTA
K4	15[192]18[192]BLK	TCAAATATAACCTCCGGCTTAGGTAACAATTTCATTTGAAGGCGAATT
L4	18[207]16[208]BLK	CGCGCAGATTACCTTTTTTAATGGGAGAGACT
M4	15[224]17[223]BLK	CCTAAATCAAAATCATAGGTCTAAACAGTA
N4	18[239]16[240]BLK	CCTGATTGCAATATATGTGAGTGATCAATAGT
O4	15[256]18[256]BLK	GTGATAAAAAGACGCTGAGAAGAGATAACCTTGCTTCTGTTCGGGAGA
P4	18[271]16[272]BLK	CTTTTACAAAATCGTCGCTATTAGCGATAG
A5	13[32]15[31]BLK	AACGCAAAATCGATGAACGGTACCGGTTGA
B5	16[47]14[48]BLK	ACAAACGGAAAAGCCCCAAAAACACTGGAGCA
C5	13[64]15[63]BLK	TATATTTTGTCATTGCCTGAGAGTGGAAGATT
D5	16[79]14[80]BLK	GCGAGTAAAAATATTTAAATTGTTACAAAG
E5	13[96]15[95]BLK	TAGGTAAACTATTTTTGAGAGATCAAACGTTA
F5	16[111]14[112]BLK	TGTAGCCATTAAAATTCGCATTAAATGCCGGA
G5	13[128]15[127]BLK	GAGACAGCTAGCTGATAAATTAATTTTTGT
H5	13[160]14[144]BLK	GTAATAAGTTAGGCAGAGGCATTTATGATATT
I5	16[143]15[159]BLK	GCCATCAAGCTCATTTTTTAACCACAAATCCA
J5	16[175]14[176]BLK	TATAACTAACAAAGAACGCGAGAACGCCAA
K5	13[192]15[191]BLK	GTAAAGTAATCGCCATATTTAACAAAACTTTT
L5	16[207]14[208]BLK	ACCTTTTTATTTTAGTTAATTTCATAGGGCTT
M5	13[224]15[223]BLK	ACAACATGCCAACGCTCAACAGTCTTCTGA
N5	16[239]14[240]BLK	GAATTTATTTAATGGTTTGAAATATTCTTACC
O5	13[256]15[255]BLK	GTTTATCAATATGCGTTATACAAACCGACCGT
P5	16[271]14[272]BLK	CTTAGATTTAAGGCGTTAAATAAAGCCTGT
A6	11[32]13[31]BLK	AACAGTTTTGTACCAAAAACATTTTATTTC
B6	14[47]12[48]BLK	AACAAGAGGGATAAAAATTTTTAGCATAAAGC
C6	11[64]13[63]BLK	GATTTAGTCAATAAAGCCTCAGAGAACCCTCA
D6	14[79]12[80]BLK	GCTATCAGAAATGCAATGCCTGAATTAGCA
E6	11[96]13[95]BLK	AATGGTCAACAGGCAAGGCAAAGAGTAATGTG
F6	14[111]12[112]BLK	GAGGGTAGGATTCAAAAGGGTGAGACATCCAA
G6	11[128]13[127]BLK	TTTGGGGATAGTAGTAGCATTAAAAGGCCG
H6	11[160]12[144]BLK	CCAATAGCTCATCGTAGGAATCATGGCATCAA
I6	14[143]13[159]BLK	CAACCGTTTCAAATCACCATCAATTCGAGCCA

J6	14[175]12[176]BLK	CATGTAATAGAATATAAAGTACCAAGCCGT
K6	11[192]13[191]BLK	TATCCGGTCTCATCGAGAACAAGCGACAAAAG
L6	14[207]12[208]BLK	AATTGAGAATTCTGTCCAGACGACTAAACCAA
M6	11[224]13[223]BLK	GCGAACCTCCAAGAACGGGTATGACAATAA
N6	14[239]12[240]BLK	AGTATAAAGTTCAGCTAATGCAGATGTCTTTC
O6	11[256]13[255]BLK	GCCTTAAACCAATCAATAATCGGCACGCGCCT
P6	14[271]12[272]BLK	TTAGTATCACAATAGATAAGTCCACGAGCA
A7	9[32]11[31]BLK	TTTACCCCAACATGTTTTAAATTTCCATAT
B7	12[47]10[48]BLK	TAAATCGGGATTCCCAATTCTGCGATATAATG
C7	9[64]11[63]BLK	CGGATTGCAGAGCTTAATTGCTGAAACGAGTA
D7	12[79]10[80]BLK	AAATTAAGTTGACCATTAGATACTTTTGCG
E7	9[96]11[95]BLK	CGAAAGACTTTGATAAGAGGTCATATTTCGCA
F7	12[111]10[112]BLK	TAAATCATATAACCTGTTTAGCTAACCTTTAA
G7	9[128]11[127]BLK	GCTTCAATCAGGATTAGAGAGTTATTTTCA
H7	9[160]10[144]BLK	AGAGAGAAAAAAATGAAAATAGCAAGCAAACT
I7	12[143]11[159]BLK	TTCTACTACGCGAGCTGAAAAGGTTACCGCGC
J7	12[175]10[176]BLK	TTTTATTTAAGCAAATCAGATATTTTTTGT
K7	9[192]11[191]BLK	TTAGACGGCCAAATAAGAAACGATAGAAGGCT
L7	12[207]10[208]BLK	GTACCGCAATTCTAAGAACGCGAGTATTATTT
M7	9[224]11[223]BLK	AAAGTCACAAAATAAACAGCCAGCGTTTTA
N7	12[239]10[240]BLK	CTTATCATTCCCGACTTGCGGGAGCCTAATTT
O7	9[256]11[255]BLK	GAGAGATAGAGCGTCTTTCCAGAGGTTTTGAA
P7	12[271]10[272]BLK	TGTAGAAATCAAGATTAGTTGCTCTTACCA
A8	7[32]9[31]BLK	TTTAGGACAAATGCTTTAAACAATCAGGTC
B8	10[47]8[48]BLK	CTGTAGCTTGACTATTATAGTCAGTTCATTGA
C8	7[56]9[63]BLK	ATGCAGATACATAACGGGAATCGTCATAAATAAAGCAAAG
D8	10[79]8[80]BLK	GATGGCTTATCAAAAAGATTAAGAGCGTCC
E8	7[96]9[95]BLK	TAAGAGCAAATGTTTAGACTGGATAGGAAGCC
F8	10[111]8[112]BLK	TTGCTCCTTTCAAATATCGCGTTTGAGGGGGT
G8	7[120]9[127]BLK	CGTTTACCAGACGACAAAGAAGTTTTGCCATAATTCGA
H8	7[160]8[144]BLK	TTATTACGAAGAACTGGCATGATTGCGAGAGG
I8	10[143]9[159]BLK	CCAACAGGAGCGAACCAGACCGGAGCCTTTAC
J8	10[175]8[176]BLK	TTAACGTCTAACATAAAAACAGGTAACGGA
K8	7[184]9[191]BLK	CGTAGAAAATACATACCGAGGAAACGCAATAAGAAGCGCA
L8	10[207]8[208]BLK	ATCCCAATGAGAATTAACTGAACAGTTACCAG
M8	7[224]9[223]BLK	AACGCAAAGATAGCCGAACAAACCCTGAAC
N8	10[239]8[240]BLK	GCCAGTTAGAGGGTAATTGAGCGCTTTAAGAA
O8	7[248]9[255]BLK	GTTTATTTTGTCACAATCTTACCGAAGCCCTTTAATATCA

P8	10[271]8[272]BLK	ACGCTAACACCCACAAGAATTGAAAATAGC
A9	5[32]7[31]BLK	CATCAAGTAAAACGAACTAACGAGTTGAGA
B9	8[47]6[48]BLK	ATCCCCCTATACCACATTCAACTAGAAAAATC
D9	8[79]6[80]BLK	AATACTGCCCAAAAGGAATTACGTGGCTCA
E9	5[96]7[95]BLK	TCATTCAGATGCGATTTTAAGAACAGGCATAG
F9	8[111]6[112]BLK	AATAGTAAACACTATCATAACCCTCATTGTGA
H9	5[160]6[144]BLK	GCAAGGCCTCACCAGTAGCACCATGGGCTTGA
I9	8[143]7[159]BLK	CTTTTGCAGATAAAAACCAAAATAAAGACTCC
J9	8[175]6[176]BLK	ATACCCAACAGTATGTTAGCAAATTAGAGC
L9	8[207]6[208]BLK	AAGGAAACATAAAGGTGGCAACATTATCACCG
M9	5[224]7[223]BLK	TCAAGTTTCATTAAAGGTGAATATAAAAGA
N9	8[239]6[240]BLK	AAGTAAGCAGACACCACGGAATAATATTGACG
P9	8[271]6[272]BLK	AATAGCTATCAATAGAAAATTCAACATTCA
A10	3[32]5[31]BLK	AATACGTTTGAAAGAGGACAGACTGACCTT
B10	6[47]4[48]BLK	TACGTTAAAGTAATCTTGACAAGAACCGAACT
D10	6[79]4[80]BLK	TTATACCACCAAATCAACGTAACGAACGAG
E10	3[96]5[95]BLK	ACACTCATCCATGTTACTTAGCCGAAAGCTGC
F10	6[111]4[112]BLK	ATTACCTTTGAATAAGGCTTGCCCAAATCCGC
H10	3[160]4[144]BLK	TTGACAGGCCACCACCAGAGCCGCGATTTGTA
I10	6[143]5[159]BLK	GATGGTTTGAACGAGTAGTAAATTTACCATTA
J10	6[175]4[176]BLK	CAGCAAAAGGAAACGTCACCAATGAGCCGC
L10	6[207]4[208]BLK	TCACCGACGCACCGTAATCAGTAGCAGAACCG
M10	3[224]5[223]BLK	TTAAAGCCAGAGCCGCCACCCTCGACAGAA
N10	6[239]4[240]BLK	GAAATTATTGCCTTTAGCGTCAGACCGGAACC
P10	6[271]4[272]BLK	ACCGATTGTCGGCATTTTCGGTCATAATCA
A11	1[32]3[31]BLK	AGGCTCCAGAGGCTTTGAGGACACGGGTAA
B11	4[47]2[48]BLK	GACCAACTAATGCCACTACGAAGGGGGTAGCA
C11	1[64]4[64]BLK	TTTATCAGGACAGCATCGGAACGACACCAACCTAAAACGAGGTCAATC
D11	4[79]2[80]BLK	GCGCAGACAAGAGGCAAAAGAATCCCTCAG
E11	1[96]3[95]BLK	AAACAGCTTTTTGCGGGATCGTCAACACTAAA
F11	4[111]2[112]BLK	GACCTGCTCTTTGACCCCCAGCGAGGGAGTTA
G11	1[128]4[128]BLK	TGACAACTCGCTGAGGCTTGCATTATACCAAGCGCGATGATAAA
H11	1[160]2[144]BLK	TTAGGATTGGCTGAGACTCCTCAATAACCGAT
I11	4[143]3[159]BLK	TCATCGCCAACAAAGTACAACGGACGCCAGCA
J11	4[175]2[176]BLK	CACCAGAAAGGTTGAGGCAGGTCATGAAAG
K11	1[192]4[192]BLK	GCGGATAACCTATTATTCTGAAACAGACGATTGGCCTTGAAGAGCCAC
L11	4[207]2[208]BLK	CCACCCTCTATTCACAAACAAATACCTGCCTA
M11	1[224]3[223]BLK	GTATAGCAAACAGTTAATGCCCAATCCTCA

N11	4[239]2[240]BLK	GCCTCCCTCAGAATGGAAAGCGCAGTAACAGT
O11	1[256]4[256]BLK	CAGGAGGTGGGGTCAGTGCCTTGAGTCTCTGAATTTACCGGGAACCAG
P11	4[271]2[272]BLK	AAATCACCTTCCAGTAAGCGTCAGTAATAA
A12	0[47]1[31]BLK	AGAAAGGAACAACTAAAGGAATTCAAAAAAA
B12	2[47]0[48]BLK	ACGGCTACAAAAGGAGCCTTTAATGTGAGAAT
C12	0[79]1[63]BLK	ACAACTTTCAACAGTTTCAGCGGATGTATCGG
D12	2[79]0[80]BLK	CAGCGAAACTTGCTTTCGAGGTGTTGCTAA
E12	0[111]1[95]BLK	TAAATGAATTTTCTGTATGGGATTAATTTCTT
F12	2[111]0[112]BLK	AAGGCCGCTGATACCGATAGTTGCGACGTTAG
G12	0[143]1[127]BLK	TCTAAAGTTTTGTCGTCTTTCCAGCCGACAA
H12	0[175]0[144]BLK	TCCACAGACAGCCCTCATAGTTAGCGTAACGA
I12	2[143]1[159]BLK	ATATTCGGAACCATCGCCCACGCAGAGAAGGA
J12	2[175]0[176]BLK	TATTAAGAAGCGGGGTTTTGCTCGTAGCAT
K12	0[207]1[191]BLK	TCACCAGTACAAACTACAACGCCTAGTACCAG
L12	2[207]0[208]BLK	TTTCGGAAGTGCCGTCGAGAGGGTGAGTTTCG
M12	0[239]1[223]BLK	AGGAACCCATGTACCGTAACACTTGATATAA
N12	2[239]0[240]BLK	GCCCGTATCCGGAATAGGTGTATCAGCCCAAT
O12	0[271]1[255]BLK	CCACCCTCATTTTCAGGGATAGCAACCGTACT
P12	2[271]0[272]BLK	GTTTTAACTTAGTACCGCCACCCAGAGCCA

Supplementary Table 7 | List of biotinylated staples

No	Pos	Name	Sequence	Mod
1	C02	18[63]20[56]BIOTIN	ATTAAGTTTACCGAGCTCGAATTCGGGAAACCTGTCGTGC	5'-BT
2	C09	4[63]6[56]BIOTIN	ATAAGGGAACCGGATATTCATTACGTCAGGACGTTGGGAA	5'-BT
3	G02	18[127]20[120]BIOTIN	GCGATCGGCAATTCCACACAACAGGTGCCTAATGAGTG	5'-BT
4	G09	4[127]6[120]BIOTIN	TTGTGTCGTGACGAGAAACACCAAATTTCAACTTTAAT	5'-BT
5	K02	18[191]20[184]BIOTIN	ATTCATTTTTGTTTGGATTATACTAAGAAACCACCAGAAG	5'-BT
6	K09	4[191]6[184]BIOTIN	CACCCTCAGAAACCATCGATAGCATTGAGCCATTTGGGAA	5'-BT
7	O02	18[255]20[248]BIOTIN	AACAATAACGTAAAACAGAAATAAAAATCCTTTGCCCGAA	5'-BT
8	O09	4[255]6[248]BIOTIN	AGCCACCACTGTAGCGCGTTTTCAAGGGAGGGAAGGTAAA	5'-BT

A.3 SUPPORTING INFORMATION FOR ASSOCIATED PUBLICATION P3

Supporting Information

Super-resolution microscopy with DNA-PAINT

By

Jörg Schnitzbauer*, **Maximilian T. Strauss***, Thomas Schlichthärle, Florian Schüder, Ralf Jungmann
* *These authors contributed equally to this work*

published in

Nature Protocols (2017)

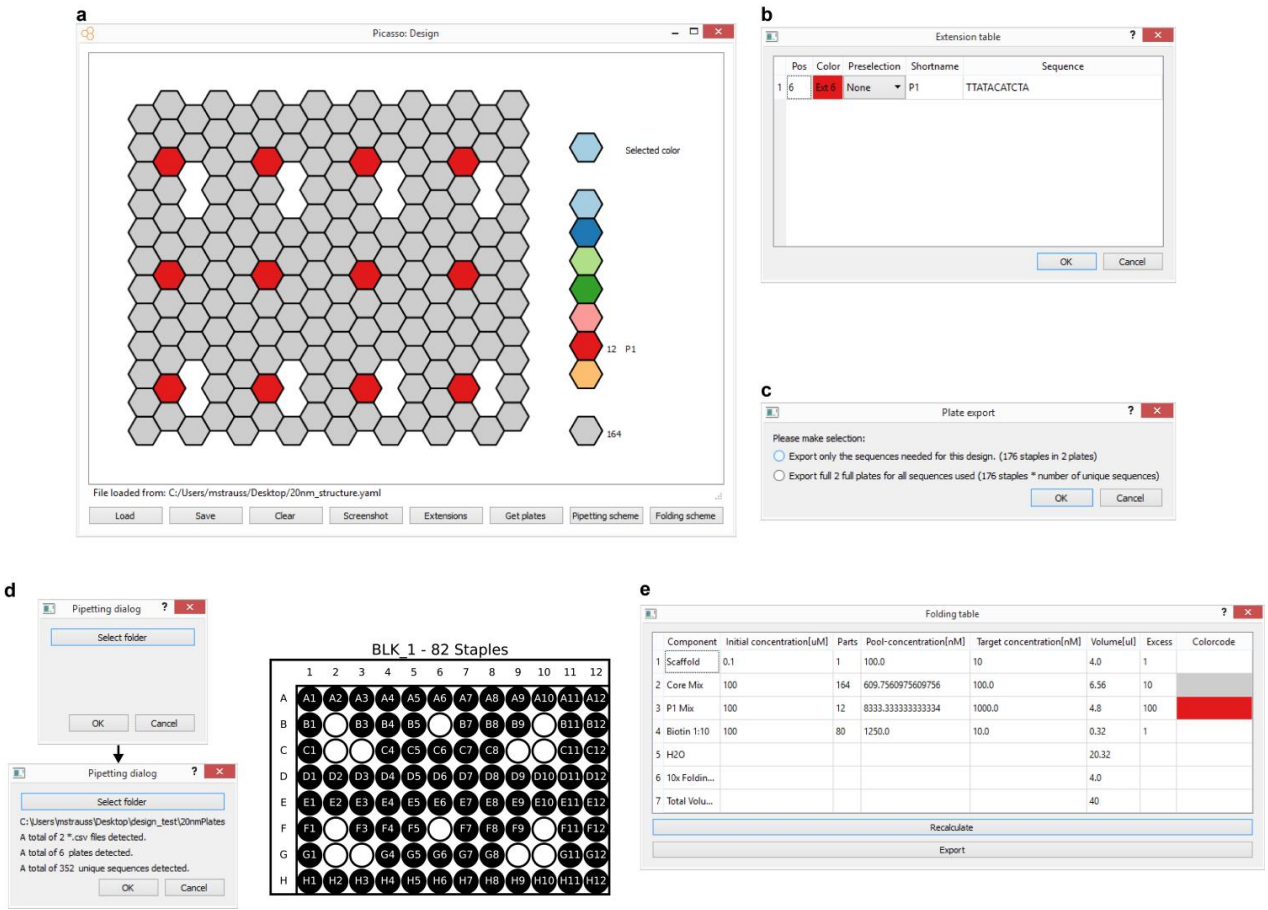

Supplementary Figure 1

Overview of “Picasso: Design”

(a) The main window showing the origami canvas with the hexagonal tiles. **(b)** Extensions dialog to set extensions corresponding to each selected color. **(c)** Plate export dialog to specify the export format of the plates. **(d)** Pipetting dialog to select a folder with *.csv files to generate a list of sequences that need to be pipetted and to create a visual pipetting aid. **(e)** Folding table to calculate volumes that are needed for pipetting.

Supplementary Figure 2

Overview of “Picasso: Simulate”

The main window has two preview windows, the left one to display the positions of structures in the full frame, the right one to display an individual structure. Structural parameters such as number and structure definition can be set in the group box “Structure”. All PAINT-related parameters, *i.e.* mean dark and bright times are set with the “PAINT parameters” group box. The group box “Imager parameters” is used to define properties of the simulated imaging probe.

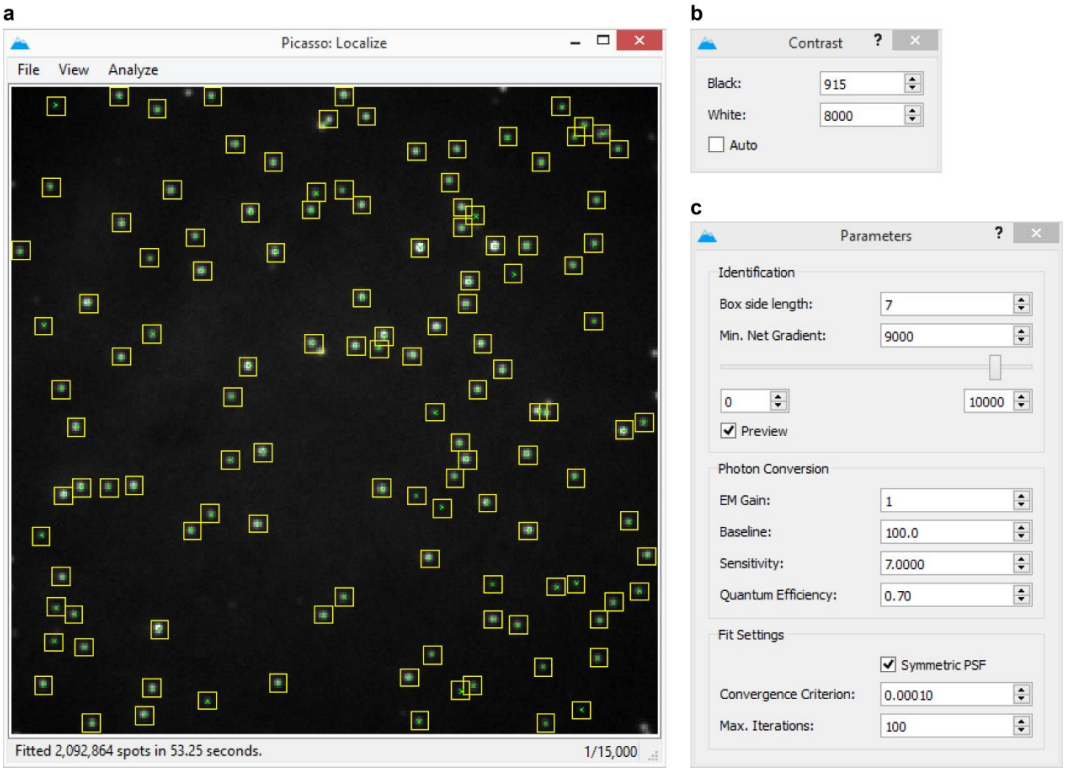

Supplementary Figure 3

Overview of “Picasso: Localize”

(a) The main window after the analysis of a movie file. Yellow boxes indicate the identification of a spot, green crosses show the fitted subpixel coordinate. **(b)** The contrast setting dialog. **(c)** The parameters setting dialog.

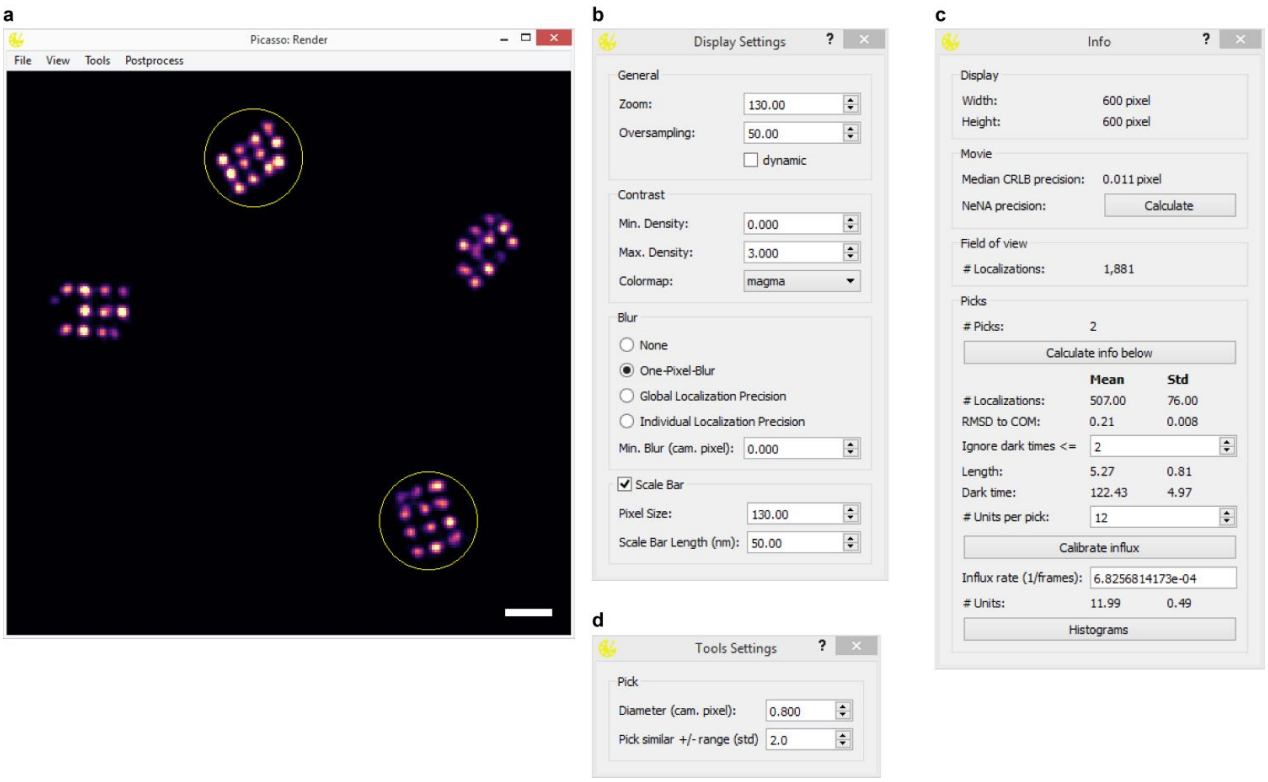

Supplementary Figure 4

Overview of “Picasso: Render”

(a) The main window with two picked regions of interest (yellow circles). **(b)** The display settings dialog for the render scene in **(a)**. **(c)** The info dialog for the picked regions in **(a)**. **(d)** The tools settings dialog.

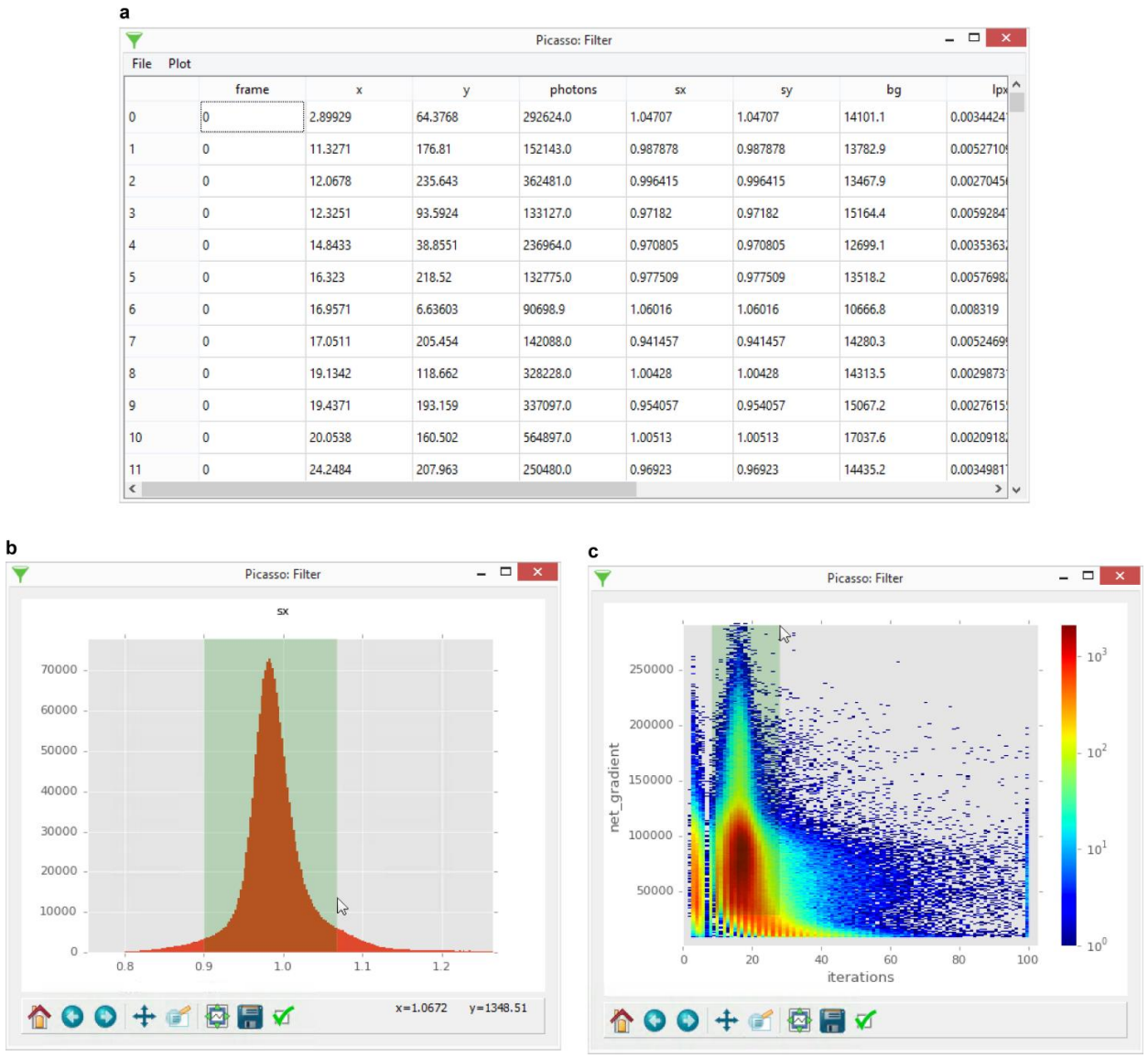

Supplementary Figure 5

Overview of “Picasso: Filter”

(a) The main window showing properties (columns) of localizations (rows). **(b)** Filtering in a histogram of a property column. **(c)** Filtering in a two-dimensional histogram of two property columns. The green areas in **(b)** and **(c)** have been selected with a pressed left mouse button. After releasing the mouse button, any localization with property values outside the green range will be removed.

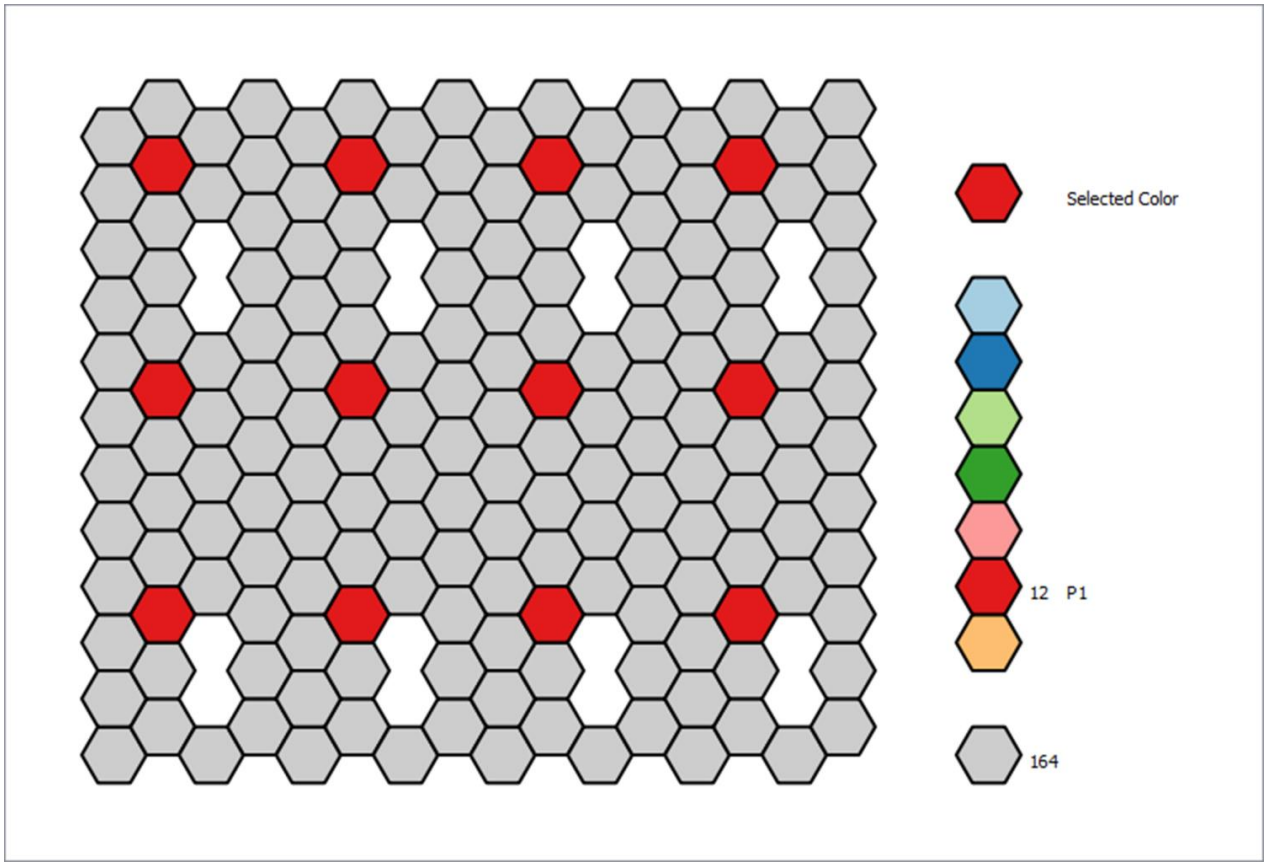

Supplementary Figure 6

20 nm DNA origami grid

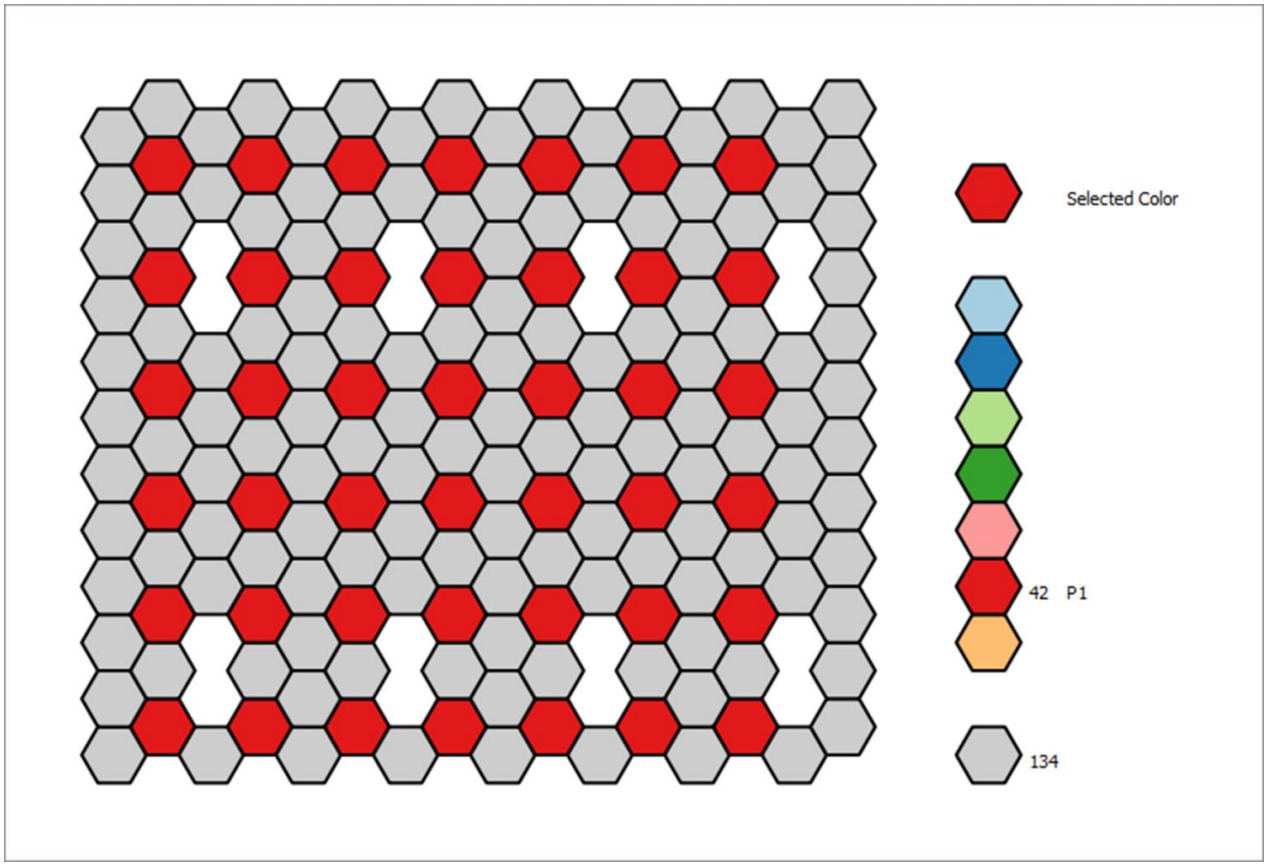

Supplementary Figure 7

10 nm DNA origami grid

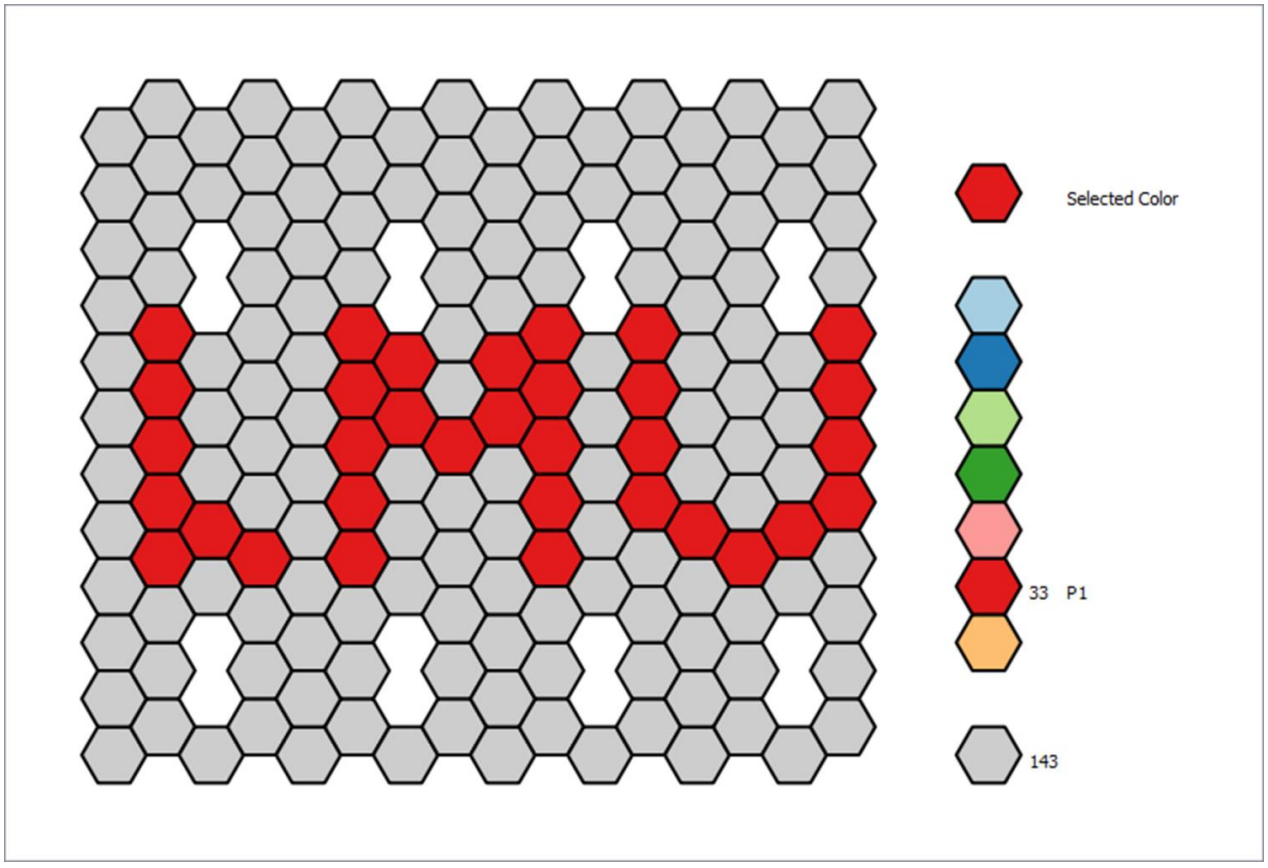

Supplementary Figure 8

LMU Logo

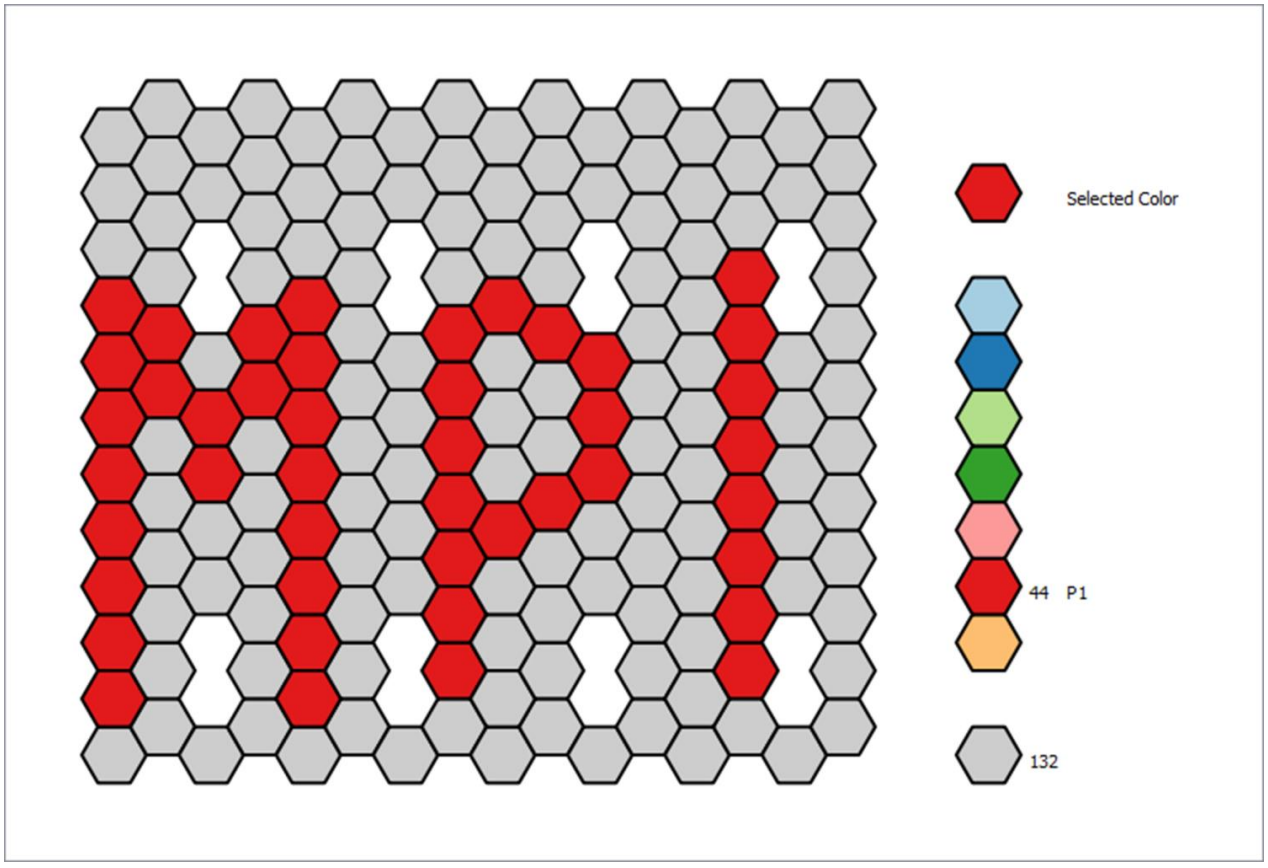

Supplementary Figure 9

MPI Logo

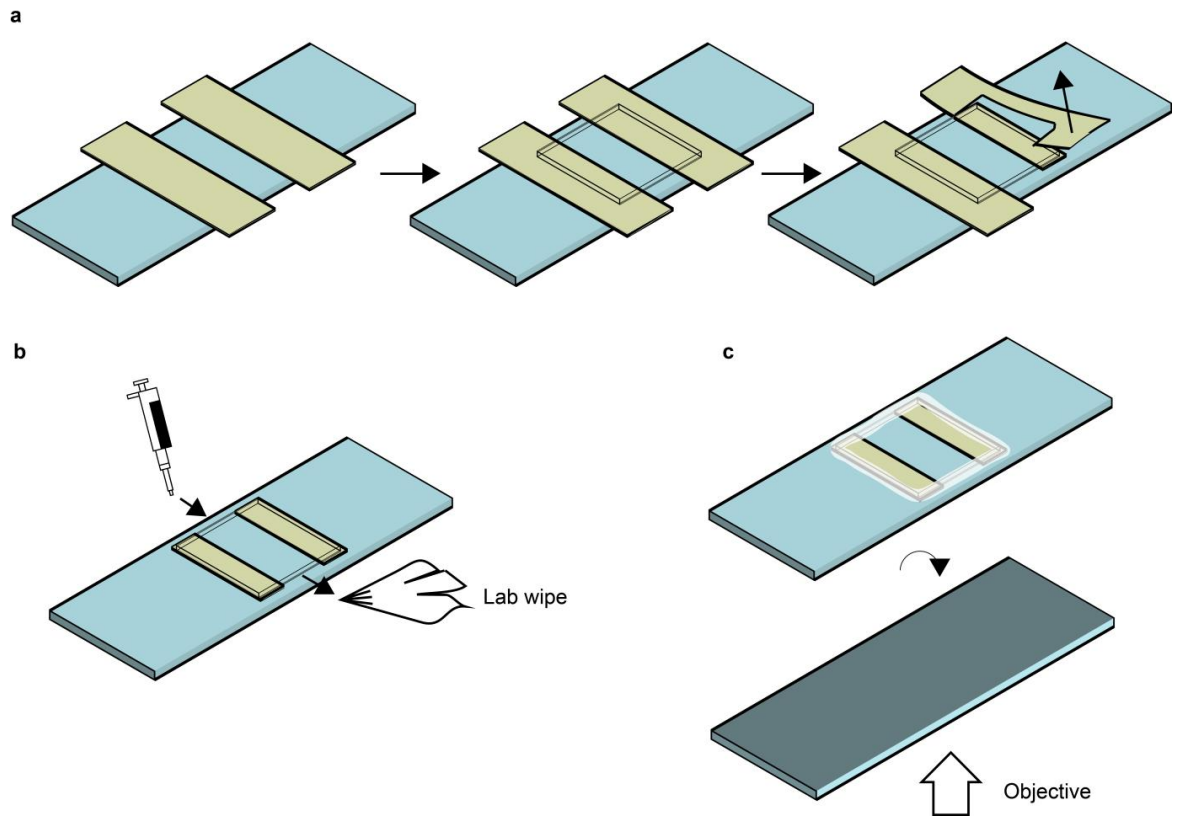

Supplementary Figure 10

Custom-made flow chamber

(a) Two stripes of double-sided sticky tape are placed on a 76x26 mm microscopy slide with a distance of ~ 8mm. A coverglass is placed on top of the sticky tape stripes. After pressing the coverglass thoroughly against the sticky tape, overlapping tape can be removed. (b) To immobilize DNA nanostructures, fluids are pipetted from one side while simultaneously being sucked out with a lab wiper from the other side. (c) The coverglass is sealed with epoxy glue and can be used with the coverglass facing towards the objective in a microscope stage once the glue is hardened.

Nature Protocols: doi:10.1038/nprot.2017.024

Supplementary Manual

This manual describes details about the Picasso program.

File Format and Name Conventions

Movie Files

Picasso accepts two type of raw movie files: TIFF (preferably from µManager, https://www.micro-manager.org) and raw binary data (file extension ".raw").

When loading raw binary files, the user will be prompted for movie metadata such as the number of frames, number of pixels, etc. Alternatively, this metadata can be supplied by an accompanying metadata file with the same filename as the raw binary file, but with the extension ".yaml". See "YAML Metadata Files" for more details.

HDF5 Files

HDF5 is a generic and efficient binary file format for storing data (https://support.hdfgroup.org/HDF5/). In Picasso, HDF5 files are used for storing tabular data of localization properties with the file extension ".hdf5". Furthermore, Picasso saves statistical properties of groups of localizations in an HDF5 file.

Generally, several datasets can be stored within an HDF5 file. These datasets are accessible by specifying a path within the HDF5 file, similar to a path of an operating system. When saving localizations, Picasso stores tabular data under the path "/locs". When saving statistical properties of groups of localizations, Picasso saves the table under the path "/groups".

Importing HDF5 files in MATLAB and Origin

In MATLAB, execute the command "locs = h5read(filename, dataset)". Replace dataset with '/locs' for localization files and with '/groups' for pick property files.

In Origin, select "File > Import > HDF5" or drag and drop the file into the main window.

Localization HDF5 Files

Localization HDF5 files must always be accompanied by a YAML metadata file with the same filename, but with the extension '.yaml'. See "YAML Metadata File" for more details. The localization table is stored as a dataset of the HDF5 file in the path "/locs". This table can be visualized by opening the HDF5 file with "Picasso: Filter". The localization table can have an unlimited number of columns. **Table 1** describes the meaning of Picasso's main column names.

Nature Protocols: doi:10.1038/nprot.2017.024

Column Name	Description	C Data Type
frame	The frame in which the localization occurred, starting with zero for the first frame.	unsigned long
x	The subpixel x coordinate in camera pixels	float
y	The subpixel y coordinate in camera pixels	float
photons	The total number of detected photons from this event, not including background or camera offset	float
sx	The Point Spread Function width in camera pixels	float
sy	The Point Spread Function height in camera pixels	float
bg	The number of background photons per pixel, not including the camera offset	float
lpx	The localization precision in x direction, in camera pixels, as estimated by the Cramer-Rao Lower Bound of the Maximum Likelihood fit.	float
lpy	The localization precision in y direction, in camera pixels, as estimated by the Cramer-Rao Lower Bound of the Maximum Likelihood fit.	float
net_gradient	The net gradient of this spot which is defined by the sum of gradient vector magnitudes within the fix box, projected to the spot center.	float
likelihood	The log-likelihood of the fit	float
iterations	The number of iterations of the fit procedure	long
group	(Optional) An identifier to assign multiple localizations to groups, for example by picking regions of interest	long
len	(Optional) The length of the event, if localizations from consecutive frames have been linked	long
n	(Optional) The number of localizations in this event, if localizations from consecutive frames have been linked, potentially diverging from the “len” column due to a transient dark time tolerance	long
photon_rate	(Optional) The mean number of photons per frame, if localizations from consecutive frames have been linked. The total number of photons is set in the “photons” column.	float

Table 1 | Name, description and data type for the main columns used in Picasso.

HDF5 Pick Property Files

When selecting “File > Save pick properties” in “Picasso: Render”, the properties of picked regions are stored in an HDF5 file. Within the HDF5 file, the data table is stored in the path “/groups”.

Each row in the “groups” table corresponds to one picked region. For each localization property (see **Table 1**), two columns are generated in the “groups” table: the mean and standard deviation of the respective column

Nature Protocols: doi:10.1038/nprot.2017.024

over the localizations in a pick region. For example, if the localization table contains a column “len”, the “groups” table will contain a column “len_mean” and “len_std”.
Furthermore, the following columns are included: “group” (the group identifier), “n_events” (the number of localizations in the region) and “n_units” (the number of units from a qPAINT measurement).

YAML Metadata Files

YAML files are document-oriented text files that can be opened and changed with any text editor (http://www.yaml.org). In Picasso, YAML files are used to store metadata of movie or localization files.
Each localization HDF5 file must always be accompanied with a YAML file of the same filename, except for the extension, which is “.yaml”. Deleting this YAML metadata file will result in failure of the Picasso software!
Raw binary files may be accompanied by a YAML metadata file to store data about the movie dimensions, etc. While the metadata file in this case is not required, it reduces the effort of typing in this metadata each time the movie is loaded with “Picasso: Localize”. To generate such a YAML metadata file, load the raw movie into “Picasso: Localize”, then enter all required information in the appearing dialog. Check the checkbox “Save info to yaml file” and click ok. The movie will be loaded and the metadata saved in a YAML file. This file will be detected the next time this raw movie is loaded and the metadata does not need to be entered again.

Supplementary Table 1: Laser power conversion table

Set Power (mW)	Power at sample (mW)	Power density at sample (kW/cm^2)
20	13.7	0.82
30	20.8	1.24
40	28	1.67
50	34.8	2.07
60	42.2	2.52
70	48.5	2.89

Power was set at the driver unit of the Coherent Sapphire Laser, 200 mW nominal power, 561 nm. Laser power was measured with a digital power meter (THORLABS, PM100D) by placing a microscopy slide thermal power sensor (THORLABS, S170C) with immersion oil in the sample holder. The power density was calculated as an average of the the gaussian illumination with an area of 256 px^2 with pixel size of 160 nm.

Nature Protocols: doi:10.1038/nprot.2017.024

Supplementary Table 2: DNA-PAINT sequences

Shortname	Docking sequence	Imager sequence
P1	TTATACATCTA	CTAGATGTAT-Dye
P2	TTATCTACATA	TATGTAGATC-Dye
P3	TTTCTTCATTA	GTAATGAAGA-Dye
P4	TTATGAATCTA	GTAGATTCAT-Dye
P5	TTTCAATGTAT	CATACATTGA-Dye
P6	TTTTAGGTAAA	CTTTACCTAA-Dye
P7	TTAATTGAGTA	GTACTCAATT-Dye
P8	TTATGTTAATG	CCATTAACAT-Dye
P9	TTAATTAGGAT	CATCCTAATT-Dye
P10	TTATAATGGAT	GATCCATTAT-Dye

Supplementary Table 3: List of core staples

Position	Name	Sequence
A1	21[32]23[31]BLK	TTTTCACTCAAAGGGCGAAAAACCATCACC
B1	23[32]22[48]BLK	CAAATCAAGTTTTTTGGGGTCGAAACGTGGA
C1	21[56]23[63]BLK	AGCTGATTGCCCTTCAGAGTCCACTATTAAAGGGTGCCGT
D1	23[64]22[80]BLK	AAAGCACTAAATCGGAACCCTAATCCAGTT
E1	21[96]23[95]BLK	AGCAAGCGTAGGGTTGAGTGTTGTAGGGAGCC
F1	23[96]22[112]BLK	CCCGATTTAGAGCTTGACGGGGAAAAAGAATA
G1	21[120]23[127]BLK	CCCAGCAGGCGAAAAATCCCTTATAAATCAAGCCGGCG
H1	21[160]22[144]BLK	TCAATATCGAACCTCAAATATCAATTCCGAAA
I1	23[128]23[159]BLK	AACGTGGCGAGAAAGGAAGGGAAACCAGTAA
J1	23[160]22[176]BLK	TAAAAGGGACATTCTGGCCAACAAAGCATC
K1	21[184]23[191]BLK	TCAACAGTTGAAAGGAGCAAATGAAAAATCTAGAGATAGA
L1	23[192]22[208]BLK	ACCCTTCTGACCTGAAAGCGTAAGACGCTGAG
M1	21[224]23[223]BLK	CTTTAGGGCCTGCAACAGTGCCAATACGTG
N1	23[224]22[240]BLK	GCACAGACAATATTTTTGAATGGGGTCAGTA
O1	21[248]23[255]BLK	AGATTAGAGCCGTCAAAAAACAGAGGTGAGGCCTATTAGT
P1	23[256]22[272]BLK	CTTTAATGCGCGAACTGATAGCCCCACCAG
A2	19[32]21[31]BLK	GTCGACTTCGGCCAACGCGCGGGGTTTTTC
B2	22[47]20[48]BLK	CTCCAACGCAGTGAGACGGGCAACCAGCTGCA

Nature Protocols: doi:10.1038/nprot.2017.024

D2	22[79]20[80]BLK	TGGAACAACCGCCTGGCCCTGAGGCCCGCT
E2	19[96]21[95]BLK	CTGTGTGATTGCGTTGCGCTCACTAGAGTTGC
F2	22[111]20[112]BLK	GCCCGAGAGTCCACGCTGGTTTGCAGCTAACT
H2	19[160]20[144]BLK	GCAATTCACATATTCCTGATTATCAAAGTGTA
I2	22[143]21[159]BLK	TCGGCAAATCCTGTTTGATGGTGGACCCTCAA
J2	22[175]20[176]BLK	ACCTTGCTTGGTCAGTTGGCAAAGAGCGGA
L2	22[207]20[208]BLK	AGCCAGCAATTGAGGAAGGTTATCATCATTTT
M2	19[224]21[223]BLK	CTACCATAGTTTGAGTAACATTTAAAATAT
N2	22[239]20[240]BLK	TTAACACCAGCACTAACAACTAATCGTTATTA
P2	22[271]20[272]BLK	CAGAAGATTAGATAATACATTTGTCGACAA
A3	17[32]19[31]BLK	TGCATCTTTCCCAGTCACGACGGCCTGCAG
B3	20[47]18[48]BLK	TTAATGAACTAGAGGATCCCCGGGGGGTAACG
D3	20[79]18[80]BLK	TTCCAGTCGTAATCATGGTCATAAAAGGGG
E3	17[96]19[95]BLK	GCTTTCCGATTACGCCAGCTGGCGGCTGTTTC
F3	20[111]18[112]BLK	CACATTAAAATTGTTATCCGCTCATGCGGGCC
H3	17[160]18[144]BLK	AGAAAACAAAGAAGATGATGAAACAGGCTGCG
I3	20[143]19[159]BLK	AAGCCTGGTACGAGCCGGAAGCATAGATGATG
J3	20[175]18[176]BLK	ATTATCATTCAATATAATCCTGACAATTAC
L3	20[207]18[208]BLK	GCGGAACATCTGAATAATGGAAGGTACAAAAT
M3	17[224]19[223]BLK	CATAAATCTTTGAATACCAAGTGTTAGAAC
N3	20[239]18[240]BLK	ATTTTAAAATCAAAATTATTTGCACGGATTCG
P3	20[271]18[272]BLK	CTCGTATTAGAAATTGCGTAGATACAGTAC
A4	15[32]17[31]BLK	TAATCAGCGGATTGACCGTAATCGTAACCG
B4	18[47]16[48]BLK	CCAGGGTTGCCAGTTTGAGGGGACCCGTGGGA
C4	15[64]18[64]BLK	GTATAAGCCAACCCGTCGGATTCTGACGACAGTATCGGCCGCAAGGCG
D4	18[79]16[80]BLK	GATGTGCTTCAGGAAGATCGCACAATGTGA
E4	15[96]17[95]BLK	ATATTTTGGCTTTCATCAACATTATCCAGCCA
F4	18[111]16[112]BLK	TCTTCGCTGCACCGCTTCTGGTGCGGCCTTCC
G4	15[128]18[128]BLK	TAAATCAAAATAATTCGCGTCTCGGAAACCAGGCAAAGGGAAGG
H4	15[160]16[144]BLK	ATCGCAAGTATGTAAATGCTGATGATAGGAAC
I4	18[143]17[159]BLK	CAACTGTTGCGCCATTCGCCATTCAAACATCA
J4	18[175]16[176]BLK	CTGAGCAAAAATTAATTACATTTTGGGTTA
K4	15[192]18[192]BLK	TCAAATATAACCTCCGGCTTAGGTAACAATTTCATTTGAAGGCGAATT

Nature Protocols: doi:10.1038/nprot.2017.024

L4	18[207]16[208]BLK	CGCGCAGATTACCTTTTTTAATGGGAGAGACT
M4	15[224]17[223]BLK	CCTAAATCAAAATCATAGGTCTAAACAGTA
N4	18[239]16[240]BLK	CCTGATTGCAATATATGTGAGTGATCAATAGT
O4	15[256]18[256]BLK	GTGATAAAAAGACGCTGAGAAGAGATAACCTTGCTTCTGTTCGGGAGA
P4	18[271]16[272]BLK	CTTTTACAAAATCGTCGCTATTAGCGATAG
A5	13[32]15[31]BLK	AACGCAAAATCGATGAACGGTACCGGTTGA
B5	16[47]14[48]BLK	ACAAACGGAAAAGCCCCAAAAACACTGGAGCA
C5	13[64]15[63]BLK	TATATTTTGTCATTGCCTGAGAGTGGAAGATT
D5	16[79]14[80]BLK	GCGAGTAAAAATATTTAAATTGTTACAAAG
E5	13[96]15[95]BLK	TAGGTAAACTATTTTTGAGAGATCAAACGTTA
F5	16[111]14[112]BLK	TGTAGCCATTAAAATTCGCATTAAATGCCGGA
G5	13[128]15[127]BLK	GAGACAGCTAGCTGATAAATTAATTTTTGT
H5	13[160]14[144]BLK	GTAATAAGTTAGGCAGAGGCATTTATGATATT
I5	16[143]15[159]BLK	GCCATCAAGCTCATTTTTTAACCACAAATCCA
J5	16[175]14[176]BLK	TATAACTAACAAAGAACGCGAGAACGCCAA
K5	13[192]15[191]BLK	GTAAAGTAATCGCCATATTTAACAAAACTTTT
L5	16[207]14[208]BLK	ACCTTTTTATTTTAGTTAATTTCATAGGGCTT
M5	13[224]15[223]BLK	ACAACATGCCAACGCTCAACAGTCTTCTGA
N5	16[239]14[240]BLK	GAATTTATTTAATGGTTTGAAATATTCTTACC
O5	13[256]15[255]BLK	GTTTATCAATATGCGTTATACAAACCGACCGT
P5	16[271]14[272]BLK	CTTAGATTTAAGGCGTTAAATAAAGCCTGT
A6	11[32]13[31]BLK	AACAGTTTTGTACCAAAAACATTTTATTTC
B6	14[47]12[48]BLK	AACAAGAGGGATAAAAATTTTTAGCATAAAGC
C6	11[64]13[63]BLK	GATTTAGTCAATAAAGCCTCAGAGAACCCTCA
D6	14[79]12[80]BLK	GCTATCAGAAATGCAATGCCTGAATTAGCA
E6	11[96]13[95]BLK	AATGGTCAACAGGCAAGGCAAAGAGTAATGTG
F6	14[111]12[112]BLK	GAGGGTAGGATTCAAAAGGGTGAGACATCCAA
G6	11[128]13[127]BLK	TTTGGGGATAGTAGTAGCATTAAAAGGCCG
H6	11[160]12[144]BLK	CCAATAGCTCATCGTAGGAATCATGGCATCAA
I6	14[143]13[159]BLK	CAACCGTTTCAAATCACCATCAATTCGAGCCA
J6	14[175]12[176]BLK	CATGTAATAGAATATAAAGTACCAAGCCGT
K6	11[192]13[191]BLK	TATCCGGTCTCATCGAGAACAAGCGACAAAAG
L6	14[207]12[208]BLK	AATTGAGAATTCTGTCCAGACGACTAAACCAA

Nature Protocols: doi:10.1038/nprot.2017.024

M6	11[224]13[223]BLK	GCGAACCTCCAAGAACGGGTATGACAATAA
N6	14[239]12[240]BLK	AGTATAAAGTTCAGCTAATGCAGATGTCTTTC
O6	11[256]13[255]BLK	GCCTTAAACCAATCAATAATCGGCACGCGCCT
P6	14[271]12[272]BLK	TTAGTATCACAATAGATAAGTCCACGAGCA
A7	9[32]11[31]BLK	TTTACCCCAACATGTTTTAAATTTCCATAT
B7	12[47]10[48]BLK	TAAATCGGGATTCCCAATTCTGCGATATAATG
C7	9[64]11[63]BLK	CGGATTGCAGAGCTTAATTGCTGAAACGAGTA
D7	12[79]10[80]BLK	AAATTAAGTTGACCATTAGATACTTTTGCG
E7	9[96]11[95]BLK	CGAAAGACTTTGATAAGAGGTCATATTTCGCA
F7	12[111]10[112]BLK	TAAATCATATAACCTGTTTAGCTAACCTTTAA
G7	9[128]11[127]BLK	GCTTCAATCAGGATTAGAGAGTTATTTTCA
H7	9[160]10[144]BLK	AGAGAGAAAAAAATGAAAATAGCAAGCAAACT
I7	12[143]11[159]BLK	TTCTACTACGCGAGCTGAAAAGGTTACCGCGC
J7	12[175]10[176]BLK	TTTTATTTAAGCAAATCAGATATTTTTTGT
K7	9[192]11[191]BLK	TTAGACGGCCAAATAAGAAACGATAGAAGGCT
L7	12[207]10[208]BLK	GTACCGCAATTCTAAGAACGCGAGTATTATTT
M7	9[224]11[223]BLK	AAAGTCACAAAATAAACAGCCAGCGTTTTA
N7	12[239]10[240]BLK	CTTATCATTCCCGACTTGCGGGAGCCTAATTT
O7	9[256]11[255]BLK	GAGAGATAGAGCGTCTTTCCAGAGGTTTTGAA
P7	12[271]10[272]BLK	TGTAGAAATCAAGATTAGTTGCTCTTACCA
A8	7[32]9[31]BLK	TTTAGGACAAATGCTTTAAACAATCAGGTC
B8	10[47]8[48]BLK	CTGTAGCTTGACTATTATAGTCAGTTCATTGA
C8	7[56]9[63]BLK	ATGCAGATACATAACGGGAATCGTCATAAATAAAGCAAAG
D8	10[79]8[80]BLK	GATGGCTTATCAAAAAGATTAAGAGCGTCC
E8	7[96]9[95]BLK	TAAGAGCAAATGTTTAGACTGGATAGGAAGCC
F8	10[111]8[112]BLK	TTGCTCCTTTCAAATATCGCGTTTGAGGGGGT
G8	7[120]9[127]BLK	CGTTTACCAGACGACAAAGAAGTTTTGCCATAATTCGA
H8	7[160]8[144]BLK	TTATTACGAAGAACTGGCATGATTGCGAGAGG
I8	10[143]9[159]BLK	CCAACAGGAGCGAACCAGACCGGAGCCTTTAC
J8	10[175]8[176]BLK	TTAACGTCTAACATAAAAACAGGTAACGGA
K8	7[184]9[191]BLK	CGTAGAAAATACATACCGAGGAAACGCAATAAGAAGCGCA
L8	10[207]8[208]BLK	ATCCCAATGAGAATTAACTGAACAGTTACCAG
M8	7[224]9[223]BLK	AACGCAAAGATAGCCGAACAAACCCTGAAC

Nature Protocols: doi:10.1038/nprot.2017.024

N8	10[239]8[240]BLK	GCCAGTTAGAGGGTAATTGAGCGCTTTAAGAA
O8	7[248]9[255]BLK	GTTTATTTTGTCACAATCTTACCGAAGCCCTTTAATATCA
P8	10[271]8[272]BLK	ACGCTAACACCCACAAGAATTGAAAATAGC
A9	5[32]7[31]BLK	CATCAAGTAAAACGAACTAACGAGTTGAGA
B9	8[47]6[48]BLK	ATCCCCCTATACCACATTCAACTAGAAAAATC
D9	8[79]6[80]BLK	AATACTGCCCAAAAGGAATTACGTGGCTCA
E9	5[96]7[95]BLK	TCATTCAGATGCGATTTTAAGAACAGGCATAG
F9	8[111]6[112]BLK	AATAGTAAACACTATCATAACCCTCATTGTGA
H9	5[160]6[144]BLK	GCAAGGCCTCACCAGTAGCACCATGGGCTTGA
I9	8[143]7[159]BLK	CTTTTGCAGATAAAAACCAAAATAAAGACTCC
J9	8[175]6[176]BLK	ATACCCAACAGTATGTTAGCAAATTAGAGC
L9	8[207]6[208]BLK	AAGGAAACATAAAGGTGGCAACATTATCACCG
M9	5[224]7[223]BLK	TCAAGTTTCATTAAAGGTGAATATAAAAGA
N9	8[239]6[240]BLK	AAGTAAGCAGACACCACGGAATAATATTGACG
P9	8[271]6[272]BLK	AATAGCTATCAATAGAAAATTCAACATTCA
A10	3[32]5[31]BLK	AATACGTTTGAAAGAGGACAGACTGACCTT
B10	6[47]4[48]BLK	TACGTTAAAGTAATCTTGACAAGAACCGAACT
D10	6[79]4[80]BLK	TTATACCACCAAATCAACGTAACGAACGAG
E10	3[96]5[95]BLK	ACACTCATCCATGTTACTTAGCCGAAAGCTGC
F10	6[111]4[112]BLK	ATTACCTTTGAATAAGGCTTGCCCAAATCCGC
H10	3[160]4[144]BLK	TTGACAGGCCACCACCAGAGCCGCGATTTGTA
I10	6[143]5[159]BLK	GATGGTTTGAACGAGTAGTAAATTTACCATTA
J10	6[175]4[176]BLK	CAGCAAAAGGAAACGTCACCAATGAGCCGC
L10	6[207]4[208]BLK	TCACCGACGCACCGTAATCAGTAGCAGAACCG
M10	3[224]5[223]BLK	TTAAAGCCAGAGCCGCCACCCTCGACAGAA
N10	6[239]4[240]BLK	GAAATTATTGCCTTTAGCGTCAGACCGGAACC
P10	6[271]4[272]BLK	ACCGATTGTCGGCATTTTCGGTCATAATCA
A11	1[32]3[31]BLK	AGGCTCCAGAGGCTTTGAGGACACGGGTAA
B11	4[47]2[48]BLK	GACCAACTAATGCCACTACGAAGGGGGTAGCA
C11	1[64]4[64]BLK	TTTATCAGGACAGCATCGGAACGACACCAACCTAAAACGAGGTCAATC
D11	4[79]2[80]BLK	GCGCAGACAAGAGGCAAAAGAATCCCTCAG
E11	1[96]3[95]BLK	AAACAGCTTTTTGCGGGATCGTCAACACTAAA
F11	4[111]2[112]BLK	GACCTGCTCTTTGACCCCCAGCGAGGGAGTTA

Nature Protocols: doi:10.1038/nprot.2017.024

G11	1[128]4[128]BLK	TGACAACTCGCTGAGGCTTGCATTATACCAAGCGCGATGATAAA
H11	1[160]2[144]BLK	TTAGGATTGGCTGAGACTCCTCAATAACCGAT
I11	4[143]3[159]BLK	TCATCGCCAACAAAGTACAACGGACGCCAGCA
J11	4[175]2[176]BLK	CACCAGAAAGGTTGAGGCAGGTCATGAAAG
K11	1[192]4[192]BLK	GCGGATAACCTATTATTCTGAAACAGACGATTGGCCTTGAAGAGCCAC
L11	4[207]2[208]BLK	CCACCCTCTATTCACAAACAAATACCTGCCTA
M11	1[224]3[223]BLK	GTATAGCAAACAGTTAATGCCCAATCCTCA
N11	4[239]2[240]BLK	GCCTCCCTCAGAATGGAAAGCGCAGTAACAGT
O11	1[256]4[256]BLK	CAGGAGGTGGGGTCAGTGCCTTGAGTCTCTGAATTTACCGGGAACCAG
P11	4[271]2[272]BLK	AAATCACCTTCCAGTAAGCGTCAGTAATAA
A12	0[47]1[31]BLK	AGAAAGGAACAACTAAAGGAATTCAAAAAAA
B12	2[47]0[48]BLK	ACGGCTACAAAAGGAGCCTTTAATGTGAGAAT
C12	0[79]1[63]BLK	ACAACTTTCAACAGTTTCAGCGGATGTATCGG
D12	2[79]0[80]BLK	CAGCGAAACTTGCTTTCGAGGTGTTGCTAA
E12	0[111]1[95]BLK	TAAATGAATTTTCTGTATGGGATTAATTTCTT
F12	2[111]0[112]BLK	AAGGCCGCTGATACCGATAGTTGCGACGTTAG
G12	0[143]1[127]BLK	TCTAAAGTTTTGTCGTCTTTCCAGCCGACAA
H12	0[175]0[144]BLK	TCCACAGACAGCCCTCATAGTTAGCGTAACGA
I12	2[143]1[159]BLK	ATATTCGGAACCATCGCCCACGCAGAGAAGGA
J12	2[175]0[176]BLK	TATTAAGAAGCGGGGTTTTGCTCGTAGCAT
K12	0[207]1[191]BLK	TCACCAGTACAAACTACAACGCCTAGTACCAG
L12	2[207]0[208]BLK	TTTCGGAAGTGCCGTCGAGAGGGTGAGTTTCG
M12	0[239]1[223]BLK	AGGAACCCATGTACCGTAACACTTGATATAA
N12	2[239]0[240]BLK	GCCCGTATCCGGAATAGGTGTATCAGCCCAAT
O12	0[271]1[255]BLK	CCACCCTCATTTTCAGGGATAGCAACCGTACT
P12	2[271]0[272]BLK	GTTTTAACTTAGTACCGCCACCCAGAGCCA

Supplementary Table 4: List of biotinylated staples

No	Position	Name	Sequence	Mod
1	C02	18[63]20[56]BIOTIN	ATTAAGTTTACCGAGCTCGAATTCGGGAAACCTGTCGTGC	5'-BT
2	C09	4[63]6[56]BIOTIN	ATAAGGGAACCGGATATTCATTACGTCAGGACGTTGGGAA	5'-BT
3	G02	18[127]20[120]BIOTIN	GCGATCGGCAATTCCACACAACAGGTGCCTAATGAGTG	5'-BT
4	G09	4[127]6[120]BIOTIN	TTGTGTCGTGACGAGAAACACCAAATTTCAACTTTAAT	5'-BT

Nature Protocols: doi:10.1038/nprot.2017.024

5	K02	18[191]20[184]BIOTIN	ATTCATTTTTGTTTGGATTATACTAAGAAACCACCAGAAG	5'-BT
6	K09	4[191]6[184]BIOTIN	CACCCTCAGAAACCATCGATAGCATTGAGCCATTTGGGAA	5'-BT
7	O02	18[255]20[248]BIOTIN	AACAATAACGTAAAACAGAAATAAAAATCCTTTGCCCGAA	5'-BT
8	O09	4[255]6[248]BIOTIN	AGCCACCACTGTAGCGCGTTTTCAAGGGAGGGAAGGTAAA	5'-BT

Supplementary Table 5: Exemplary folding table

Component	Initial conc. (µM)	Parts	Pool conc. (nM)	Target conc. (nM)	Volume (µl)	Excess
Scaffold	0.1	1	100	10	4	1
Core Mix	100	164	609.7560976	100	6.56	10
P1 Mix	100	12	8333.333333	1000	4.8	100
Biotin 1:10	100	80	1250	10	0.32	1
H_2O					20.32	
10x Folding Buffer					4	
Total Volume					40	

Supplementary Table 6: Experimental conditions

Figure	Type	Sample	Imager	Buffer	Frames	t_{int}	c_i	Power	PPT	Camera
1b, 7c	in vitro	20 nm grids	P1	B+	7500	300 ms	5 nM	1.5 kW/cm^2	Yes	EMCCD
1d, e	in situ	Microtubules	P3	C	50000	100 ms	2 nM	2.5 kW/cm^2	No	EMCCD
2d–f	in vitro	Exchange rectangle	P1,P3	B+	7500	300 ms	10 nM	6 kW/cm^2	Yes	EMCCD
2g	in situ	Microtubules / Mitochondria	P1,P3	C	20000	150 ms	0.8 nM	2 kW/cm^2	No	EMCCD
3d–f 4d, f	in vitro	10 and 20 nm grids, LMU logo	P1	B+	80000	350 ms	0.7 nM	4.5 kW/cm^2	Yes	sCMOS
4b, c, e	in vitro	10 and 20 nm grids, MPI logo	P1	B+	80000	350 ms	1 nM	4.5 kW/cm^2	Yes	sCMOS

Nature Protocols: doi:10.1038/nprot.2017.024

For full details on acquisition settings see corresponding YAML files.

Supplementary Table 7: Dye recommendations

Excitation	Rank	Excitation wavelength (nm)	Dye	Compatible with PCA/PCD/Trolox System
Red	1	640	Atto647N	Yes
	2	640	Cy5	Yes
	3	640	Atto655	No
Green	1	561	Cy3b	Yes
	2	561	Atto565	Yes
	3	561	Cy3	Yes
Blue	1	488	Atto488	Yes
	2	488	Alexa488	Yes

Nature Protocols: doi:10.1038/nprot.2017.024

BIBLIOGRAPHY

[1] J. R. Lakowicz. “Introduction to Fluorescence.” In: *Principles of Fluorescence Spectroscopy* (2006), pp. 1–26 (cit. on pp. 2–4).

[2] G. G. Stokes, M A, and F. R. S. “XXX. On the change of refrangibility of light.” In: *Philosophical Transactions of the Royal Society of London* 142.0 (1852), pp. 463–562 (cit. on p. 3).

[3] G. C. Roberts. *Encyclopedia of Biophysics*. Springer Verlag, 2012 (cit. on p. 3).

[4] M. Tokunaga, N. Imamoto, and K. Sakata-Sogawa. “Highly inclined thin illumination enables clear single-molecule imaging in cells.” In: *Nature Methods* 5.2 (2008), pp. 159–161 (cit. on p. 6).

[5] E. J. Ambrose. “A Surface Contact Microscope for the study of Cell Movements.” In: *Nature* 178.4543 (1956), pp. 1194–1194 (cit. on p. 6).

[6] D Axelrod. “Cell-substrate contacts illuminated by total internal reflection fluorescence.” In: *The Journal of cell biology* 89.1 (1981), pp. 141–145 (cit. on p. 7).

[7] K. N. Fish. “Total internal reflection fluorescence (TIRF) microscopy.” In: *Current protocols in cytometry* Chapter 12.1 (2009), Unit12.18–12.18.13 (cit. on p. 7).

[8] E. Abbe. “Beiträge zur Theorie des Mikroskops und der mikroskopischen Wahrnehmung.” In: *Archiv für Mikroskopische Anatomie* (1873) (cit. on p. 8).

[9] H. Blom and J. Widengren. “Stimulated Emission Depletion Microscopy.” In: *Chemical reviews* 117.11 (2017), pp. 7377–7427 (cit. on pp. 8, 9).

[10] C. Cremer and B. R. Masters. “Resolution enhancement techniques in microscopy.” In: *The European Physical Journal H* 38.3 (2013), pp. 281–344 (cit. on p. 9).

[11] S. W. Hell and J Wichmann. “Breaking the Diffraction Resolution Limit by Stimulated-Emission - Stimulated-Emission-Depletion Fluorescence Microscopy.” In: *Optics letters* 19.11 (1994), pp. 780–782 (cit. on p. 9).

[12] J. Keller, A. Schoenle, and S. W. Hell. “Efficient fluorescence inhibition patterns for RESOLFT microscopy.” In: *Optics Express* 15.6 (2007), pp. 3361–3371 (cit. on p. 9).

[13] B. Harke, J. Keller, C. K. Ullal, V. Westphal, A. Schoenle, and S. W. Hell. “Resolution scaling in STED microscopy.” In: *Optics Express* 16.6 (2008), pp. 4154–4162 (cit. on p. 9).

[14] R. E. Thompson, D. R. Larson, and W. W. Webb. “Precise nanometer localization analysis for individual fluorescent probes.” In: *Biophysical journal* 82.5 (2002), pp. 2775–2783 (cit. on p. 10).

[15] E. Betzig, G. H. Patterson, R. Sougrat, O. W. Lindwasser, S. Olenych, J. S. Bonifacino, M. W. Davidson, J. Lippincott-Schwartz, and H. F. Hess. “Imaging intracellular fluorescent proteins at nanometer resolution.” In: *Science (New York, N.Y.)* 313.5793 (2006), pp. 1642–1645 (cit. on p. 10).

[16] S. T. Hess, T. P. K. Girirajan, and M. D. Mason. “Ultra-high resolution imaging by fluorescence photoactivation localization microscopy.” In: *Biophysical journal* 91.11 (2006), pp. 4258–4272 (cit. on p. 10).

[17] M. J. Rust, M. Bates, and X. Zhuang. “Sub-diffraction-limit imaging by stochastic optical reconstruction microscopy (STORM).” In: *Nature Methods* 3.10 (2006), pp. 793–795 (cit. on p. 10).

[18] F. Balzarotti, Y. Eilers, K. C. Gwosch, A. H. Gynna, V. Westphal, F. D. Stefani, J. Elf, and S. W. Hell. “Nanometer resolution imaging and tracking of fluorescent molecules with minimal photon fluxes.” In: *Science (New York, N.Y.)* 355.6325 (2017), pp. 606–612 (cit. on pp. 10, 87).

[19] A. Sharonov and R. M. Hochstrasser. “Wide-field subdiffraction imaging by accumulated binding of diffusing probes.” In: *Proceedings of the National Academy of Sciences of the United States of America* 103.50 (2006), pp. 18911–18916 (cit. on p. 10).

[20] G. Giannone, E. Hosy, F. Levet, A. Constals, K. Schulze, A. I. Sobolevsky, M. P. Rosconi, E. Gouaux, R. Tampé, D. Choquet, et al. “Dynamic superresolution imaging of endogenous proteins on living cells at ultra-high density.” In: *Biophysical journal* 99.4 (2010), pp. 1303–1310 (cit. on p. 10).

[21] R. Jungmann, C. Steinhauer, M. Scheible, A. Kuzyk, P. Tinnefeld, and F. C. Simmel. “Single-molecule kinetics and super-resolution microscopy by fluorescence imaging of transient binding on DNA origami.” In: *Nano letters* 10.11 (2010), pp. 4756–4761 (cit. on pp. 11, 81).

[22] R. Jungmann, M. S. Avendaño, J. B. Woehrstein, M. Dai, W. M. Shih, and P. Yin. “Multiplexed 3D cellular super-resolution imaging with DNA-PAINT and Exchange-PAINT.” In: *Nature Methods* 11.3 (2014), pp. 313–318 (cit. on p. 12).

[23] R. Jungmann, M. S. Avendaño, M. Dai, J. B. Woehrstein, S. S. Agasti, Z. Feiger, A. Rodal, and P. Yin. "Quantitative super-resolution imaging with qPAINT." In: *Nature Methods* 13.5 (2016), pp. 439–442 (cit. on p. 12).

[24] B. Alberts, J. Wilson, and T. Hunt. *Molecular biology of the cell.* New York: Garland Science, 2008 (cit. on p. 13).

[25] P. Yakovchuk, E. Protozanova, and M. D. Frank-Kamenetskii. "Base-stacking and base-pairing contributions into thermal stability of the DNA double helix." In: *Nucleic acids research* 34.2 (2006), pp. 564–574 (cit. on p. 13).

[26] Spiffistan. "Space-filling model animation of B-DNA, made with qutemol." In: *https://commons.wikimedia.org/wiki/File:Bdna.gif* (2007) (cit. on p. 14).

[27] M. P. Ball. "Chemical structure of DNA." In: *https://commons.wikimedia.org/wiki/File:DNA_chemical_structure.svg* (2016) (cit. on p. 14).

[28] N. C. Seeman. "Nucleic acid junctions and lattices." In: *Journal of Theoretical Biology* 99.2 (1982), pp. 237–247 (cit. on p. 15).

[29] N. C. Seeman and H. F. Sleiman. "DNA nanotechnology." In: *Nature Reviews Materials* 3 (2017), 17068 EP – (cit. on p. 15).

[30] P. W. K. Rothemund. "Folding DNA to create nanoscale shapes and patterns." In: *Nature* 440.7082 (2006), pp. 297–302 (cit. on p. 15).

[31] S. M. Douglas, A. H. Marblestone, S. Teerapittayanon, A. Vazquez, G. M. Church, and W. M. Shih. "Rapid prototyping of 3D DNA-origami shapes with caDNAno." In: *Nucleic acids research* 37.15 (2009), pp. 5001–5006 (cit. on p. 15).

[32] E. Benson, A. Mohammed, J. Gardell, S. Masich, E. Czeizler, P. Orponen, and B. Högberg. "DNA rendering of polyhedral meshes at the nanoscale." In: *Nature* 523.7561 (2015), pp. 441–444 (cit. on p. 15).

[33] D.-N. Kim, F. Kilchherr, H. Dietz, and M. Bathe. "Quantitative prediction of 3D solution shape and flexibility of nucleic acid nanostructures." In: *Nucleic acids research* 40.7 (2012), pp. 2862–2868 (cit. on p. 15).

[34] B. Wei, M. Dai, and P. Yin. "Complex shapes self-assembled from single-stranded DNA tiles." In: *Nature* 485.7400 (2012), pp. 623–626 (cit. on p. 15).

[35] Y. Ke, L. L. Ong, W. M. Shih, and P. Yin. "Three-dimensional structures self-assembled from DNA bricks." In: *Science (New York, N.Y.)* 338.6111 (2012), pp. 1177–1183 (cit. on p. 15).

[36] L. L. Ong, N. Hanikel, O. K. Yaghi, C. Grun, M. T. Strauss, P. Bron, J. Lai-Kee-Him, F. Schueder, B. Wang, P. Wang, et al. "Programmable self-assembly of three-dimensional nanostructures from 10,000 unique components." In: *Nature* 552.7683 (2017), pp. 72–77 (cit. on p. 15).

[37] R. Jungmann, M. Scheible, A. Kuzyk, G. Pardatscher, C. E. Castro, and F. C. Simmel. "DNA origami-based nanoribbons: assembly, length distribution, and twist." In: *Nanotechnology* 22.27 (2011), pp. 275301–7 (cit. on p. 15).

[38] I. H. Stein, V. Schüller, P. Böhm, P. Tinnefeld, and T. Liedl. "Single-molecule FRET ruler based on rigid DNA origami blocks." In: *Chemphyschem : a European journal of chemical physics and physical chemistry* 12.3 (2011), pp. 689–695 (cit. on p. 17).

[39] J. J. Schmied, A. Gietl, P. Holzmeister, C. Forthmann, C. Steinhauer, T. Dammeyer, and P. Tinnefeld. "Fluorescence and super-resolution standards based on DNA origami." In: *Nature Methods* 9.12 (2012), pp. 1133–1134 (cit. on p. 17).

[40] C. Lin, R. Jungmann, A. M. Leifer, C. Li, D. Levner, G. M. Church, W. M. Shih, and P. Yin. "Submicrometre geometrically encoded fluorescent barcodes self-assembled from DNA." In: *Nature Chemistry* 4.10 (2012), pp. 832–839 (cit. on p. 17).

[41] C. Steinhauer, R. Jungmann, T. L. Sobey, F. C. Simmel, and P. Tinnefeld. "DNA Origami as a Nanoscopic Ruler for Super-Resolution Microscopy." In: *Angewandte Chemie International Edition* 48.47 (2009), pp. 8870–8873 (cit. on p. 17).

[42] J. B. Woehrstein, M. T. Strauss, L. L. Ong, B. Wei, D. Y. Zhang, R. Jungmann, and P. Yin. "Sub–100-nm metafluorophores with digitally tunable optical properties self-assembled from DNA." In: *Science advances* 3.6 (2017), e1602128 (cit. on pp. 19, 111).

[43] K. F. Wagenbauer, C. H. Wachauf, and H. Dietz. "Quantifying quality in DNA self-assembly." In: *Nature communications* 5 (2014), p. 3691 (cit. on p. 32).

[44] C. Myhrvold, M. Baym, N. Hanikel, L. L. Ong, J. S. Gootenberg, and P. Yin. "Barcode extension for analysis and reconstruction of structures." In: *Nature communications* 8 (2017), p. 14698 (cit. on p. 32).

[45] M. T. Strauss, F. Schueder, D. Haas, P. C. Nickels, and R. Jungmann. "Quantifying absolute addressability in DNA origami with molecular resolution." In: *Nature communications* 9.1 (2018), p. 1600 (cit. on pp. 35, 143).

[46] U. Endesfelder, S. Malkusch, F. Fricke, and M. Heilemann. “A simple method to estimate the average localization precision of a single-molecule localization microscopy experiment.” In: *Histochemistry and cell biology* 141.6 (2014), pp. 629–638 (cit. on p. 46).

[47] J. Schnitzbauer, M. T. Strauss, T. Schlichthaerle, F. Schueder, and R. Jungmann. “Super-resolution microscopy with DNA-PAINT.” In: *Nature protocols* 12 (2017), 1198 EP – (cit. on pp. 47, 167).

[48] V. Venkataramani, F. Herrmannsdörfer, M. Heilemann, and T. Kuner. “SuReSim: simulating localization microscopy experiments from ground truth models.” In: *Nature Methods* 13.4 (2016), pp. 319–321 (cit. on p. 79).

[49] T. Novák, T. Gajdos, J. Sinkó, G. Szabó, and M. Erdélyi. “TestSTORM: Versatile simulator software for multimodal super-resolution localization fluorescence microscopy.” In: *Scientific Reports* 7.1 (2017), p. 951 (cit. on p. 79).

[50] A. Girsault, T. Lukes, A. Sharipov, S. Geissbuehler, M. Leutenegger, W. Vandenberg, P. Dedecker, J. Hofkens, and T. Lasser. “SOFI Simulation Tool: A Software Package for Simulating and Testing Super-Resolution Optical Fluctuation Imaging.” In: *PLoS ONE* 11.9 (2016), e0161602 (cit. on p. 79).

[51] D. Kroese, T. Brereton, T. Taimre, and Z. I. Botev. “Why the Monte Carlo method is so important today.” In: *Wiley Interdisciplinary Reviews: Computational Statistics* (2014) (cit. on p. 79).

[52] S. Bänfer, D. Schneider, J. Dewes, M. T. Strauss, S.-A. Freibert, T. Heimerl, U. G. Maier, H.-P. Elsässer, R. Jungmann, and R. Jacob. “Molecular mechanism to recruit galectin-3 into multivesicular bodies for polarized exosomal secretion.” In: *Proceedings of the National Academy of Sciences of the United States of America* 115.19 (2018), E4396–E4405 (cit. on pp. 84, 85).

[53] M. Dai, R. Jungmann, and P. Yin. “Optical imaging of individual biomolecules in densely packed clusters.” In: *Nature nanotechnology* 11.9 (2016), pp. 798–807 (cit. on p. 87).

[54] Yikrazuul. “reaction scheme using a snap-tag.” In: *https://de.wikipedia.org/wiki/Datei:SNAP-tag.svg* (2012) (cit. on p. 102).

[55] N. E. Biolabs. “SNAP-Tag Overview Tutorial.” In: *https://youtu.be/NBRk3f6q-_M* (2011) (cit. on p. 102).

[56] K. H. Bui, A. von Appen, A. L. DiGuilio, A. Ori, L. Sparks, M.-T. Mackmull, T. Bock, W. Hagen, A. Andres-Pons, J. S. Glavy, et al. “Integrated Structural Analysis of the Human Nuclear Pore Complex Scaffold.” In: *Cell* 155.6 (2013), pp. 1233–1243 (cit. on p. 102).